Damage Mechanics Approaches for Sharp and Diffuse Fracture Propagation: Application to Ice Sheet Fracture and Composite Delamination

By

Stephen Jiménez

Dissertation

Submitted to the Faculty of the

Graduate School of Vanderbilt University

in partial fulfillment of the requirements

for the degree of

DOCTOR OF PHILOSOPHY

in

Civil Engineering

December 16, 2017

Nashville, Tennessee

Approved:

Ravindra Duddu, Ph.D.

Prodyot K. Basu, Ph.D.

Caglar Oskay, Ph.D.

Haoxiang Luo, Ph.D.

I offer thanks to my Lord and Savior Jesus Christ for placing me at Vanderbilt University and gifting me with the opportunity to pursue a Ph.D. It is humbling to know how much I am blessed to participate in this program.

I also thank my parents, my brother Daniel, and all other relatives and friends who have loved and supported me throughout these past few years.

I would like to thank Dr. Ravindra Duddu for guiding and mentoring me throughout my studies. Without his help, I would not have developed the problem-solving skills nor the engineering knowledge which I now possess.

Lastly, I would like to extend my thanks to the teaching faculty and my fellow students at Vanderbilt University. I have truly enjoyed being part of the Vanderbilt community.

TABLE OF CONTENTS

LIST OF TABLES

LIST OF FIGURES

CHAPTER 1

INTRODUCTION

The purpose of this dissertation is to develop damage mechanics approaches for the numerical modeling of fracture evolution along sharp (e.g., zero-thickness) and diffuse interfaces resulting from creep or fatigue degradation. Throughout this work, three computational damage mechanics frameworks, namely the cohesive zone model (CZM), continuum damage mechanics (CDM), and the phase field model (PFM) for brittle fracture, are implemented within the finite element analysis and extended to incorporate time- and rate- dependent damage mechanisms. The CZM is a robust methodology for simulating sharp crack growth and friction sliding under non-monotonic mixed-mode loading conditions, whereas gradient and nonlocal CDM and PFM approaches are suited for modeling the evolution of diffuse crack interfaces. The selection of the CZM is motivated by the need to simulate interface degradation in laminate composites subjected to high-cycle fatigue loading, whereas CDM is employed to model time-dependent crevasse propagation in polar ice sheets undergoing creep deformations. The CZM and PFM are also deployed to model the time-independent, brittle fracture of polar ice sheets by simulating the evolution of water-filled crevasses.

Damage mechanics is the study of fracture initiation and propagation in materials undergoing mechanical loading. The fundamental concept is to characterize the presence of microscopic defects, such as micro-cracks or micro-voids, within the macroscopic material behavior. Consider, for example, a distribution of micro-voids within a material volume; during loading the voids can gradually grow in size, thus weakening the material until they coalesce into a macro-crack. From this perspective, damage is physically interpreted as the ratio of the area of micro-defects S_i^D to the total area S_i^T of material along its principal planes, that is, cross-sectional cuts of the material normal to each principal direction

$i = \{1,2,3\}$ [Lemaitre, 1992]. Depending on the size scale of damage with respect to the system, the damage front can be represented as either a sharp interface with zero thickness or a diffuse interface with finite (nonzero) thickness. Traditional CDM methods characterize damage as a volume representing the void space throughout the diffuse interface; for example, an idealized (isotropic) damaged medium is assumed to comprise uniformly distributed, spherical micro-voids. The CZM, on the other hand, projects damage onto a sharp interface, and so damage is characterized as an area representing micro-cracks across the interface. In either of these frameworks, the state of damaged or degraded material is generally characterized using a damage tensor $\boldsymbol{D}$, however in the simplified case of isotropic damage, a scalar variable $D = S^D/S^T$ sufficiently describes the damaged material state. Thus, for undamaged (virgin) material $D = 0$, whereas for a fully damaged material $D = 1$. Partially damaged material (i.e., where $0 < D < 1$) becomes more stressed and compliant, which is accounted by the principle of effective stress [Kachanov, 1958, Rabotnov, 1963] and the hypothesis of strain equivalence [Lemaitre, 1971] or energy equivalence [Sidoroff, 1981]. In practice, damage-induced compliance is incorporated into a material's constitutive behavior by reducing the stiffness or viscosity with the factor $(1-D)$. This implementation of damage is appropriate for modeling fracture evolution in both sharp and diffuse interfaces, which is demonstrated through the work presented in this dissertation. Moreover, damage mechanics offers a convenient framework wherein multiple damage mechanisms (e.g., quasi-static loading, cyclic loading, hydraulic fracture, or even corrosion) can simultaneously degrade material.

The first objective of this dissertation is to apply the CZM framework to model the high-cycle fatigue delamination of composites. In the past two decades, the CZM has been extensively used within the finite element analysis to simulate the progressive growth of delamination and debonding in composite structures, whose design is increasingly dictated by lighter weight and better performance requirements. In this approach, special interface elements known as cohesive elements are placed along potential crack paths (e.g., the lami-

nate interface) between bulk (continuum) elements. Then, cohesive (or traction-separation) laws derived from damage mechanics formulations are defined to prescribe the constitutive behavior of the cohesive elements placed along the finite element edges. A variety of cohesive laws have been developed in the literature for monotonic loading scenarios featuring bilinear, trapezoidal, polynomial, or exponential shapes [van den Bosch et al., 2006]; generally, these cohesive laws feature an initial linear-elastic response to loading followed by damage-softening behavior. More recently, CZMs have been developed to investigate high-cycle fatigue debonding and delamination growth, which are the dominant modes of failure for subcritical cyclic loading in laminated composite structures [Mi et al., 1998b]. The CZM is a damage mechanics approach for simulating fracture [Alfano and Crisfield, 2001], and thus it is phenomenological in nature. Although many of the CZM parameters have a physical interpretation, they are actually calibrated by fitting the model results to experimental data. Consequently, the viability of CZMs as reliable and accurate progressive damage accumulation models rests on the use and development of cohesive laws that are minimally sensitive to phenomenological parameters.

The significance of static cohesive parameters (e.g., the initial stiffness and cohesive strength) has already been investigated for monotonic (static) loading cases, and several studies reported that the shape of the cohesive law has little effect on global load-displacement behavior so long as the critical fracture energy is held constant [Valoroso and Champaney, 2006, Gustafson and Waas, 2009]. However, there are some static loading studies where numerical results are sensitive to the CZM parameters, particularly the cohesive strength (i.e., maximum traction) and the shape of the damage-softening regime [Chandra et al., 2002, de Borst, 2003]. Recent studies have also demonstrated a dependency of global numerical results on the loading rate. For high-cycle fatigue loading, the approach has generally been to decompose damage into static and fatigue components and employ power-law functions to describe fatigue damage accumulation over large numbers of cycles [Robinson et al., 2005, Harper and Hallett, 2010, Khoramishad et al., 2010, de Moura and Gonçalves,

2014, Jimenez et al., 2014]. Typically, the power law function is defined based on either the interface separation or the strain energy release rate (SERR) by introducing two new parameters, namely, the damage coefficient and exponent. These two model parameters are then calibrated by matching numerical results to the experimental data in the Paris regime, wherein the crack growth rate with respect to loading cycles $\mathrm{d}a/\mathrm{d}N$ varies linearly with the strain energy release rate ΔG or the stress intensity factor ΔK when plotted on a log-log scale [Paris et al., 1961, Paris and Erdogan, 1963]. A key point is that the interaction between static and fatigue damage under cyclic loading introduces a non-physical dependence of fatigue crack growth rate on static model parameters of cohesive stiffness and cohesive strength, which are usually taken as penalty parameters under monotonic loading cases [Pascoe et al., 2013]. Additionally, the crack growth rate predictions may be affected by the lack of smoothness of cohesive law (e.g. bilinear shape with C^0 continuity) due to an abrupt change from linear elastic behavior to damage-induced softening behavior. To this end, we establish a reliable CZM approach for modeling fatigue delamination of composites which alleviates spurious sensitivity to the constituent cohesive parameters.

The second objective of this dissertation is to apply the CDM framework to model crevasse (fracture) evolution as a diffused damage interface within polar ice sheets/shelves undergoing large creep deformations. Over the long time scales of glacier and ice sheet evolution (decades to centuries or longer), it is well established that the rheology of ice is best represented as a non-Newtonian (nonlinearly viscous) fluid, using the power law creep equation known as the Glen's law [Glen, 1955, Nye, 1957, Cuffey and Paterson, 2010, van der Veen, 2013] in glaciology. By incorporating this nonlinearly viscous rheology, several studies have established that the three-dimensional (3D) nonlinear incompressible Stokes equations (hereafter referred to as the Stokes equations for brevity) provide the most accurate description of momentum balance for modeling the flow of glaciers in comparison to other approaches [Leng et al., 2012, 2013]. Furthermore, recent advances in higher-order finite element discretization and scalable solvers for the solution of Stokes

equations [Worthen et al., 2014, Isaac et al., 2015] enable us to simulate the dynamics of large glaciers, or even the entire Antarctic land ice sheet by utilizing the coverage and spatial resolution of ice sheet geometry data available from high-resolution satellite imagery. In order to use the Stokes formulation to predict glacier and ice sheet evolution, however, it is necessary to account for iceberg calving, which requires that we also simulate the damage induced crevasse formation and propagation occurring on much shorter time scales (days to months). Crevasse initiation and propagation affect the stability of ice sheets by accelerating their flow, promoting iceberg calving, and triggering catastrophic collapse of glaciers and ice shelves [Vieli and Nick, 2011, Schulson and Duval, 2009]. Modeling and simulation of creep fracture (damage) mechanisms and its relation to the flow behavior (rheology) of ice sheets/shelves can be useful in providing reliable estimates for mass loss from ice sheets, a key component of sea level. Current numerical ice sheet/shelf models used to study their stability employ empirical calving laws and do not account for the physics of fracture, severely limiting their predictive capability and reliability. Furthermore, due to the vast separation of time scales associated with flow and fracture processes, the time between fracture inception and iceberg calving events associated with complete failure can exceed decades and sometimes centuries. This is particularly challenging because it becomes necessary to couple the solid mechanics of creep fracture with the fluid mechanics of viscous flow in a consistent yet computationally feasible manner. To this end, we apply the CDM framework to develop a novel formulation that combines the nonlinear Stokes formulation with a nonlocal creep damage model. An updated-Lagrangian description of motion is selected to account for the large creep deformations of polar ice sheets and to facilitate the transport of diffuse damage, thus enabling the physically accurate modeling of crevasse evolution in glaciers and land ice sheets.

The third objective of this dissertation is to apply the CZM, CDM, and PFM to model the propagation of water-filled surface and basal crevasses through polar ice sheets. Empirical calving models [Meier and Post, 1987, van der Veen, 1996, 2002, Nick et al., 2007,

2009] describe the calving behavior of tidewater glaciers to a reasonable extent but lack a mechanistic basis despite significant efforts [Benn et al., 2007b]. As an alternative, theoretical calving laws rooted in linear elastic fracture mechanics (LEFM) and dislocation mechanics have been utilized to predict the penetration depth of water-filled crevasses through ice [Weertman, 1973, van der Veen, 1998a, Nick et al., 2010a, Krug et al., 2014]. The theoretical fracture mechanics models assume brittle fracture of ice under the action of tensile stresses induced by both the longitudinal creeping flow of glaciers and hydrostatic pressure resulting from meltwater or seawater filling the crevasse. While iceberg calving is linked to brittle fracture of linear elastic ice over shorter time scales [Rist et al., 1999, van der Veen, 1998a,b], over longer times scales glacier and ice sheet flow is better described by the Glen's law [Glen, 1955, Cuffey and Paterson, 2010]. This presents computational challenges when trying to incorporate the fracture mechanics models into numerical ice sheet models, which generally incorporate the nonlinearly viscous rheology. The alternative approach to modeling calving within numerical ice flow models is damage mechanics; and thus, to this end, we apply the CDM framework to model the initiation and propagation of water-filled surface and basal crevasses and compare the CDM approach against the theoretical fracture mechanics models. We also consider the application of the CZM and PFM for modeling crevasse evolution, which are both time-independent approaches for simulating brittle failure. The CZM also assumes the crack is a zero-thickness interface instead of a diffuse damage zone and is thus more inherently consistent with the fracture mechanics models.

CHAPTER 2

A DISCRETE DAMAGE ZONE MODEL FOR MIXED-MODE DELAMINATION OF COMPOSITES UNDER HIGH-CYCLE FATIGUE

2.1 Introduction

Laminated composite materials are widely used in aerospace structural applications requiring low weight and high mechanical performance. In these laminated composites, delamination (i.e. separation of layers or plies) and debonding (i.e. failure of adhesive bond-lines) are the two most dominant failure modes [Mi et al., 1998a, Blackman et al., 1991]. Since delamination occurs at relatively low loads under cyclic loading, mechanical fatigue is the most common cause of delamination failure in composite structures. Typically, delamination in structural components during service develops or grows under varying mixed mode and temperature conditions due to the multi-axial cyclic loading, curved structural geometry, different lamina ply orientation, and dynamic environmental changes [Sjogren and Asp, 2002, Blanco et al., 2004]. Therefore, it is important that the computational techniques used for predicting fatigue delamination are able to efficiently capture the dependence of crack growth rates on the mode-mix ratio and temperature. To this end, we present a discrete damage zone model, which belongs to the class of discrete cohesive zone models, and its finite element implementation.

When material nonlinearities are negligible and the size of the fracture process zone at the crack tip is small, linear elastic fracture mechanics (LEFM) presents a convenient way for modeling delamination [Blackman et al., 1991, 2003c,a, Nilsson et al., 2001, Skallerud and Zhang, 1997]. Analysis of fatigue-driven delamination using LEFM involves relating the fatigue crack growth rate with the amplitude of the fracture energy release rate and mode mix ratio using the Paris law [Paris et al., 1961, Paris and Erdogan, 1963]. However, LEFM is more suitable for brittle materials wherein the size of the fracture process

zone at the crack tip is negligible, rather than for quasi-brittle, ductile or some composite materials wherein the size of the fracture is significant [Bazant, 1999]. An alternative approach is based on the cohesive zone model (CZM) [Hillerborg et al., 1976, Xu and Needleman, 1994] that assumes a bounded stress within the cohesive zone, as originally proposed by Barenblatt [Barenblatt, 1962] and Dugdale [Dugdale, 1960]. In this approach, special elements known as cohesive interface elements are placed along potential crack paths (e.g. laminate interfaces), usually, within a finite element model. Then, cohesive laws or traction-separation laws are defined to prescribe the constitutive behavior of the continuum interface element placed along the finite element edges. There exists a great variety in traction-separation laws (e.g. bilinear, exponential, polynomial etc.), but broadly they all describe the same global load-displacement behavior [Chandra et al., 2002]. The discrete implementation of the CZM involves placing spring elements at the interface finite elements nodes, rather than at finite element edges like in the continuum implementation. [Cui and Wisnom, 1993, Xie et al., 2006, Xie and Waas, 2006, Liu et al., 2012]. The discrete approach has been found to avoid computational issues that lead to convergence and mesh sensitivity [Cui and Wisnom, 1993, Xie et al., 2006, Xie and Waas, 2006]. However, the approach of placing discrete elements between the interface nodes could give a similar discretized system of equations compared to that given by the Newton-Cotes integration scheme in continuum elements, but the stress distribution along the interface would be different [Do et al., 2013]. In addition employing spring-type elements also avoids convergence issues related with large deformations and associated element distortion, which continuum elements may exhibit. Due to the simplicity of the approach and its compatibility with finite element analysis, the CZM is a popular method for investigating fracture and delamination. However, most CZMs (both continuum and discrete) considered reversible elastic behavior of the interface and investigated delamination, debonding and crack growth under monotonic quasi-static loading [Schellenkens and de Borst, 1993, Alfano and Crisfield, 2001, Camanho et al., 2003, Mi et al., 1998a, Park et al., 2009, Xu and

Needleman, 1994, van den Bosch et al., 2006, Robinson et al., 2000, Li and Ghosh, 2006, Alfano et al., 2009, Blackman et al., 2003b, Li et al., 2006, Goyal et al., 2008, Liljedahl et al., 2006, Yang and Ravi-Chandar, 1998].

Alfano and Crisfield [2001] have shown that CZMs can be recast within the more general damage mechanics framework. Consequently, cohesive laws can be augmented with damage models and this allows one to model delamination or subcritical crack growth under non-monotonic and cyclic fatigue loading, within the irreversible damage mechanics framework. There exist several models that extend the CZMs for monotonic loading into forms suitable for cyclic loading by introducing a damage variable to incorporate irreversibility. In an early model de Andres et al. [1999] attempted to apply a cohesive law wherein a damage parameter for the cohesive zone material was explicitly adjusted with increasing number of loading cycles. Yang et al. [2001] developed a cohesive law that describes separately the unloading and reloading processes and creates a hysteresis loop between unloading and reloading paths. Later, Roe and Siegmund [2003], Siegmund [2004] developed fatigue crack growth by incorporating a damage evolution equation for cyclic loading using the effective stress concept. Other approaches detailed in [Nguyen et al., 2001, Goyal et al., 2004] also incorporated irreversible behavior into their cohesive formulations for cyclic loading; however, in all these formulations damage accumulation was calculated using cycle-by-cycle analysis, and so they are only suitable for low cycle fatigue analysis.

For high-cycle fatigue, tracking the damage variable in time during each individual cycle would be computationally expensive. Instead, it would be more efficient to formulate fatigue damage growth relations in cycle-based format by assuming the damage increment per cycle to be very small [Paas et al., 1993, Peerlings et al., 2000]. With this idea in mind, Robinson and co-workers [Robinson et al., 2005, Munoz et al., 2006] extended the bilinear cohesive law for the continuum interface element by incorporating the Peerlings law for fatigue damage [Peerlings et al., 2000]. Later, Turon et al. [2007a] proposed a

new damage model for the delamination in composites under high-cycle fatigue by relating the damage evolution rate $\mathrm{d}D/\mathrm{d}N$ to the crack propagation rate $\mathrm{d}a/\mathrm{d}N$ given by the Paris law. Recently, Harper and Hallett [2010] presented a new fatigue damage formulation that preserves the direct link with linear elastic fracture mechanics and detailed the extraction of strain energy release rate from the cohesive zone. More recently, Landry and LaPlante [2012] developed a new model for progressive delamination in composite structures subjected to mode I fatigue loading of varying amplitudes. In all these models for high-cycle fatigue, a separate damage variable is introduced into a continuum cohesive zone model given by a bilinear traction separation law. However, one can derive the traction-separation law using a suitable damage growth law and, thus, model interlaminar degradation due to static and fatigue damage components in a more unified and efficient way. This is the idea behind the discrete damage zone model [Liu et al., 2012], wherein the interface constitutive (force-separation) law was derived assuming that the interface degraded according to Mazar's exponential damage law [Mazars, 1986]. Since the fracture process zone behind the delaminated material is interpreted as a damage zone, rather than a cohesive zone, it is appropriate to call it the discrete damage zone model (DDZM). Recently, DDZM has also been implemented within the extended finite element method [Wang and Waisman, 2014]. This avoids the need for meshes conforming to the discontinuities and adaptive remeshing during the growth of discontinuities.

In this chapter, we extend the DDZM for the mixed mode fatigue delamination analysis of laminated composites within the framework of the finite element method. The proposed cohesive element is a discrete nonlinear spring placed at the finite element nodes of the laminate interface [Liu et al., 2012]. Since the constitutive law governing the discrete interface element's behavior is derived entirely from the perspective of damage mechanics it can naturally account for the permanent reduction in material strength and stiffness when the material is loaded beyond the elastic limit (irreversibility of damage). The model has been implemented in the commercial finite element analysis software Abaqus via the user de-

fined subroutine UEL. The unique features of the proposed DDZM for fatigue delamination are: (1) the application of discrete elements as opposed to continuum interface elements; (2) the description of interface damage growth as a function of interface separation directly from the continuum damage models of Mazars [1986] and Peerlings et al. [2000]; (3) the incorporation of mode-mix ratio- and temperature- dependence of fatigue damage parameters; and (4) the lack of pathological mesh dependence of the approach with refinement. The remainder of this chapter is organized as follows: In Section 2.2 the formulation of the DDZM for high-cycle fatigue is discussed; in Section 2.3 the numerical implementation and the time integration scheme are described; in Section 2.4 the numerical results of mode I, mode II and mixed mode delamination analysis are presented and the respective mesh convergence behavior is investigated. Additionally, model calibration and validation is discussed for varying mode-mix conditions at room temperature of 20 °C and at an elevated temperature of 100 °C. Finally, some concluding remarks are given in Section 2.5.

2.2 Discrete Damage Zone Model (DDZM) formulation

In the DDZM, the interface element is a two dimensional spring-like element that connects the interface finite element nodes (not the finite element edges) and resists both displacement along and perpendicular to its axis. Because of its discrete form, the DDZM spring element behavior involves the force in the spring and the extension of the spring, the latter being equal to interface separation as the initial length of the spring is taken to be zero. The cohesive stress can now be obtained by dividing the force in the spring element by its corresponding area of support; thus, the cohesive stress is approximated to be constant over the nodal area of support. For example, for a structured 2D finite element mesh, the relationship between spring force F and interfacial cohesive stress σ can be simply written as $F = \sigma h$, where h is the characteristic element size, assuming the out-of-plane dimension to be unity. In this section, we will first review the interface element's constitutive law for monotonic loading [Liu et al., 2012] and then extend it for high-cycle fatigue loading.

2.2.1 Discrete element constitutive law for monotonic loading

The force-separation relationship for the discrete spring element is derived from the continuum damage evolution law governing the material behavior under monotonic loading (see Figure 2.1). Let δ denote the interface separation and F denote the force in the spring for any general mixed-mode loading scenario. Superscripts "cr" and "max" denote critical and maximum values, respectively. The elastic regime is defined by the region $\delta \in [0, \delta^{\text{cr}})$ and the softening (damage) regime is given by $\delta \in [\delta^{\text{cr}}, \delta^{\text{max}}]$. The irreversibility of damage implies that beyond the elastic regime (i.e. at any point $\delta^* > \delta^{\text{cr}}$ when the damage in the spring is $D_{\text{s}} = D_{\text{s}}^*$), if the spring is unloaded and then reloaded it will behave as a linear spring with reduced stiffness, $K^* = (1 - D_{\text{s}}^*)K^0$, until it begins to damage further. This irreversible constitutive behavior is depicted in Figure 2.1a, wherein the blue arrows show

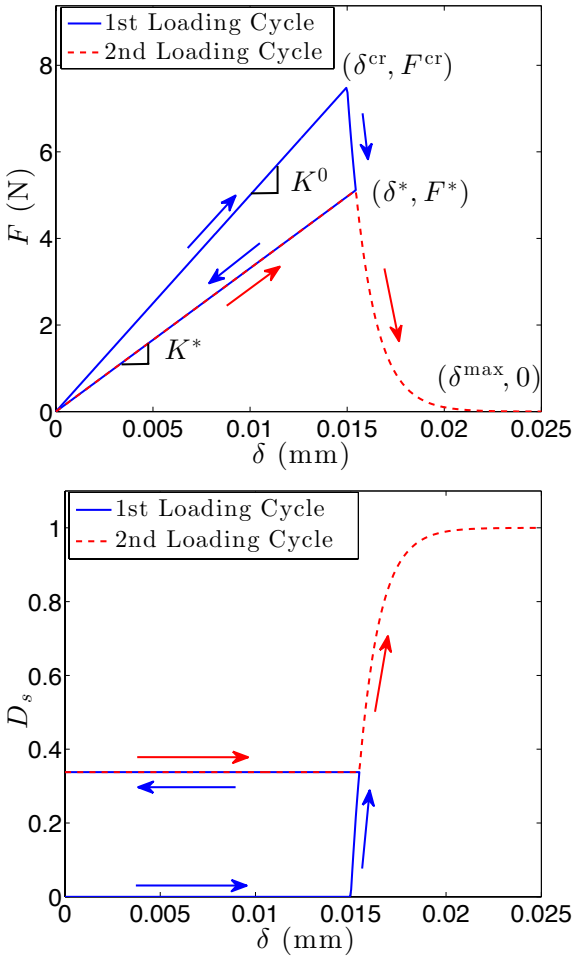

Figure 2.1: Discrete element constitutive law for monotonic loading (exponential)

the initial loading and unloading paths and the red arrows show the reloading path. During unloading and reloading when $\delta \leq \delta^*$ the damage remains constant ($D_s = D_s^*$) as indicated by the horizontal arrows in Figure 2.1b. The relationship between the force in the spring, F^*, and the interface separation δ^* is given by,

$$F^* = K^* \delta^* = (1 - D_s^*) K^0 \delta^{cr} \frac{\delta^*}{\delta^{cr}} = (1 - D_s^*) F^{cr} \frac{\delta^*}{\delta^{cr}}, \tag{2.1}$$

where K^0 is initial or undamaged stiffness of the spring and the critical or maximum force sustained by the spring without any damage $F^{cr} = K^0 \delta^{cr}$.

To obtain the $F - \delta$ relationship one needs to introduce a suitable damage evolution law into the above equation (2.1). By choosing a different damage law one can define a unique, material-specific interface constitutive or cohesive law. Herein, we consider an interface damage law, which is functionally similar to the continuum damage law proposed by Mazars [1986] for brittle materials, given by,

$$D_s = \begin{cases} 0, & \text{if} \quad \delta < \delta^{cr}, \\ 1 - \dfrac{1}{\exp\left(B(\delta - \delta^{cr})\right)}, & \text{if} \quad \delta \geq \delta^{cr}, \end{cases} \tag{2.2}$$

where D_s denotes static damage occurring at the interface under monotonic loading. Introducing the above equation (2.2) for damage into the force-separation relation (2.1), we get,

$$F = \begin{cases} F^{cr} \dfrac{\delta}{\delta^{cr}}, & \text{if} \quad \delta < \delta^{cr}, \\ F^{cr} \dfrac{\delta}{\delta^{cr} \exp\left(B(\delta - \delta^{cr})\right)}, & \text{if} \quad \delta \geq \delta^{cr}. \end{cases} \tag{2.3}$$

It turns out that the exponentially softening portion ($\delta \geq \delta^{cr}$) of the above force-separation law is functionally similar to the normal traction-separation law (mode I) proposed by Xu and Needleman [1994]. There are three static damage model parameters that need to be identified under monotonic loading: (1) the critical separation for damage initiation, δ^{cr};

(2) the initial or undamaged stiffness of the spring element, K^0; and (3) the static damage coefficient, B. It can be shown that the constitutive relations for these parameters for mode I and mode II depend on the critical fracture energies, $G_{\mathrm{IC}}, G_{\mathrm{IIC}}$, normal and tangential cohesive strengths, $\sigma_{\max}, \tau_{\max}$ and a mesh size parameter, h. The procedure to identify these parameters from linear elastic fracture mechanics (LEFM) principles is detailed in Section 2.3.

2.2.2 Discrete element constitutive law for cyclic loading

Under cyclic loading, fatigue-driven delamination or fracture is experimentally observed to consist of three stages: initiation, stable growth and failure. In the stable crack growth regime, the crack or delamination front propagates by a small amount per loading cycle and the log-log plot of the crack growth rate per cycle versus the amplitude of the fracture energy release rate is typically linear, known as the Paris law [Paris et al., 1961, Paris and Erdogan, 1963]. It is important to note that as the fatigue damage component grows and once the interfacial separation reaches the critical value, δ^{cr}, static damage also inevitably increases and interacts with the fatigue damage. Therefore, interface damage is a combination of both static damage and fatigue damage. In fact, scanning electron micrographs of fracture surfaces showed no significant difference between static and fatigue delamination, from which Asp et al. [2001] deduced the failure mechanisms to be the same in static and fatigue loading. Hence, it is reasonable to assume an additive split of the damage rate as [Payan and Hochard, 2002, Robinson et al., 2005],

$$\frac{\partial D}{\partial t} = \dot{D} = \dot{D}_{\mathrm{s}} + \dot{D}_{\mathrm{f}}, \tag{2.4}$$

where $\dot{D}$ represents the total damage rate in the discrete spring element. By differentiating equation (2.2) with respect to time, the static damage rate $\dot{D}_{\mathrm{s}}$ is obtained as,

$$\dot{D}_{\mathrm{s}} = \frac{B\dot{\delta}}{\exp(B(\delta - \delta^{\mathrm{cr}}))}, \text{ if } \delta \geq \delta^{\mathrm{cr}}. \tag{2.5}$$

Based on the continuum damage model proposed by Peerlings et al. [2000] for high-cycle fatigue, we write a fatigue damage rate in terms of the interface separation rate $\dot{\delta}$ as,

$$\dot{D}_{\mathrm{f}} = C\exp(\lambda D)\left(\frac{\delta}{\delta^{\mathrm{f}}}\right)^{\beta}\frac{\dot{\delta}}{\delta^{\mathrm{f}}}, \text{ if } G - G_{\text{threshold}} \geq 0, \tag{2.6}$$

where C, β and λ are fatigue damage model parameters; δ^{f} is an interface separation (normalizing) constant introduced solely for dimensional reasons [Robinson et al., 2005]; and $G_{\text{threshold}}$ is a strain energy release rate threshold for fatigue damage initiation. Notice that there are four fatigue damage model parameters that need to be identified under cyclic loading: (1) fatigue damage coefficient, C; (2) fatigue damage exponent, β; (3) damage magnification coefficient, λ; (4) and strain energy release rate threshold, $G_{\text{threshold}}$. The parameters C and β are purely phenomenological and are determined from the Paris plots of experimental data which is detailed in Section 2.4. The parameter λ is a chosen constant, which accounts for dependence of damage rate on the current state of damage. Experiments conducted by Asp et al. [2001] report different values of $G_{\text{threshold}}$ for mode I, mode II, and 50% mode II failure. However, in all the numerical examples considered G is greather than $G_{\text{threshold}}$, so the fatigue crack grows with loading cycles.

Following the approach described in the previous section, the constitutive $(F-\delta)$ relation between the force in the discrete spring element, F, and the interfacial separation, δ, under cyclic loading at time t is given by,

$$F(t) = K(t)\ \delta(t) = \big(1 - D(t)\big)K^0\ \delta(t), \tag{2.7}$$

In order to obtain the total damage at a given time $t = t(N + \Delta N)$ we can incrementally integrate equation (2.4) in time as,

$$D\big(t(N+\Delta N)\big) = D\big(t(N)\big) + \int_{t(N)}^{t(N+\Delta N)} \frac{\partial D}{\partial t}\, \mathrm{d}t. \tag{2.8}$$

However, in the case of high-cycle fatigue loading composed of well-defined discrete cycles, it is computationally efficient to express the damage growth rate as a number of cycles N as,

$$D\big(t(N+\Delta N)\big) = D(N+\Delta N) = D(N) + \int_{N}^{N+\Delta N} \frac{\partial D}{\partial N}\, \mathrm{d}N. \tag{2.9}$$

Thus, for high-cycle fatigue, the number of cycles, N, is usually considered to be a continuous, time-like variable and a damage rate per cycle $\dfrac{\partial D}{\partial N}$ is defined, as suggested in Peerlings et al. [2000].

Next, let us plot the constitutive $(F-\delta)$ behavior of a single discrete element by assuming an actual loading history, wherein the load fluctuations are idealized as sinusoidal as shown in Figure 2.2. For the sake of computational efficiency, the applied numerical load is increased linearly to the maximum value $F_{\mathrm{a}} < F^{\mathrm{cr}}$ (load amplitude) and then kept constant, as given by the blue solid line in Figure 2.2. The $F-\delta$ law follows the path indicated by the solid red line in Figure 2.3(a) under cyclic loading. Since $F_{\mathrm{a}} = F$ for equilibrium, F linearly increases and then remains a constant as fatigue damage evolves with the number of loading cycles. Once the separation $\delta = \delta^{\mathrm{cr}}$ static damage initiates and grows rapidly leading to the failure of the spring element. Because this is a force-controlled experiment the failure is abrupt and one cannot capture softening behavior. Thus, the spring fails even when the load amplitude F_{a} is less than the critical force F^{cr} due to fatigue (subcritical failure). The total damage versus the separation $(D-\delta)$ under fatigue loading is given by the solid red line in Figure 2.3(b) and the curves corresponding to the static and fatigue damage components are indicated by the green and blue dashed lines. As expected, in the initial stages when $\delta < \delta^{\mathrm{cr}}$ we see that $D = D_{\mathrm{f}}$ and $D_{\mathrm{s}} = 0$, and for $\delta > \delta^{\mathrm{cr}}$ we see that D_{s}

grows rapidly until element failure.

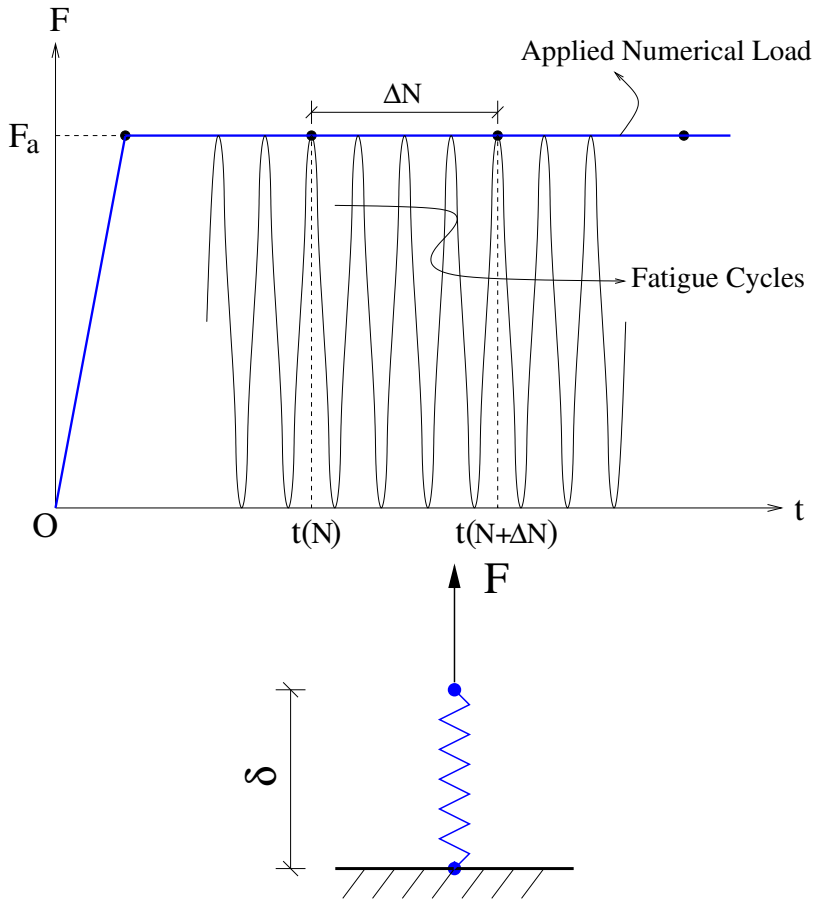

Figure 2.2: Test simulation using one discrete spring element, wherein one end of the element is fixed and a force or load F is applied at the other end. The cycles describe the load fluctuations and the blue solid lines show the applied loading.

Remark 1 *The current DDZM describes damage evolution using Mazars [1986] law, assuming linear secant behavior during unloading and reloading, as shown in Figure 2.1(a). For high cycle fatigue, since individual loading cycles are not analyzed and damage accumulates over several cycles, this assumption of a linear secant behavior is not an issue. For low cycle fatigue, however, Pettersson et al. [2006] report that friction-like processes (sliding, viscosity) contribute to irreversible strains during cycle-by-cycle shear loading experiments, leading to non-secant behavior. The damage mechanics framework employed in the DDZM provides the flexibility to incorporate such non-secant (plastic) unloading behavior.*

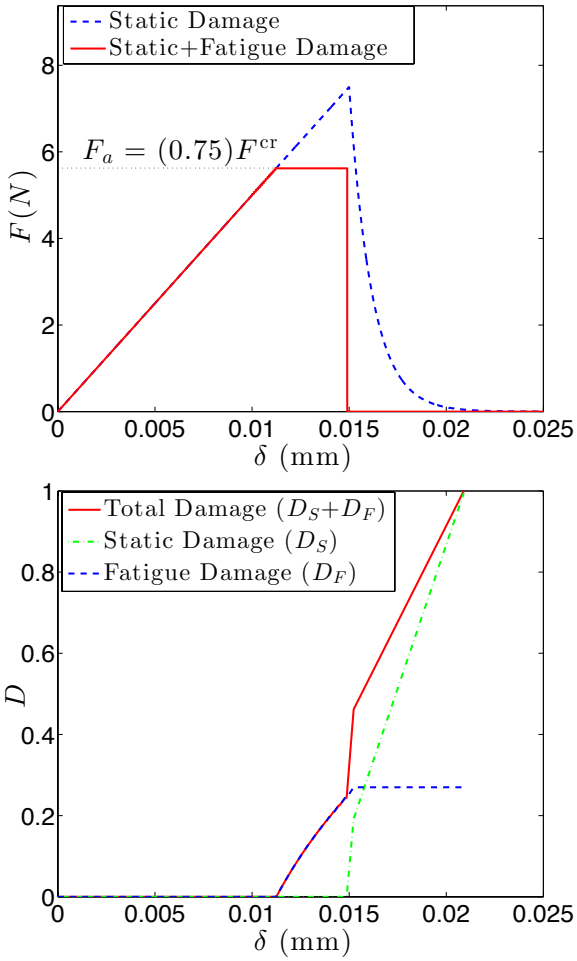

Figure 2.3: Discrete element constitutive law for cyclic loading

Remark 2 *In a general case scenario, one needs to specify the stress ratio associated with the fatigue loading history [Walker, 1970]. The stress ratio, R_F, may be defined in the current model as the ratio of the minimum to maximum forces in the spring, that is, $R_F = \left(F^{\min}/F^{\max}\right)$. In this study, we only consider a particular case when $R_F = 0$, that is, $F^{\min} = 0$, as shown in Figure 2.2(a); however, positive R_F effects can be incorporated by defining a corrected strain energy release rate $G^* = (1 - R_F^2)G_{\mathrm{C}}$ instead of G_{C} in the mixed mode equations [Kawashita and Hallett, 2012].*

2.2.3 Temperature dependence of the damage rate

Experiments of Asp [1998] indicate that the rate of deterioration of the laminate interface depends on the environmental conditions such as temperature and humidity. In this section, we only restrict our attention to the temperature dependence of damage rate under mechanical fatigue. Sjogren and Asp [2002] reported that at an elevated temperature of 100 °C fracture behavior changed during static and fatigue delamination tests, implying that both static and fatigue damage model parameters are temperature dependent. Herein, we assume only the static damage coefficient B and fatigue damage coefficient C to be temperature dependent. The parameter $B(T)$ at temperature, T, is directly determined using a temperature dependent fracture energy criterion, as detailed in Section 2.3.2. The parameter $C(T)$ is calculated by assuming that temperature dependence of fatigue damage rate follows the Arrhenius relation,

$$\dot{D}_{\mathrm{f}}(T) = \dot{D}_{\mathrm{f}}(T_{\mathrm{rm}}) \exp\left(-\frac{Q}{R}\left(\frac{1}{T} - \frac{1}{T_{\mathrm{rm}}}\right)\right), \tag{2.10}$$

where Q is the damage activation energy, R is the universal gas constant (which is equal to the Botlzmann's constant) and $\dot{D}_{\mathrm{f}}(T_{\mathrm{rm}})$ is the fatigue damage rate component at room temperature $T_{\mathrm{rm}} = 20$ °C. Substituting the expression for $\dot{D}_{\mathrm{f}}$ from equation (2.6) on both sides of equation (2.10) and assuming that only C is temperature dependent, we arrive at

the following relation,

$$C(T) = C(T_{\text{rm}}) \exp\left(-\frac{Q}{R}\left(\frac{1}{T} - \frac{1}{T_{\text{rm}}}\right)\right). \tag{2.11}$$

The calibration of the damage activation energy Q from experimental data is detailed in Section 2.4.4.

Remark 3 *For metals and alloys, under mechanical fatigue at elevated temperatures there exist several degradation mechanisms, namely, oxidation, creep and microstructure evolution of grain size, which are observed to be temperature dependent. Neu and Sehitoglu [1989] proposed the Arrhenius relation for incorporating the temperature dependence of oxidation and creep damage mechanisms for low cycle thermomechanical fatigue of steel alloys. For carbon fiber epoxy composites, under high cycle fatigue, the temperature dependent damage mechanisms have not been well reported in the literature. Therefore, we can only hypothesize that the increase in damage (crack growth) rate at elevated temperatures, due to enhanced degradation of the epoxy resin at the carbon fiber interface, follows the Arrhenius relation.*

2.3 Numerical Implementation

2.3.1 Kinematics

The discrete damage zone model is implemented in the commercial finite element analysis software Abaqus. The continuum bulk elements are defined as bilinear (4 noded) quadrilateral elements and the discrete spring elements are defined via the user defined element subroutine UEL. The element definition and node numbering for a typical spring element is shown in Figure 2.4. Since the spring elements are initially inactive, their initial

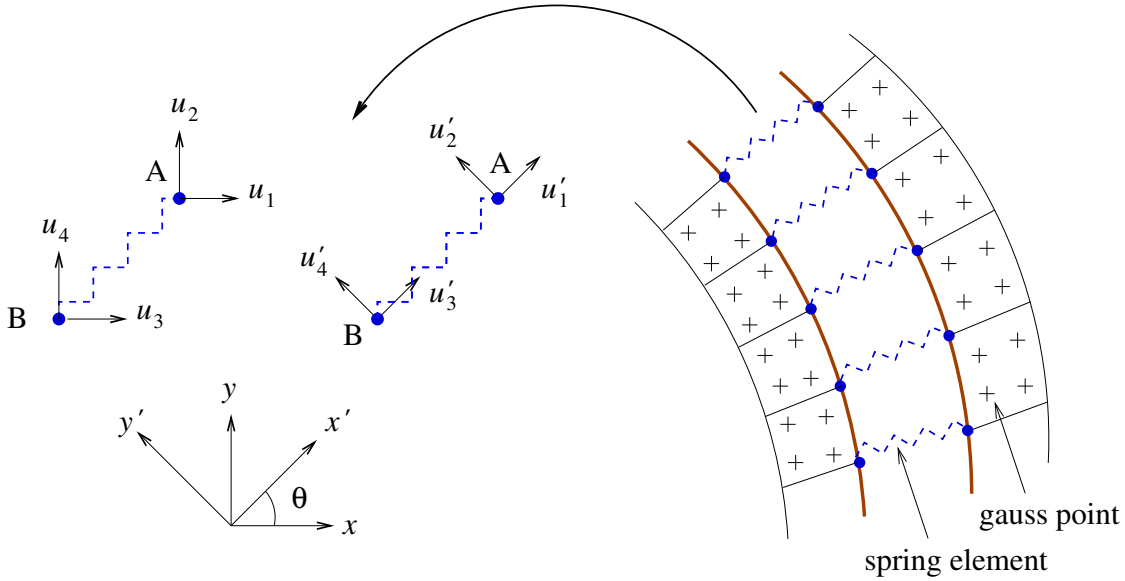

Figure 2.4: Sketch of the discrete element and the definition of the degrees of freedom in global and local coordinates. The inclination of the spring is denoted by θ.

lengths are set to zero. The displacement degrees of freedom (DOFs) at nodes A and B are given by,

$$\boldsymbol{u}^A = \left(u_x^A, u_y^A\right)^T = (u_1, u_2)^T, \tag{2.12a}$$

$$\boldsymbol{u}^B = \left(u_x^B, u_y^B\right)^T = (u_3, u_4)^T, \tag{2.12b}$$

where (x,y) denotes the global Cartesian coordinate directions. Thus, the vector of displacement of the discrete spring element is,

$$\boldsymbol{u} = (u_1, u_2, u_3, u_4)^T. \tag{2.13}$$

The vector displacement in local coordinates (x',y') can be given in terms of the global displacement vector as,

$$\boldsymbol{u}' = \left(u_1', u_2', u_3', u_4'\right)^T = \boldsymbol{R}\boldsymbol{u}, \tag{2.14}$$

where $\boldsymbol{R}$ is the anticlockwise rotation matrix that is a function of the inclination θ of the spring element given by,

$$\boldsymbol{R} = \begin{bmatrix} \cos\theta & \sin\theta & 0 & 0 \\ -\sin\theta & \cos\theta & 0 & 0 \\ 0 & 0 & \cos\theta & \sin\theta \\ 0 & 0 & -\sin\theta & \cos\theta \end{bmatrix}. \tag{2.15}$$

The normal and tangential (or shear) separations in the discrete interface elements are given by,

$$\delta_{\mathrm{n}} = \langle u_1' - u_3' \rangle, \tag{2.16}$$

$$\delta_{\mathrm{t}} = u_2' - u_4'. \tag{2.17}$$

where the Macaulay brackets have been employed in (2.16) and are defined as $\langle X \rangle = X$ when $X \geq 0$ and $\langle X \rangle = 0$ when $X < 0$.

Remark 4 *The initial lengths of the discrete interface elements are set to zero because the delamination interface is still intact. Negative normal separations of the spring means overlap or interpenetration of laminate layers, which is not physical; however, numerical errors in the calculations can sometimes lead to small negative values of* δ_{n}. *Therefore, it is*

important to define δ_n as the normal crack opening displacement in equation (2.16) using Macaulay brackets, so that it is always positive.

2.3.2 Mixed mode criteria

In real composite components, fatigue delamination rarely develops under a constant propagation mode such as pure mode I or pure mode II. Instead, delamination develops under a changing mode-mix ratio, generally, involving both mode I and mode II displacements. In order to simulate the intricate mixed mode failure under fatigue loading, an equivalent displacement parameter is usually defined [Robinson et al., 2005, Qiu et al., 2001, Alfano and Crisfield, 2001, Jiang et al., 2007]. Herein, for the general mixed mode loading we define the equivalent separation as,

$$\delta_e = \sqrt{\delta_n^2 + \delta_t^2}. \tag{2.18}$$

Clearly, δ_e is equal to δ_n and δ_t under pure mode I and mode II, respectively. Next, we prescribe the damage initiation criterion under mixed mode by computing an equivalent critical separation δ_e^{cr} using the critical separations under pure mode I and mode II denoted δ_n^{cr} and δ_t^{cr}, respectively. Jiang et al. [2007] proposed a quadratic damage initiation criterion for calculating δ_e^{cr} as,

$$\frac{1}{\delta_e^{cr}} = \sqrt{\left(\frac{\cos \mathrm{I}}{\delta_n^{cr}}\right)^2 + \left(\frac{\cos \mathrm{II}}{\delta_t^{cr}}\right)^2}, \tag{2.19}$$

where $\cos \mathrm{I} = \delta_n/\delta_e$ and $\cos \mathrm{II} = \delta_t/\delta_e$.

The potential energy stored in a spring element for mixed mode loading is given by,

$$\Phi = \frac{1}{2} K_n \delta_n^2 + \frac{1}{2} K_t \delta_t^2, \tag{2.20}$$

where K_n and K_t are the damaged axial (normal) stiffness and transverse (tangential) stiff-

ness, respectively, given by,

$$K_{\mathrm{n}} = (1-D)\,K_{\mathrm{n}}^{0} \;\;,\;\; K_{\mathrm{t}} = (1-D)\,K_{\mathrm{t}}^{0}, \tag{2.21}$$

and a "0" in the superscript denotes the initial or undamaged stiffness. Herein, we take $K_{\mathrm{n}}^{0} = K_{\mathrm{t}}^{0} = 20,000 * h$ N/mm, where h is the characteristic size of the structured mesh, so that artificial stiffness redution is less than 15%, and convergence is not affected. Using the linear elastic fracture mechanics (LEFM) principle that the maximum force in the spring corresponds to the critical separation and cohesive strength, we calculate the critical separations under mode I and mode II as,

$$\delta_{\mathrm{n}}^{\mathrm{cr}} = \frac{F_{\mathrm{n}}^{\mathrm{cr}}}{K_{\mathrm{n}}^{0}} = \frac{\sigma_{\max} h}{K_{\mathrm{n}}^{0}}; \;\; \delta_{\mathrm{t}}^{\mathrm{cr}} = \frac{F_{\mathrm{t}}^{\mathrm{cr}}}{K_{\mathrm{t}}^{0}} = \frac{\tau_{\max} h}{K_{\mathrm{t}}^{0}}. \tag{2.22}$$

Thus, $\delta_{\mathrm{n}}^{\mathrm{cr}}$ and $\delta_{\mathrm{t}}^{\mathrm{cr}}$ are not independent model parameters and depend on the cohesive strengths and initial stiffnesses.

Remark 5 *In equation (2.21) we assume isotropic damage, so a single scalar internal variable D is used to describe the degraded interface element stiffness in both normal and tangential directions. It is possible to consider anisotropic damage by defining two separate damage variables,* D_{n} *and* D_{t} *in each direction; however, one has to define a mixed mode interaction relationship to ensure that when* $D_{\mathrm{n}} = 1$ *then* $D_{\mathrm{t}} = 1$ *since the interface has completely decohered [Liu et al., 2012]. The reader may also refer to the recent paper by [Wang and Waisman, 2014] for such a modified mixed-mode failure criterion.*

Next, considering the LEFM principle that the area under the force-separation curve of the discrete element corresponds to the fracture energy, we get,

$$G_{\mathrm{C}} = \frac{1}{h}\int_{0}^{\delta_{\mathrm{e}}^{\mathrm{cr}}} K_{\mathrm{e}}^{0}\,\delta_{\mathrm{e}}\;\mathrm{d}\delta + \frac{1}{h}\int_{\delta_{\mathrm{e}}^{\mathrm{cr}}}^{\delta_{\mathrm{e}}^{\max}} \frac{K_{\mathrm{e}}^{0}\;\delta_{\mathrm{e}}}{\exp\left(B(T)\left(\delta_{\mathrm{e}} - \delta_{\mathrm{e}}^{\mathrm{cr}}\right)\right)}\;\mathrm{d}\delta \tag{2.23}$$

where the critical fracture energy G_C under mixed mode is defined as [Blanco et al., 2004],

$$G_C(\Psi, T) = g_2(T)\Psi^2 + g_1(T)\Psi + g_0(T), \tag{2.24}$$

the equivalent undamaged spring stiffness under mixed mode is (see Appendix Appendix B for the derivation),

$$K_e^0 = \frac{K_n^0 K_t^0}{\Psi K_n^0 + (1-\Psi)K_t^0}, \tag{2.25}$$

the mode mix ratio is defined as,

$$\Psi = \frac{G_{II}}{G_I + G_{II}}, \tag{2.26}$$

so that for pure mode I fracture Ψ = 0, and for pure mode II fracture Ψ = 1. By solving equation (2.23) we can obtain the static damage coefficient $B(T)$ as a function of the mode mix ratio Ψ at temperature, T. Note that the temperature dependent coefficients of the quadratic fit in equation (2.24), namely, g_0, g_1, g_2 are calculated by using the values of $G_{IC} = G_C(\Psi = 0), G_{IIC} = G_C(\Psi = 1), G_C(\Psi = 0.5)$, provided in Table 2.2. Just like G_C, the phenomenological fatigue parameters C and β are also dependent on the mode mix ratio, so we propose a quadratic relation for any real number $\Psi \in [0,\ 1]$ as,

$$\log C = c_2\Psi^2 + c_1\Psi + c_0 \tag{2.27}$$

$$\beta = b_2\Psi^2 + b_1\Psi + b_0 \tag{2.28}$$

The calibration of the coefficients for the quadratic fit for C and β is discussed in Section 2.4.

Table 2.1: Static damage model parameters (For a structured mesh h is the distance between adjacent nodes, and the critical separations are calculated using Eq. 2.22).

Parameter	K_n^0	K_t^0	σ_{max}	τ_{max}
Units	N/mm	N/mm	MPa	MPa
Value	20,000*h	20,000*h	90	140

Table 2.2: Variation of strain energy release rate with temperature [Sjogren and Asp, 2002]

Strain Energy Units	G_{IC} N/mm	G_{IIC} N/mm	$G_C(\Psi = 0.5)$ N/mm
$20°C$	0.26	1.002	0.447
$100°C$	0.249	0.701	0.535

2.3.3 Damage evolution over loading cycles

When dealing with high-cycle fatigue loading, it is computationally efficient to describe the damage evolution law in terms of number of loading cycles N, as given by equation (2.9). Let us now define the increment in damage ΔD between loading cycles,

$$D(N+\Delta N) - D(N) = \Delta D = \Delta D_s + \Delta D_f. \tag{2.29}$$

In the above equation, the increment of static damage component is given by,

$$\begin{aligned} \Delta D_s &= D_s(N+\Delta N) - D_s(N) \\ &= -\exp(-B(\delta_e(N+\Delta N) - \delta_e^{cr})) + \exp(-B(\delta_e(N) - \delta_e^{cr})), \end{aligned} \tag{2.30}$$

where $\delta_e(N+\Delta N)$ and $\delta_e(N)$ represent the interface separations (or extensions in the discrete spring element) at time $t(N+\Delta N)$ and $t(N)$, respectively. Evaluating the fatigue damage increment ΔD_f is a bit more involved since $\dot{D}_f$ is a function of the total damage D. Starting with equation (2.6) in the time-rate form and following the procedure detailed in Robinson et al. [2005] we can obtain cycle-rate form,

$$\frac{\partial D_f}{\partial N} \approx \frac{C}{1+\beta} \exp(\lambda D) \left(\frac{\delta_e}{\delta^f} \right)^{1+\beta}. \tag{2.31}$$

where δ^f is a normalizing constant that is independent of the mode-mix ratio Ψ. Assuming that $\dfrac{\partial D_f}{\partial N}$ does not change rapidly with the number of loading cycles N, we can extrapolate

the increment of fatigue damage component for a fixed increment of loading cycles ΔN as,

$$\begin{aligned}\Delta D_{\mathrm{f}} &= D_{\mathrm{f}}(N+\Delta N) - D_{\mathrm{f}}(N) \\ &= \int_{N}^{N+\Delta N} \frac{\partial D_{\mathrm{f}}}{\partial N}\,\mathrm{d}N \\ &= \int_{N}^{N+\Delta N} \frac{C}{1+\beta}\exp(\lambda D)\left(\frac{\delta_{\mathrm{e}}}{\delta_{\mathrm{e}}^{\max}}\right)^{1+\beta}\mathrm{d}N. \end{aligned} \tag{2.32}$$

Now, assuming D is a continuous function in the open interval between N and $N+\Delta N$, there exists a $\mu \in [0,1]$ (according to the first mean value theorem for integrals) such that,

$$\Delta D_{\mathrm{f}} = \Delta N \frac{C}{1+\beta}\exp(\lambda D_{\mu})\left(\frac{\delta_{\mu}}{\delta_{\mathrm{e}}^{\max}}\right)^{1+\beta}, \tag{2.33}$$

where D_{μ} and δ_{μ} are given as,

$$D_{\mu} = (1-\mu)\; D(N) + \mu\; D(N+\Delta N) \tag{2.34}$$

$$\delta_{\mu} = (1-\mu)\; \delta_{\mathrm{e}}(N) + \mu\; \delta_{\mathrm{e}}(N+\Delta N) \tag{2.35}$$

If $\mu = 0$, then we get an explicit scheme and for nonzero values of μ the scheme becomes implicitly, so we perform nonlinear iterations using the Newton-Raphson method, as detailed in Algorithm 1. We found that choosing a value of $\mu = 0.5$ (trapezoidal rule) was optimal based on a 'one element' convergence test (not shown here).

2.3.4 Abaqus UEL algorithm

In order to define the discrete element via the UEL subroutine in Abaqus, we need to define the element stiffness matrix, $\mathbf{K}$ (AMATRX), and the residual force vector, $\mathbf{r}$ (RHS),

Algorithm 1 : Newton-Raphson method for implicit damage evaluation

Let us assume all the variables are known at step $t(N)$ and we proceed to compute the variables at step $t(N+\Delta N)$,

(1) Initialize the damage variable ${}^{k}D$ and the residual ${}^{k}\hat{r}$ at iteration $k=1$

$$\begin{aligned} {}^{1}\hat{r} &= 1.0 \\ {}^{1}D &= D(N) \end{aligned}$$

(2) Evaluate the increment in static damage increment

$$\Delta D_{\mathrm{s}} = -\exp(-B(\delta_{\mathrm{e}}(N+\Delta N)-\delta_{\mathrm{e}}^{\mathrm{cr}}))+\exp(-B(\delta_{\mathrm{e}}(N)-\delta_{\mathrm{e}}^{\mathrm{cr}}))$$

(3) While ${}^{k}\hat{r} \geq \mathrm{TOL}$, at iteration $k \in \{1,2,3,...\}$

(i) Evaluate the increment in fatigue damage increment

$$\begin{aligned} {}^{k}D_{\mu} &= (1-\mu)\, D(N)+\mu\ {}^{k}D \\ \delta_{\mu} &= (1-\mu)\ \delta_{\mathrm{e}}(N)+\mu\ \delta_{\mathrm{e}}(N+\Delta N) \\ \Delta D_{\mathrm{f}} &= \Delta N \frac{C}{1+\beta}\exp(\lambda\ {}^{k}D_{\mu})\left(\frac{\delta_{\mu}}{\delta_{\mathrm{e}}^{\max}}\right)^{1+\beta} \end{aligned}$$

(ii) Compute the residual and the corresponding Jacobian

$$\begin{aligned} {}^{k}\hat{r} &= {}^{k}D-D(N)-\Delta D_{\mathrm{s}}(N)-\Delta D_{\mathrm{f}}(N) \\ \left[\frac{\partial\ {}^{k}\hat{r}}{\partial\ {}^{k}D}\right] &= 1-\lambda\mu\Delta N\frac{C}{1+\beta}\exp(\lambda\ {}^{k}D_{\mu})\left(\frac{\delta_{\mu}}{\delta_{\mathrm{e}}^{\max}}\right)^{1+\beta} \end{aligned}$$

(iii) Update the damage and iteration counter

$$\begin{aligned} {}^{k+1}D &= {}^{k}D-\left[\frac{\partial\ {}^{k}\hat{r}}{\partial\ {}^{k}D}\right]^{-1}{}^{k}\hat{r} \\ k &= k+1 \end{aligned}$$

(4) Finally, after convergence, update the damage variable at $t(N+\Delta N)$

$$D(N+\Delta N) = {}^{k}D$$

in global coordinates. The element residual force vector is given by,

$$\boldsymbol{r} = \begin{Bmatrix} r_1 \\ r_2 \\ r_3 \\ r_4 \end{Bmatrix} = \boldsymbol{R}^{\mathrm{T}} \left(-\frac{\mathrm{d}\Phi}{\mathrm{d}\boldsymbol{u}'} \right) = \boldsymbol{R}^{\mathrm{T}} \begin{Bmatrix} -K_{\mathrm{n}} \langle u_1' - u_3' \rangle \\ -K_{\mathrm{t}} (u_2' - u_4') \\ K_{\mathrm{n}} \langle u_1' - u_3' \rangle \\ K_{\mathrm{t}} (u_2' - u_4') \end{Bmatrix}. \tag{2.36}$$

The equilibrium of the discrete interfacial element requires that, $r_1 = -r_3$ and $r_2 = -r_4$. The corresponding element stiffness matrix in the global coordinates is given by,

$$\boldsymbol{K} = -\frac{\mathrm{d}\boldsymbol{r}}{\mathrm{d}\boldsymbol{u}} \approx \boldsymbol{R}^{\mathrm{T}} \begin{bmatrix} K_{\mathrm{n}} & 0 & -K_{\mathrm{n}} & 0 \\ 0 & K_{\mathrm{t}} & 0 & -K_{\mathrm{t}} \\ -K_{\mathrm{n}} & 0 & K_{\mathrm{n}} & 0 \\ 0 & -K_{\mathrm{t}} & 0 & K_{\mathrm{t}} \end{bmatrix} \boldsymbol{R}. \tag{2.37}$$

Note that we approximate the element stiffness matrix with the secant stiffness since it is always non-negative unlike the tangent stiffness which is negative for the softening regime. The detailed Abaqus user element (UEL) algorithm for the mixed mode implementation is given in Algorithm 2.

Algorithm 2 : Abaqus UEL algorithm for the discrete spring element

Let us assume all the variables are known at time $t(N)$ and we proceed to compute the variables at time $t(N+\Delta N)$. For brevity of notation we skip the cycle number $(N+\Delta N)$, for example, δ_{e} denotes $\delta_{\mathrm{e}}(N+\Delta N)$, by default.

(1) Compute both the normal, shear separations and equivalent separation in mixed mode

$$\delta_{\mathrm{n}} = \langle u_1'(N) - u_3'(N) \rangle; \quad \delta_{\mathrm{t}} = u_2'(N) - u_4'(N); \quad \delta_{\mathrm{e}} = \sqrt{\delta_{\mathrm{n}}^2 + \delta_{\mathrm{t}}^2}.$$

(2) Compute static damage as

$$\begin{aligned}
&\text{if } \ (\delta_{\mathrm{e}} < \delta_{\mathrm{e}}^{\mathrm{cr}}) \ \text{ then} \\
&\quad D_{\mathrm{s}} = 0, \\
&\text{else} \\
&\quad D_{\mathrm{s}} = 1 - \exp\left(-B(\delta_{\mathrm{e}} - \delta_{\mathrm{e}}^{\mathrm{cr}})\right). \\
&\text{end if}
\end{aligned}$$

(3) Compute the total damage, D, according to Algorithm 1 and then calculate fatigue damage component for post processing as

$$D_{\mathrm{f}} = D - D_{\mathrm{s}}.$$

(4) Compute the degraded stiffness and update the stiffness matrix

$$\begin{aligned}
K_{\mathrm{n}} &= (1-D)\, K_{\mathrm{n}}^0. \\
K_{\mathrm{t}} &= (1-D)\, K_{\mathrm{t}}^0,
\end{aligned}$$

(5) Compute the internal force of the spring element and update the right hand side vector,

$$\boldsymbol{r} = -\boldsymbol{K}\boldsymbol{u}.$$

2.4 Numerical Examples

In this section, we first calibrate the fatigue damage model parameters by comparing our numerical results with the Paris law fit of published experimental data from the double cantilever beam (DCB) test, the end notch fracture (ENF) test and the mixed mode bending (MMB) test [Asp et al., 2001]. We also examine the mesh convergence behavior for high-cycle fatigue loading under different mode-mix conditions. Next, we use the calibrated model to simulate delamination under two different mode-mix ratios and verify our model predictions with those given in [Blanco et al., 2004]. For the sake of fatigue delamination analysis we consider a carbon fiber/epoxy composite HTA/6376C and the bulk and interface material properties are given in Table 2.3 [Juntti et al., 1999]. In this section, only proportional loading is considered wherein the mode ratio is held constant during the entire loading time.

Table 2.3: Material properties for carbon fibre/epoxy composite [Blanco et al., 2004, Asp et al., 2001, Harper and Hallett, 2010]

Material Parameter	E_{xx}	$E_{yy} = E_{zz}$	$G_{xy} = G_{xz}$	$\nu_{xy} = \nu_{xz}$
Units	N/mm^2	N/mm^2	N/mm^2	-
HTA/6376C	1.20e5	1.05e4	5.25e3	0.3

2.4.1 Mode I fatigue: double cantilever beam (DCB) test

The setup of the double cantilever beam fatigue test is shown in Figure 2.5. A fixed boundary condition is applied at the right end of the beam. The specimen arms at the left end are loaded with opposing loads P in order to initiate pure Mode I delamination. The corresponding fracture energy release rate G_{I} is related to the applied load P as [Reeder and Crews, 1990, Williams, 1988],

$$G_{\mathrm{I}} = \frac{P^2 a_0^2}{W E_{xx} I} \tag{2.38}$$

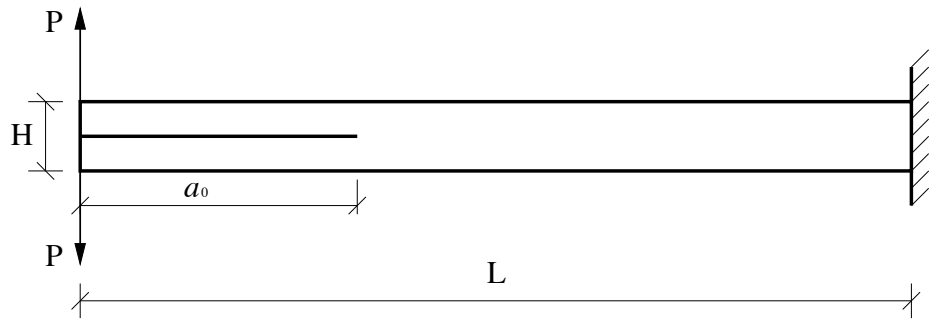

Figure 2.5: Boundary conditions of the mode I double cantilever beam (DCB) test under fatigue loading. The dimensions are: $L = 150$ mm, $H = 3.1$ mm, and $a_0 = 35$ mm.

where W is the width of the beam set perpendicular to its plane taken to be 1 mm, E_{xx} is the Young's modulus in the global $x-$direction and I is the second moment inertia of each specimen arm whose thickness is half that of the beam. The simulation is load controlled, wherein the loading is increased linearly from zero to the maximum value (or amplitude) and then held constant, as indicated by the solid blue line in Figure 2.2. As pointed out in Section 2.3.3, for high-cycle fatigue we calculate damage accumulation over a fixed number of cycles rather than calculating over each cycle. Therefore, the load is held constant at the maximum value and the fatigue damage is updated as given in Algorithm 2.

Remark 6 *Since we apply a constant load P to the specimen arms in the current DCB test, the bending moment in the beam M increases linearly and the energy release rate* G_{I} *increases quadratically with crack length* a_0*. Therefore, the crack growth rate is not a constant and the crack length increases rapidly with number of cycles in Figure 2.6(b). Alternatively, one may apply a constant moment M to the specimen arms, rather than a load P, and with this type of loading the energy release rate at the delamination front is independent of crack length and so the crack growth rate will be a constant [Robinson et al., 2005].*

We employ a uniform structured mesh with 4 noded plane stress quadrilateral elements (CPS4 in Abaqus) with the discrete elements placed at the finite element nodes. For accurate numerical analysis, the maximum length of a cohesive element $l_{\mathrm{el,max}}$ for mode I is

[Harper and Hallett, 2008],

$$l_{\text{el,max}} = \frac{1}{6}\left(E_I' \frac{G_{\text{IC}}}{\sigma_{\text{max}}^2}\right)^{1/4}\left(\frac{H}{2}\right)^{3/4}. \tag{2.39}$$

In the above expression, the parameter E_I' is given by [Harper and Hallett, 2008],

$$\frac{1}{E_I'} = \sqrt{\frac{b_{11}b_{33}}{2}}\sqrt{\sqrt{\frac{b_{33}}{b_{11}}} + \frac{2b_{31}+b_{55}}{2b_{11}}}, \tag{2.40}$$

where $b_{11} = 1/E_{xx}, b_{33} = 1/E_{zz}, b_{31} = -\nu_{xz}/E_{zz}$, and $b_{55} = 1/G_{xz}$. For the carbon fiber/epoxy composite HTA/6376C, the maximum cohesive element length $l_{\text{el,max}}$ for mode I failure is 0.079 mm, as given by equation (2.39). To satisfy this condition, we choose the mesh size h = 0.075 mm so that discrete interface elements (springs) are spaced apart by 0.075 mm. To demonstrate the convergence of DDZM results upon mesh refinement, we also evaluate smaller mesh sizes h = 0.0625 mm and h = 0.03125 mm. Finally, we consider a large mesh size h = 0.125 mm to show that DDZM results tend to diverge if the mesh is too coarse.

To calibrate the fatigue parameters for the carbon/epoxy composite we perform simulations for different values of P and plot the crack growth rate, da/dN, versus the energy release rate ratio, $G_{\text{I}}/G_{\text{IC}}$, using a log-log scale in Figure 2.6(a). The parameters are calibrated by comparing with the least squares best fit line [Blanco et al., 2004] of the experimental data of [Asp et al., 2001]. The fatigue parameters chosen for Mode I delamination are given in Table 2.4. This Paris plot demonstrates the mesh independence of the DDZM results so long as the mesh size is not too coarse (i.e. $h \leq 0.075$ mm). Next, for a particular value of applied load P ($G_{\text{I}}/G_{\text{IC}} = 0.4$), we plot the crack length versus the number of loading cycles in Figure 2.6(b). This plot demonstrates that all three meshes predict the same initial crack growth rate (initial slope of the curves); however, as the crack length a increases with the number of cycles the predictions deviate. This is a consequence of applying the load P, wherein as crack length a increases the moment at the crack tip in-

creases and small errors in crack length can be magnified over time. The differences in crack length predictions when a moment M is applied, rather than a load P, will be much less pronounced (see Remark 6).

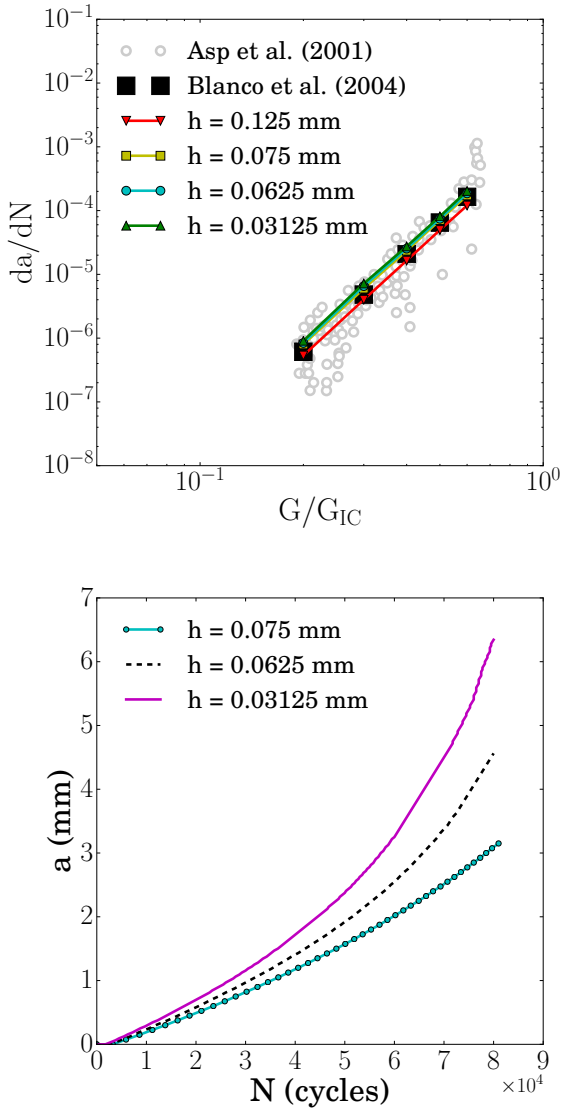

Figure 2.6: Numerical results for mode I fatigue delamination and the corresponding parameter values are: $C = 5.80e9$, $\beta = 8.81$, and $\lambda = 0.5$

2.4.2 Mode II fatigue: end notch fracture (ENF) test

The setup of the end notch fracture test is shown in Figure 2.7. The beam is simply supported at both ends and two loads of magnitude P are applied symmetrically. The

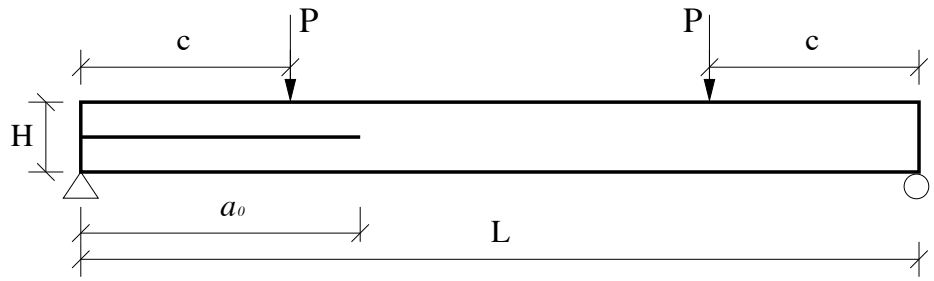

Figure 2.7: Boundary conditions of the mode II end notch fracture (ENF) test under fatigue loading. The dimensions are: $L = 150$ mm, $H = 3.1$ mm, $a_0 = 35$ mm, and $c = 25$ mm.

corresponding fracture energy release rate G_{II} is related to the applied load P as [Reeder and Crews, 1990, Williams, 1988, Robinson et al., 2005],

$$G_{\text{II}} = \frac{3P^2c^2}{16WEI} \tag{2.41}$$

where c is the distance between the applied concentrated load to the end of the beam shown in Figure 2.7. The simulation is load controlled and the load is increased linearly from zero to the maximum value (amplitude) and then held constant. In order to avoid the continuum finite elements from overlapping during the simulation of the ENF test a contact surface is defined along the expected delamination path.

Remark 7 *In the four point ENF test, the bending moment, M, in the beam between the two loads is a constant for a given load P and so the energy release rate at the delamination front is independent of the crack length. Therefore, the crack growth rate is a constant and the crack length increases linearly with number of cycles in Figure 2.8(b).*

For the carbon fiber/epoxy composite HTA/6376C, the maximum cohesive element length for mode II failure is 0.42 mm, as given by a mode II equivalent of equation (2.39)

(the reader is referred to [Harper and Hallett, 2008] for greater detail). To satisfy this condition, we choose the mesh size $h = 0.3125$ mm so that discrete interface elements (springs) are spaced apart by 0.3125 mm. To demonstrate the convergence of DDZM results upon mesh refinement, we also evaluate smaller mesh sizes $h = 0.0625$ mm and $h = 0.03125$ mm. Finally, we consider a large mesh size $h = 0.5$ mm to show that DDZM results tend to diverge if the mesh is too coarse.

To calibrate the Mode II fatigue parameters, we perform simulations for different values of P and plot the crack growth rate, da/dN, versus the energy release rate ratio, $G_{\mathrm{II}}/G_{\mathrm{IIC}}$, using a log-log scale as shown in Figure 2.8(a). The parameters are calibrated by comparing with the least squares best fit line [Blanco et al., 2004] of the experimental data of [Asp et al., 2001]. The fatigue parameters chosen for Mode II delamination are given in Table 2.4. This Paris plot demonstrates the mesh independence of the DDZM results so long as the mesh size is not too coarse (i.e. $h \leq 0.5$ mm). Next, for a particular value of applied load P ($G_{\mathrm{II}}/G_{\mathrm{IIC}} = 0.3$), we plot the crack length versus the number of loading cycles in Figure 2.8(b). This plot demonstrates that all three meshes predict the same initial crack growth rate (initial slope of the curves); however, the predicted crack length a is different, which is on the order of the mesh size differences. Since the moment at the crack tip is a constant during the ENF test (see Remark 7), the errors in crack length do not get magnified over time and the crack growth is linear with time (or cycles).

2.4.3 Mixed mode fatigue: mixed mode bending (MMB) test

The standard mixed mode bending test was first suggested by Reeder and Crews [Reeder and Crews, 1990]. The set up of the mixed mode bending test is shown in Figure 2.9. Fixed boundary condition is applied at the right end of the beam. Loads are applied at the left end and the ratio ρ defines a function that controls the mode mix ratio Ψ. Actually, the moment M is a resultant of an applied load P at the left end of the beam and so $M = Pa_0$. Following the definition of mode mix ratio Ψ in Equation (2.26), the ratio between the lower and

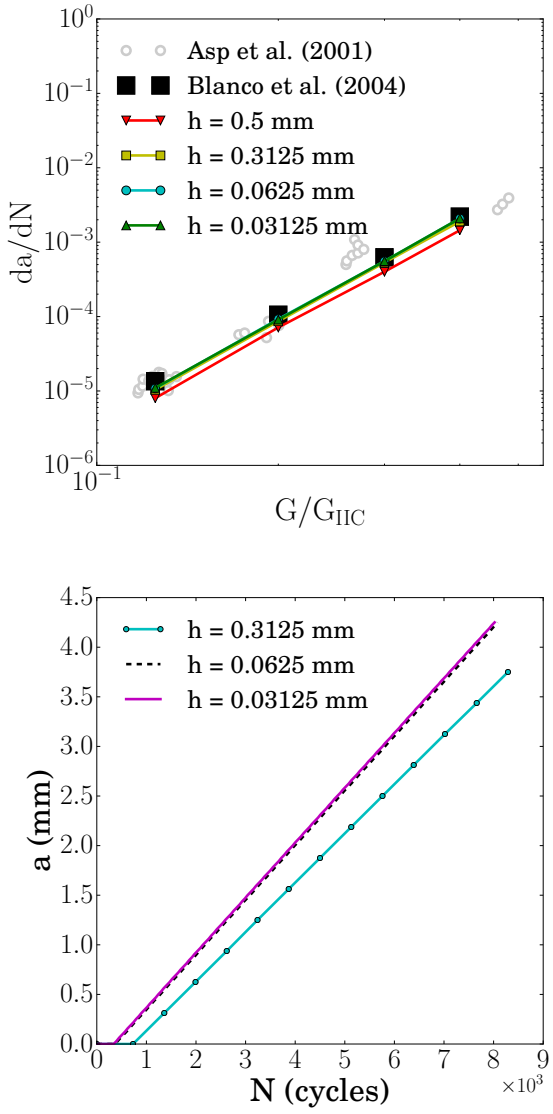

Figure 2.8: Numerical results for mode II fatigue delamination and the corresponding parameter values are: C = 3.81e7, β = 8.0, and λ = 0.5

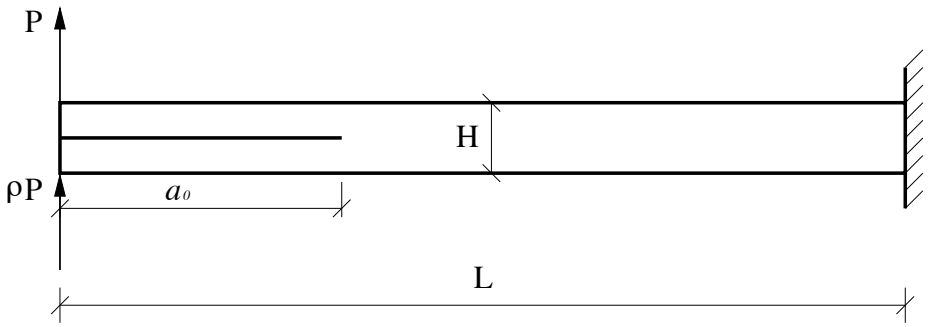

Figure 2.9: Boundary conditions of the mixed mode bending (MMB) test under fatigue loading. The dimensions are: $L = 150$ mm, $H = 3.1$ mm, and $a_0 = 35$ mm.

upper moments applied is given as (see Appendix Appendix A for a detailed derivation),

$$\rho = \frac{1 - \frac{\sqrt{3}}{2}(\Psi^{-1} - 1)^{1/2}}{1 + \frac{\sqrt{3}}{2}(\Psi^{-1} - 1)^{1/2}} \tag{2.42}$$

The above relationship between the applied moment ratio ρ and Ψ is shown in Figure 2.10. When $\rho = -1$ we get the exact configuration of the DCB test and when $\rho = 1$ we have a cantilever beam under uniform bending moment yielding a similar stress state as the ENF test. The total energy release rate G is the sum of the energy release rates in the normal and

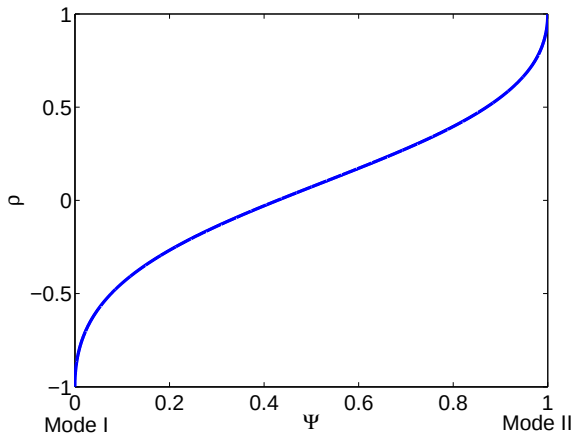

Figure 2.10: The curve of applied load ratio ρ versus mixed mode ratio Ψ.

shear modes, that is [Reeder and Crews, 1990]

$$G = G_{\mathrm{I}} + G_{\mathrm{II}}, \tag{2.43}$$

where,

$$G_{\mathrm{I}} = \left(\frac{2\sqrt{3}}{(\Psi^{-1}-1)^{-1/2} + \frac{\sqrt{3}}{2}} \right)^2 \frac{3M^2}{48WEI}, \tag{2.44}$$

$$G_{\mathrm{II}} = \left(\frac{4}{1 + \frac{\sqrt{3}}{2}(\Psi^{-1}-1)^{1/2}} \right)^2 \frac{3M^2}{64WEI}. \tag{2.45}$$

Remark 8 *Note that in the MMB test, if we apply a constant load M to the specimen arms instead of a load P, then the moment in the beam will be a constant and independent of the crack length a_0. Therefore, the energy release rate at the delamination front will be independent of crack length and the crack growth rate will be a constant with number of cycles. The Paris plots are the same for an applied moment or load since the initial crack length a_0 is much larger than the increase in crack length Δa for a small number of cycles ΔN. So, the increase in crack length does not affect calculations of the crack growth rate $da/dN \approx \Delta a/\Delta N$.*

For the carbon fiber/epoxy composite HTA/6376C, the maximum cohesive element length for mixed mode failure is 0.079 mm, as given by the methodology in [Harper and Hallett, 2008]. To satisfy this condition, we choose the mesh size h = 0.075 mm so that discrete interface elements (springs) are spaced apart by 0.075 mm. To demonstrate the convergence of DDZM results upon mesh refinement, we also evaluate smaller mesh sizes h = 0.0625 mm and h = 0.03125 mm. Finally, we consider a large mesh size h = 0.125 mm to show that DDZM results tend to diverge if the mesh is too coarse.

To calibrate the model parameters, we perform the simulations for different values of P for a mode-mix ratio of $\Psi = 0.5$ (i.e. 50% Mode II) and plot the crack growth rate, da/dN, versus the energy release rate ratio, G/G_{C}, using log-log axes as shown in Figure 2.11(a). The parameters are calibrated by comparing with the least squares best fit line [Blanco et al., 2004] of the experimental data of Asp et al. [2001]. The fatigue parameters chosen

for 50% Mode II delamination are given in Table 2.4. This Paris plot demonstrates the mesh independence of the DDZM results so long as the mesh size is not too coarse (i.e. $h \leq 0.075$ mm). Next, for a particular value of applied load P ($G/G_{\mathrm{C}} = 0.25$), we plot the crack length versus the number of fatigue cycles in Figure 2.11(b). This plot demonstrates that all three meshes predict the same initial crack growth rate (initial slope of the curves); however, as the crack grows with number of cycles the predictions from $h = 0.075,\ 0.0625,\ 0.03125$ mm deviate. This is again a consequence of the application of a load P, instead of a moment M at the left end of the beam, as discussed earlier in Section 2.4.1.

Until now, we have calibrated the parameters C, β for three cases with mode ratio $\Psi = \{0, 0.5, 1.0\}$ as given in Table 2.4. Note that the damage magnifier $\lambda = 0.5$ does not change with mode-mix ratio Ψ. We now calculate values for C and β using equations (2.27) and (2.28), respectively, for two mode mix ratios $\Psi = \{0.25, 0.75\}$ and then verify the model results with those of Blanco et al. [2004] at room temperature. The constants c_0, c_1, c_2, b_0, b_1, and b_2 are obtained by fitting the quadratic relations in equations (2.27) and (2.28) to values of C and β for the three mode mix ratios in Table 2.4. Solving for the constants gives: $c_2 = -43.14$, $c_1 = 38.11$, and $c_0 = 22.48$, $b_2 = -13.38$. $b_1 = 12.57$, and $b_0 = 8.81$. The curves of C and β versus mode ratio Ψ are shown below in Figure 2.12(a). For mode mix ratio $\Psi = 0.25$, the parameters are calculated as $C = 5.38e12$ and β = 11.12. For Ψ= 0.75, the parameters are calculated as C = 4.36e11 and β = 10.71. The results given by this method are presented on a Paris plot in Figure 2.12(b) and show good agreement with Blanco et al. [2004]. This demonstrates the viability of using the quadratic relation to evaluate C and β for arbitrary mixed mode ratios.

Table 2.4: Summary of fatigue damage model parameters

	units	Mode I	Mode II	Mixed Mode
C	cycle^{-1}	5.8e9	3.81e7	2.27e13
β	-	8.81	8.0	11.75
λ	-	0.5	0.5	0.5
δ^{f}	mm^{-1}	0.03	0.03	0.03

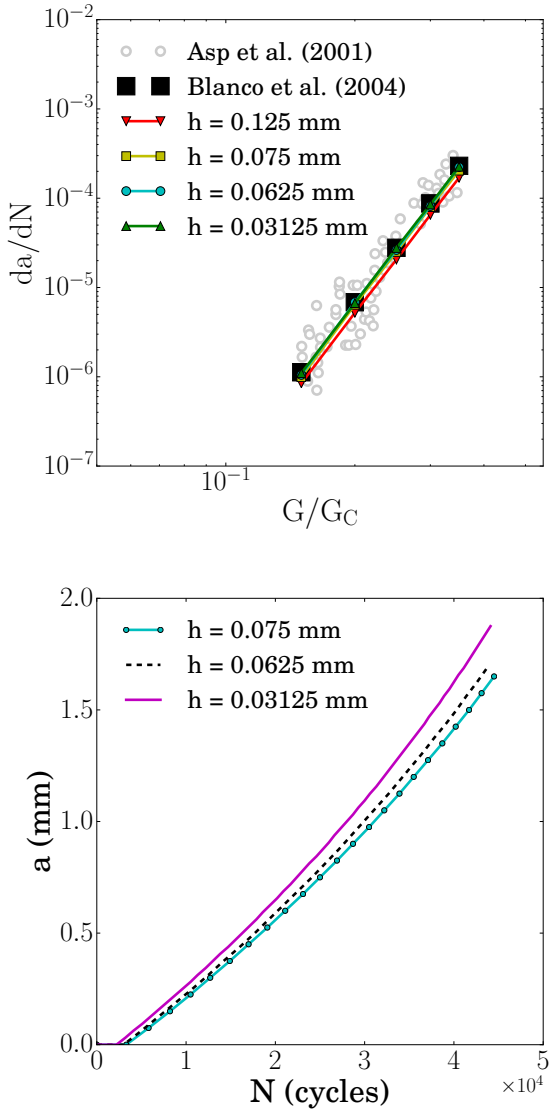

Figure 2.11: Numerical results for Mixed Mode fatigue delamination and the corresponding parameter values are: $C = 2.27\text{e}13$, $\beta = 11.75$, and $\lambda = 0.5$

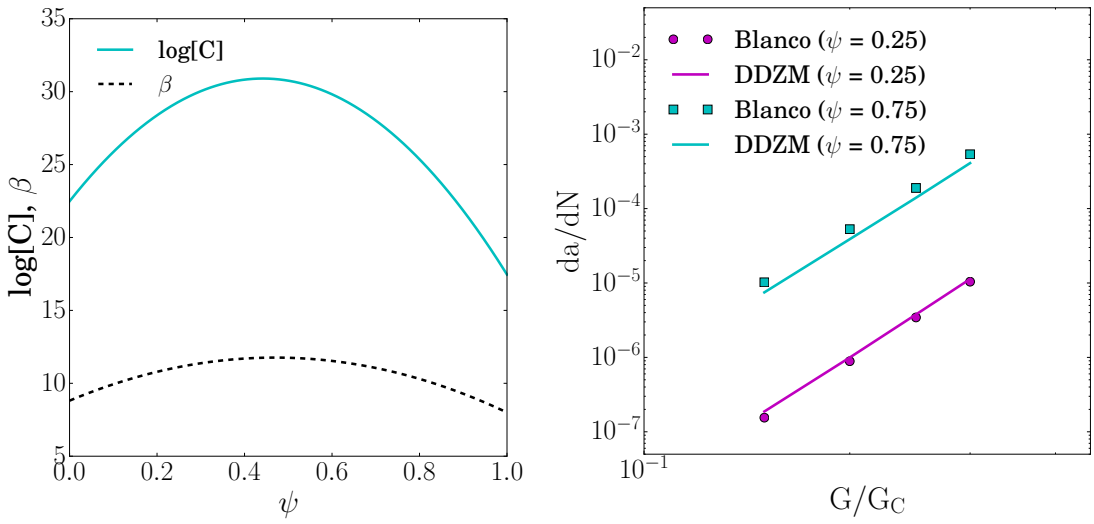

Figure 2.12: Crack propagation rate vs. normalized strain energy release rate for verification tests at mode ratio $\Psi = 0.25$ and $\Psi = 0.75$, and the distribution of parameters of C and β over mode ratio Ψ, where $c_2 = -43.14$, $c_1 = 38.11$, and $c_0 = 22.48$, $b_2 = -13.38$. $b_1 = 12.57$, and $b_0 = 8.81$.

2.4.4 Delamination at elevated temperatures

In this section, we calibrate the temperature dependence of fatigue delamination from the experimental data of Sjogren and Asp [2002]. In Figure 2.13, we plot the experimental data available at two different temperatures $T = 20$ °C (room temperature) and $T = 100$ °C for each of the three mode cases: pure mode I, pure mode II and mixed mode with $\Psi = 0.5$ (50% mode II). The experimental data suggests that crack growth occurs at a faster rate at elevated temperature $T = 100$ °C under both pure mode I and 50% mode II loading, as shown in Figures 2.13(a) and 2.13(c). However, under pure mode II loading, the crack growth rate is observed to decrease because the mechanisms of damage are different at the two temperatures. It is plausible that an increase in the ductility of epoxy resin with temperature could lead to such behavior [Khan et al., 2002]. Assuming the damage activation energy, $Q = 25$ KJ/mol, a reasonable fit with the experimental data is obtained for pure mode I and 50% mode II cases, but the fit is not good for pure mode II case. This leads us to believe that the Arrhenius relation is suitable for incorporating temperature dependence

so long as the main damage mechanism remains the same. Moreover, the model-predicted increase in crack growth rate under pure mode II is much smaller than that under mode I or 50% mixed mode. This is because G_{IIC} reduces substantially at $T = 100$ °C, so the applied load P of the ENF test also decreases according to equation (2.41). Furthermore, we assume that the elastic parameters of the element's force-separation law (e.g., K_t^0 and δ_t^{cr}) remain unchanged; therefore, only the static damage coefficient $B(T)$ is altered to satisfy the reduced energy criterion (see section 2.3.2). However, fatigue damage coefficient $C(T)$ increases with temperature according to the Arrhenius relation (2.11). With a weaker load P, unaltered elastic behavior, smaller B and larger C, crack growth rate does not increase by much at $T = 100$ °C under mode II. This effect is not observed in mode I or 50% mixed mode because the decrease in G_{IC} is marginal, and $G_{\mathrm{C}}(\Psi{=}0.5)$ actually increases at elevated temperatures. Thus, from this study it is evident that the parameter C is temperature dependent; however, more detailed experiments are required to understand the damage mechanisms in composites at various temperatures.

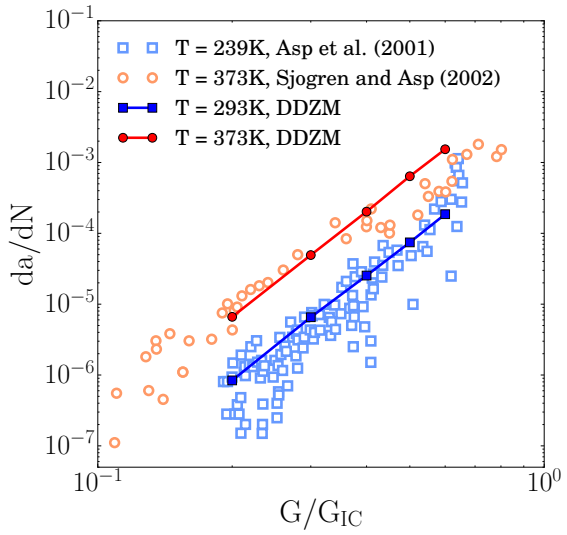

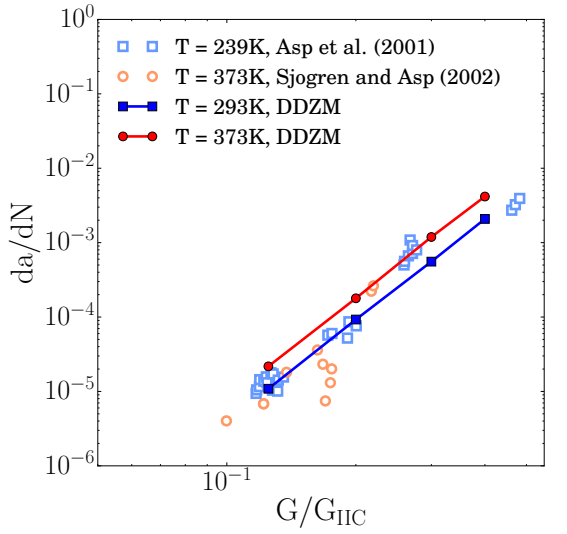

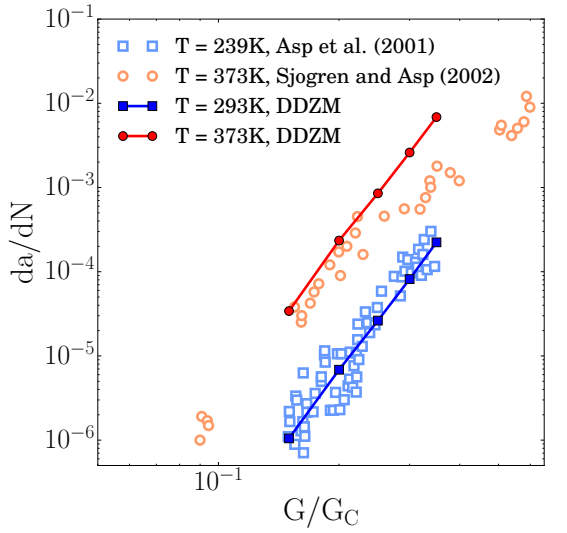

Figure 2.13: Paris plots of mode I, mode II and mixed mode with $\Psi = 0.5$ fatigue delamination at room temperature and high temperature

2.5 Conclusions

A discrete damage zone model (DDZM) for temperature dependent mixed mode delamination in composites under high cycle fatigue loading was developed from the original model for quasi-static loading [Liu et al., 2012], by adding fatigue and static damage components. The proposed model employs the interface element as a discrete spring placed at the finite element nodes and its constitutive law is derived entirely from damage laws, specifically, by combining Mazars law for static damage growth [Mazars, 1986] and Peerlings law for fatigue damage growth [Peerlings et al., 2000]. The model parameters were calibrated under pure mode I, pure mode II, and 50% mode II loadings. A quadratic relation was proposed to evaluate the parameters for other mode mix ratios (25% and 75% mode II) and then model results were verified with the numerical results of [Blanco et al., 2004], which demonstrates the validity of the model. The advantage of the DDZM approach is that it offers a lot of flexibility for incorporating different damage models to describe interface failure behavior under different loading and environmental conditions.

Overall, the contribution of this chapter is three-fold: (1) it formalizes mixed-mode relations for fatigue delamination prediction for any arbitrary mode mix ratio; (2) it proposes the Arrhenius relation for the temperature dependence of fatigue damage; and (3) it presents the finite element implementation of DDZM that ensures convergence with mesh refinement. The current model would be extremely useful in studying delamination in structural components wherein curved geometries and different lamina ply orientation can result in varying mode mix ratios.

Acknowledgements

We gratefully acknowledge the funding from our sponsors: SKJ and RD were supported by the Vanderbilt University Discovery Grant Program; XL and HW were supported by the National Science Foundation under grant CMMI-0856161.

CHAPTER 3

ON THE PARAMETRIC SENSITIVITY OF COHESIVE ZONE MODELS FOR HIGH-CYCLE FATIGUE DELAMINATION OF COMPOSITES

3.1 Introduction

3.1.1 Preamble

As the design of composite structures is increasingly dictated by lighter weight and better performance requirements, the prediction of long term performance degradation of laminated composite materials using accurate progressive damage accumulation models is becoming ever more important. In the past two decades, the cohesive zone model (CZM) has been extensively used to model and simulate the progressive growth of delamination and debonding in composites within the framework of the finite element method (FEM) because it does not require remeshing as the crack propagates. A variety of CZMs have been developed in the literature for monotonic loading scenarios featuring bilinear, trapezoidal, polynomial, or exponential shapes [van den Bosch et al., 2006]. More recently, CZMs have been developed to investigate high-cycle fatigue debonding and delamination growth, which are the dominant modes of failure for subcritical cyclic loading in laminated composite structures [Mi et al., 1998b]. A more detailed literature review of the CZMs for monotonic (static) and cyclic (fatigue) loading is given in the following Section 3.1.2. It is important to note that the CZM is essentially a damage mechanics approach for simulating fracture [Alfano and Crisfield, 2001] and is phenomenological in nature. Although many of the CZM parameters have a physical interpretation, they are actually calibrated by fitting the model results to experimental data. Consequently, the viability of CZMs as reliable and accurate progressive damage accumulation models rests on the use and development of cohesive laws that are minimally sensitive to phenomenological parameters. To this end,

this study investigates the effect of the shape, strength and stiffness parameters of static cohesive laws on delamination crack growth rate under high-cycle fatigue loading.

The significance of static cohesive parameters (e.g., initial stiffness and cohesive strength) has already been investigated for monotonic (static) loading cases, and several studies reported that the shape of the cohesive law has little effect on global load-displacement behavior so long as the critical fracture energy is held constant [Valoroso and Champaney, 2006, Gustafson and Waas, 2009]. However, there are some static loading studies where numerical results are sensitive to the CZM parameters, particularly the cohesive strength (i.e., maximum traction) and the shape of the damage-softening regime [Chandra et al., 2002, de Borst, 2003]. For high-cycle fatigue loading, the approach has generally been to decompose damage into static and fatigue components and employ power-law functions to describe fatigue damage accumulation over large numbers of cycles [Robinson et al., 2005, Harper and Hallett, 2010, Khoramishad et al., 2010, de Moura and Gonçalves, 2014, Jimenez et al., 2014]. Typically, the power law function is defined based on either the interface separation or the strain energy release rate (SERR) by introducing two new parameters, namely, the damage coefficient and exponent. These two model parameters are then calibrated by matching numerical results to the experimental data in the Paris regime, wherein the crack growth rate with respect to loading cycles $\mathrm{d}a/\mathrm{d}N$ varies linearly with the strain energy release rate ΔG or the stress intensity factor ΔK when plotted on a log-log scale [Paris et al., 1961, Paris and Erdogan, 1963]. A key point is that the interaction between static and fatigue damage under cyclic loading introduces a non-physical dependence of fatigue crack growth rate on static model parameters of cohesive stiffness and cohesive strength, which are usually taken as penalty parameters under monotonic loading cases [Pascoe et al., 2013]. Additionally, the crack growth rate predictions are affected by the lack of smoothness of cohesive law (e.g. bilinear shape with C^0 continuity) due to the abrupt change from linear elastic behavior to damage-induced softening behavior. Moreover, the power law fatigue damage functions based on interface separation and SERR

exhibit different parametric sensitivities depending on the numerical implementation. To the best of the authors' knowledge, there exist no prior investigations that assess the sensitivity of crack growth rate results to CZM parameters for high-cycle fatigue loading of laminated composites.

The main contribution of this chapter is with respect to the assessment of the sensitivity of interface separation and SERR based fatigue damage model predictions to static cohesive stiffness and strength parameters and to the shape (smoothness) of the cohesive law. The second contribution is the investigation of the additive and non-additive decompositions for combining static and fatigue damage components during cyclic loading, along with a sensitivity study between constrained and unconstrained damage update algorithms at the crack tip. The main conclusion of this chapter is that the SERR based fatigue damage function leads to a more reliable formulation for predicting delamination crack growth under high-cycle fatigue loading.

3.1.2 Literature review

The various approaches for numerical simulation of delamination can be classified into linear elastic fracture mechanics (LEFM) approaches and continuum damage mechanics (CDM) approaches. The cohesive zone model (CZM), developed by Hillerborg et al. [1976] using the concept of a bounded stress field within the vicinity of a crack tip [Dugdale, 1960, Barenblatt, 1962] can be recast into the CDM approach [Alfano and Crisfield, 2001]. In the CZM, cohesive elements are placed along potential crack interfaces and their constitutive behavior is defined by a traction-separation ($T-\delta$) law. Typically, the cohesive element is assumed to have zero thickness and the crack interface separation δ is calculated from the relative displacement of its nodes once the interface begins to open. The $T-\delta$ function generally features an initial elastic regime followed by a softening regime that can take a variety of shapes. Although the bilinear cohesive law is the simplest and also the most commonly employed $T-\delta$ law, other prominent formulations incorporate the expo-

nential functions [Xu and Needleman, 1994] and polynomial functions [Park et al., 2009] which were derived from thermodynamically based energy potentials. In early studies, CZMs were used to investigate crack growth under monotonic loading [Schellenkens and de Borst, 1993, Yang and Ravi-Chandar, 1998, Mi et al., 1998b, Robinson et al., 2000] and were not designed with an inelastic (irreversible) response to separation. Later, CZMs were formulated for non-monotonic loading by incorporating loading history dependent state variables to account for the irreversibility of damage accumulation in the material behind the crack tip [Foulk et al., 2000, Alfano and Crisfield, 2001, Park et al., 2009]. For example, Foulk et al. [2000] developed cohesive laws with a response dependent on the maximum separation during loading history; whereas, Alfano and Crisfield [2001] and Yang et al. [2001] presented CZM formulations by incorporating an irreversible damage variable, D_{s}, to represent interface degradation and permanently weaken the cohesive element. In general, following the damage mechanics framework the $T-\delta$ law can be written as Alfano and Crisfield [2001],

$$T = (1-D_{\mathrm{s}})K^0\delta, \tag{3.1}$$

where K^0 is the initial (undamaged) cohesive stiffness, and the scalar internal state variable $D_{\mathrm{s}} \in [0,1]$ controlling the shape of the softening regime. To ensure the irreversibility of damage, the condition $\dot{D}_{\mathrm{s}} \geq 0$ is imposed.

For monotonic (static) loading, at least two strength parameters are required to define the $T-\delta$ law, namely, the critical fracture energy G_{C} and cohesive strength $T_{\max}$, and additional shape and stiffness parameters are specified depending on the assumed shape of the cohesive law [Xu and Needleman, 1994]. Under pure mode I (normal separation) and mode II (tangent separation) conditions, the corresponding critical fracture energies are denoted by G_{IC} and G_{IIC}, and the corresponding cohesive strengths are denoted $\sigma_{\max}$ and $\tau_{\max}$, respectively. Since, in reality, debonding and delamination failures take place under variable mode-mix ratios with both normal and tangent separations, the mixed-mode behavior is conveniently described in terms of mode I and mode II parameters through an

interaction criterion [Jiang et al., 2007]. The mode I critical fracture energy G_{IC} (or critical SERR) is a material property that can be determined experimentally through a double-cantilever beam (DCB) test, and there is relatively little uncertainty in its value [Gustafson and Waas, 2009]. Oftentimes, G_{IC} is the only known cohesive parameter of a material [Diehl, 2008]. The standard procedure for retrieving G_{IIC} is the end notched flexure (ENF) test; however, the accuracy of this test is disputed [O'Brien, 1998, Pascoe et al., 2013].

Cohesive strength parameters σ_{max} and τ_{max} are the maximum tractions that the interface can sustain in the normal and tangential directions, respectively. The value of σ_{max} may be calibrated through various experiments [Gustafson and Waas, 2009], however there is no standard procedure for this measurement. Ferracin et al. [2003] suggested a combined numerical and experimental approach for determining σ_{max} by conducting a wedge-peel test and comparing the deformation of adherent arms to simulation results where a CZM is applied along the adhesive fracture process zone. Some authors regard σ_{max} as an adjustable penalty parameter because in many cases it does not heavily influence global load-displacement results, so long as a sufficiently large value is chosen [Xie et al., 2006, Turon et al., 2007b]. The value of τ_{max} can be determined from a single lap joint (SLJ) test, however, care must be taken to account for uncertainty of G_{IC} and G_{IIC} which can significantly affect the calibrated result [Gustafson and Waas, 2009]. The other stiffness and strength related parameters K_n^0, δ_n^c, and δ_n^u are usually dependent on G_{IC} and σ_{max}; likewise, K_t^0, δ_t^c, and δ_t^u are usually dependent on G_{IIC} and τ_{max}. Lee et al. [2010] proposed an iterative nonlinear optimization scheme to calibrate σ_{max}, τ_{max}, K_n^0, and K_t^0 from experimental data, provided that G_{IC} and G_{IIC} are known. Additionally, some $T - \delta$ laws define independent shape parameters to control the initial stiffness and the shape of the damage-softening zone without affecting either T_{max} or G_C [Park et al., 2009]. As Needleman [2014] suggested, the shape of the cohesive law can play a substantial role in numerical results when the size of the cohesive zone is large compared to the entire fracture surface. Given the uncertainty in the experimental determination of cohesive strength (σ_{max}, τ_{max}) and lack of certainty in

the selection of stiffness parameters (K_{n}^0, K_{t}^0) and cohesive shape, it is imperative that we develop CZM formulations that they are minimally sensitive to these parameters.

For cyclic loading, fatigue degradation is typically incorporated into the cohesive element's constitutive behavior by additively decomposing damage into static and fatigue components [Robinson et al., 2005, Harper and Hallett, 2010, Khoramishad et al., 2010, Kawashita and Hallett, 2012, de Moura and Gonçalves, 2014, Jimenez et al., 2014]. This approach assumes that static and fatigue delamination are governed by the same microscale failure mechanism (i.e., nucleation and growth of microvoids and microcracks), which is justified by fractographic analysis that shows little difference between static and fatigue fracture surfaces [Asp et al., 2001]. The interface stiffness is therefore weakened by a total damage variable D_{t} as,

$$T = (1 - D_{\mathrm{t}})K^0\delta; \qquad D_{\mathrm{t}} \in [0,1]; \qquad \dot{D}_{\mathrm{t}} \geq 0 \tag{3.2}$$

where damage is additively decomposed as,

$$D_{\mathrm{t}} = D_{\mathrm{s}} + D_{\mathrm{f}}. \tag{3.3}$$

However, for high-cycle fatigue analysis, D_{f} is evolved over increments of loading cycles ΔN by selecting an appropriate fatigue damage rate function. While this approach is applicable for constant amplitude loading with stress ratio $R = 0$, it is still possible to incorporate overload effects associated with occasional spikes in loading amplitude within this cycle-based analysis framework [Ural et al., 2009, Bouvard et al., 2009, Khoramishad et al., 2011]. Since the focus of this chapter is to assess the parametric sensitivity of the different CZMs for high-cycle fatigue delamination, we only consider constant amplitude loading with stress ratio $R = 0$.

Typically, the fatigue damage growth rate $\mathrm{d}D_{\mathrm{f}}/\mathrm{d}N$ is assumed to be a power law function of either the interface separation δ or the strain energy release rate ΔG or $G_{\max}$ with at

least two parameters, namely, the damage coefficient C and exponent parameter m. Robinson et al. [2005] proposed a separation based fatigue damage rate function using the continuum damage law of Peerlings et al. [2000]. Munoz et al. [2006] and Jimenez et al. [2014] followed the approach of Robinson et al. [2005] to investigate the time step size and mesh size dependence of the finite element implementation. Khoramishad et al. [2010] proposed a strain based fatigue damage rate function, wherein the strain is defined using the interface separation of cohesive elements with non-zero initial thickness. Harper and Hallett [2010] proposed a SERR based fatigue damage rate function by relating it to crack growth rate given by the Paris law. Later, Kawashita and Hallett [2012] developed a nonlocal crack tip tracking algorithm using a simplified SERR based function within the finite element method to alleviate directional mesh bias and to preserve consistency with LEFM in the Paris law regime. While Robinson et al. [2005] and Harper and Hallett [2010] followed an additive approach for combining static and fatigue damage components wherein both components affected cohesive strength and stiffness, Khoramishad et al. [2010] adopted a different non-additive approach, wherein the static damage affected only the static stiffness parameter and the fatigue damage affected only the static cohesive strength parameter. However, there are no studies in the literature that investigated the sensitivity of crack growth rate predictions to cohesive strength, stiffness or shape parameters for any of the above separation based or SERR based fatigue damage functions following the additive and non-additive approaches.

3.1.3 Outline

The rest of this chapter is organized as follows: in Section 3.2 the damage mechanics formulation of static cohesive zone models is reviewed for bilinear, exponential and polynomial shapes of traction-separation ($T-\delta$) laws along with the mixed-mode failure criteria. Section 3.3 describes the cycle-based damage evolution under mixed-mode high-cycle fatigue along with three damage rate functions based on interface separation, strain,

and strain energy release rate laws. Section 3.4 presents parametric sensitivity studies investigating the effect of static cohesive parameters and cohesive shape on fatigue delamination growth, for all combinations of the static and fatigue damage functions, under mode I and mixed mode configurations. The performance of the additive and non-additive damage decomposition schemes and constrained and unconstrained damage update strategies is also compared through numerical studies. Finally, Section 3.5 presents some concluding remarks and possible directions of future work. The setup of the mode I and mixed-mode simulations, the effect of static cohesive parameters on static (monotonic) delamination growth, and the calibration of fatigue damage parameters are provided in Appendix D and Appendix E.

3.2 Static CZM formulation

In the finite element implementation of the CZM, cohesive elements are introduced along laminate interfaces to simulate delamination crack growth. The constitutive behavior of the cohesive element is generally prescribed by a $T-\delta$ law that features an initial elastic response to resist crack opening followed by an irreversible damage-induced softening response. In the damage mechanics framework, the 2-D mixed-mode $T-\delta$ law is defined as,

$$\begin{Bmatrix} T_{\mathrm{t}} \\ T_{\mathrm{n}} \end{Bmatrix} = (1 - D_{\mathrm{s}}(\delta_{\mathrm{n}}, \delta_{\mathrm{t}})) \begin{bmatrix} K_{\mathrm{t}}^{0} & 0 \\ 0 & K_{\mathrm{n}}^{0} \end{bmatrix} \begin{Bmatrix} \delta_{\mathrm{t}} \\ \delta_{\mathrm{n}} \end{Bmatrix}, \tag{3.4}$$

where the subscripts "n" and "t" indicate normal (mode I) and tangent (mode II) directions with respect to the local interface orientation. In the above equation, the variable D_{s} is a scalar internal state variable if damage is assumed to be isotropic, however it is possible to incorporate anisotropic damage by defining D_{s} as a second order tensor [Liu et al., 2012]. The parameters of the static damage function $D_{\mathrm{s}}(\delta_{\mathrm{n}}, \delta_{\mathrm{t}})$ can be determined from the following three linear elastic fracture mechanics (LEFM) principles [Park et al., 2009, Liu et al., 2012]:

(I) The critical fracture energy is equal to the area under the $T-\delta$ curve, so for pure mode I and mode II we have,

$$\int_{0}^{\delta_{\mathrm{n}}^{\mathrm{u}}} T_{\mathrm{n}}(\delta_{\mathrm{n}}, 0)\mathrm{d}\delta_{\mathrm{n}} = G_{\mathrm{IC}} \ , \qquad \int_{0}^{\delta_{\mathrm{t}}^{\mathrm{u}}} T_{\mathrm{t}}(0, \delta_{\mathrm{t}})\mathrm{d}\delta_{\mathrm{t}} = G_{\mathrm{IIC}} \ . \tag{3.5}$$

(II) The maximum traction $T_{\max}$ is equal to the interface cohesive strength,

$$T_{\mathrm{n}}(\delta_{\mathrm{n}}^{\mathrm{c}}, 0) = \sigma_{\max} \ , \qquad T_{\mathrm{t}}(0, \delta_{\mathrm{t}}^{\mathrm{c}}) = \tau_{\max} \ ; \tag{3.6}$$

(III) For $T-\delta$ laws with C^1 continuity or greater, the maximum traction should occur at

critical separation δ^{c},

$$\left.\frac{\partial T_{\mathrm{n}}}{\partial \delta_{\mathrm{n}}}\right|_{\delta_{\mathrm{n}}=\delta_{\mathrm{n}}^{\mathrm{c}},\ \delta_{\mathrm{t}}=0} = 0\ , \qquad \left.\frac{\partial T_{\mathrm{t}}}{\partial \delta_{\mathrm{t}}}\right|_{\delta_{\mathrm{n}}=0,\ \delta_{\mathrm{t}}=\delta_{\mathrm{t}}^{\mathrm{c}}} = 0\ . \tag{3.7}$$

3.2.1 Bilinear law

The bilinear traction-separation law, commonly used for its simplicity and flexibility, has a linear damage-softening response following an initial linear-elastic response so that it has a triangular shape (Figure 3.1). The function has C^0 continuity and is not differentiable at the point δ^{c}, so it fails to satisfy the smoothness conditions in (3.7). The bilinear law has three independent static parameters: critical fracture energy G_{C}, cohesive strength $T_{\max}$, and initial stiffness K^0 for a given fracture mode (i.e., mode I and mode II in 2-D). The normal and tangential critical and ultimate separations are not independent parameters and can be calculated as,

$$\delta_{\mathrm{n}}^{\mathrm{c}} = \frac{\sigma_{\max}}{K_{\mathrm{n}}^0}\ , \qquad \delta_{\mathrm{t}}^{\mathrm{c}} = \frac{\tau_{\max}}{K_{\mathrm{t}}^0}\ , \tag{3.8}$$

$$\delta_{\mathrm{n}}^{\mathrm{u}} = 2\frac{G_{\mathrm{IC}}}{\sigma_{\max}}\ , \qquad \delta_{\mathrm{t}}^{\mathrm{u}} = 2\frac{G_{\mathrm{IIC}}}{\tau_{\max}}\ . \tag{3.9}$$

While there is less uncertainty in the values of G_{IC} and G_{IIC} from experimental studies, the strength parameters $\sigma_{\max}$, and $\tau_{\max}$ are usually calibrated or selected by comparing numerical simulations with experimental data, giving rise to larger uncertainty in their values. Moreover, in the bilinear law the stiffness parameters K_{n}^0 and K_{t}^0 serve as a penalty parameters that are chosen without any physical basis, solely to avoid convergence issues and minimize artificial compliance effects.

Remark 9 *The normal cohesive stiffness K_{n}^0 of the bilinear law should be sufficiently large to minimize artificial compliance in the finite element implementation. For a composite material composed of two bulk layers bonded by a cohesive interface, the artificial compliance can be characterized by the ratio R_E of effective Young's modulus $\widetilde{E}$ to original*

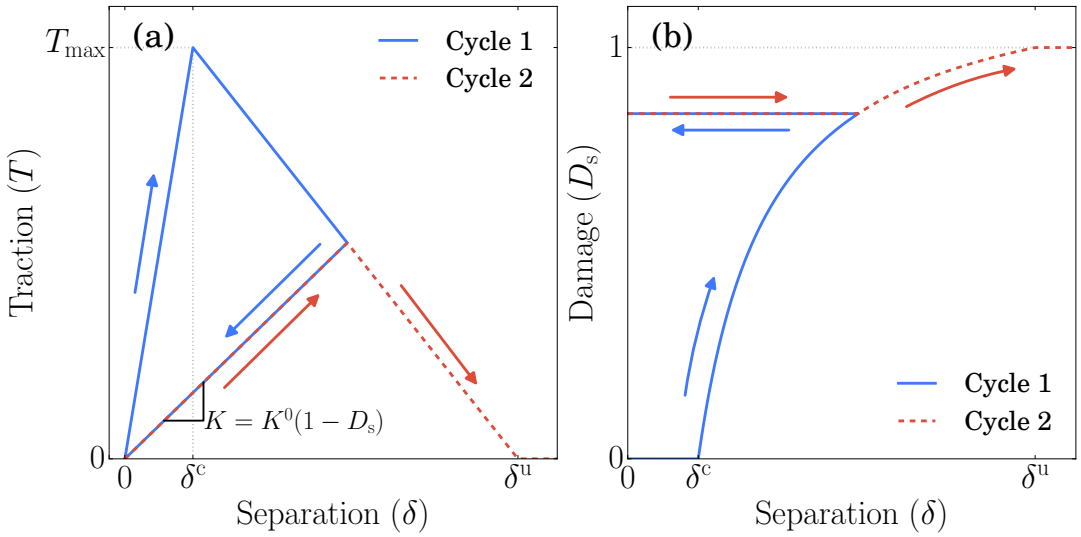

Figure 3.1: Irreversible bilinear cohesive zone model: (a) the $T-\delta$ law and (b) static damage versus separation. The traction and damage profiles follow the path indicated by blue arrows during initial loading and unloading, and red arrows during reloading.

Young's modulus E of the bulk material in the direction normal to the interface as [Blal et al., 2011],

$$R_E = \frac{\widetilde{E}}{E} = \frac{K_{\mathrm{n}}^0}{\frac{E}{H} + K_{\mathrm{n}}^0} \tag{3.10}$$

where H is the total thickness of the double cantilever beam normal to the interface. As $K_{\mathrm{n}}^0 \to \infty$ the ratio $R_E \to 1$, which is desirable, but selecting a very large value for K_{n}^0 can lead to numerical stability issues [de Borst, 2003]. The tangential stiffness parameter K_{t}^0 is chosen such that $K_{\mathrm{t}}^0 \geq K_{\mathrm{n}}^0$ so that both stiffnesses are on the same order of magnitude.

The traction response for general mixed-mode failure may be obtained by defining D_{s} in the equivalent (or resultant) space. The equivalent interface separation, δ_{e}, is taken as the magnitude of the separation vector,

$$\delta_{\mathrm{e}} = \sqrt{\langle \delta_{\mathrm{n}} \rangle^2 + (\delta_{\mathrm{t}})^2} \tag{3.11}$$

where $\langle x \rangle$ denotes Macaulay brackets, such that, $\langle x \rangle = \max(0, x)$. Thus, a negative value of δ_{n} indicates that the interfacial surfaces are in contact with each other, so it does not

contribute to damage or decohesion. Adopting the quadratic damage initiation criterion of Jiang et al. [2007], the equivalent critical separation δ_e^c can defined as,

$$\frac{1}{\delta_e^c} = \sqrt{\left(\frac{\cos \mathrm{I}}{\delta_n^c}\right)^2 + \left(\frac{\cos \mathrm{II}}{\delta_t^c}\right)^2}, \tag{3.12}$$

where the direction cosines $\cos \mathrm{I} = \dfrac{\delta_n}{\delta_e}$ and $\cos \mathrm{II} = \dfrac{\delta_t}{\delta_e}$. Next, a generalized power criterion is used for describing mixed-mode failure as,

$$\left(\frac{G_\mathrm{I}}{G_\mathrm{IC}}\right)^\alpha + \left(\frac{G_\mathrm{II}}{G_\mathrm{IIC}}\right)^\alpha = 1. \tag{3.13}$$

Choosing $\alpha = 1$, an expression for the corresponding equivalent ultimate separation δ_e^u when $D_s = 1$ can be written as,

$$\frac{1}{\delta_e^u} = \left(\frac{K_n^0\ \delta_e^c\ (\cos \mathrm{I})^2}{2G_\mathrm{IC}}\right) + \left(\frac{K_t^0\ \delta_e^c\ (\cos \mathrm{II})^2}{2G_\mathrm{IIC}}\right) \tag{3.14}$$

Now that δ_e, δ_e^c, and δ_e^u have been defined, the static damage function corresponding to the bilinear cohesive law can be defined as [Alfano and Crisfield, 2001, Robinson et al., 2005, Jiang et al., 2007],

$$D_s = \begin{cases} 0, & \text{if} \quad \delta_e < \delta_e^c \\ \dfrac{\delta_e^u\,(\delta_e - \delta_e^c)}{\delta_e\,(\delta_e^u - \delta_e^c)}, & \text{if} \quad \delta_e^c \le \delta_e < \delta_e^u \\ 1, & \text{if} \quad \delta_e^u \le \delta_e \end{cases}, \qquad \dot{D}_s \ge 0. \tag{3.15}$$

When $\delta_e < \delta_e^c$, damage does not accumulate, and the cohesive element retains its full strength. Once $\delta_e > \delta_e^c$ damage rapidly grows until $\delta_e \ge \delta_e^u$ where the cohesive element fully fails. The condition $\dot{D}_s \ge 0$ ensures the irreversibility of damage so that unloading and reloading is governed by the degraded (secant) stiffness, as shown in Figure 3.1. The piecewise linear $T - \delta$ relation can be obtained by substituting equation (3.15) into equa-

tion (3.4).

Remark 10 *Following the work of Alfano and Crisfield [2001], we consider that static damage D_s affects the secant cohesive stiffness K^0, according to equation (3.1). Jiang et al. [2007] suggested an alternative damage description for the bilinear traction-separation law, wherein D_s affects the cohesive strength $\hat{T}_{max}$ where, for $\delta > \delta^c$,*

$$\hat{T}_{max} = (1 - D_s) T_{max} \; ; \qquad D_s = \frac{\delta - \delta^c}{\delta^u - \delta^c} \tag{3.16}$$

such that static damage varies linearly for all $\delta \in (\delta^c, \delta^u]$. Both damage definitions can be calibrated to predict similar evolution of the total damage variable D_t with respect to loading cycles, so from this standpoint either approach may be appropriate for fatigue delamination analysis.

3.2.2 Polynomial law

The polynomial cohesive law was originally developed by Needleman [1987] and was later modified by Foulk et al. [2000] to account for irreversible mixed-mode fracture. Unlike the bilinear law, the polynomial law (see Fig. 3.2) is a continuously differentiable function for monotonic loading and satisfies the LEFM relation in equation (3.7). This law has only two independent model parameters: cohesive strength T_{max} and ultimate separation δ^u for a given fracture mode. The traction response for normal and tangent directions is given by [Foulk et al., 2000] ,

$$T_n = \left(\frac{27}{4}\right) \sigma_{max} \left(\frac{\langle \delta_n \rangle}{\delta_n^u}\right) (1 - \lambda_{max})^2 , \tag{3.17a}$$

$$T_t = \left(\frac{27}{4}\right) \tau_{max} \left(\frac{\delta_t}{\delta_t^u}\right) (1 - \lambda_{max})^2 , \tag{3.17b}$$

where σ_{max} and τ_{max} are the maximum normal and tangent tractions, respectively, so as to be consistent with LEFM principles defined in equations (3.6) and (3.7), and λ_{max} is the

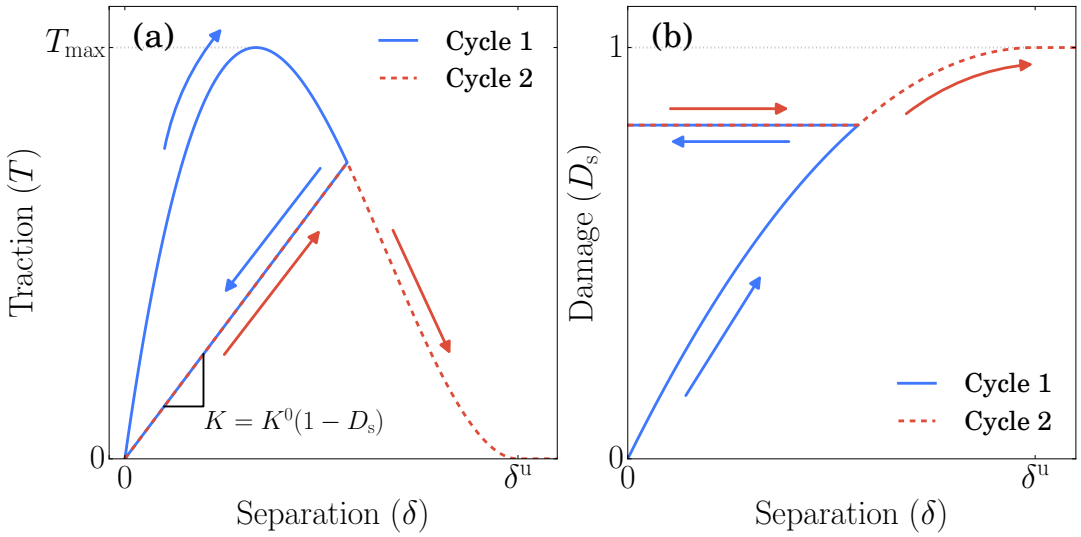

Figure 3.2: Irreversible polynomial cohesive zone model: (a) the $T-\delta$ law and (b) static damage versus separation. The traction and damage profiles follow the path indicated by blue arrows during initial loading and unloading, and red arrows during reloading.

state variable characterizing the maximum effective separation throughout loading history, defined by,

$$\lambda_{\max} = \sqrt{\left(\frac{\langle \delta_n \rangle}{\delta_n^u}\right)^2 + \left(\frac{\delta_t}{\delta_t^u}\right)^2}; \quad \lambda_{\max} \in [0,1]; \quad \dot{\lambda}_{\max} \geq 0. \tag{3.18}$$

Since $\lambda_{\max}$ remains a constant during unloading and reloading, the traction unloads and reloads along the secant direction until $\lambda_{\max}$ is once again exceeded, as shown in Figure 3.2.

Let us now recast the polynomial cohesive law into the damage mechanics framework using an isotropic damage variable D_s. Since the softening regime is controlled by the $(1-\lambda_{\max})^2$ term for both modes of failure, it is appropriate to define a mixed-mode static damage function as,

$$(1-D_s) = (1-\lambda_{\max})^2; \quad D_s \in [0,1]; \quad \dot{D}_s > 0, \tag{3.19}$$

Substituting the relation for $\lambda_{\max}$ in (3.18) into the above equation, we get,

$$D_{\mathrm{s}} = 1 - \left(1 - \sqrt{\left(\frac{\langle \delta_{\mathrm{n}} \rangle}{\delta_{\mathrm{n}}^{\mathrm{u}}}\right)^2 + \left(\frac{\delta_{\mathrm{t}}}{\delta_{\mathrm{t}}^{\mathrm{u}}}\right)^2}\right)^2. \tag{3.20}$$

The maximum separations $\delta_{\mathrm{n}}^{\mathrm{u}}$ and $\delta_{\mathrm{t}}^{\mathrm{u}}$ can now be determined according to (3.5) by equating the area under the mode I and mode II $T-\delta$ curves to G_{IC} and G_{IIC}, respectively. For example, for pure mode I loading $\delta_{\mathrm{t}} = 0$ and $\lambda_{\max} = \delta_{\mathrm{n}}/\delta_{\mathrm{n}}^{\mathrm{u}}$, so we can obtain,

$$\int_0^{\delta_{\mathrm{n}}^{\mathrm{u}}} T_{\mathrm{n}} \mathrm{d}\delta_{\mathrm{n}} = \int_0^{\delta_{\mathrm{n}}^{\mathrm{u}}} \left(\frac{27}{4}\right) \sigma_{\max} \left(\frac{\delta_{\mathrm{n}}}{\delta_{\mathrm{n}}^{\mathrm{u}}}\right) \left(1 - \frac{\delta_{\mathrm{n}}}{\delta_{\mathrm{n}}^{\mathrm{u}}}\right)^2 \mathrm{d}\delta_{\mathrm{n}} = \frac{9}{16} \sigma_{\max} \delta_{\mathrm{n}}^{\mathrm{u}} = G_{\mathrm{IC}}. \tag{3.21}$$

The pure mode II analogue of (3.21) is obtained by considering $\delta_{\mathrm{n}} = 0$ and $\lambda_{\max} = \delta_{\mathrm{t}}/\delta_{\mathrm{t}}^{\mathrm{u}}$. Thus, we can define $\delta_{\mathrm{n}}^{\mathrm{u}}$ and $\delta_{\mathrm{t}}^{\mathrm{u}}$ in terms of critical fracture energies and the cohesive strength parameters as,

$$\delta_{\mathrm{n}}^{\mathrm{u}} = \frac{16}{9}\left(\frac{G_{\mathrm{IC}}}{\sigma_{\max}}\right), \qquad \delta_{\mathrm{t}}^{\mathrm{u}} = \frac{16}{9}\left(\frac{G_{\mathrm{IIC}}}{\tau_{\max}}\right). \tag{3.22}$$

Thus, the recast polynomial cohesive law has two independent model parameters: critical fracture energy G_{C} and cohesive strength $T_{\max}$ for a given fracture mode (i.e., mode I and mode II in 2-D). The initial stiffnesses K_{n}^0 and K_{t}^0 are not independent parameters and can be obtained as,

$$K_{\mathrm{n}}^0 = \left.\frac{\partial T_{\mathrm{n}}}{\partial \delta_{\mathrm{n}}}\right|_{\delta_{\mathrm{n}}=\delta_{\mathrm{t}}=0} = \frac{27}{4}\left(\frac{\sigma_{\max}}{\delta_{\mathrm{n}}^{\mathrm{u}}}\right) = \frac{243}{64}\left(\frac{\sigma_{\max}^2}{G_{\mathrm{IC}}}\right), \tag{3.23a}$$

$$K_{\mathrm{t}}^0 = \left.\frac{\partial T_{\mathrm{t}}}{\partial \delta_{\mathrm{t}}}\right|_{\delta_{\mathrm{n}}=\delta_{\mathrm{t}}=0} = \frac{27}{4}\left(\frac{\tau_{\max}}{\delta_{\mathrm{t}}^{\mathrm{u}}}\right) = \frac{243}{64}\left(\frac{\tau_{\max}^2}{G_{\mathrm{IIC}}}\right). \tag{3.23b}$$

Remark 11 *The cohesive strength parameters $\sigma_{\max}$ and $\tau_{\max}$ for the polynomial cohesive law may be selected by comparing numerical simulations with analytical LEFM solutions*

[Park et al., 2009]. While selecting larger values for $\sigma_{\max}$ and $\tau_{\max}$ yields a better fit with analytical solutions, this decreases the length of the fracture process zone (FPZ); consequently, one needs to reduce the size of cohesive elements in order to resolve the FPZ with at least three cohesive elements for the sake of accuracy [Harper and Hallett, 2008]. Thus, the cohesive strengths are generally treated as adjustable (penalty) parameters with the goal of improving convergence rates and limiting computational expense [Turon et al., 2007b], which gives rise to uncertainty on their values in the literature.

3.2.3 Exponential law

Let us consider the exponential traction-separation law proposed by Liu et al. [2012] based on the continuum damage model of Mazars [1986]. This $T-\delta$ law features an initial linear-elastic regime followed by an exponential softening regime (see Fig. 3.3) that satisfies the smoothness condition (3.7) at critical separation when approached from the softening regime, but not when approached from the elastic regime. As noted by Liu et al. [2012], the softening portion of this exponential $T-\delta$ law matches that of the potential-based cohesive zone model proposed in Xu and Needleman [1994] for pure mode I loading. The static damage function corresponding to this mixed-mode exponential law is given by,

$$D_{\mathrm{s}} = \begin{cases} 0, & \text{if} \quad \delta_{\mathrm{e}} < \delta_{\mathrm{e}}^{\mathrm{c}} \\ 1-\exp\left(1-\frac{\delta_{\mathrm{e}}}{\delta_{\mathrm{e}}^{\mathrm{c}}}\right), & \text{if} \quad \delta_{\mathrm{e}} \geq \delta_{\mathrm{e}}^{\mathrm{c}} \end{cases}, \qquad \dot{D}_{\mathrm{s}} \geq 0, \tag{3.24}$$

where equivalent separation δ_{e} is given by (3.11), and equivalent critical separation $\delta_{\mathrm{e}}^{\mathrm{c}}$ is given by (3.12). The exponential $T-\delta$ relation can now be obtained by substituting equation (3.24) into equation (3.4). The mixed mode implementation of the exponential law is similar to that of the bilinear law, except for the difference in damage functions describing the softening regime. In order to determine $\delta_{\mathrm{e}}^{\mathrm{c}}$, we invoke the LEFM relation

(3.5) that area under the $T-\delta$ curve is equal to the critical fracture energy G_{C}, that is,

$$\int_0^{\infty} \sigma_{\max} \frac{\delta_{\mathrm{n}}}{\delta_{\mathrm{n}}^{\mathrm{c}}} \exp\left(1-\frac{\delta_{\mathrm{n}}}{\delta_{\mathrm{n}}^{\mathrm{c}}}\right) \mathrm{d}\delta = \exp(1)\delta_{\mathrm{n}}^{\mathrm{c}}\sigma_{\max} = G_{\mathrm{IC}}, \tag{3.25a}$$

$$\int_0^{\infty} \tau_{\max} \frac{\delta_{\mathrm{t}}}{\delta_{\mathrm{t}}^{\mathrm{c}}} \exp\left(1-\frac{\delta_{\mathrm{t}}}{\delta_{\mathrm{t}}^{\mathrm{c}}}\right) \mathrm{d}\delta = \exp(1)\delta_{\mathrm{t}}^{\mathrm{c}}\tau_{\max} = G_{\mathrm{IIC}}. \tag{3.25b}$$

From the above relations we can determine the critical separations as,

$$\delta_{\mathrm{n}}^{\mathrm{c}} = \frac{G_{\mathrm{IC}}}{\sigma_{\max}\exp(1)}\ , \qquad \delta_{\mathrm{t}}^{\mathrm{c}} = \frac{G_{\mathrm{IIC}}}{\tau_{\max}\exp(1)}\ . \tag{3.26}$$

The initial stiffness can be calculated as,

$$K_{\mathrm{n}}^0 = \left.\frac{\partial T_{\mathrm{n}}}{\partial \delta_{\mathrm{n}}}\right|_{\delta_{\mathrm{n}}=\delta_{\mathrm{t}}=0} = \frac{\sigma_{\max}}{\delta_{\mathrm{n}}^{\mathrm{c}}} = \frac{\sigma_{\max}^2\exp(1)}{G_{\mathrm{IC}}}, \tag{3.27a}$$

$$K_{\mathrm{t}}^0 = \left.\frac{\partial T_{\mathrm{t}}}{\partial \delta_{\mathrm{t}}}\right|_{\delta_{\mathrm{n}}=\delta_{\mathrm{t}}=0} = \frac{\tau_{\max}}{\delta_{\mathrm{t}}^{\mathrm{c}}} = \frac{\tau_{\max}^2\exp(1)}{G_{\mathrm{IIC}}}. \tag{3.27b}$$

Note that the exponential $T-\delta$ law does not have an ultimate separation δ^{u}; rather, the traction will approach 0 with exponential decay as the separation approaches infinity. Thus, the exponential law has only two independent model parameters: critical fracture energy G_{C} and cohesive strength $T_{\max}$ for a given fracture mode (i.e., mode I and mode II in 2-D). Also, any uncertainty in the values of $\sigma_{\max}$ and $\tau_{\max}$ leads to a larger uncertainty in the values of K_{n}^0 and K_{t}^0 because the initial stiffness is proportional to the square of the cohesive strength.

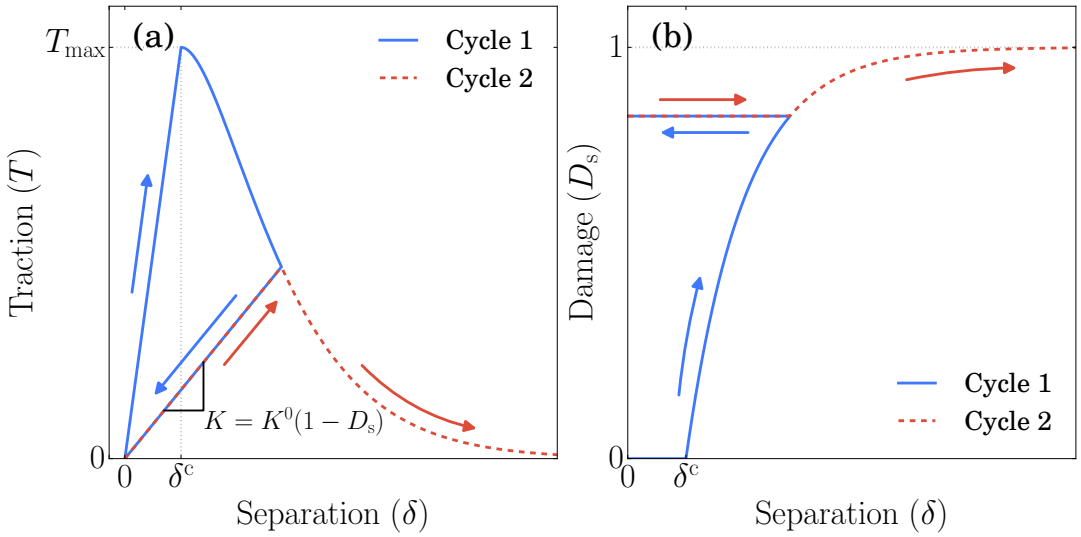

Figure 3.3: Irreversible exponential cohesive zone model: (a) the $T - \delta$ law and (b) static damage versus separation. The traction and damage profiles follow the path indicated by blue arrows during initial loading and unloading, and red arrows during reloading.

3.3 Fatigue CZM formulation

The irreversible damage mechanics formulation of the CZM can be naturally extended for modeling fatigue delamination by incorporating a fatigue damage state variable D_{f} in addition to its static counterpart D_{s}. For high-cycle fatigue loading, D_{f} is computed at any step k of the simulation as,

$$ {}^{k}D_{\mathrm{f}} = {}^{k-1}D_{\mathrm{f}} + \Delta D_{\mathrm{f}} = {}^{k-1}D_{\mathrm{f}} + \left(\frac{\mathrm{d}D_{\mathrm{f}}}{\mathrm{d}N}\right)\Delta N, \tag{3.28} $$

where ΔD_{f} is the fatigue damage increment over a certain number of loading cycles $\Delta N = {}^{k}N - {}^{k-1}N$. The fatigue damage rate $\mathrm{d}D_{\mathrm{f}}/\mathrm{d}N$ is defined such that it can adequately describe the experimental Paris law data, wherein the fatigue crack growth rate with respect to loading cycles $\mathrm{d}a/\mathrm{d}N$ varies linearly with the normalized strain energy release rate $\Delta G/G_{\mathrm{C}}$ when plotted on a log-log scale as,

$$ \frac{\mathrm{d}a}{\mathrm{d}N} = C\left(\frac{\Delta G}{G_{\mathrm{C}}}\right)^{m} \tag{3.29} $$

Hence, high-cycle fatigue damage rate functions are usually formulated as power laws with a damage coefficient parameter C and an exponent parameter m that are calibrated from experimental data. The power law function may be formulated in terms of interface separation δ, interface strain ε, or strain energy release rate $G_{\max}$.

For mixed-mode fatigue loading, the values for C, m, and the critical fracture energy G_{C} are functions of mode-mix ratio ψ defined by,

$$ \psi = \frac{G_{\mathrm{II}}}{G_{\mathrm{I}} + G_{\mathrm{II}}}, \tag{3.30} $$

where G_{I} and G_{II} are the mode I and mode II strain energies, respectively. Obviously, for pure mode I failure, $\psi = 0$, and for pure mode II failure, $\psi = 1$. Among the most common methods for evaluating G_{C} at arbitrary mode-mix ratios is the B-K criterion [Kenane and

Benzeggagh, 1997] given by,

$$G_{\mathrm{C}} = G_{\mathrm{IC}} + (G_{\mathrm{IIC}} - G_{\mathrm{IC}})\,(\psi)^{\eta}\,. \tag{3.31}$$

The B-K criterion is included in the commercial software Abaqus for its standard cohesive elements; however, it only allows monotonic variation between the mode I and mode II extremes which may not be suited for fitting C and m for all materials. To avoid this, Blanco et al. [2004] proposed an alternative quadratic criterion for evaluating C, m, and G_{C} at arbitrary mode-mix ratios as,

$$G_{\mathrm{C}} = g_0 + g_1\psi + g_2\psi^2, \tag{3.32}$$

where g_0, g_1, and g_2 are the coefficients obtained by fitting a quadratic polynomial to known instances of G_{C} at three separate mode-mix ratios. Similarly, the parameters C and m are also defined using the quadratic criterion and the corresponding coefficients are calibrated to fit Paris data at three mode-mix ratios.

3.3.1 SERR-based fatigue damage rate function

Let us first consider the fatigue damage rate function derived by Kawashita and Hallett [2012] by relating damage growth rate to crack growth rate in the Paris regime. While Kawashita and Hallett [2012] additively combined fatigue damage with static damage corresponding to the bilinear $T-\delta$ law, in this section we investigate the performance of the fatigue damage function when combined with static damage corresponding to exponential and polynomial $T-\delta$ laws as well. The fatigue damage rate with respect to number of loading cycles N at a given simulation step k as derived by Kawashita and Hallett [2012] reads,

$$\frac{\mathrm{d}D_{\mathrm{f}}}{\mathrm{d}N} = \left(\frac{1-D_{\mathrm{s}}}{h}\right) C_1 \left(\frac{\Delta G}{G_{\mathrm{C}}}\right)^{m_1}, \quad \text{for all} \;\; G_{\max} > G_{\mathrm{th}}, \tag{3.33}$$

where h is the mesh size (i.e., length of the cohesive element), ΔG is the strain energy release rate, G_{C} is the critical fracture energy for a given mode-mix ratio ψ and C_1 and m_1 are corresponding fatigue parameters. Thus, this function introduces two empirical parameters C_1 and m_1 into the CZM formulation; however, they can be calibrated directly from Paris data with greater confidence, unlike the static cohesive strength and stiffness parameters. Since this function only represents the Paris regime, it is assumed that the SERR amplitude $G_{\max}$ exceeds the threshold SERR, G_{th}, so fatigue crack growth rate is positive.

Following Kawashita and Hallett [2012], a trapezoidal rule is employed to numerically calculate the strain energy release rate ΔG corresponding to the area under the $T-\delta$ curve integrated from zero to the current separation δ^k at step k as,

$$\Delta G_{\mathrm{I}} = \sum_{k=1}^{N_{inc}} \left(\frac{{}^{k}T_{\mathrm{n}} + {}^{k-1}T_{\mathrm{n}}}{2} \right) \left({}^{k}\delta_{\mathrm{n}} - {}^{k-1}\delta_{\mathrm{n}} \right), \tag{3.34a}$$

$$\Delta G_{\mathrm{II}} = \sum_{k=1}^{N_{inc}} \left(\frac{{}^{k}T_{\mathrm{t}} + {}^{k-1}T_{\mathrm{t}}}{2} \right) \left({}^{k}\delta_{\mathrm{t}} - {}^{k-1}\delta_{\mathrm{t}} \right), \tag{3.34b}$$

where N_{inc} is the number of simulation steps up to the current step. The total strain energy release rate is given by the sum of the mode I and II contributions, that is,

$$\Delta G = \Delta G_{\mathrm{I}} + \Delta G_{\mathrm{II}}. \tag{3.35}$$

Remark 12 *Kawashita and Hallett [2012] presented a nonlocal crack tip tracking algorithm for the above SERR based fatigue damage rate function (Eq. 3.33) in order to alleviate directional mesh bias when simulating delamination propagation in 3-D. However, for simulating delamination in 2-D for mode I double cantilever beam or mixed-mode bending tests, wherein the crack is a simple 1D interface known a-priori, the nonlocal crack tip algorithm is not required; therefore, it is not implemented herein.*

3.3.2 Separation-based fatigue damage rate function

Let us next consider the fatigue damage rate function derived by Robinson et al. [2005] based on the continuum damage law of Peerlings et al. [2000]. While Robinson et al. [2005] additively combined this fatigue damage function with the static damage function corresponding to the bilinear $T-\delta$ law, in this section we also investigate the performance of the fatigue damage function when combined with the static damage functions corresponding to the exponential and polynomial $T-\delta$ laws. The fatigue damage rate with respect to loading cycles at a given simulation step k is,

$$\frac{\mathrm{d}D_{\mathrm{f}}}{\mathrm{d}N} = \frac{C_2}{m_2+1}\exp(\lambda D)\left(\frac{\delta}{\delta_{\mathrm{f}}}\right)^{m_2+1}, \quad \text{for all} \;\; G_{\max} > G_{\mathrm{th}}, \tag{3.36}$$

where D is the accumulated total damage, λ is a chosen damage magnification parameter that accounts for the increase in damage rate near existing damage features, C_2 and m_2 are the damage coefficient and exponent parameters, respectively, and δ_{f} is an assumed normalizing constant. Since the damage rate depends on the current state of damage an implicit scheme is adopted to determine the damage increment as,

$$\Delta D_{\mathrm{f}} = \Delta N\left(\frac{C_2}{m_2+1}\right)\exp\left(\lambda D_{\mu}\right)\left(\frac{\delta_{\mu}}{\delta_{\mathrm{f}}}\right)^{m_2+1} \tag{3.37}$$

where D_{μ} and δ_{μ} are the linear combinations of damage and separation, respectively, at some past cycle N and the current cycle $N+\Delta N$ at step k. An iterative Newton-Raphson method is used to determine ΔD_{f} and is described in Appendix H.

3.3.3 Strain-based fatigue damage rate function

Let us next consider the fatigue damage rate function proposed by Khoramishad et al. [2010], wherein interface strain was defined as ratio of the separation and an initial thickness of the cohesive interface. While Khoramishad et al. [2010] non-additively combined

fatigue damage with static damage corresponding to the bilinear $T-\delta$ laws, in this section we investigate the performance of the fatigue damage function when additively combined with static damage corresponding to the bilinear, exponential and polynomial $T-\delta$ laws. The fatigue damage rate with respect to loading cycles at a given simulation step k is,

$$\frac{\mathrm{d}D_{\mathrm{f}}}{\mathrm{d}N}=\begin{cases}0, & \text{if} \quad \varepsilon_{\mathrm{pr}}<\varepsilon_{\mathrm{th}}\\ C_3(\varepsilon_{\mathrm{pr}}-\varepsilon_{\mathrm{th}})^{m_3}, & \text{if} \quad \varepsilon_{\mathrm{pr}}\geq\varepsilon_{\mathrm{th}}\end{cases}, \tag{3.38}$$

where C_3 and m_3 are fatigue parameters, $\varepsilon_{\mathrm{th}}$ is a strain threshold, and $\varepsilon_{\mathrm{pr}}$ is the maximum principal strain in the interface element defined as,

$$\varepsilon_{\mathrm{pr}}=\frac{\langle\varepsilon_{\mathrm{n}}\rangle}{2}+\sqrt{\left(\frac{\langle\varepsilon_{\mathrm{n}}\rangle}{2}\right)^2+\left(\frac{\varepsilon_{\mathrm{t}}}{2}\right)^2}. \tag{3.39}$$

The above function proposed for non-zero initial thickness cohesive elements can also be implemented using zero initial thickness elements by defining strain ε to be equal to the interface separation divided by a normalizing constant l_{f} representing a fictitious initial thickness of the adhesive interface. The maximum principal strain of the cohesive element can now be determined as,

$$\varepsilon_{\mathrm{pr}}=\frac{1}{l_{\mathrm{f}}}\left(\frac{\langle\delta_{\mathrm{n}}\rangle}{2}+\sqrt{\left(\frac{\langle\delta_{\mathrm{n}}\rangle}{2}\right)^2+\left(\frac{\delta_{\mathrm{t}}}{2}\right)^2}\right) \tag{3.40}$$

In this study, we take the normalizing constant $l_{\mathrm{f}}=0.05$ mm, and $\varepsilon_{\mathrm{th}}=0$. Thus, in the current form, this function introduces only two parameters C_3 and m_3, similar to the other two power law fatigue damage rate functions.

Remark 13 *In continuum damage mechanics, the presence of existing damage is generally assumed to increase fatigue damage growth rate [Peerlings et al., 2000]. While this damage rate magnification is accounted for in the separation based function in equation (3.37), it is not considered in the strain based function in equation (3.38). In contrast, in the SERR*

based function in equation (3.33), derived by Kawashita and Hallett [2012] based on the Paris law, existing (static) damage slightly decreases fatigue damage growth rate, which is quite intriguing. Detailed experimental and theoretical studies are necessary to ascertain if this can be related to crack shielding of delamination due to damage.

3.3.4 Solution strategy

The different cohesive zone models for fatigue delamination obtained by combining the three static damage functions with the three fatigue damage rate functions are implemented within the commercial finite element software Abaqus using the user-element (UEL) subroutine. The user-defined interface element is a 4-noded element with two initially overlapping sets of nodes (i.e., initial thickness is zero) along the crack interface. A detailed numerical implementation of this user element for simulating static delamination in Abaqus is given in [Park and Paulino, 2012]. Herein, we briefly describe the algorithm for extending this user element for simulating fatigue delamination. First, the global displacement vector $\mathbf{u}$ is transformed to the local coordinate system with the axes parallel (tangent) and perpendicular (normal) to the crack interface. Next, the normal and tangential interface separations (δ_{n}, δ_{t}) are determined from the relative displacement of opposite nodes belonging to the two crack surfaces. Using standard linear shape functions and a two-point Gauss integration rule, D_{s} and D_{f} are calculated at each integration point and the elemental stiffness matrix and RHS vector are computed in the local coordinate system. Finally, the elemental stiffness matrix and RHS vector are transformed back to the global coordinate system and assembled into the global stiffness matrix and RHS vector. The values δ_{n}, δ_{t}, T_{n}, T_{t}, D_{s}, D_{f}, D_{t}, ΔG_{I}, ΔG_{II}, and N_{total} are stored as state variables at every integration point, where N_{total} is the total number of elapsed cycles. Algorithm 3 summarizes the solution strategy for any combination of the $T-\delta$ laws from Section 3.2 and the fatigue damage rate functions from Section 3.3.

Algorithm 3 : General solution scheme

At any simulation step $k+1$, the following is known from step k: nodal displacement vector ${}^{k}\mathbf{u}$, and state variables ${}^{k}\delta_{\mathrm{n}}$, ${}^{k}\delta_{\mathrm{t}}$, ${}^{k}T_{\mathrm{n}}$, ${}^{k}T_{\mathrm{t}}$, ${}^{k}D_{\mathrm{s}}$, ${}^{k}D_{\mathrm{f}}$, ${}^{k}D_{\mathrm{t}}$, ${}^{k}\Delta G_{\mathrm{I}}$, ${}^{k}\Delta G_{\mathrm{II}}$, and ${}^{k}N_{\mathrm{total}}$. At the initial step $k=0$, all of the state variables are equivalent to zero.

(1) Compute separations ${}^{k+1}\delta_{\mathrm{n}}$ and ${}^{k+1}\delta_{\mathrm{t}}$ from nodal displacements using ${}^{k}\mathbf{u}$ and linear FE shape functions.

(2) Compute static damage ${}^{k+1}D_{\mathrm{s}}$ from the prescribed $T-\delta$ law. Ensure that ${}^{k+1}D_{\mathrm{s}} \geq {}^{k}D_{\mathrm{s}}$.

(3) Compute fatigue damage increment ΔD_{f} based on interface separations or SERR.

(i) Compute ΔG according to Eq. (3.35) if using SERR-based damage rate function.

(ii) ${}^{k+1}N_{\mathrm{total}} = {}^{k}N_{\mathrm{total}} + \Delta N$ if fatigue cycling is being applied.

(iii) Compute ΔD_{f}. Ensure $\Delta D_{\mathrm{f}} \geq 0$. Then, ${}^{k+1}D_{\mathrm{f}} = {}^{k}D_{\mathrm{f}} + \Delta D_{\mathrm{f}}$

(4) Compute total damage ${}^{k+1}D_{\mathrm{t}} = {}^{k+1}D_{\mathrm{s}} + {}^{k+1}D_{\mathrm{f}}$. Ensure that ${}^{k+1}D_{\mathrm{t}} \geq {}^{k}D_{\mathrm{t}}$.

(5) Compute the elemental stiffness matrix at integration point i as,

$$\mathbf{K} = (1 - {}^{k+1}D_{\mathrm{t}}) \begin{bmatrix} K_{\mathrm{t}}^{0} & 0 \\ 0 & K_{\mathrm{n}}^{0} \end{bmatrix}$$

(6) Compute the tractions at integration point i as,

$$\mathbf{T} = \begin{Bmatrix} {}^{k+1}T_{\mathrm{t}} \\ {}^{k+1}T_{\mathrm{n}} \end{Bmatrix} = \mathbf{K} \begin{Bmatrix} {}^{k+1}\delta_{\mathrm{t}} \\ {}^{k+1}\delta_{\mathrm{n}} \end{Bmatrix}$$

(7) Assemble **AMATRX** and **RHS** arrays using $\mathbf{K}$ and $\mathbf{T}$ at each integration point.

(8) Store state variables ${}^{k+1}\delta_{\mathrm{n}}$, ${}^{k+1}\delta_{\mathrm{t}}$, ${}^{k+1}T_{\mathrm{n}}$, ${}^{k+1}T_{\mathrm{t}}$, ${}^{k+1}D_{\mathrm{s}}$, ${}^{k+1}D_{\mathrm{f}}$, ${}^{k+1}D_{\mathrm{t}}$, ${}^{k+1}\Delta G_{\mathrm{I}}$, ${}^{k+1}\Delta G_{\mathrm{II}}$, and ${}^{k+1}N_{\mathrm{total}}$ at each integration point.

3.4 Numerical studies of fatigue delamination models

In this section, we investigate the influence of static cohesive parameters, the shape of the $T-\delta$ law, damage composition and damage update schemes on fatigue delamination growth under high-cycle fatigue loading. Numerical simulations are conducted using two loading configurations: the mode I double cantilever beam (DCB) test and the mixed-mode bending (MMB) test for the carbon fiber-epoxy laminated composite HTA/6376C. Material properties of HTA/6367C obtained from Asp et al. [2001] are provided below in Table E1. We use a uniform, structured mesh to simulate the DCB and MMB tests in Abaqus software with CPS4 (four-noded continuum plane stress) elements and zero-thickness four-noded (cohesive) interface elements via the user element (UEL) subroutine. To ensure numerical accuracy, it is essential that a sufficient number of interface elements lie within the numerical cohesive (damage) zone. Therefore, the structured finite element mesh size is taken as $h = 0.25$ mm so that it is less than the maximum allowable cohesive element length defined in Harper and Hallett [2008].

Table 3.1: Material properties of carbon fiber/epoxy laminated composite HTA/6367C obtained from Asp et al. [2001]

Property (Units)	E_{11} (MPa)	$E_{22} = E_{33}$ (MPa)	$G_{12} = G_{13}$ (MPa)	$\nu_{12} = \nu_{13}$
Value	1.2×10^5	1.05×10^4	5.52×10^3	0.3

3.4.1 Influence of static CZM parameters on mode I fatigue crack growth

Pure mode I delamination is a simplified case that is ideal for observing the influence of static cohesive parameters associated with normal traction-separation behavior on fatigue crack growth rate. Herein, we investigate the influence of stiffness and strength parameters, and the shape of the $T-\delta$ law on mode I fatigue delamination crack growth rate predicted by the three fatigue damage functions presented in Section 3.3. As a part of this study,

we also verified that under static (monotonic) loading, delamination growth is relatively insensitive to these parameters so long as the critical fracture energy is assumed a constant. The double cantilever beam (DCB) setup with applied moment M is chosen for mode I experiments and the fatigue parameters C_i and m_i are calibrated to the least squares fit [Blanco et al., 2004] to experimental data given by Asp et al. [2001]. (The reader is referred to Appendix D.) Fatigue parameters C_i and m_i for $i = \{1, 2, 3\}$, reportedin Table E3, are calibrated for the three different damage functions using the static cohesive parameters for the bilinear law given in Table E2.

Table 3.2: Static cohesive parameters for the bilinear law (all values except K_{n}^0 and K_{t}^0 are assumed from Harper and Hallett [2010])

Parameter (Units)	K_{n}^0 $\left(\frac{\mathrm{N}}{\mathrm{mm}^3}\right)$	K_{t}^0 $\left(\frac{\mathrm{N}}{\mathrm{mm}^3}\right)$	G_{IC} $\left(\frac{\mathrm{N}}{\mathrm{mm}}\right)$	G_{IIC} $\left(\frac{\mathrm{N}}{\mathrm{mm}}\right)$	G_{C} $\left(\frac{\mathrm{N}}{\mathrm{mm}}\right)$	$\sigma_{\max}$ $\left(\frac{\mathrm{N}}{\mathrm{mm}^2}\right)$	$\tau_{\max}$ $\left(\frac{\mathrm{N}}{\mathrm{mm}^2}\right)$
	1×10^4	2×10^4	0.26	1.002	0.447	30	60

Table 3.3: Fatigue damage parameters

Parameter (Units)	Mode I	Mixed Mode
C_1 $(\mathrm{mm/cycle})$	1.62×10^{-3}	1.125×10^{-1}
m_1 $(--)$	4.2	5.5
C_2 $(1/\mathrm{cycle})$	6.0	7×10^4
m_2 $(--)$	3.6	6.5
C_3 $(1/\mathrm{cycle})$	6×10^{-1}	8.75×10^4
m_3 $(--)$	4.2	8.0

Remark 14 *In a DCB test with a constant moment applied to the cantilever arms, G_{I} is independent of crack length a and so the crack growth rate $\mathrm{d}a/\mathrm{d}N$ is a constant throughout the test. Therefore, the crack length increment $\hat{a} = a - a_0$ increases linearly with number of cycles N after crack propagation begins and $\mathrm{d}a/\mathrm{d}N$ can be easily measured by calculating the slope of the $\hat{a}$ versus N curve. In a DCB test with constant load applied to the cantilever arms, however, G_{I} is dependent on crack length a and so $\mathrm{d}a/\mathrm{d}N$ is not constant.*

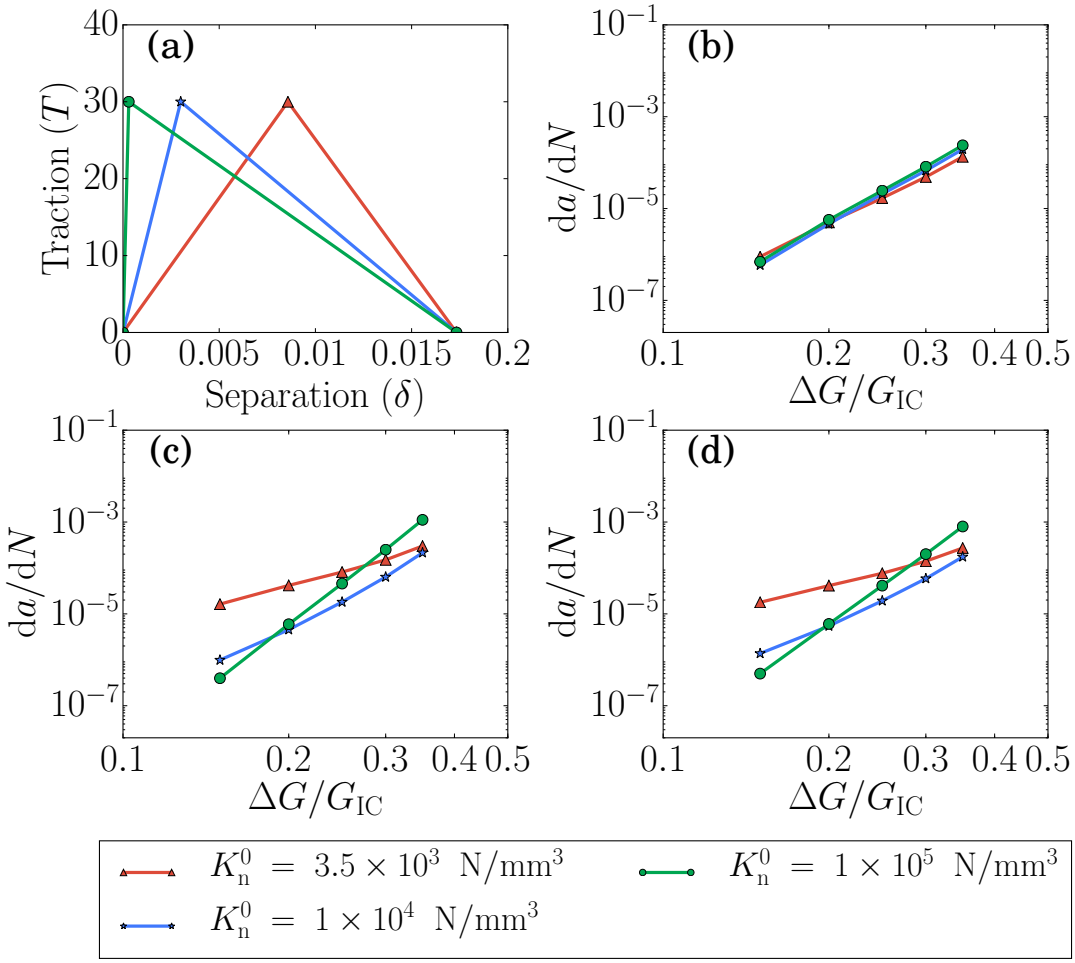

Figure 3.4: The sensitivity of fatigue crack growth rates to cohesive stiffness under pure mode I loading. (a) Bilinear $T-\delta$ law for $K_{\mathrm{n}}^0 = 3.5\times10^3, 1\times10^4, 1\times10^5$ N/mm^3. Mode I crack growth rates predicted by: (b) the SERR based function; (c) the separation based function; (d) the strain based function.

First, we investigate the influence of the normal cohesive stiffness on mode I fatigue crack growth rates by taking $K_{\mathrm{n}}^0 = \{3.5\times10^3, 10^4, 10^5\}$ N/mm^3, while holding the strength parameter $\sigma_{\max}$ and critical fracture energy G_{IC} constant for the bilinear cohesive law as shown in Figure 3.4a. Crack growth rates predicted by the three fatigue damage functions for each value of K_{n}^0 using the DCB test are shown in Figures 3.4b-d. These plots reveal that the crack growth rates predicted by the SERR based function are relatively insensitive to the value of K_{n}^0, whereas those predicted by the strain and separation based functions display a strong sensitivity to K_{n}^0. This must be because the damage evolution predicted by the SERR

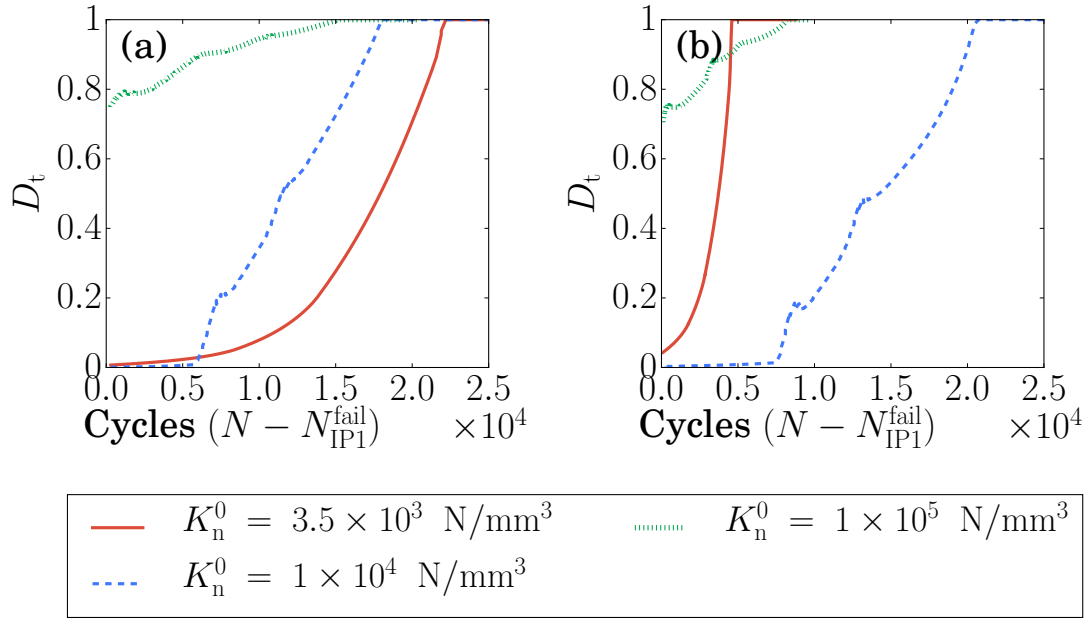

Figure 3.5: Total damage D_t at the fourth integration point versus cycles passed since failure of the first integration point $N - N_{IP\,1}^{fail}$, predicted by the (a) SERR based function and (b) separation based function for different values of cohesive stiffness K_n^0 under pure mode I loading. Note that the blue dashed lines correspond to the K_n^0 value used during model calibration.

based function is relatively insensitive to K_n^0. To confirm this we observe the evolution of total damage D_t at the fourth integration point (IP 4) along the crack interface against the number of loading cycles $N - N_{IP\,1}^{fail}$ since the failure of the first integration point (IP 1) for the 40% $\Delta G/G_{IC}$ load case. As evident from Figure 3.5, the SERR based function predicts failure (i.e., $D_t = 1$) at approximately the same number cycles for all values of K_n^0, unlike the separation based function. This study suggests that it is advantageous to formulate the fatigue damage rate as a function of the strain energy release rate (SERR) rather than interface separation.

Another interesting observation from Figure 3.4b is that the Paris plots obtained from the SERR based function are linear for the high and intermediate stiffness case ($K_n^0 = 10^5$ or 10^4 N/mm^3), whereas for the low stiffness case ($K_n^0 = 3.5 \times 10^3$ N/mm^3) the Paris plots seem to be slightly nonlinear. The nonlinearity of the low stiffness case is attributed to

a discrepancy in the computed SERR (Eq. 3.34) in elements behind the crack tip at low load ratios (e.g., 20% $\Delta G/G_{\mathrm{IC}}$). We find that using a low value of stiffness in the CZM formulation overpredicts the SERR in comparison to that predicted using intermediate and high values of stiffness at low load ratios; however, this discrepancy does not arise at higher load ratios (e.g., 60% $\Delta G/G_{\mathrm{IC}}$). Hence, the rate of fatigue crack crack growth is only overpredicted at low load ratios (e.g., 20% $\Delta G/G_{\mathrm{IC}}$) when using low stiffness. Results from the separation and strain based functions, shown in Figures 3.4c and 3.4d, also indicate that the Paris plots are only linear in the high stiffness case, which is attributed to the interaction between static and fatigue damage components in the low and moderate stiffness cases.

Remark 15 *Generally, a high value of K_{n}^0 is chosen for the cohesive interface in order to avoid inducing an artificial compliance in static delamination analysis. However, in the case of fatigue delamination analysis using a high value of initial stiffness for the static bilinear cohesive law is recommended to avoid discrepancies in crack growth rate predictions arising from the interaction between D_{f} and D_{s} components. Since the maximum allowable cohesive element length required for accurate numerical analysis is not a function of K_{n}^0 [Harper and Hallett, 2008], selecting a high value of K_{n}^0 does not increase the computational cost so long as numerical convergence is not issue.*

Next, we investigate the influence of the mode I cohesive strength on fatigue crack growth results by taking $\sigma_{\max} = \{15, 30, 45\}$ N/mm^2, while holding stiffness parameter K_{n}^0 and critical fracture energy G_{IC} constant for the bilinear cohesive law as shown in Figure 3.6a. Crack growth rates predicted by the three fatigue damage functions for each value of $\sigma_{\max}$ using the DCB test are shown in Figures 3.6b-d. These plots reveal that all three damage functions show sensitivity to the value of $\sigma_{\max}$, although the strain and separation based fatigue damage functions exhibit substantially higher sensitivity than the SERR based function. As expected the crack growth rate is smaller when the cohesive

strength is assumed to be large (i.e., $\sigma_{\max} = 45$ N/mm^2) because at any given load ratio, $\Delta G/G_{\mathrm{IC}}$, the static damage initiates much later owing to the bigger elastic regime. An interesting point is that the Paris plot obtained using the low value of $\sigma_{\max}$ is linear for all three damage functions; however, the Paris plot obtained using the high value of $\sigma_{\max}$ is nonlinear, which is attributed to the increase in the size of the elastic zone with an increase in $\sigma_{\max}$ in the bilinear law. Indeed, altering $\sigma_{\max}$ drastically changes the shape of the bilinear cohesive law as opposed to altering K_{n}^0 (see Figs. 3.4a and 3.6a), thus, greatly affecting damage initiation and damage evolution. This study suggests that it may not be appropriate to treat the cohesive strength $\sigma_{\max}$ as an adjustable parameter (see Remark 11) and it is important to reliably calibrate it from integrated experimental and numerical approach, perhaps using the technique described in [Ferracin et al., 2003].

Remark 16 *The fatigue crack growth rates predicted by the SERR based function are far less sensitive to the cohesive stiffness parameter than the strength parameter because the SERR calculated using the trapezoidal rule (Eq. 3.34) is far less sensitive to* K_{n}^0 *than to* $\sigma_{\max}$. *This can be confirmed from Figure 3.7, wherein the evolution of the normalized SERR at the fourth integration point (IP 4) is plotted for different values of* K_{n}^0 *and* $\sigma_{\max}$ *for the 40%* $\Delta G/G_{\mathrm{IC}}$ *load.*

Finally, we study the influence of the shape of the $T-\delta$ law on mode I fatigue crack growth rates by considering bilinear, exponential and polynomial laws, while holding the critical fracture energy G_{IC} and cohesive strength $\sigma_{\max}$ constant as shown in Figure 3.8a. Since cohesive stiffness is not a free parameter in the polynomial and exponential laws, it is not possible to simultaneously hold K_{n}^0 constant in this study; instead, K_{n}^0 is computed from equations (3.23) and (3.27) as 1.31×10^4 and 9.41×10^3 N/mm^3 for the polynomial and exponential laws, respectively. For the bilinear law, we choose $K_{\mathrm{n}}^0 = 10^4$ N/mm^3 so that the normal stiffness has the same order of magnitude for all three static CZMs. Crack growth

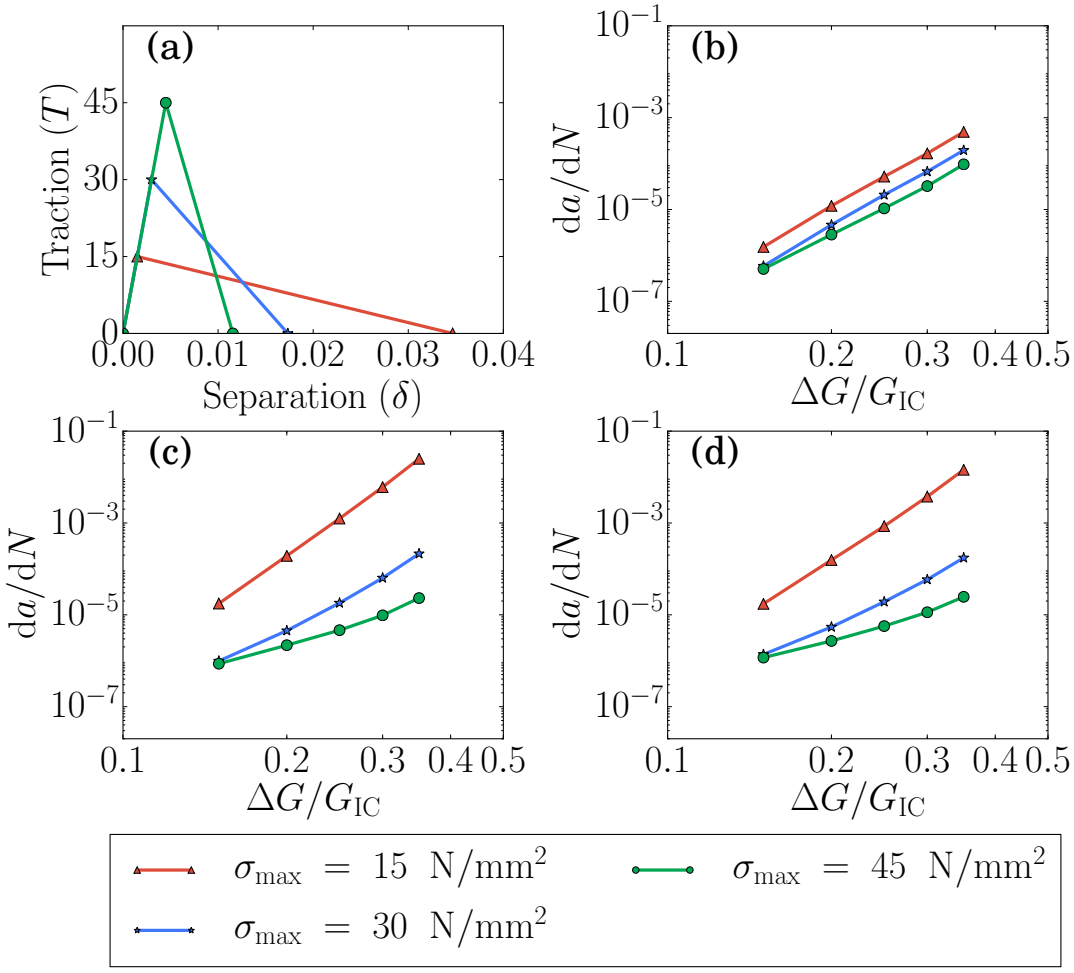

Figure 3.6: The sensitivity of fatigue crack growth rates to cohesive strength under pure mode I loading. (a) Bilinear $T-\delta$ law for $\sigma_{\max} = 15, 30, 45$ N/mm^2. Mode I crack growth rates predicted by: (b) the SERR based function; (c) the separation based function; (d) the strain based function.

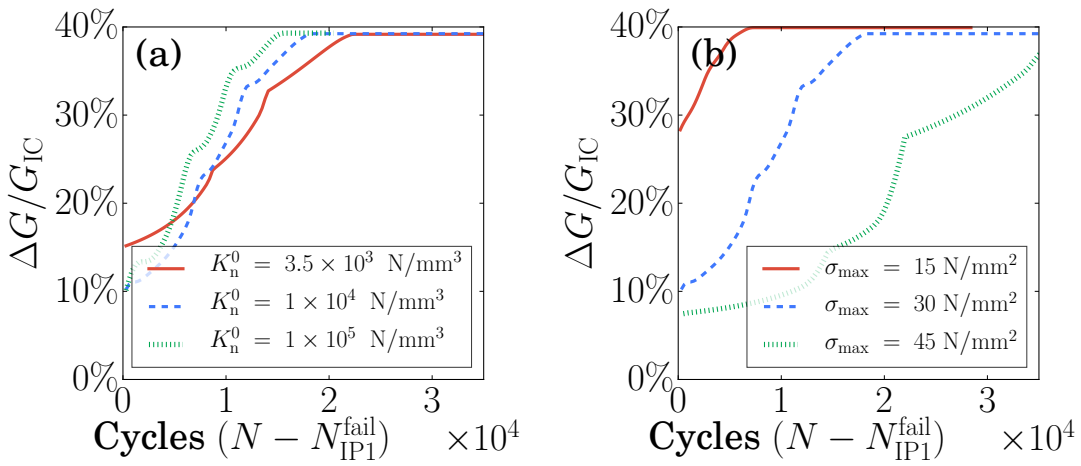

Figure 3.7: Sensitivity of SERR computation using equation (3.34) at the fourth integration point (IP 4) for different values of (a) cohesive stiffness K_{n}^0 and (b) cohesive strength $\sigma_{\max}$ under pure mode I loading, while all other static parameters are held constant at the values given in Table E2.

rates predicted by the three fatigue damage functions for each cohesive law using the DCB test are shown in Figures 3.8b-d. All three fatigue damage rate functions show minimal sensitivity to the cohesive shape, with the separation and strain based models showing a slight dependence. As evident from 3.8b-d, the polynomial law with C^1 continuity yields linear Paris plots, whereas the bilinear and exponential with only C^0 continuity yield identical but slightly nonlinear Paris plots. This nonlinearly arises from the fact that in both bilinear and exponential laws, there occurs an abrupt transition from an initial elastic state ($D_{\mathrm{s}} = 0$) to a damage-softening state (wherein D_{s} accumulates rapidly). In contrast, the polynomial law has no elastic regime and thus no abrupt transition from an undamaged to damaged state which can lead to nonlinearity of Paris plots. This study suggests that it is appropriate to employ static cohesive laws with at least C^1 smoothness, satisfying the LEFM principle in equation (3.7), for modeling fatigue delamination growth.

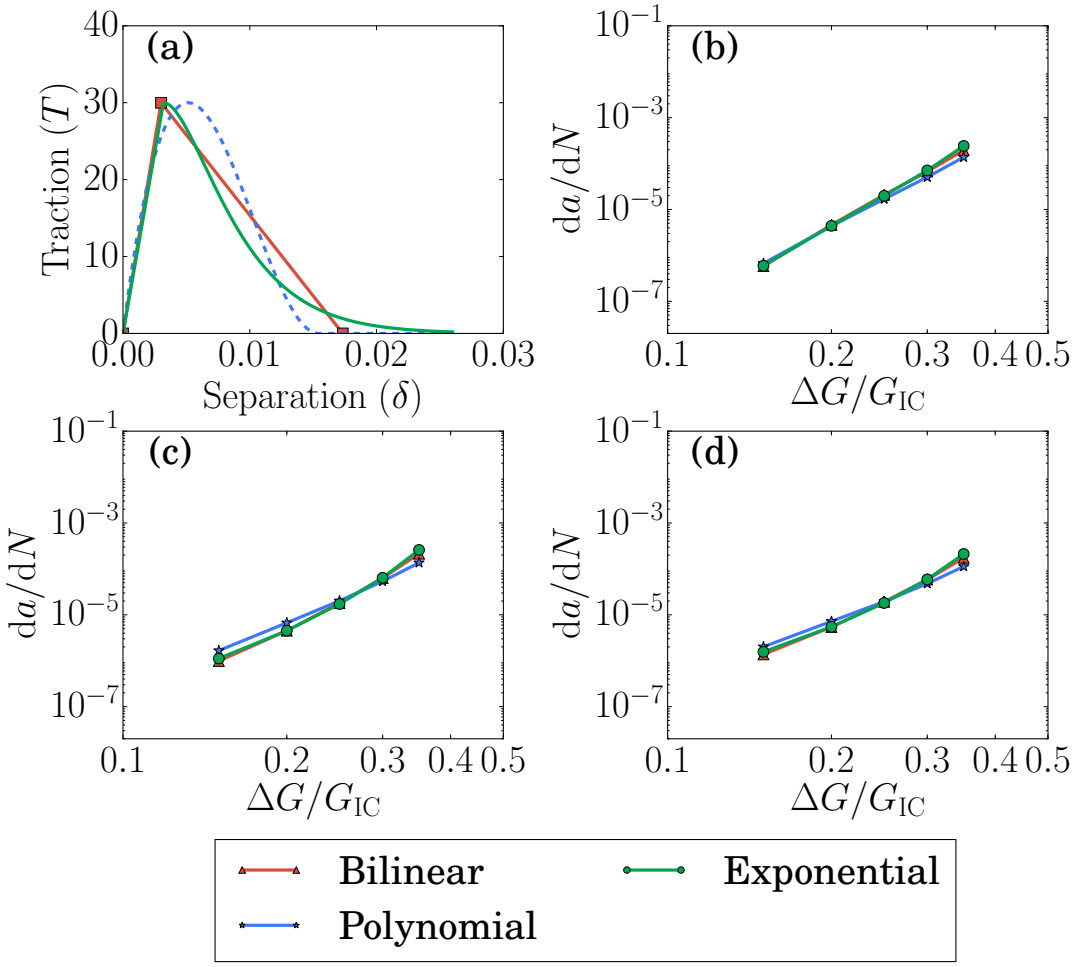

Figure 3.8: The sensitivity of fatigue crack growth rates to the shape of the $T-\delta$ law under pure mode I loading. (a) Shape of bilinear, polynomial, and exponential traction-separation laws. Mode I crack growth rates predicted by: (b) the SERR based function; (c) the separation based function; (d) the strain based function.

3.4.2 Influence of static CZM parameters on 50% mixed-mode fatigue crack growth

Mixed-mode delamination is a more realistic failure mode in composite structures and is necessary for studying the combined effects of mode I and mode II static parameters on fatigue crack growth rate. Herein, we investigate the influence of normal and tangential stiffness and strength parameters and cohesive shape on fatigue delamination crack growth rates at 50% mixed mode case (i.e., $\psi = 0.5$). The setup of the mixed mode bending (MMB) test with applied moments chosen for this study is described in Appendix E, along with the calibration of the fatigue parameters C_i and m_i for $i = \{1, 2, 3\}$ reported in Table E3 for the three different damage functions.

First, we investigate the influence of the normal and tangent cohesive stiffnesses, K_{n}^0 and K_{t}^0, on fatigue crack growth rates, while holding the static parameters $\sigma_{\max}$, $\tau_{\max}$, G_{IC}, and G_{IIC} constant. The cohesive stiffness K_{n}^0 is varied from 10^4 to 10^5 $\mathrm{N/mm^3}$ and K_{t}^0 from 2×10^4 to 2×10^5 $\mathrm{N/mm^3}$, so that there are four total combinations of K_{n}^0 and K_{t}^0. The results obtained from this study are shown in Figure 3.9. For different combinations of K_{n}^0 and K_{t}^0, the Paris plots obtained from the SERR based function match very well with one another, whereas those obtained from the separation and strain based functions show much discrepancy. From Figures 3.9b and 3.9c it is apparent that the Paris plots are linear in all cases except when both K_{n}^0 and K_{t}^0 are chosen to be small. This suggests that the requirements on the value of K_{n}^0 may be relaxed provided K_{t}^0 is chosen sufficiently high. Another interesting observation is that for the high values of $K_{\mathrm{t}}^0 = 2 \times 10^5$ $\mathrm{N/mm^3}$, the fatigue crack growth rate predictions are much more sensitive to the value of K_{n}^0 for the separation and strain based functions. Thus, this study emphasizes the significance of formulating the fatigue damage rate as a function of the strain energy release rate (SERR).

Next, we investigate the influence of normal and tangential cohesive strengths $\sigma_{\max}$ and $\tau_{\max}$ on mixed mode fatigue crack growth rates, while holding static parameters G_{IC}, G_{IIC}, K_{n}^0, and K_{t}^0 constant. The cohesive strength $\sigma_{\max}$ is varied from 30 to 45 $\mathrm{N/mm^2}$ and $\tau_{\max}$ from 30, 45, to 60 $\mathrm{N/mm^2}$. As expected, the SERR based function is less sensitive to the

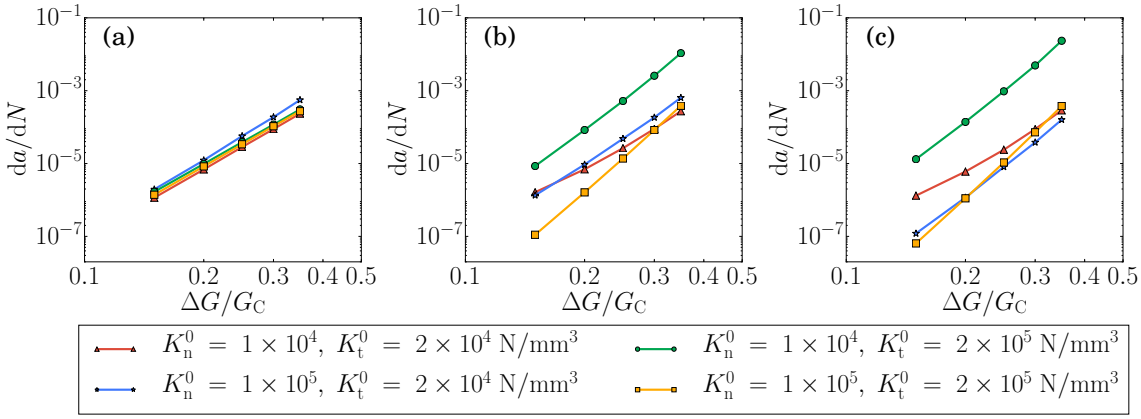

Figure 3.9: The sensitivity of fatigue crack growth rates to normal and tangent cohesive stiffnesses, K_n^0 and K_t^0 respectively, under 50% mixed mode loading. Mixed mode crack growth rates predicted by: (a) the SERR based function; (b) the separation based function; (c) the strain based function.

variations in both σ_{max} and τ_{max} than the strain and separation based fatigue damage functions. The same trend observed in mode I simulations is also observed in 50% mixed mode simulations in that for small values of σ_{max} and τ_{max} the model predicts faster crack growth, whereas for large values of σ_{max} and τ_{max} the model predicts slower crack growth. This is because assuming small values for cohesive strengths increases the numerical cohesive zone length, and the load redistribution among the interface elements in the large numerical cohesive zone post damage initiation is responsible for the reduction in crack growth rate. Thus, this study emphasizes the need for a more robust methodology for calibrating cohesive strength parameters.

Finally, we study the influence of the shape of the traction-separation ($T-\delta$) law on mixed mode fatigue crack growth rates. We consider the bilinear, exponential and polynomial cohesive laws and select the static cohesive parameters G_{IC}, G_{IIC}, σ_{max}, and τ_{max} given in Table E2. Since K_n^0 and K_t^0 are not independent parameters for the polynomial and exponential $T-\delta$ laws, we calculate $K_n^0 = 1.31 \times 10^4$ and $K_t^0 = 1.36 \times 10^4$ for the polynomial law and $K_n^0 = 9.41 \times 10^3$ N/mm^3 and $K_t^0 = 9.77 \times 10^3$ N/mm^3 for the exponential law. We select $K_n^0 = 10^4$ and $K_t^0 = 10^4$ N/mm^3 so that the stiffness of the bilinear cohesive

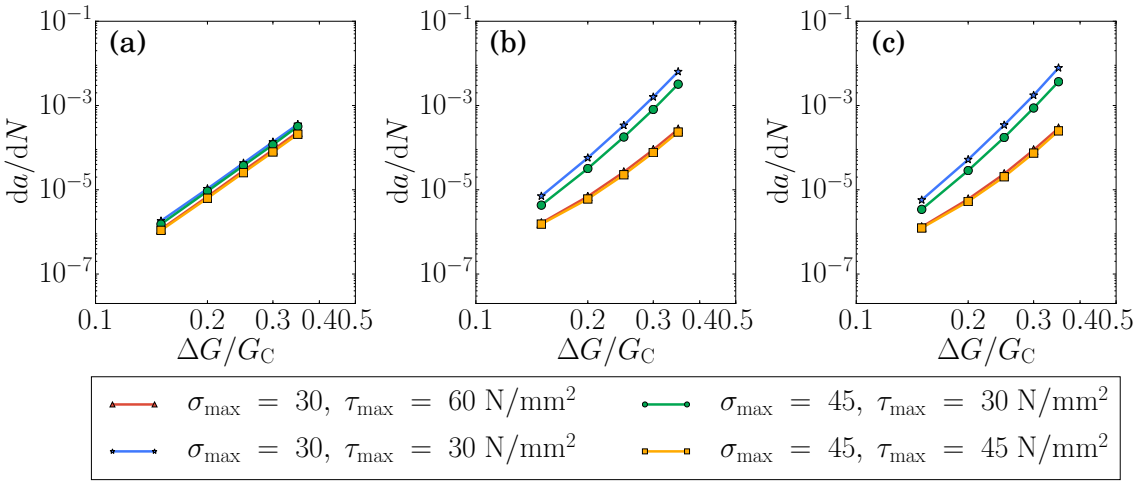

Figure 3.10: The sensitivity of fatigue crack growth rates to normal and tangent cohesive strengths, σ_{max} and τ_{max} respectively, under 50% mixed mode loading. Mixed mode crack growth rates predicted by: (a) the SERR based function; (b) the separation based function; (c) the strain based function.

law is of the same order magnitude as that of the other two cohesive laws. Crack growth rates are measured for each $T-\delta$ law using the MMB test, and results are shown in Figure 3.11. The numerical results from the three fatigue damage rate functions show almost no sensitivity to the cohesive shape; however, the polynomial law with C^1 shape continuity yields linear Paris plots, whereas some nonlinearity is observed with bilinear and exponential laws. This study illustrates that using static cohesive laws with higher-order smoothness is more consistent in the Paris (stable crack growth) regime.

3.4.3 Non-additive damage decomposition

In all the sensitivity studies presented in the previous two sections, damage was additively decomposed into static and fatigue components, but both components are assumed to affect the cohesive stiffness of the interface element. In this section, we compare this additive damage decomposition scheme with a non-additive scheme proposed by Khoramishad et al. [2010], wherein the cohesive stiffness parameters K_n^0 and K_t^0 are affected by static damage, D_s, and the cohesive strength parameters σ_{max} and τ_{max} are affected only by fa-

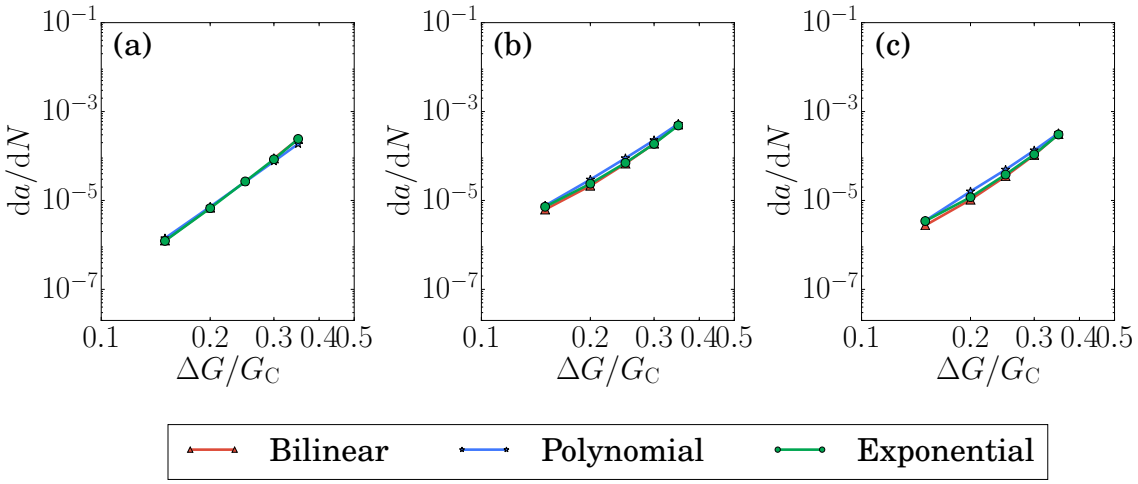

Figure 3.11: The sensitivity of fatigue crack growth rates to the shape of the $T-\delta$ law under 50% mixed mode loading. Mixed mode crack growth rates predicted by: (a) the SERR based function; (b) the separation based function; (c) the strain based function.

tigue damage, D_{f}. The numerical implementation of the non-additive scheme involves reducing the critical separations based on fatigue damage and cohesive stiffnesses based on static damage as,

$$\hat{\delta}^{\mathrm{c}} = (1-D_{\mathrm{f}})\delta^{\mathrm{c}} \tag{3.41}$$

$$K = (1-D_{\mathrm{s}})K^{0} \tag{3.42}$$

After fatigue damage initiates, the reduced critical separation $\hat{\delta}^{\mathrm{c}}$ replaces the critical separation δ^{c} in all the static damage calculations. The differences in the evolution of the static cohesive law governed by the additive and non-additive formulations is illustrated in Figure 3.12. The dashed black line depicts the static bilinear $T-\delta$ law when $D_{\mathrm{s}} = D_{\mathrm{f}} = 0$ during the first loading cycle. The solid black and grey lines show the response at subsequent loading cycles when one or both of the damage components D_{s} and D_{f} are non-zero. The traction-separation response obtained from the additive scheme when $D_{\mathrm{s}} = 0$ and $D_{\mathrm{f}} > 0$

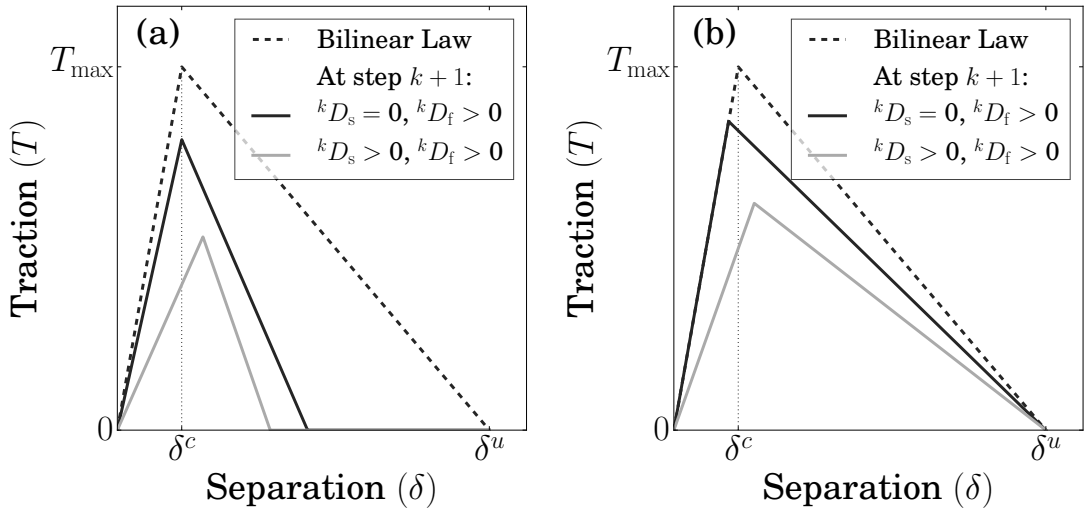

Figure 3.12: Influence of (a) additive and (b) non-additive damage implementation on the CZM shape.

(solid black line in Fig. 3.12a) is different from the response obtained from the non-additive scheme (solid black line in Fig. 3.12b). The differences in the cohesive response are very stark considering that the ultimate separation remains constant in the non-additive scheme, whereas it evolves with loading cycles in the additive scheme. An important difference is that the cohesive element's failure occurs when $D_s + D_f = 1$ in the additive scheme, whereas failure occurs when either $D_s = 1$ or $D_f = 1$ in the non-additive scheme. Thus, the two decomposition schemes represent widely different traction-separation behaviors once damage initiates.

We now investigate the sensitivity of the fatigue CZM formulation to normal cohesive stiffness K_n^0 under pure mode I loading using the non-additive decomposition scheme. The Paris plots obtained from the non-additive damage scheme (dashed lines) are shown in Figures 3.13a-c and compared with those obtained from the additive damage scheme (solid lines). Evidently, the non-additive scheme predicts slower crack growth compared to the additive scheme for a given K_n^0 using any fatigue damage function; this occurs because more loading cycles are required to reach the non-additive failure criterion (i.e., $D_s = 1$

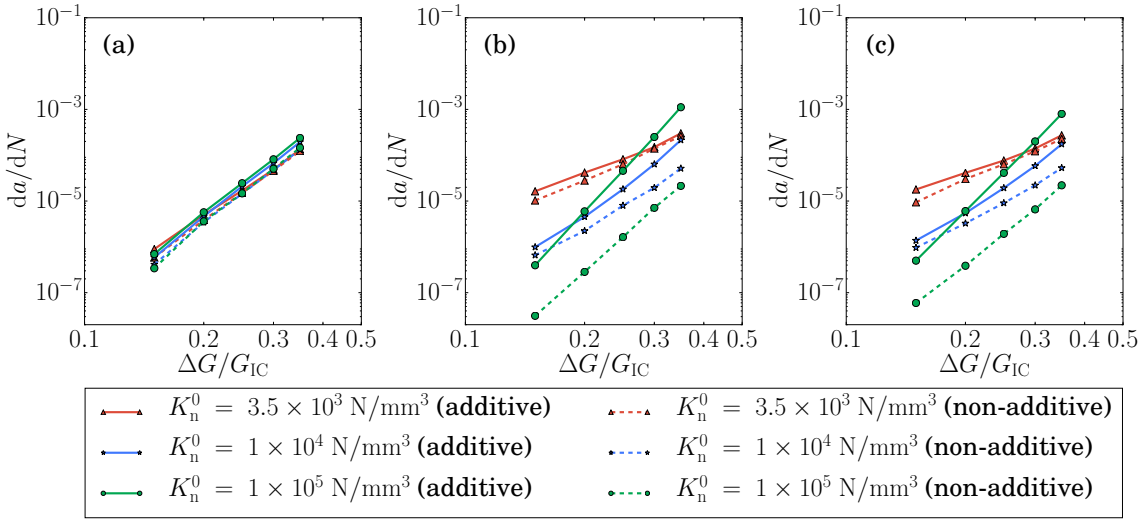

Figure 3.13: Paris plot of mode I fatigue crack growth given by the additive damage scheme and the non-additive damage schemes predicted by: (a) the SERR based function; (b) the separation based function; and (c) strain based function. Solid lines denote the additive damage scheme, and dashed lines denote the non-additive scheme.

or $D_{\mathrm{f}} = 1$) than the additive failure criterion (i.e., $D_{\mathrm{s}} + D_{\mathrm{f}} = 1$). Note that in both additive and non-additive damage schemes, D_{f} and D_{s} do not have to evolve simultaneously; or in other words, fatigue damage can evolve in the absence of static damage. An important observation is that the SERR based function works reasonably well with both damage decomposition schemes, whereas the separation and strain based functions show larger sensitivity to K_{n}^0 when using the non-additive scheme. Sensitivity studies with respect to the cohesive strength parameter $\sigma_{\max}$ revealed a similar trend in that separation and strain based functions show slower crack growth rates when using the non-additive scheme (results not shown here). This study suggests that the additive scheme may be more consistent when using separation based fatigue damage functions owing to the reduced sensitivity to K_{n}^0, however, both models work reasonably well when using the SERR based fatigue damage rate function. We also believe it is appropriate to additively combine D_{s} and D_{f} since both static and fatigue damage involves the nucleation and growth of microcracks and microvoids within the laminate interface, as observed from fractographic analysis [Asp et al., 2001].

Remark 17 *In the non-additive scheme one needs to uncouple static and fatigue damage. By removing the* $(1-D_{\mathrm{s}})$ *factor from equation (3.33), we obtain an uncoupled form of the SERR based function which defines failure when* $D_{\mathrm{f}}=1$*,*

$$\Delta D_{\mathrm{f}}=\Delta N\left(\frac{1}{h}\right)C_1\left(\frac{\Delta G}{G_{\mathrm{C}}}\right)^{m_1}. \tag{3.43}$$

The uncoupled form of the separation based function reads,

$$\Delta D_{\mathrm{f}}=\Delta N\left(\frac{C_2}{m_2+1}\right)\exp\left(\lambda D_{\mathrm{f},\mu}\right)\left(\frac{\delta_\mu}{\delta_{\mathrm{f}}}\right)^{m_2+1} \tag{3.44}$$

wherein only existing fatigue damage magnifies its growth rate.

3.4.4 Constrained damage update

In this section, we investigate the sensitivity of the fatigue CZM formulation using the SERR based function to static parameters in relation to numerical damage update strategies for mode I fatigue delamination. Kawashita and Hallett [2012] proposed a crack tip tracking algorithm in 3-D, wherein fatigue damage D_{f} is constrained to occur only in the cohesive element closest to the crack tip. Additionally, a numerical fix was proposed to correct for errors in the point-wise computation of SERR by extracting the maximum value of ΔG from previously failed elements around the crack tip to substitute into equation (3.33). Since D_{f} is restricted to only one element at the crack tip, the strategy results in element-by-element failure during delamination propagation. Herein, we implement this constrained damage update algorithm by restricting D_{f} to occur only in the integration point closest to the crack tip; in other words, D_{f} is allowed to accumulate at the next integration point only after complete failure ($D_{\mathrm{t}}=1$) occurs at the prior integration point. We also

store the location of the crack tip and the maximum value of ΔG throughout loading history as global (COMMON) variables in the Abaqus UEL subroutine for fatigue damage rate calculation. For this current study, we set the mode I fatigue parameters equal to the corresponding Paris law parameters for carbon fibre-epoxy composite HTA/6367C, that is, $C_1 = C = 2.21 \times 10^{-3}$ and $m_1 = m = 5.09$ [Blanco et al., 2004]. In analogy, the previous numerical strategy wherein D_{f} is allowed to accumulate at all integration points is referred to as the unconstrained damage update.

Remark 18 *An advantage of the crack tip tracking algorithm proposed by Kawashita and Hallett [2012] is that it allows us to directly use the experimental Paris law parameters C and m as the SERR based fatigue damage rate function parameters C_1 and m_1; thus, calibration of the CZM is not necessary anymore. Since fatigue damage is constrained to one crack tip element, the algorithm seems more consistent with the LEFM based Paris law.*

We simulate the mode I DCB test with the constrained algorithm for different values of $\Delta G/G_{\mathrm{IC}}$ in order to investigate the sensitivity of the SERR based fatigue damage function to static parameters. First, we vary the normal cohesive stiffness by taking $K_{\mathrm{n}}^0 = \{3.5 \times 10^3,$ 10^4, and $10^5\}$ N/mm^3 while holding cohesive strength $\sigma_{\max}$ and critical fracture energy G_{IC} constant at the values given in Table E2. Next, we take $\sigma_{\max} = \{15, 30, 45\}$ N/mm^2 while holding K_{n}^0 and G_{IC} constant at the values given in Table E2. The predicted fatigue crack growth rates are shown in Figures 3.14a-b as Paris plots. It is evident that the constrained algorithm makes the SERR based fatigue damage function much less sensitive to static cohesive parameters, particularly the cohesive strength $\sigma_{\max}$. As remarked earlier, changing the cohesive strength parameter alters the numerical cohesive zone length in the finite element simulation, which affects the crack growth rate predictions. By restricting fatigue damage growth to only one integration point at a time, the constrained damage up-

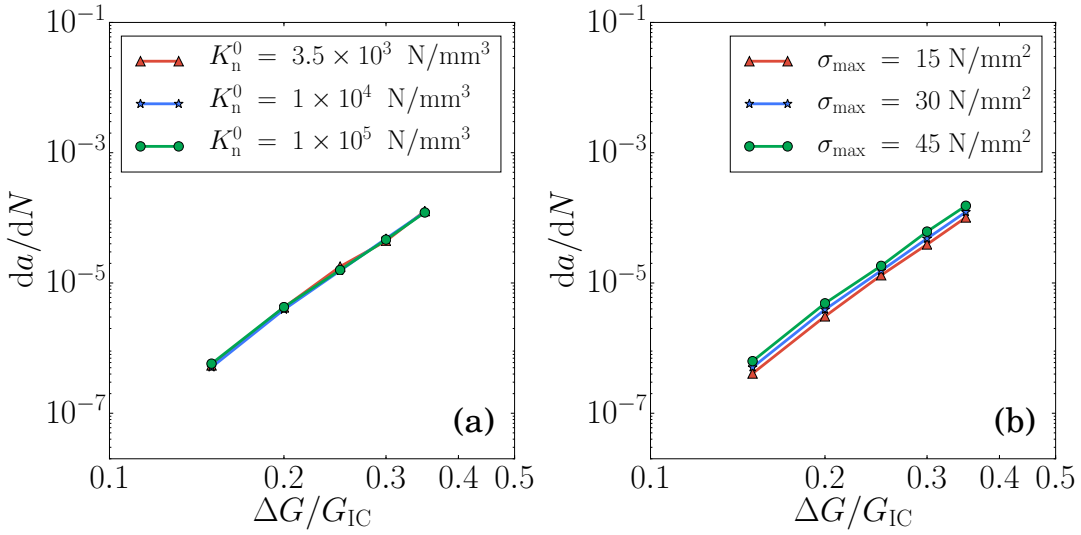

Figure 3.14: Sensitivity of the SERR based fatigue damage function with constrained damage update algorithm to (a) normal cohesive stiffness K_n^0 and (b) normal cohesive strength σ_{max} under pure mode I loading.

date algorithm removes the effects the numerical cohesive zone length on crack growth rate predictions. While the constrained algorithm is consistent with LEFM analysis (i.e., Paris law) and alleviates spurious parametric sensitivity, it is difficult to justify restricting fatigue damage to only the crack tip element rather than all the elements in the cohesive zone from a mechanistic standpoint, except for large element sizes when the entire damage zone is contained in the crack tip element.

3.5 Conclusions

We investigated the issue of parametric sensitivity of CZMs for high-cycle fatigue delamination with respect to static cohesive parameter and fatigue damage functions based on strain energy release rate (SERR), separation and strain. Lets us summarize the key points from the sensitivity studies for mode I and mixed mode delamination. The separation and strain based fatigue damage functions are highly sensitive to cohesive stiffness and strength parameters but are relatively less sensitive to cohesive shape. The SERR based fatigue damage function is almost insensitive to cohesive stiffness and shape but is slightly sensitive to cohesive strength. Considering that the initial stiffness is usually treated as an adjustable penalty parameter, it seems more appropriate to formulate fatigue damage rate as a function of the SERR. Unlike bilinear and exponential static cohesive laws, the polynomial cohesive law has a higher-order smoothness (C^1 continuity) and yields linear Paris plots in combination with all three fatigue damage functions; this is attributed to the lack of sudden transition between a linear-elastic and damage-softening regime in the polynomial law. Considering the high sensitivity of fatigue crack growth rate predictions to the cohesive strength and that it is factor in determining the cohesive zone size, more robust methodologies are necessary to establish the interface cohesive strength for a given composite material.

Given that the CZM remains an efficient methodology for modeling cyclic crack growth, it is important to devise numerical strategies that alleviate spurious sensitivity to static cohesive parameters; therefore, we investigated the differences between the additive and non-additive decomposition schemes and the constrained and unconstrained damage update strategies. Our investigations revealed that the traction-separation behavior described by the additive and non-additive schemes are widely different once damage initiates and that using the additive schemes leads to slightly reduced sensitivity. The constrained damage update algorithm reduces the sensitivity of the SERR based function to static cohesive parameters by controlling the accumulation of fatigue damage along the interface, which

may be appropriate when the interface element size is larger than the cohesive zone length. The current form of the SERR based function, derived from the Paris law, is only suitable for positive stress ratios ($R \geq 0$) and constant amplitude loading in the stable crack growth regime. Future research work should entail describing all three regimes of fatigue crack growth, that is, slow, stable and unstable regimes [Shivakumar et al., 2006] and moisture-enhanced delamination [Katnam et al., 2011].

Acknowledgement

This work was supported by the Vanderbilt University Discovery Grant Program.

CHAPTER 4

AN UPDATED-LAGRANGIAN DAMAGE MECHANICS FORMULATION FOR MODELING THE CREEPING FLOW AND FRACTURE OF ICE SHEETS

4.1 Introduction

Fracture initiation and propagation affect the stability of ice sheets by accelerating their flow, promoting iceberg calving, and triggering catastrophic collapse of glaciers and ice shelves [Vieli and Nick, 2011, Schulson and Duval, 2009]. Modeling and simulation of creep fracture (damage) mechanisms and its relation to the flow behavior (rheology) of ice sheets/shelves can be useful in providing reliable estimates for mass loss from ice sheets, a key component of sea level. Current numerical ice sheet/shelf models used to study their stability employ empirical calving laws and do not account for the physics of fracture, severely limiting their predictive capability and reliability. The purpose and scope of this chapter is to present an updated-Lagrangian damage mechanics formulation to enable physically accurate modeling of fracture evolution in glaciers and land ice sheets that are slowly but continuously deforming under the force of gravity. In the proposed formulation, we employ high-order mixed finite element discretizations for the solution of nonlinear incompressible Stokes flow equations and nonlocal damage approaches that ensure stability and mesh-insensitivity of numerical simulations.

Over the long time scales of glacier and ice sheet evolution (decades to centuries or longer) it is well established that the rheology of ice is well represented by a non-Newtonian shear thinning (nonlinearly viscous) fluid, using the power law creep equation known as the Glen's law [Glen, 1955, Nye, 1957, Cuffey and Paterson, 2010, van der Veen, 2013] in glaciology. By incorporating this viscous rheology, several studies have established that the three-dimensional (3D) nonlinear incompressible Stokes equations (hereafter referred

to as the Stokes equations for brevity) provide the most accurate description of momentum balance for modeling the flow of glaciers, compared to other approaches (see [Leng et al., 2012, 2013] for more references and verification studies). The advantage of using the Stokes equations is that we can accurately model glacier flow by accounting for the topography (or geometry) and complex basal boundary conditions at the ice-bedrock interface [Tezaur et al., 2015b]. Moreover, recent advances in higher-order finite element discretization and scalable solvers for the solution of Stokes equations [Worthen et al., 2014, Isaac et al., 2015] enable us to utilize the coverage and spatial resolution of ice sheet geometry data available from high-resolution satellite imagery and simulate the dynamics of large glaciers or even the entire Antarctic land ice sheet. However, to use the Stokes formulation to predict glacier and ice sheet evolution we need to account for iceberg calving, and this requires that we also simulate the damage induced crevasse formation and propagation, occurring on much shorter time scales (days to months). Furthermore, due to the vast separation of time scales associated with flow and fracture processes, the time between fracture inception and iceberg calving events associated with complete failure can exceed decades and sometimes centuries. This is particularly challenging because it requires us to couple the solid mechanics of creep fracture with the fluid mechanics of viscous flow in a consistent yet computationally feasible manner. To address this, we propose a new updated-Lagrangian formulation that can consistently describe short and long time scale behavior.

To account for the physical mechanisms of creep fracture behind crevasse propagation and iceberg calving, researchers have often relied upon theoretical models based on linear elastic fracture mechanics (LEFM) (see e.g., [Weertman, 1980b, Van der Veen, 1998a,b, Benn et al., 2007a]) or Nye-zero stress models (see e.g., [Nick et al., 2010b, Bassis, 2011, Bassis and Walker, 2012]). These models (viz., LEFM and Nye-zero stress) assume that ice behaves like a brittle elastic solid and represent fractures as sharp interfaces initiating and propagating from preexisting defects (either starter cracks or notches); however, this

is inconsistent with the creeping flow and fracture behavior of ice evident from laboratory experiments, field investigations, and satellite observations. As an alternative to the LEFM approach, Pralong et al. [Pralong and Funk, 2005] have proposed an Eulerian damage mechanics approach based on nonlinear Stokes flow and continuum creep damage mechanics. While this approach describes the physics of flow (deformation) and fracture of ice bodies, it suffers from numerical accuracy issues of pathological mesh dependence and directional mesh bias associated with local damage models and artificial dissipation of damage associated with advection in an Eulerian description. To overcome such numerical issues, Duddu et al., [Duddu and Waisman, 2012, 2013c, Duddu et al., 2013, Mobasher et al., 2016] modeled ice as a Maxwell-type viscoelastic solid (see Appendix F) in conjunction with a continuum damage mechanics approach using a Lagrangian finite element method. The Maxwell viscoelastic model is well calibrated and validated against laboratory experiments on polycrystalline ice in [Duddu and Waisman, 2012], and the nonlocal integral damage approach within a total Lagrangian formulation is shown to alleviate mesh sensitivity issues in [Duddu and Waisman, 2013c]; however, this pure displacement (one-field) formulation could suffer from numerical instabilities (e.g., oscillations in stress/pressure fields) when describing large incompressible viscous deformation combined with small elastic deformation. This issue may be resolved by introducing stabilization in the form of "hourglass" control and reduced integration techniques (see, e.g., [Flanagan and Belytschko, 1981, Belytschko et al., 1984]) or by using the $\bar{\mathrm{B}}$-type projection technique (see, e.g., [Elguedj et al., 2008]). Instead, we pursue a velocity-pressure (two-field) formulation, assuming Stokes flow, in conjunction with nonlocal damage mechanics for simulating creep fracture of ice within a mixed Galerkin finite element framework.

It is well known that using equal-order interpolation of velocity and pressure fields in the mixed Galerkin finite element formulation of incompressible Stokes, Navier-Stokes, and Darcy flow problems is not stable and causes numerical "checkerboard" instability in the pressure field (see e.g., [Masud and Hughes, 2002, Nakshatrala et al., 2006, Turner

et al., 2009, 2010]). This numerical instability occurs because same-order interpolations for unknown variables do not satisfy the inf-sup condition, most popularly known as the Ladyzhenskaya–Babuška–Brezzi (LBB) stability condition [Brezzi and Fortin, 1991, Szabo and Babuška, 1991, Brink and Stein, 1996]. To ensure numerical stability and optimal convergence, several methodologies have been proposed in the literature for enabling stable equal-order interpolation of velocity and pressure fields. An in-depth review of the various stabilized or enriched finite element methods can be found in [Elguedj et al., 2008, Turner et al., 2009]; herein, we wish to acknowledge a few important articles related to these methods: Streamline Upwind Petrov-Galerkin (SUPG, see, e.g., [Brooks and Hughes, 1982, Hughes et al., 1986]), Galerkin Least Squares (GLS, see e.g., [Hughes et al., 1989]), variational multi-scale method (VMS, see e.g., [Franca et al., 1992, Hughes, 1995, Hughes and Sangalli, 2007, Bazilevs, 2007, Turner et al., 2009]), bubble enriched finite element methods (see, e.g., [Arnold et al., 1984, Baiocchi et al., 1993]). An alternative, more straightforward strategy is to use use different order interpolation for velocity and pressure variables, which is pursued in this chapter in conjunction with triangular elements by using cubic and linear polynomials for interpolating velocity and pressure fields, respectively. Recently, we also employed different order interpolation for velocity and Jacobian determinant variables in conjunction with quadrilateral elements [Duddu et al., 2012, Foucard et al., 2015] to simulate large deformations in hyperelastic solids within an Eulerian framework.

An important aspect in ice sheet modeling is that we need to track the changes in the physical geometry (i.e., shape and the size) of the ice sheet domain due to large deformations accruing over decadal time scales. Typically, over such long times scales an Eulerian framework (see e.g., [Pralong and Funk, 2005, Borstand et al., 2012, Albrecht and Levermann, 2014] is employed, wherein domain boundaries are typically fixed and the material is advected out. While the advantage of the Eulerian formulation over the Lagrangian formulation is that it enables the efficient simulation of ice sheet flow without requiring remeshing, it cannot track changes in geometry of the domain and material discontinuities

such as fracture and damage zones; therefore, it is not ideal for simulating the fracture of ice sheets. In this context, the primary goal of this work is twofold: first, to present a novel mixed finite element implementation of the updated-Lagrangian formulation of the incompressible Stokes flow [Onate and Carbonell, 2014] in conjunction with a mesh-update procedure, which can be ideal for modeling flow and fracture in ice sheets on long times scales; second, to demonstrate that the nonlinearly viscous Stokes flow constitutive model reproduces the results of the previously established Maxwell-viscoelastic constitutive model with to respect crevasse depths and glacial displacement over short time scales (days to months); third, to conduct numerical verification and mesh convergence studies along with a comparison of gradient and integral nonlocal models for time dependent creep damage. The secondary goal of this work is to present computational algorithms and strategies for simulating crevasse propagation. To the best of our knowledge, there exist no other formulations in the literature that incorporate nonlocal creep damage into nonlinear Stokes rheology to simulate fracture initiation and propagation. The rest of this chapter is organized as follows: in Section 4.2 we present the governing equations of the Stokes flow rheological model for damaged ice; in Section 4.3 we discuss the solution strategy and finite element implementation of the new formulation in the open-source software FEniCS along with detailed algorithms; in Section 4.4 we provide numerical examples to verify and compare the new formulation with a manufactured Stokes solution and the previously established Maxwell viscoelastic model, including constant velocity and gravity-driven creep flow tests; and finally, in Section 4.5 we offer some concluding remarks.

4.2 Model formulation

In this section, we present the details of the rheological model for damaged ice used to describe the deformation flow and creep fracture of ice-sheets and ice-shelves. We first explain our notation for variables, the domain configurations and kinematics of the continuum. We next review the key concepts of the nonlocal continuum damage model for temperature-dependent creep fracture previously presented in [Duddu and Waisman, 2012, 2013c] and propose a modification to consider isotropic damage evolution only under a tensile state of stress. Finally, we present the strong and weak forms of the governing equations of the Stokes flow model, assuming that ice behaves as a non-Newtonian (or nonlinearly viscous) fluid, including the effects of creep damage on its viscosity.

4.2.1 Notation

All model equations are presented in indicial notation; for example, vectors are denoted as $\boldsymbol{a} = a_i \hat{\boldsymbol{e}}_i$ with components a_i and orthogonal basis vectors $\hat{\boldsymbol{e}}_i$ of the Cartesian coordinate system. Similarly, second-order tensors are denoted by the dyadic notation as $\boldsymbol{A} = A_{ij} \hat{\boldsymbol{e}}_i \otimes \hat{\boldsymbol{e}}_j$ with components A_{ij}. The equations are presented in three-dimensional space with the spatial indices $i, j \in \{1,2,3\}$, although the simulations are conducted assuming two-dimensional plane strain approximation. We adopt Einstein's convention where repeated spatial indices imply summation. To denote the value of a vector or tensor at time step n we use the left superscript; for iterative procedures we use m as the counter and set it as a left subscript surrounded by parentheses; and we reserve the right superscript for exponents (italicized) or descriptors (unitalicized). For example, ${}^{n}_{(m)}\varepsilon^{\mathrm{e}}_{ij}$ denotes the elastic (e) component of the second-order strain tensor ε_{ij} at time step n and iteration m. Any symbol written without the left superscript is assumed to be at time step n.

4.2.2 Domain description

We employ the updated-Lagrangian description, rather than a total Lagrangian or Eulerian description, to efficiently simulate the viscous flow and fracture of ice. In the updated-Lagrangian description, the positions of the material points in the continuum and their motion is described using a reference configuration that dynamically evolves as the domain deforms. For this reason, we will distinguish the *initial* reference configuration from *current* and *updated* reference configurations, as illustrated in Figure 4.1. The *initial* reference configuration is denoted by ${}^0\Omega$ and contains all the material points with initial spatial coordinates ${}^0\boldsymbol{x}$. The current spatial coordinates of the material points in the domain ${}^n\Omega$ are denoted by ${}^n\boldsymbol{x} = {}^n x_i \hat{\boldsymbol{e}}_i$. At any given time step n, the *current* reference domain ${}^n\Omega$ is bounded by the union of the Dirichlet and Neumann boundaries ${}^n\Gamma^{\mathrm{D}}$ and ${}^n\Gamma^{\mathrm{N}}$, respectively. The *updated* reference configuration is defined by the domain ${}^{n+1}\Omega$ after the material points are translated using a displacement increment ${}^n\Delta\boldsymbol{u}$ between time steps n and $n+1$. The kinematics of the moving continuum and the procedure for calculating $\Delta\boldsymbol{u}$ are described in the following section.

4.2.3 Kinematics

The current velocity of material particles in the domain ${}^n\Omega$ is denoted by $\boldsymbol{v}(\boldsymbol{x},t) = v_i \hat{\boldsymbol{e}}_i$ and the corresponding strain-rate is defined as

$$\dot{\varepsilon}_{ij} = \frac{1}{2}\left(\frac{\partial\, v_i}{\partial\, x_j} + \frac{\partial\, v_j}{\partial\, x_i}\right). \tag{4.1}$$

In the literature, the above quantity is commonly referred to as the *rate of deformation* tensor. Generally, in the total Lagrangian description the displacement $\boldsymbol{u}$ of each material point in the current configuration ${}^n\Omega$ is defined by the difference between its current and

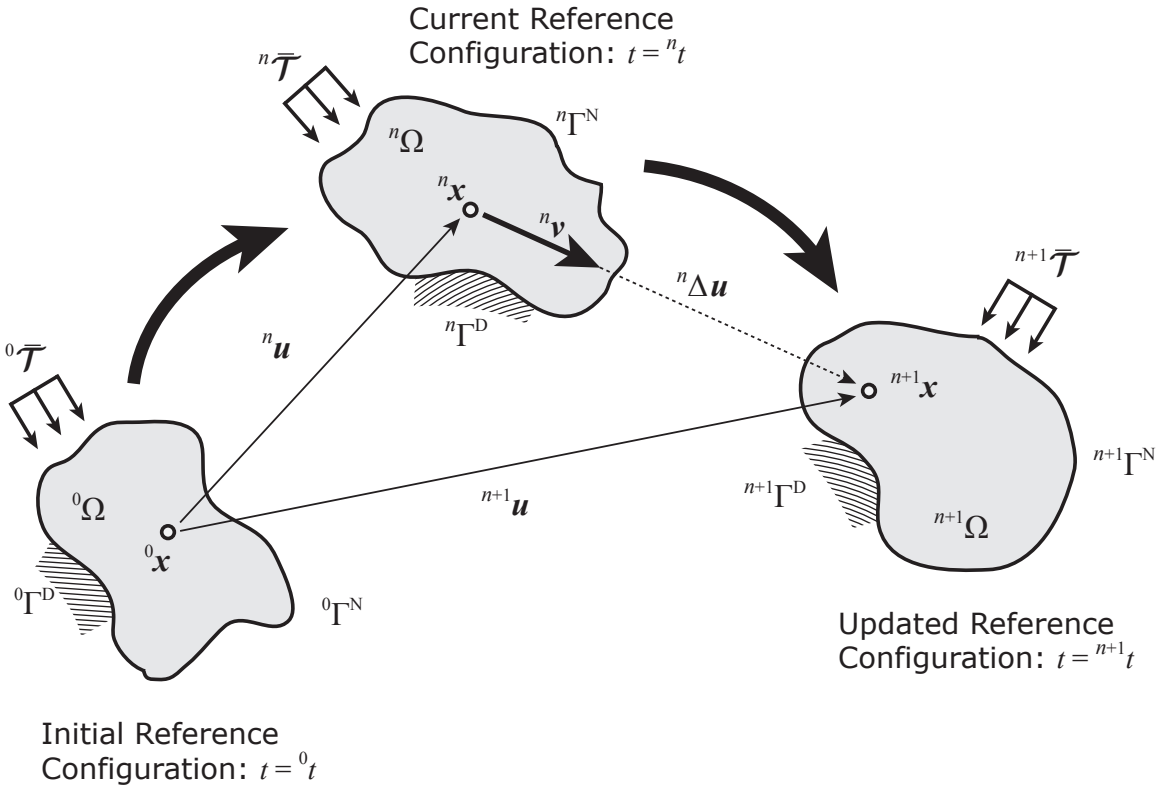

Figure 4.1: Illustration of reference domain configurations in the updated-Lagrangian description (redrawn from [Onate and Carbonell, 2014]). The initial, current, and updated reference configurations are defined the by domains indicated by ${}^{0}\Omega$, ${}^{n}\Omega$, and ${}^{n+1}\Omega$, respectively. The symbols Γ^{D} and Γ^{N} respectively denote the Dirichlet and Neumann boundaries, and $\bar{\mathcal{T}}$ is a vector of applied tractions.

initial spatial coordinates

$$u_i = x_i - {}^0x_i. \tag{4.2}$$

In the updated-Lagrangian framework, the displacement of material particles between ${}^n\Omega$ to ${}^{n+1}\Omega$ is defined using the displacement increment as

$$\Delta u_i = {}^{n+1}u_i - u_i = {}^{n+1}x_i - x_i. \tag{4.3}$$

The displacement increment ${}^n\Delta\boldsymbol{u}$ can be obtained by integrating the flow velocity over time [Onate and Carbonell, 2014]

$$\Delta u_i = \int_{n_t}^{n+1_t} v_i(\boldsymbol{x},\tau)d\tau. \tag{4.4}$$

Note that between the times ${}^nt$ and ${}^{n+1}t$ the domain continuously moves with a variable velocity field $v_i(\boldsymbol{x},\tau)$ from ${}^n\Omega$ with known coordinates $\boldsymbol{x}$ to the updated configuration ${}^{n+1}\Omega$ with unknown coordinates ${}^{n+1}\boldsymbol{x}$ [Bathe et al., 1975]; therefore, an iterative scheme is required to account for the change in reference configuration [Onate and Carbonell, 2014]. However, assuming small changes in particle velocities during the time increment $\Delta t = {}^{n+1}t - {}^nt$, we approximate the displacement increment and update the nodal coordinates as

$$\Delta u_i \;\; = {}^{n+1}v_i(\boldsymbol{x},t)\;\Delta t, \tag{4.5}$$

$${}^{n+1}x_i \;\;\;\; = {}^nx_i + \Delta u_i. \tag{4.6}$$

The procedure for computing velocity ${}^{n+1}v_i(\boldsymbol{x},t)$ is detailed in the Section 4.2.6.

4.2.4 Nonlocal creep continuum damage model

The continuum damage model for creep fracture is built on the principle of effective stress [Kachanov, 1958, Rabotnov, 1963] and the hypothesis of strain equivalence [Lemaitre, 1971], which states that "the strain associated with a damaged state under the applied stress is equivalent to the strain associated with its undamaged state under the effective stress." Here, we assume damage evolves isotropically under tension, so it is represented by a scalar variable $D \in [0,1]$, where $D = 0$ and $D = 1$ represent an undamaged (virgin) and a fully damaged state, respectively, at a material point in the continuum. The effective Cauchy stress tensor $\widetilde{\sigma}_{ij}$ can be defined in terms of the actual Cauchy stress tensor σ_{ij} as

$$\widetilde{\sigma}_{ij} = \frac{\sigma_{ij}}{(1-D)}. \tag{4.7}$$

The process of creep damage is generally associated with progressive degradation due to the growth of microcracks and microvoids [Betten et al., 1998, 1999]. To account for the time-dependent degradation mechanisms, the local rate of evolution of damage $\dot{D}^{\text{loc}}$ at a material point is phenomenologically defined by a dynamic damage evolution function f as

$$\dot{D}^{\text{loc}} = \frac{\partial D^{\text{loc}}}{\partial t} = \begin{cases} f(\sigma_{ij}, D), & \text{if} \quad \sigma_{kk} \geq 0, \\ 0, & \text{if} \quad \sigma_{kk} < 0. \end{cases} \tag{4.8}$$

Remark 19 *Laboratory experimental studies indicate that ice exhibits tension-compression asymmetry in its mechanical response to loading. While damage evolution in ice under tension is clearly observed to be due to the growth and coalescence of microcracks and microvoids, damage evolution under compression is also complicated by recrystallization process, as noted in [Duddu and Waisman, 2013a]. Because ice is much stronger in compression than in tension, crevasses (fractures) are always observed in regions under tensile*

stress states; so, we only consider damage evolution under tension.

Remark 20 *The isotropic damage variable D can be physically interpreted as the ratio of the area of spherical micro-voids to the total area along a cross-sectional cut of a representative volume element at a material point [Lemaitre, 1992]; therefore, in Equation (4.8), damage growth due to nucleation and growth of spherical micro-voids is permitted only when the stress state at a material point is predominantly tensile, that is, when the hydrostatic stress* $\sigma_{kk} > 0$.

We next define the damage evolution function f for the generalized multi-axial stress state as [Murakami et al., 1988]

$$f = \hat{B}\frac{\langle \chi \rangle^r}{(1-D)^{k_\sigma}}, \tag{4.9}$$

where $\hat{B}$ and r are material parameters controlling the damage growth rate; k_σ is a stress-dependent term; $\langle \cdot \rangle$ represents the Macaulay brackets, such that $\langle \chi \rangle = \max\{\chi, 0\}$; and the effective Hayhurst stress χ is defined as [Hayhurst, 1972]

$$\chi = \alpha \widetilde{\sigma}^{(\mathrm{I})} + \beta \widetilde{\sigma}^{\mathrm{v}} + (1-\alpha-\beta)\widetilde{\sigma}_{kk}. \tag{4.10}$$

In the above equation, α and β are material parameters corresponding to brittle and ductile crack growth mechanisms, respectively; $\widetilde{\sigma}^{(\mathrm{I})}$ is the maximum principal stress in the effective space; $\widetilde{\sigma}^{\mathrm{v}}$ is the effective von Mises stress; and $\widetilde{\sigma}_{kk}$ is the trace of the effective Cauchy stress tensor (i.e, the first invariant of the effective stress). Because χ is a weighted average of stress invariants, it is invariant with coordinate transformation. The stress-dependent

parameter k_σ is an experimentally calibrated parameter defined as

$$k_\sigma = k_1 + k_2 \sigma_{kk}, \text{ if } \quad \sigma_{kk} \geq 0. \tag{4.11}$$

The parameter k_σ accounts for the tertiary creep behavior, wherein the presence of pre-existing damage in polycrystalline ice accelerates crack growth rate under tension leading up to rupture.

4.2.4.1 Nonlocal integral damage

To ensure thermodynamic consistency and to alleviate mesh dependence issues with the numerical implementation of local damage models [Bazant and Pijaudier-Cabot, 1988, Pijaudier-Cabot and Bazant, 1987b, de Borst, 2001, Verhoosel et al., 2011, Jirásek and Grassl, 2008], we define a nonlocal damage rate $\dot{D}$ at a specific material point at spatial location $\boldsymbol{x}$ in the reference configuration Ω as

$$\dot{D}(\boldsymbol{x}) = \frac{\int_\Omega \Phi(\boldsymbol{x} - \hat{\boldsymbol{x}}) \dot{D}^{\text{loc}}(\hat{\boldsymbol{x}}) \, \mathrm{d}\hat{\boldsymbol{x}}}{\int_\Omega \Phi(\boldsymbol{x} - \hat{\boldsymbol{x}}) \, \mathrm{d}\hat{\boldsymbol{x}}}, \tag{4.12}$$

where $\hat{\boldsymbol{x}} = \hat{x}_i \hat{\boldsymbol{e}}_i$ denotes the spatial coordinates of any material point in Ω, and Φ can be selected as either Gaussian or Green's weighting function defined by

$$\Phi(\boldsymbol{x} - \hat{\boldsymbol{x}}) = \begin{cases} \exp\left(-\kappa \frac{||\boldsymbol{x} - \hat{\boldsymbol{x}}||^2}{l_c^2}\right) & \text{(Gaussian)}, \\ \exp\left(-2\sqrt{\kappa} \frac{||\boldsymbol{x} - \hat{\boldsymbol{x}}||}{l_c}\right) & \text{(Green's)}. \end{cases} \tag{4.13}$$

In the above equation, the shape parameter κ is a positive constant and l_c is a chosen nonlocal length scale for purely numerical reasons. In our simulation studies, we take $l_c = 10$ m and $\kappa = 2$, and all other damage model parameters and their values are listed

in Table 5.2. The numerical implementation of the nonlocal integral is detailed in Section 4.3.2.

4.2.4.2 Implicit gradient damage

We next present an implicit gradient formulation for computing the nonlocal damage rate [Peerlings et al., 2001, de Borst and Verhoosel, 2016]. The implicit gradient can be simply derived by expanding the local damage rate $\dot{D}^{\text{loc}}$ as a Taylor series about $\hat{\boldsymbol{x}}$ as

$$\dot{D}^{\text{loc}}(\hat{\boldsymbol{x}}) = \dot{D}^{\text{loc}}(\boldsymbol{x}) + \frac{\partial \dot{D}^{\text{loc}}}{\partial x_i}(\hat{x}_i - x_i) + \frac{1}{2!}\frac{\partial \dot{D}^{\text{loc}}}{\partial x_i \partial x_j}(\hat{x}_i - x_i)\left(\hat{x}_j - x_j\right) + \ldots \tag{4.14}$$

By substituting the above expression and the kernel function (Eq. 4.13) into Equation (4.12), the nonlocal damage rate can be defined as

$$\dot{D}(\boldsymbol{x}) = \dot{D}^{\text{loc}}(\boldsymbol{x}) + \frac{l_c^2}{4\kappa}\frac{\partial^2}{\partial x_i^2}\dot{D}^{\text{loc}}(\boldsymbol{x}) + \frac{l_c^4}{32\kappa^2}\frac{\partial^4}{\partial x_i^2 \partial x_j^2}\dot{D}^{\text{loc}}(\boldsymbol{x}) + \ldots \tag{4.15}$$

The partial differential equation corresponding to the implicit gradient formulation can be obtained by taking the Laplacian of Equation (4.15), multiplying by $\frac{l_c^2}{4\kappa}$, subtracting that expression from Equation (4.15) and then neglecting higher-order gradient terms to yield a simple form as follows:

$$\dot{D} - \frac{l_c^2}{4\kappa}\frac{\partial^2}{\partial x_i^2}\dot{D} = \dot{D}^{\text{loc}}. \tag{4.16}$$

The numerical implementation of the implicit gradient formulation is provided in Section 4.3.2.

Table 4.1: Damage law parameters obtained from [Duddu and Waisman, 2013c].

Parameter	Value	Units
$\hat{B}$	5.23×10^{-7}	MPa $^{-r}$ s^{-1}
r	0.43	–
k_1	-2.63	–
k_2	7.24	MPa^{-1}
α	0.21	–
β	0.63	–
l_c	10	m
κ	2	–

4.2.5 Rheology of damaged ice

The rheological model describes the nonlinear viscous flow behavior of damaged ice based on Glen's flow law [Glen, 1955, Nye, 1953]. Assuming polycrstalline ice to be isotropic and incompressible, the viscous strain rate of damaged ice is given by

$$\dot{\varepsilon}_{ij} = A(\widetilde{\tau}^{\text{eq}})^{N-1}\widetilde{\tau}_{ij}. \tag{4.17}$$

where $\widetilde{\tau}_{ij}$ is the effective deviatoric stress, coefficient A and exponent N are viscous flow parameters, and the effective equivalent deviatoric stress $\widetilde{\tau}^{\text{eq}}$ is defined in terms of the second invariant as

$$\widetilde{\tau}^{\text{eq}} = \sqrt{\frac{1}{2}\widetilde{\tau}_{ij}\widetilde{\tau}_{ij}}. \tag{4.18}$$

Note that the viscous flow of ice is faster at higher temperatures, and this is accounted for by defining an Arrhenius-type relation for the temperature dependence of the viscous flow coefficient A [van der Veen, 2013]. In this study, however, we conduct all the simulations using the material properties of ice at a constant temperature $T = -10^{\circ}C$, as given in Table E1.

Table 4.2: Material properties of ice at $-10^{\circ}C$ obtained from [Duddu and Waisman, 2013c] and [van der Veen, 2013].

Property	Value	Units
B	111.8	MPa $s^{1/3}$
N	3	–
ρ_{ice}	917	kg/m^3

The constitutive law in Equation (4.17) can be inverted and rewritten as

$$\widetilde{\tau}_{ij} = B\,(\dot{\varepsilon}^{\text{eq}})^{\frac{1}{N}-1}\,\dot{\varepsilon}_{ij}, \tag{4.19}$$

where $B = A^{-1/N}$ and the equivalent strain rate is

$$\dot{\varepsilon}^{\text{eq}} = \sqrt{\frac{1}{2}\dot{\varepsilon}_{ij}\dot{\varepsilon}_{ij}}. \tag{4.20}$$

Equation (4.19) represents a generalized constitutive flow law for a damaged non-Newtonian fluid-like material as given by

$$\tau_{ij} = 2(1-D)\eta\,\dot{\varepsilon}_{ij}, \tag{4.21}$$

where the nonlinear viscosity $\eta = \frac{1}{2}B\left([\dot{\varepsilon}^{\text{eq}}]^2+\gamma\right)^{\frac{1-N}{2N}}$ and $\gamma = 10^{-14}s^{-2}$ is a small regularization parameter introduced to avoid problems with the nonlinear solver when using a zero or constant velocity initial guess (i.e., when $\dot{\varepsilon}^{\text{eq}} = 0$) [Tezaur et al., 2015a]. The Cauchy stress tensor σ_{ij} can then be obtained as

$$\sigma_{ij} = \tau_{ij} - p\delta_{ij}. \tag{4.22}$$

In the above equation, $p = -\frac{1}{3}\sigma_{kk}$ is the pressure and δ_{ij} represents the Kronecker's delta where $\delta_{ij} = 1$ if $i = j$, and $\delta_{ij} = 0$ otherwise.

4.2.6 Strong form

The strong form of the governing equations is specified by the incompressible Stokes equations describing the creeping flow of the continuum based on momentum balance. In this two-field formulation, the unknown fields are the vector velocity field ${}^{n+1}\boldsymbol{v} = \boldsymbol{v}\left({}^{n+1}\boldsymbol{x}, {}^{n+1}t\right)$ and the scalar pressure field ${}^{n+1}p = p\left({}^{n+1}\boldsymbol{x}, {}^{n+1}t\right)$ which are defined as functions of the updated reference coordinates ${}^{n+1}\boldsymbol{x}$ over the updated configuration ${}^{n+1}\Omega$. For incompressible, isotropic fluids, the strong form of the Stokes flow equations are written as

$$\left.\begin{aligned} \frac{\partial\, {}^{n+1}\tau_{ij}}{\partial\, {}^{n+1}x_j} - \frac{\partial\, {}^{n+1}p}{\partial\, {}^{n+1}x_i} + \psi({}^{n}D)\, {}^{n+1}b_i = 0 \\ \psi({}^{n}D)\frac{\partial\, {}^{n+1}v_i}{\partial\, {}^{n+1}x_i} = 0 \end{aligned}\right\} \quad \text{on } {}^{n+1}\Omega, \tag{4.23}$$

where τ_{ij} is the deviatoric stress tensor, and b_i is the external force vector. The function $\psi({}^{n}D)$ is incorporated to relax the incompressibility constraint and disregard the density of fully damaged material points, and is taken as

$$\psi({}^{n}D) = \begin{cases} 1, & \text{if} \quad {}^{n}D < D^{\max}, \\ \xi, & \text{if} \quad {}^{n}D = D^{\max}, \end{cases} \tag{4.24}$$

where $D^{\max} \approx 1$ is the prescribed maximum value for damage and $\xi \approx 0 = 10^{-16}$ is chosen as a very small number to avoid rank deficiency of the tangent matrix. We assume $\psi(D)$ as a discontinuous (step) function, as opposed to a continuous function, because we wish to relax incompressibility and disregard density only after the macro-crack appears (i.e., ${}^{n}D = D^{\max}$) and not during micro-crack nucleation and growth; however, the mechanics of damaged (viscous) ice is a complicated issue, so the discontinuous form in Equation (4.24) is considered for purely numerical reasons in this study.

Remark 21 *While it may be physically consistent to assume that fully damaged ice no longer behaves like an incompressible medium, disregarding the density of damaged ice may not be physically consistent because it can remain in the crevasse as rubble or ice mélange [Amundson et al., 2010] and exert cryostatic stress due to self-weight. Furthermore, meltwater can now percolate into the fully damaged zone and exert hydrostatic pressure along the edges of the crack (or crevasse) [Mobasher et al., 2016].*

Remark 22 *From a computational standpoint, applying the body force due to gravity while the viscosity of damaged ice tends to zero is problematic because it leads to excessive displacements and distortions in damaged regions of the finite element mesh; therefore, we introduce $\psi(D)$ into the body force term in Equation (4.24) to disregard body force at fully damaged material points. Modeling fully damaged ice either as an anisotropic material with tension-compression asymmetry [Duddu and Waisman, 2012] or as a granular material using the Mohr-Coulomb failure theory [Moore, 2014] could overcome this problem; however, the numerical implementation would become very cumbersome as we need to switch between rheological models based on the damaged state.*

Upon substituting the kinematic equation (Eq. 4.1) and constitutive relation (Eq. 4.21), the strong form can be rewritten in terms of velocity, effective pressure, and prior damage in the updated configuration as

$$\left.\begin{aligned} \frac{\partial}{\partial\, {}^{n+1}x_j}\left\{[1-{}^{n}D]\,\eta\left({}^{n+1}\boldsymbol{v}\right)\left[\frac{\partial\, {}^{n+1}v_i}{\partial\, {}^{n+1}x_j}+\frac{\partial\, {}^{n+1}v_j}{\partial\, {}^{n+1}x_i}\right]\right\} \\ -[1-{}^{n}D]\frac{\partial\, {}^{n+1}\widetilde{p}}{\partial\, {}^{n+1}x_i}+\psi\left({}^{n}D\right){}^{n+1}b_i=0 \\ \\ \psi\left({}^{n}D\right)\frac{\partial\, {}^{n+1}v_i}{\partial\, {}^{n+1}x_i}=0 \end{aligned}\right\} \quad \text{on } {}^{n+1}\Omega, \tag{4.25}$$

together with the Dirichlet and Neumann boundary conditions

$$\begin{aligned} {}^{n+1}v_i &= {}^{n+1}\bar{v}_i \quad \text{on } {}^{n+1}\Gamma^{\mathrm{D}}, \\ {}^{n+1}\sigma_{ij}\,{}^{n+1}\hat{n}_j &= {}^{n+1}\bar{\mathscr{T}}_i \quad \text{on } {}^{n+1}\Gamma^{\mathrm{N}}, \end{aligned} \tag{4.26}$$

where ${}^{n+1}\bar{v}_i$ are applied velocities, ${}^{n+1}\bar{\mathscr{T}}_i$ are applied tractions, and ${}^{n+1}\hat{n}_j$ is a outward unit normal vector to the surface of the boundary. In Equation (4.25), the viscosity η is a nonlinear function of the velocity defined as, $\eta\left({}^{n+1}\boldsymbol{v}\right) = \frac{1}{2}B\left([{}^{n+1}\dot{\varepsilon}^{\mathrm{eq}}]^2+\gamma\right)^{\frac{1-N}{2N}}$, where ${}^{n+1}\dot{\varepsilon}^{\mathrm{eq}}$ is defined in Equation (4.20); and the effective pressure $\widetilde{p} = (1-D)^{-1}p$.

4.2.7 Weak form

The weak form of Equation (4.25) is obtained by incorporating test functions $\boldsymbol{w}$ and q, integrating by parts, and then applying Gauss's theorem. The weak or variational form can be stated as follows:

Find ${}^{n+1}\boldsymbol{v} \in \mathscr{V}$ and ${}^{n+1}\widetilde{p} \in \mathscr{S}$ such that $\forall\ \boldsymbol{w} \in \mathscr{V}$ and $q \in \mathscr{S}$:

$$\left.\begin{aligned} &\int_{{}^{n+1}\Omega} \frac{\partial\, w_i}{\partial\, {}^{n+1}x_j}\left\{[1-{}^{n}D]\,\eta\left({}^{n+1}\boldsymbol{v}\right)\left[\frac{\partial\, {}^{n+1}v_i}{\partial\, {}^{n+1}x_j}+\frac{\partial\, {}^{n+1}v_j}{\partial\, {}^{n+1}x_i}\right]\right\}\,\mathrm{d}\Omega \\ &-\int_{{}^{n+1}\Omega}[1-{}^{n}D]\frac{\partial\, w_i}{\partial\, {}^{n+1}x_i}\,{}^{n+1}\widetilde{p}\,\mathrm{d}\Omega-\int_{{}^{n+1}\Omega}\psi\,({}^{n}D)w_i\,{}^{n+1}b_i\,\mathrm{d}\Omega \\ &\qquad\qquad -\int_{{}^{n+1}\Gamma^{\mathrm{N}}} w_i\,{}^{n+1}\bar{\mathscr{T}}_i\,\mathrm{d}\Gamma = 0 \\ &\int_{{}^{n+1}\Omega}\psi\,({}^{n}D)q\frac{\partial\, {}^{n+1}v_i}{\partial\, {}^{n+1}x_i}\,\mathrm{d}\Omega = 0 \end{aligned}\right\} \quad \text{on } {}^{n+1}\Omega, \tag{4.27}$$

where $\mathscr{V}$ and $\mathscr{S}$ are vector and scalar function spaces, respectively. Because the updated coordinates ${}^{n+1}\boldsymbol{x}$ are unknown at time step n, solving the above weak formulation will require an implicit scheme, which can be cumbersome.

Remark 23 *An alternative weak form can be stated in the current reference configuration*

${}^n\Omega$ in terms of the Green-Lagrange strain-rate tensor $\dot{E}_{ij}$ and the second Piola-Kirchhoff stress tensor S_{ij}. In this alternative form, all the gradient quantities are written in terms of the (known) current reference coordinates ${}^n\boldsymbol{x}$; however, the computation of the unknown displacement increment ${}^n\Delta\boldsymbol{u} = {}^{n+1}\boldsymbol{x} - {}^n\boldsymbol{x}$ between configurations ${}^{n+1}\Omega$ and ${}^n\Omega$ necessitates an iterative procedure, which can be cumbersome. Futhermore, the consistent tangent corresponding to this alternative weak form is much more complicated, as described in [Onate and Carbonell, 2014].

To simplify the numerical implementation, we express the above weak form over the the current reference configuration ${}^n\Omega$ (see [Onate and Carbonell, 2014] for a detailed derivation) and assume that the displacement increment gradient $\frac{\partial\, \Delta u_i}{\partial\, {}^n x_j} << 1$ and deformation gradient $F_{ij} = \frac{\partial\, {}^{n+1}x_j}{\partial\, {}^n x_j} \approx 1$. Consequently, for small time increments Δt, we can now state the approximate weak form over the current reference configuration ${}^n\Omega$ as follows:

Find ${}^{n+1}\boldsymbol{v} \in \mathscr{V}$ and ${}^{n+1}\widetilde{p} \in \mathscr{S}$ such that $\forall\ \boldsymbol{w} \in \mathscr{V}$ and $q \in \mathscr{S}$:

$$\left.\begin{aligned} \int_{{}^n\Omega} \frac{\partial\, w_i}{\partial\, {}^n x_j} \left\{ [1 - {}^nD]\, \eta\left({}^{n+1}\boldsymbol{v}\right) \left[\frac{\partial\, {}^{n+1}v_i}{\partial\, {}^n x_j} + \frac{\partial\, {}^{n+1}v_j}{\partial\, {}^n x_i} \right] \right\} \mathrm{d}\Omega \\ - \int_{{}^n\Omega} [1 - {}^nD] \frac{\partial\, w_i}{\partial\, {}^n x_i}\, {}^{n+1}\widetilde{p}\, \mathrm{d}\Omega - \int_{{}^n\Omega} \psi\left({}^nD\right) w_i\, {}^n b_i\, \mathrm{d}\Omega \\ - \int_{{}^n\Gamma^{\mathrm{N}}} w_i\, {}^n\bar{\mathscr{T}}_i\, \mathrm{d}\Gamma = 0 \\ \\ \int_{{}^n\Omega} \psi\left({}^nD\right) q \frac{\partial\, {}^{n+1}v_i}{\partial\, {}^n x_i}\, \mathrm{d}\Omega = 0 \end{aligned}\right\} \quad \text{on } {}^n\Omega. \tag{4.28}$$

In essense, the above approximate weak form reads almost exactly like the one in Equation (4.27), if we assume $\frac{\partial\, {}^n\Delta u_k}{\partial\, {}^n x_i} << 1$, so that

$$\frac{\partial}{\partial\, {}^{n+1}x_j} \approx \frac{\partial}{\partial\, {}^n x_j}, \tag{4.29}$$

and the relevant strain rate tensor ${}^{n+1}\dot{\varepsilon}_{ij}$ can now be approximated as

$$ {}^{n+1}\dot{\varepsilon}_{ij} \approx \frac{1}{2}\left[\frac{\partial\, {}^{n+1}v_i}{\partial\, {}^{n}x_j} + \frac{\partial\, {}^{n+1}v_j}{\partial\, {}^{n}x_i}\right]. \tag{4.30} $$

The advantage in using the approximate weak form in Equation (4.28) is that it can be directly solved over the current reference configuration to obtain velocity and pressure fields, and then the mesh update procedure can be implemented separately in an de-coupled manner by choosing an appropriate time step Δt, which leads to a computationally accurate yet tractable strategy.

Remark 24 *The tensile strain rate corresponding to an expanding glacier is extremely small, typically, on the order of* 10^{-8} *per second; this typically amounts to a flow velocity of a few meters per day for a typical glacier that spans tens to hundreds of kilometers in length and a few hundred meters or more in depth. Consequently, the longitudinal and transverse gradients in the displacement increment are small (given the large size scales of glaciers), so using the approximation in Equation (4.29) is reasonable for creeping flow of glaciers.*

4.3 Solution strategy

We now present the numerical strategy that combines the updated-Lagrangian description for simulating the viscous (Stokes) flow and the nonlocal integral approach for simulating creep fracture (damage) evolution. We employ a de-coupled solution procedure that is explicit in time and consists of two sequential steps: (1) solve the variational form of the Stokes flow equations using a mixed finite element discretization, in conjunction with Picard iteration and mesh update schemes; (2) compute the damage increment using a nonlocal integral or gradient approach to establish the damage rate. During the Picard iteration scheme the flow velocity ${}^{n+1}v_i$ and effective pressure ${}^{n+1}\widetilde{p}$ fields are computed over the current reference configuration ${}^{n}\Omega$, while holding damage constant ${}^{n}D$ at its previously computed value. Using the converged solutions for velocity and pressure, the Cauchy stress and the damage rate are subsequently computed to update damage. Thus, the damage update (step 2) is fully decoupled from the solution of Stokes flow problem (step 1). These two solution steps along with detailed algorithms are presented in the following sections.

Remark 25 *Unlike the fully implicit damage models in the literature that are formulated for strain-dependent and rate- or time-independent damage functions (e.g., see [Peerlings et al., 2001]), creep damage in ice is a time-dependent process, and the damage rate is a highly nonlinear function of the full stress tensor [Duddu and Waisman, 2012]. Because the solution to the nonlinear Stokes equations is instantaneous (steady-state) and damage evolution is time-dependent and highly nonlinear, it is simpler to use an explicit-time forward Euler scheme to update the damage separately; whereas, the implicit backward Euler scheme requiring a monolithic solve of the Stokes and damage evolution equations can become very cumbersome. For numerical accuracy and stability of the present scheme, we ensure that the damage increment is sufficiently small during each time step by choosing a*

suitable time increment according to Equation (4.34).

4.3.1 Solution of the variational form

We employ the finite element method to solve the variational form of the Stokes flow boundary value problem using FEniCS software. The advantage of FEniCS is that the Stokes flow problem can be directly specified in the variational form using the FEniCS Python application program interface (API). Based on the user-provided input, FEniCS interprets, assembles and solves the discretized linear system corresponding to the boundary value problem. The details of the full solution procedure are summarized in Algorithm 4. The procedure for setting up the problem in FEniCS [1] is detailed below:

i. The finite element mesh corresponding to the physical domain is provided as an XML file, which specifies triangular cells and the spacial locations of their vertices. The domain boundaries can then be defined by identifying the vertices belonging to the bottom, left, and right edges using the `SubDomain` class in FEniCS.

ii. Next, the finite element function spaces corresponding to the pressure (scalar) and velocity (vector) variables are defined over the mesh using the `FunctionSpace` and `VectorFunctionSpace` Python objects, respectively. Because we adopt a standard Galerkin formulation, we use the function spaces belonging to the Lagrange element family.

iii. Dirichlet boundary conditions on the velocity field are then defined using the `DirichletBC` Python object by providing the corresponding vector function space and the domain boundary.

iv. Trial and test functions are introduced using the `TrialFunction` and `TestFunction` Python objects, respectively, for both scalar and vector function spaces. The weak

[1] The reader is referred to the FEniCS website which provides extended documentation for the Python API along with several demos for using the software.

form is simply provided by multiplying and adding the trial and test functions and their gradients to obtain the expression in Equation (4.28); the gradient operator ∇ is provided by FEniCS as the built-in function `nabla_grad()`.

v. Due to the solution-dependent viscosity $\eta\left({}^{n+1}\boldsymbol{v}\right)$, Equation (4.28) is highly nonlinear, and so we linearize the nonlinear system using a Picard iteration scheme, as detailed in Algorithm 5. The linearized system obtained at each Picard iteration is numerically solved using an iterative method by calling the `solve()` function, which takes the weak form and boundary conditions as input. An alternative to the Picard iteration scheme is the Newton's method [Worthen et al., 2014], which can be implemented in FEniCS as detailed in Appendix H.

Remark 26 *While the Newton's method has a faster rate of convergence than Picard iterations, we encountered convergence issues in FEniCS upon introduction of notches or damage zones into the nonlinear Stokes equations. We suspect that the automated assembly of the system Jacobian (tangent) matrix by FEniCS could be introducing interpolation errors that is affecting the overall convergence of the Newton's method; however, it could also be that the Newton's method is sensitive to the regularization parameter γ when the nonlinear Stokes equations are solved over non-convex domains. Perhaps, implementing advanced algorithms with respect to the parameter γ could improve the convergence of the Newton's method, especially given the lack of a good initial guess [Tezaur et al., 2015b].*

Because FEniCS software currently only supports triangular finite elements, we select a computationally efficient and numerically (LBB) stable element for solving the incompressible Stokes equations, namely, the P3-P1 element, wherein the velocity ${}^{n+1}\boldsymbol{v}$ is resolved on a 10-noded triangle using third-order polynomial (cubic P3) interpolants and the effective pressure ${}^{n+1}\widetilde{p}$ is resolved on a 3-noded triangle using first-order polynomial

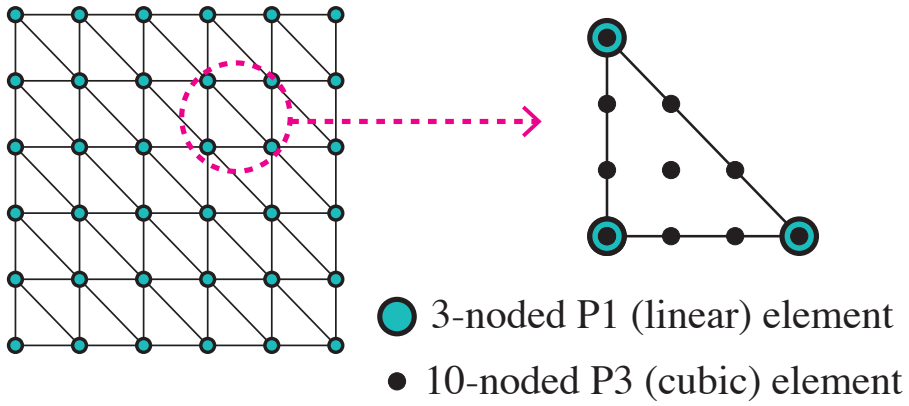

Figure 4.2: Illustration of the P3-P1 mixed finite element showing the 3-noded P1 sub-element with linear shape functions and the 10-noded P3 sub-element with cubic shape functions.

(linear P1) interpolants. An illustration of the P3–P1 mixed element and the mesh configuration is given in Figure 4.2. A stable alternative to the P3-P1 mixed element is the P2-P1 (Taylor-Hood) element, wherein the velocity is resolved using quadratic (P2) interpolation on a 6-noded triangle. Although the deviatoric stress can be calculated at the nodes of the P3 (or P2) element using the computed velocity field, we only calculate it at the nodes of the P1 element so that we can add it to the corresponding pressure to obtain the Cauchy stress. The damage variable is also interpolated using the P1 element because its evolution is dictated by the Cauchy stress. While equal low-order stabilized P1-P1 elements [Hughes and Franca, 1987, Franca and Stenberg, 1991, Gunzburger and Nicolaides, 1993] (also see Appendix G) are attractive due to their low computational cost [Zhang et al., 2011], especially in three dimensions, the pressure and stress fields predicted by low-order P1-P1 elements are not as accurate as the higher-order P2-P1 or P3-P1 elements [Leng et al., 2012, 2013]. Another viable yet computationally cheaper alternative to P2-P1 or P3-P1 elements is the enriched MINI-element [Arnold et al., 1984, Turner et al., 2009]; however, the implementation of free-slip conditions tangential to the domain boundaries is not straightforward in FEniCS and requires the use of weak form implementations.

Algorithm 4 : Stokes flow solution scheme

At any time step n, the following is known: the nodal positions ${}^{n}x_i$ (where $i \in \{1,2,3\}$), the damage variable ${}^{n}D$ at each node, and the total elapsed time ${}^{n}t$. The solution scheme for a prescribed total time t_{total} is implemented as follows:

i. Initialize at step $n = 0$:

   (a) Supply the finite element mesh with nodal positions ${}^{0}x_i$. Define boundaries, finite element function spaces, and Dirichlet boundary conditions.

   (b) Set initial values for time and damage: ${}^{0}t = 0$ and ${}^{0}D = 0$.

   (c) At each node, compute the nonlocal damage weights of neighboring nodes.

ii. While ${}^{n}t \leq t_{\text{total}}$:

   (a) Solve the Stokes flow equations (Eqs. 4.28) using Picard iterations (see Algorithm 5) on the current reference configuration ${}^{n}\Omega$ to obtain the velocity and effective pressure solutions ${}^{n+1}v_i$ and ${}^{n+1}\widetilde{p}$.

   (b) Compute ${}^{n+1}\dot{\varepsilon}_{ij}$, ${}^{n+1}\widetilde{\tau}_{ij}$, and ${}^{n+1}\widetilde{\sigma}_{ij}$ at each node belonging to the P1 elements in the mesh using Equations (4.30), (4.19), and (4.22) respectively.

   (c) Compute the nonlocal damage increment ${}^{n}\Delta D$ at each node belonging to the P1 elements using Algorithm 6.

   (d) Move the mesh by updating nodal positions: ${}^{n+1}x_i = {}^{n}\Delta u_i + {}^{n}x_i$, where the displacement increment ${}^{n}\Delta u_i = {}^{n+1}v_i \, {}^{n}\Delta t$.

   (e) Update the elapsed time: ${}^{n+1}t = {}^{n}\Delta t + {}^{n}t$ and the iteration count: $n = n+1$.

Algorithm 5 : Picard iteration scheme for Stokes flow in 2D

Let ${}^{n+1}_{(m)}v_1$ and ${}^{n+1}_{(m)}v_2$ denote the horizontal and vertical components of velocity, respectively, and ${}^{n+1}_{(m)}\widetilde{p}$ denote the effective pressure determined on the current reference configuration ${}^{n}\Omega$ at Picard iteration m. The Picard iteration scheme is implemented as follows:

i. Initialize the velocity and pressure variables at iteration $m = 0$:

   (a) Set ${}^{n+1}_{(0)}v_1 = {}^{n}v_1$ and ${}^{n+1}_{(0)}v_2 = {}^{n}v_2$ everywhere in the domain.

   (b) Set ${}^{n+1}_{(0)}\widetilde{p} = {}^{n}\widetilde{p}$ everywhere in the domain.

ii. Initialize the maximum relative error ε to be greater than the chosen tolerance ε_{tol}.

iii. While $\varepsilon > \varepsilon_{\text{tol}}$:

   (a) Compute the nonlinear viscosity $\eta\left({}^{n+1}_{(m)}\boldsymbol{v}\right) = \frac{1}{2}B\left({}^{n+1}_{(m)}[\dot{\varepsilon}^{\text{eq}}]^2 + \gamma\right)^{\frac{1-N}{2N}}$ for iteration m using ${}^{n+1}_{(m)}v_1, {}^{n+1}_{(m)}v_2$.

   (b) Solve the Stokes flow equations (Eqs. 4.28) with the viscosity $\eta\left({}^{n+1}_{(m)}\boldsymbol{v}\right)$ to obtain ${}^{n+1}_{(m+1)}v_1, {}^{n+1}_{(m+1)}v_2$, and ${}^{n+1}_{(m+1)}\widetilde{p}$. This is done in FEniCS software by using the `solve()` function.

   (c) Calculate relative L^2 error norms: $\varepsilon_1 = \frac{||{}^{n+1}_{(m+1)}v_1 - {}^{n+1}_{(m)}v_1||}{||{}^{n+1}_{(m+1)}v_1||}$, $\varepsilon_2 = \frac{||{}^{n+1}_{(m+1)}v_2 - {}^{n+1}_{(m)}v_2||}{||{}^{n+1}_{(m+1)}v_2||}$, $\varepsilon_p = \frac{||{}^{n+1}_{(m+1)}\widetilde{p} - {}^{n+1}_{(m)}\widetilde{p}||}{||{}^{n+1}_{(m+1)}\widetilde{p}||}$.

   (d) Determine the maximum relative error: $\varepsilon = \max\{\varepsilon_1, \varepsilon_2, \varepsilon_p\}$.

   (e) Update the iteration count: $m = m + 1$.

iv. Upon convergence: ${}^{n+1}v_1 = {}^{n+1}_{(m+1)}v_1$, ${}^{n+1}v_2 = {}^{n+1}_{(m+1)}v_2$, and ${}^{n+1}\widetilde{p} = {}^{n+1}_{(m+1)}\widetilde{p}$.

4.3.2 Computation of damage increment

We employ an explicit forward Euler method in conjunction with the nonlocal integral approach to compute the creep damage increment at each time step. First, the local damage rate is computed using the Cauchy stress ${}^{n+1}\sigma_{ij}$ obtained from the solution of the Stokes flow problem and the prior damage ${}^{n}D$, as summarized in Algorithm 6. Next, the nonlocal damage increment ${}^{n}\Delta D$ is calculated using the local damage increments ${}^{n}\Delta D^{\text{loc}} = {}^{n}\dot{D}^{\text{loc}}\,{}^{n}\Delta t$ as given by the weighted summation

$$ {}^{n}\Delta D\left({}^{n}\boldsymbol{x}\right) = \frac{\sum_{j=1}^{\text{N}^{\text{pts}}} \Phi\left({}^{0}\boldsymbol{x} - {}^{0}\hat{\boldsymbol{x}}_j\right) {}^{n}\Delta D^{\text{loc}}\left({}^{n}\hat{\boldsymbol{x}}_j\right)}{\sum_{j=1}^{\text{N}^{\text{pts}}} \Phi\left({}^{0}\boldsymbol{x} - {}^{0}\hat{\boldsymbol{x}}_j\right)}, \tag{4.31} $$

where ${}^{n}\Delta t$ is a chosen time increment that ensures stability of the explicit update, and N^{pts} is the number of material points (i.e., finite element nodes) ${}^{0}\hat{\boldsymbol{x}}_j$ that neighbor ${}^{0}\boldsymbol{x}$, that is, the number of points satisfying $||{}^{0}\boldsymbol{x} - {}^{0}\hat{\boldsymbol{x}}_j|| \leq l_c$. The nonlocal weights $\Phi\left({}^{0}\boldsymbol{x} - {}^{0}\hat{\boldsymbol{x}}_j\right)$ are calculated and stored in a Python dictionary at the beginning of the simulation, instead of recalculating the weights at every time step. Finally, the damage variable in the updated configuration is computed as

$$ {}^{n+1}D = {}^{n}D + {}^{n}\Delta D. \tag{4.32} $$

Remark 27 *To reduce the computational burden, we only compute the nonlocal damage weights at the beginning of the simulation using materials points ${}^{0}\boldsymbol{x}$ over the initial reference configuration. Considering that the spatial locations of material points and their relative distances change as the domain deforms, it may be necessary to periodically recalculate the nonlocal weights, especially over time scales associated with large displacements.*

As an alternative to the weighted summation in Equation (4.31), the nonlocal damage

increment can be obtained using the implicit gradient formulation presented in Section 4.2.4.2. The nonlocal damage rate ${}^{n}\dot{D}$ is computed by taking the finite element discretization of Equation (4.16), whose variational form is obtained by introducing a test function z, integrating by parts, and then applying Gauss's theorem. The variational form over the current reference configuration ${}^{n}\Omega$ is stated as follows:

Find ${}^{n}\dot{D} \in \mathscr{Z}$, such that $\forall\, z \in \mathscr{Z}$:

$$\left.\begin{aligned} \int_{{}^{n}\Omega} z\, {}^{n}\dot{D}\, \mathrm{d}\Omega \;+\; \frac{l_c^2}{4\kappa} \int_{{}^{n}\Omega} \frac{\partial\, z}{\partial\, {}^{n}x_i} \frac{\partial\, {}^{n}\dot{D}}{\partial\, {}^{n}x_i}\, \mathrm{d}\Omega \\ - \int_{{}^{n}\Omega} z\, {}^{n}\dot{D}^{\mathrm{loc}}\, \mathrm{d}\Omega = 0 \end{aligned}\right\} \quad \text{on } {}^{n}\Omega, \tag{4.33}$$

where $\mathscr{Z}$ is an appropriate scalar function space, and the local damage rate ${}^{n}\dot{D}^{\mathrm{loc}}$ is computed from Equation (4.8) at a given material point. The above equation is discretized using linear P1 interpolants and evaluated using the FEniCS `solve()` function with zero flux conditions on all external boundaries. After solving for ${}^{n}\dot{D}$, the nonlocal damage increment is calculated as ${}^{n}\Delta D = {}^{n}\dot{D}\, {}^{n}\Delta t$ for an appropriately chosen time increment ${}^{n}\Delta t$. The major advantage of the implicit gradient formulation is that nonlocal damage will always be computed over the current reference configuration ${}^{n}\Omega$ without needing to determine the updated nonlocal weights at each time step.

The simulation of creep fracture using either the integral or gradient nonlocal approaches can be quite challenging, requiring us to employ several numerical controls in order to continue computation over long times, as discussed below:

i. We restrict the value of the damage variable $D \in [0,1)$ by a maximum value $D^{\max} = 0.97$ or 0.999 in order to avoid a rank deficient tangent (stiffness) matrix. The physical implication of setting $D^{\max} < 1$ is that the fully damaged regions still possess a small residual strength, which can lead to unphysical stress redistribution. To correct this discrepancy, an element removal scheme can be implemented to remove failed elements from the finite element mesh; however, this is only valid if the damage

zone represents void space due to crack opening. The element removal scheme can be implemented as follows: before proceeding from time step n to $n+1$, we search for elements where ${}^{n+1}D = D^{\max}$ at each node (i.e., at each node of the P1 triangular element); if such a fully damaged element is found, then the mesh for the updated reference configuration ${}^{n+1}\Omega$ is rewritten without the element. The updated nodal positions ${}^{n+1}\boldsymbol{x}$ obtained from the mesh-update scheme are preserved whenever the mesh is rewritten. Note that the finite element function spaces and boundary conditions must be redefined over the new mesh, which can be automated in FEniCS without adding any significant computational cost. The advantage of the element removal scheme is that it allows us to enforce $D = 1$ and $\eta^{\text{dam}} = 0$ in fully damaged elements, while the drawback is that it could introduce mesh size dependence or directional mesh bias while simulating damage evolution.

ii. Experimental and modeling studies on creep damage in ice indicate an abrupt failure (rupture) as accumulated damage D becomes greater than 0.6 [Duddu and Waisman, 2012]. To account for this behavior, a critical damage parameter $D^{\text{cr}} = 0.6$ is introduced so that as soon as $D \geq D^{\text{cr}}$ we can immediately set damage to a maximum value $D^{\max}$ and damage rate $\dot{D}^{\text{loc}} = 0$. Although introducing the D^{cr} parameter into the damage model improves the numerical convergence in Abaqus software using the Maxwell viscoelastic model, it does not affect either the convergence of the FEniCS software using the viscous Stokes model or the crevasse growth results in any significant way.

iii. Because we employ the explicit forward Euler method to update damage in time, it is essential that we determine a stable time increment ${}^{n}\Delta t$ to compute ${}^{n}\Delta D$ according to Equation (4.32) to obtain an accurate solution. To determine an appropriate time increment, we impose the condition $\Delta D^{\text{loc}} \leq 0.05$ at every material point and then

calculate ${}^{n}\Delta t$ as

$$ {}^{n}\Delta t = \frac{\max({}^{n}\Delta D^{\text{loc}})}{\max({}^{n}\dot{D}^{\text{loc}})}, \tag{4.34} $$

where $\max({}^{n}\dot{D}^{\text{loc}}) = 0.05$ is the maximum of the local damage rates at all the material points in the domain. A consequence of the above strategy is that it prevents excessively fast growth of damage before it reaches critical damage, which minimizes changes in the damage state between ${}^{n+1}\Omega$ and ${}^{n}\Omega$ and thus alleviates numerical difficulties related to time stepping. Initially, when damage is low, the damage rate ${}^{n}\dot{D}^{\text{loc}}$ is small and so the time step ${}^{n}\Delta t$ calculated from Equation (4.34) is large. Because we use an explicit scheme to update (or move) the mesh at every time step, we impose a maximum time step of two hours; this ensures that the displacement of material points between ${}^{n+1}\Omega$ and ${}^{n}\Omega$ is sufficiently small so that the approximation in Equation (4.30) remains valid. As damage accumulates the local damage rate ${}^{n}\dot{D}^{\text{loc}}$ increases, thus causing the time step to gradually decline, with the smallest time step size reaching as low as 5 seconds close to rupture.

Algorithm 6 : Numerical implementation of nonlocal damage

The local damage increment ${}^{n}\Delta D^{\text{loc}}$ is computed during time step n based on the currently existing damage ${}^{n}D$ and effective Cauchy stress ${}^{n+1}\widetilde{\sigma}_{ij}$. The nonlocal damage increment ${}^{n}\Delta D$ is then computed as a weighted summation through the following steps:

i. Compute the local damage rate ${}^{n}\dot{D}^{\text{loc}}$ throughout the domain. At every finite element node:

   (a) Compute the effective max principal stress ${}^{n+1}\widetilde{\sigma}^{(\text{I})}$, von Mises stress ${}^{n+1}\widetilde{\sigma}^{\text{v}}$, and first stress invariant ${}^{n+1}\widetilde{\sigma}_{kk}$.

   (b) Compute the Hayhurst stress ${}^{n+1}\chi$.

   (c) Compute the damage evolution: $f = \hat{B}\dfrac{\langle {}^{n+1}\chi \rangle^{r}}{(1-{}^{n}D)^{k_\sigma}}$,
   where $k_\sigma = k_1 + k_2|{}^{n+1}\sigma_{kk}|$.

   (d) To allow only tensile damage, we enforce the condition that ${}^{n}\dot{D}^{\text{loc}} = f$ if ${}^{n+1}\sigma_{kk} \geq 0$ and ${}^{n}\dot{D}^{\text{loc}} = 0$ otherwise.

   (e) If ${}^{n}D = D^{\max}$ then ${}^{n}\dot{D}^{\text{loc}} = 0$.

ii. Compute the time step:

$$ {}^{n}\Delta t = \min\left(\frac{0.05}{\max({}^{n}\dot{D}^{\text{loc}})}, 2 \text{ hrs}\right). $$

iii. Compute the local damage increment ${}^{n}\Delta D^{\text{loc}} = {}^{n}\dot{D}^{\text{loc}}\ {}^{n}\Delta t$ at each node.

iv. Compute the nonlocal damage increment ${}^{n}\Delta D$ at each node using the integral approach (Eq. 4.31) or the implicit gradient approach (Eq. 4.33).

v. Update damage at each node: ${}^{n+1}D = {}^{n}D + {}^{n}\Delta D$.

4.4 Numerical Examples

In this section, we first verify the Picard iteration based nonlinear solver for the Stokes model by performing a verification study against a manufactured analytical solution [Dohrmann and Bochev, 2004, Worthen et al., 2014]. This verification study is repeated using the Newton's method is given in Appendix H. Following that, we establish the viability of the updated-Lagrangian formulation by simulating constant velocity and gravity-driven creep flow in idealized rectangular ice slabs and comparing the results with those obtained using the total Lagrangian formulation based on the Maxwell viscoelastic rheological model, previously established by Duddu et al. [Duddu and Waisman, 2012, 2013c, Duddu et al., 2013, Mobasher et al., 2016]. As noted earlier, the Stokes flow formulation is evaluated using the open-source finite element software FEniCS using triangular meshes, whereas the viscoelastic formulation is solved using commercial finite element software Abaqus using quadrilateral meshes. First, we benchmark the rheological models using idealized rectangular domains under simple loading conditions. Second, we introduce a notch in the rectangular domain at mid-length to determine the effects of stress concentrations (or singularities). Third, we incorporate the creep damage law detailed in Section 4.2.4 in order to simulate damage (crevasse) propagation. All simulations are performed in two dimensions assuming plane strain conditions on a rectangular slab of ice 500 m $\times$ 125 m (length $L \times$ height H) as shown in Figure 4.3. Boundary conditions (rollers) are specified in all simulations to constrain vertical displacement on the bottom edge of the domain and horizontal displacement on the left edge, thus allowing free slip. The isotropic material properties of ice at the temperature -10° C are given in Table E1. Thus, in this section, we only consider idealized rectangular geometries and boundary conditions and assume that the temperature is constant throughout the ice slab to conduct proof-of-concept studies that are still relevant for understanding crevasse propagation in glaciers and land ice sheets. Such domain geometries are commonly used to conduct fundamental studies to investigate the conditions that enable fracture in ice bodies and provide insights into the mechanisms behind iceberg

calving [Pralong and Funk, 2005, Bassis and Walker, 2012, Plate et al., 2012, Keller and Hutter, 2014b]. More realistic and complex geometries, loading, and boundary conditions shall be considered in a future paper focused on the simulation of ice sheet evolution.

Remark 28 *In reality, the topology of the grounding line is generally not a flat surface, but we assume a horizontal surface for the sake of simplicity. Further, the ice slab is often frozen to the ground if it is sufficiently far from the ocean, and so a no-slip or Coulomb friction type boundary condition may be more appropriate than free slip. The free slip boundary condition is appropriate for marine-terminating glaciers where seawater may flow beneath the ice sheet and provide lubrication between the ice slab and the ground.*

4.4.1 Numerical verification study

In this section we verify our implementation of the Stokes rheological model by demonstrating that numerical results converge to a known analytical solution with progressive mesh refinement. A previous study in [Mitchell, 2012] used linear Stokes rheology (i.e., with constant viscosity) and verified the FEniCS software for Poiseuille flow and several other gravity-driven flow benchmark examples that have exact solutions. On the verification of Stokes ice-sheet models using manufactured solutions we refer the reader to [Leng et al., 2013]. Herein, we conduct one such verification study to show that the *nonlinear* Stokes formulation converges to the manufactured solution presented in [Dohrmann and Bochev, 2004, Worthen et al., 2014] for incompressible flow, which is given by

$$\begin{aligned} v_1^* &= x_1 + x_1^2 - 2x_1x_2 + x_1^3 - 3x_1x_2^2 + x_1^2x_2, \\ v_2^* &= -x_2 - 2x_1x_2 + x_2^2 - 3x_1^2x_2 + x_2^3 - x_1x_2^2, \\ p^* &= x_1x_2 + x_1 + x_2 + x_1^3x_2^2 - 4/3, \end{aligned} \tag{4.35}$$

Table 4.3: Numerical verification study of the nonlinear Stokes model using Picard iteration scheme. The L^2 error norms $\varepsilon_{\boldsymbol{v}}$ and ε_p for velocity magnitude and pressure, respectively, given in Equations (47) are presented for different mesh sizes.

Mesh	**#DoF**	$\varepsilon_{\boldsymbol{v}}$	**Rate**	ε_p	**Rate**
4×4	187	$6.96\text{e}-4$	$--$	$1.04\text{e}-1$	$--$
8×8	659	$5.97\text{e}-5$	3.54	$1.54\text{e}-2$	2.75
16×16	2467	$5.11\text{e}-6$	3.55	$1.96\text{e}-3$	2.98
32×32	9539	$3.47\text{e}-7$	3.88	$2.68\text{e}-4$	2.87

on the unit square domain $\Omega = [0,1] \times [0,1]$. In this example we ignore damage and take $\eta(\boldsymbol{v}) = \left([\dot{\varepsilon}^{\text{eq}}]^2 + \gamma\right)^{\frac{1-N}{2N}}$, where $\dot{\varepsilon}^{\text{eq}}$ is defined in Equation (4.20). The force terms b_i are chosen to satisfy the momentum balance equation after substituting in the solutions v_1^*, v_2^*, and p^*, as given in [Worthen, 2012]. Dirichlet boundary conditions on velocity are obtained by applying Equation (46) along domain edges. In order to compare with the numerical study conducted in Section 3.3 of [Worthen et al., 2014], we employ P2-P1 (Taylor-Hood) elements and take the viscosity parameter $N = 3.5$. Starting with a 4×4 structured mesh over the unit domain Ω, we progressively refine the mesh by reducing the element size by half. For each mesh size we compute the L^2 error norms,

$$\varepsilon_{\boldsymbol{v}} = \sqrt{\frac{\sum_{k=1}^{\text{N}^{\text{P2}}} \left(||\boldsymbol{v}||_k - ||\boldsymbol{v}^*||_k\right)^2}{\sum_{k=1}^{\text{N}^{\text{P2}}} \left(||\boldsymbol{v}^*||_k\right)^2}}, \quad \varepsilon_p = \sqrt{\frac{\sum_{k=1}^{\text{N}^{\text{P1}}} \left(p_k - p_k^*\right)^2}{\sum_{k=1}^{\text{N}^{\text{P1}}} \left(p_k^*\right)^2}}, \tag{4.36}$$

for velocity magnitude and pressure, respectively, which are reported in Table H5. In the above equations, N^{P1} and N^{P2} are the number of nodes in the P2 and P1 spaces, respectively; and $||\boldsymbol{v}||_k$ and p_k are the velocity magnitude and pressure, respectively, at the k-th node. The $\varepsilon_{\boldsymbol{v}}$ and ε_p error norms decrease with quadratic convergence, which is consistent with the results reported in [Worthen et al., 2014]. A repeated study using P3-P1 elements showed similar convergence rates with smaller error norms for coarse meshes (not shown here), thus verifying the FEniCS implementation.

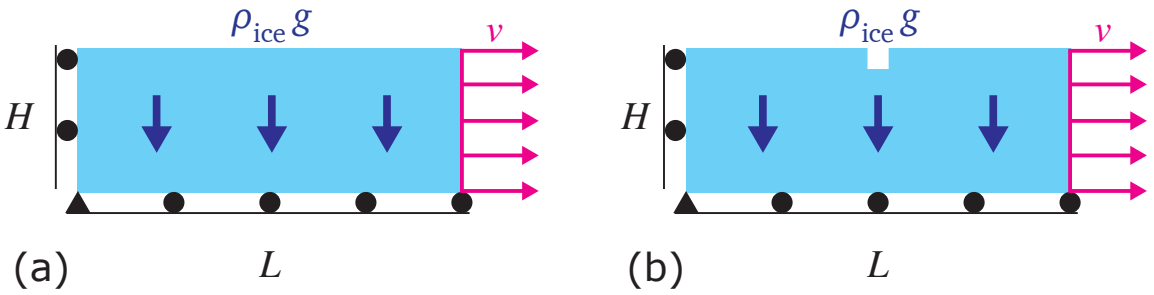

Figure 4.3: Domain setup including applied velocity v and gravitational body force $\rho_{\text{ice}}g$ with (a) no notch and (b) a 10 m $\times$ 10 m notch centered along the top surface of the slab. Domain height $H = 125$ m, length $L = 500$ m. The applied velocity $v = 0.5$ m/day and body force $\rho_{\text{ice}}g = (917\ \text{kg/m}^3 \times 9.81\ \text{m/s}^2)$.

4.4.2 Constant velocity creep flow

In this set of benchmark studies comparing the Stokes flow and Maxwell viscoelastic models, we simulate a standard creep test by disregarding gravity and prescribing a constant, uniform velocity $v = 0.5$ m/day on the right edge of the rectangular domain, as shown in Figure 4.3(a), so that the resulting strain rate of $1.157 \times 10^{-8}\ \text{s}^{-1}$ is on the order of the strain rates observed in real glaciers.

4.4.2.1 Glaciological stress predictions without damage

We first consider the case when damage is prescribed to be zero throughout the domain at all times. Both rheological models are simulated on structured finite element meshes with an element size $h = 5$ m. The results of this study are presented in Figure 4.4, wherein we plot the horizontal Cauchy stress σ_{11} predicted by each rheological model as a function of time. The viscoelastic model describes the time-dependent behavior, as shown in Figure 4.4(a), wherein stress σ_{11} gradually plateaus at 506 kPa over a short timespan ($t \approx$ 8 hours); whereas, the Stokes flow model describes the steady-state behavior, wherein the equilibrated stress $\sigma_{11} = 506$ kPa is established instantly. As shown in Figure 4.4(b), the value of σ_{11} decays (very slightly) over time in the updated-Lagrangian formulation of Stokes flow equations, because the mesh update scheme allows for the thinning of the ice

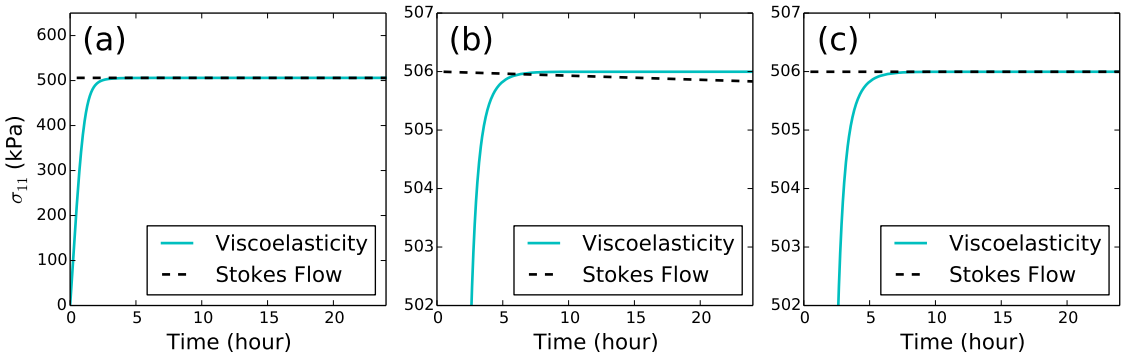

Figure 4.4: Results of the uniaxial creep test with constant strain-rate (or velocity) $v = 0.5$ m/day showing (a) horizontal Cauchy stress σ_{11} vs. time. The y-axis is scaled for a closer view of (b) σ_{11} vs. time when using the updated-Lagrangian mesh update scheme and (c) σ_{11} vs. time without the mesh update scheme.

slab with time as large viscous deformations extend the slab length. If the mesh update scheme was not implemented, then stress would not decay as displayed in Figure 4.4(c). Thus, this study verifies that for simple loading cases and in the absence of any damage, both the Stokes flow and Maxwell viscoelastic models describe the same constitutive behavior in the small deformation regime.

We now introduce a 10 m $\times$ 10 m notch at mid-length of the top surface of the rectangular domain, as shown in Figure 4.3(b), so as to study the effects of stress concentrations. The same velocity boundary conditions are specified as before, and gravity and damage are disregarded. Both rheological models are simulated on unstructured meshes that are highly refined around the notch with an element size $h = 0.25$ m. The field contour plot of the Hayhurst stress χ in the notched domain at time $t = 12$ hours predicted by the Stokes model is shown in Figures 4.5(a)–(b), which is in good qualitative agreement with that obtained from the viscoelastic model. In order to measure the quantitative differences between the stress fields predicted by the two rheological models, we consider the L^2 and L^∞ relative

error norms defined as

$$\varepsilon_{L^2} = \sqrt{\frac{\sum_{k=1}^{\mathrm{N^{IP}}} \left(\chi_k^{\mathrm{Abaqus}} - \chi_k^{\mathrm{interp}}\right)^2}{\sum_{k=1}^{\mathrm{N_{pts}}} \left(\chi_k^{\mathrm{Abaqus}}\right)^2}}, \tag{4.37}$$

$$\varepsilon_{L^\infty} = \frac{\max_k \left|\chi_k^{\mathrm{Abaqus}} - \chi_k^{\mathrm{interp}}\right|}{\max_k \left|\chi_k^{\mathrm{Abaqus}}\right|}, \tag{4.38}$$

where $\mathrm{N^{IP}}$ is the number of Abaqus integration points, χ_k^{Abaqus} is the Hayhurst stress at the k-th Abaqus integration point, and χ_k^{interp} is the Hayhurst stress interpolated from FEniCS nodes at the k-th Abaqus integration point.

The relative errors ε_{L^2} and ε_{L^∞} in Hayhurst stress χ versus time are plotted in Figure 4.5(c), wherein each measure of relative error shows a time-dependence because the stress fields predicted by the Maxwell viscoelastic model gradually increase from zero to the steady-state value, whereas in the Stokes model the steady-state stress is directly established based on the quasi-static assumption. It is evident from Figure 4.5(c) that ε_{L^2} decays quickly to about 3% after $t = 4$ hours, indicating that both rheological models predict approximately the same stresses in bulk regions of the domain; whereas, ε_{L^∞} decays to about 42%, suggesting that in the vicinity of the notch the two models predict substantially different stresses. However, this discrepancy is anticipated for at least two reasons: (1) in the Maxwell model both elastic and viscous strains are included, whereas in the Stokes model only viscous strains are considered; and (2) the Maxwell model considers compressible elasticity (Poisson's ratio $\nu = 0.35$), whereas the Stokes model enforces incompressibility. Based on this study, we suspect that the fracture behavior predicted by the two rheological models for ice would be different because the crack growth rate depends on the local differences in the Hayhurst stress, particularly in the vicinity of the notch.

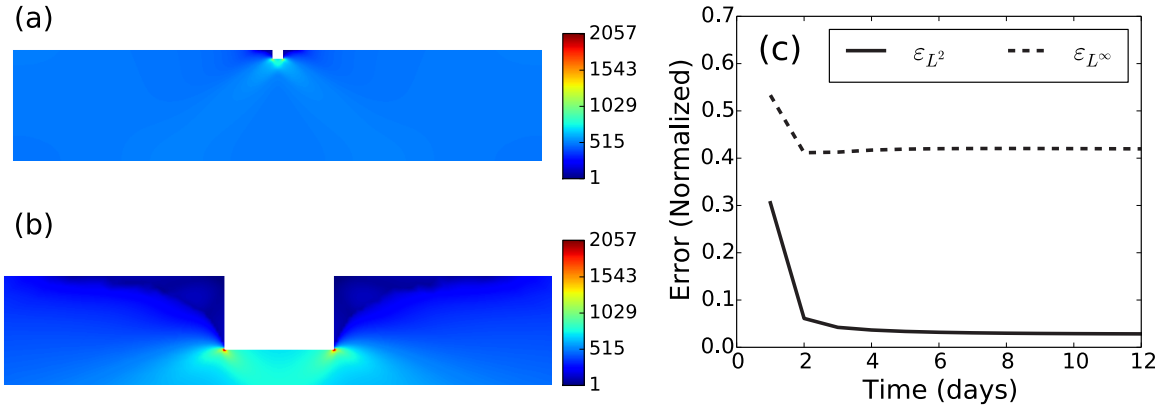

Figure 4.5: Hayhurst stress χ (in kPa) predicted by the Stokes flow rheological model for an ice slab with an applied creep velocity $v = 0.5$ m/day after 12 hours. Subfigure (a) shows χ over the whole domain; subfigure (b) shows a zoomed-in display of χ near the notch; and subfigure (c) displays the normalized errors ε_{L^2} and ε_{L^∞} (given by Eqs. 4.37 and 4.38, respectively) between viscoelastic and Stokes flow solutions for χ.

4.4.2.2 Mode I creep crack growth

In this section, we simulate and compare mode I creep fracture in ice predicted by the Maxwell viscoelastic and Stokes flow models using the nonlocal creep damage law detailed in Section 4.2.4. Additionally, we compare the Stokes model results obtained with and without the element removal scheme discussed in Section 4.3.2. We consider three metrics to compare creep fracture behavior across the different simulation studies: (1) the time required for crack tip damage initiation (i.e., when the first material point reaches $D = D^{\max}$); (2) the time for full crack penetration of the slab; and (3) the geometrical differences in damage (fracture) morphologies. We use the notched domain shown in Figure 4.3(b) with the same applied velocity and boundary conditions as in the previous study, and gravity is disregarded. To eliminate any discrepancies arising from the time-dependent strain evolution in the Maxwell viscoelastic model, we first allow the stresses to equilibrate by holding damage at zero for 12 hours and then let damage evolve. Crack growth using both rheological models is simulated on meshes that are structured around the notch and within the entire nonlocal damage zone with an element size $h = 2$ m; whereas, far from the notch and damage zone the mesh is unstructured with a maximum element size $h = 12.5$

m. The mode I crack (damage) growth results obtained from the simulations studies are shown in Figures 4.6 and 4.7.

Both Stokes flow and viscoelastic rheological models predict identical damage morphology, wherein the crack initiates beneath the notch and then propagates vertically towards the bottom of the ice slab; so we only show the Stokes flow result (without element removal) in Figure 4.6. The crevasse depth d (measured from the damage contour plots) is normalized by the domain height $H = 125$ m and plotted as a function of time for each simulation in Figure 4.7. The results in Figure 4.7(a) indicate that the crack tip damage initiation begins at 103.4 hours and 110.789 hours in the Maxwell viscoelastic model and Stokes flow model, respectively; thus, damage initiation occurs slightly earlier in the viscoelastic model. Full-depth crack penetration occurs at 108.97 and 122.6 hours for the viscoelastic and Stokes flow model, respectively; thus, the elapsed time between damage initiation and complete crack penetration is 5.57 and 11.811 hours. These discrepancies in crack growth behavior are anticipated (based on the previous study in Section 4.4.2.1), because the Hayhurst stress is larger at notch tip in comparison with that predicted by the Stokes model. Interestingly, we find that implementing the element removal scheme shows slight or no difference in the rate of damage growth compared with $D^{\max} = 0.97$ or 0.999. In Figure 4.7(b), we compare the implicit gradient and explicit integral damage approaches. The integral approach shows better agreement with the implicit gradient approach when using the Green's function to determine the nonlocal weights, because the Green's function is a weak solution to Equation (4.16) [Peerlings et al., 2001]. In Figure 4.7(c), we compare the results from P3-P1 and P2-P1 (Taylor-hood) mixed elements with that from the stabilized P1-P1 element (see the Appendix G for details on the stabilized formulation). We find that P3-P1 and P2-P1 elements predict identical crevasse growth rates; whereas, the stabilized P1-P1 element predicts a different result because the incompressibility condition is not well enforced, and consequently the Hayhurst stress under the crack tip is different. Finally, we conduct a mesh convergence study by progressively reducing the mesh size h

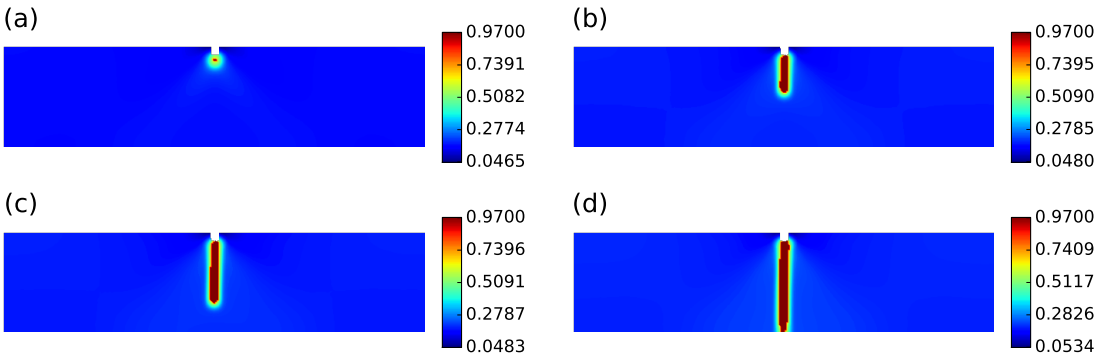

Figure 4.6: Crevasse propagation predicted by the Stokes flow rheological model for an ice slab with an applied creep velocity $v = 0.5$ m/day. The damage variable is shown at (a) 110.789 hours, (b) 119.114 hours, (c) 121.876 hours, and (d) 122.6 hours.

within the nonlocal damage zone. Figure 4.7(d) illustrates that we obtain reasonably consistent crack growth rates when taking an element size $h = 5, 2.5, 1.25$ m, so long as it is smaller than the characteristic length scale $l_c = 10$ m. In conclusion, this study indicates that Stokes flow and viscoelastic rheological models predict different damage initiation times and crack growth rates; however, it is important to note that the constant velocity creep flow is not representative of glacier deformation occurring due to gravity-induced flow.

4.4.3 Gravity-driven creep flow

For this next set of benchmark studies comparing the Stokes flow and Maxwell viscoelastic models, we simulate the gravity-driven creep test, wherein the rectangular slab of ice is deforming only due to its own self-weight, as shown in Figure 4.3(a), without any applied velocity at the right edge. Gravity loading is applied as a body force $b_2 = -\rho_{\text{ice}} g$ in the vertical dimension, where ρ_{ice} is the density of ice given in Table E1 and g is gravitational acceleration.

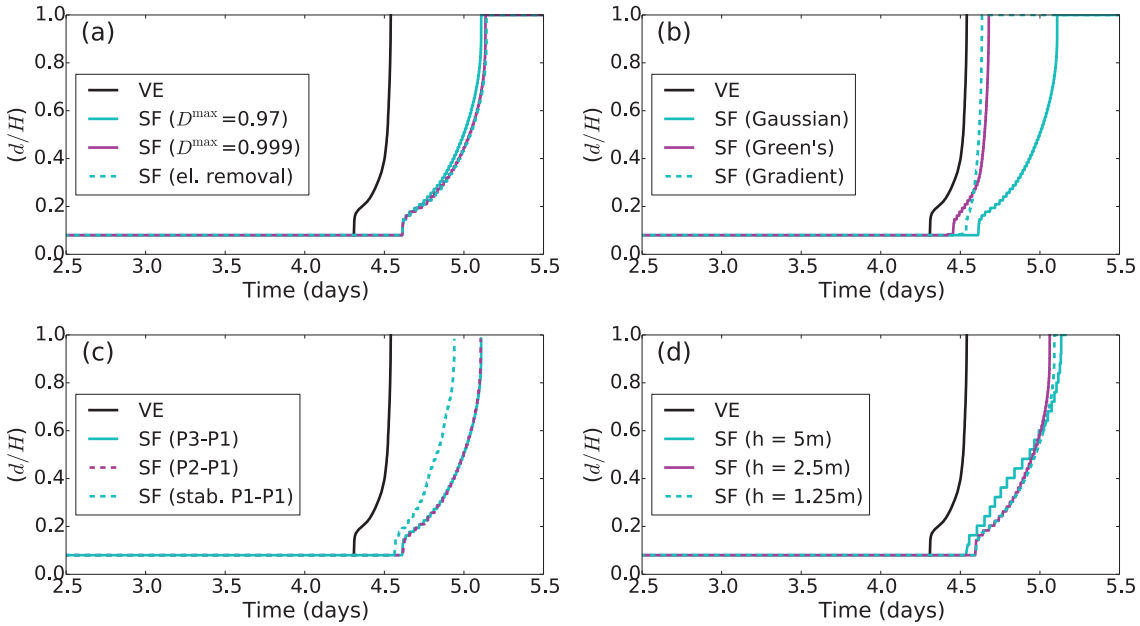

Figure 4.7: Crevasse depth (d) normalized with the domain height ($H = 125$ m) through an ice slab undergoing constant velocity creep flow, plotted as a function of time from 2.5 to 5.5 days. The abbreviations VE and SF refer to the viscoelastic and Stokes flow rheological models, respectively. Subfigure (a) shows a parametric study of $D^{\max}$ in order to compare between continuum damage and the element removal scheme. (Note that in all simulations we set $D^{\max} = 0.97$, except for the dashed magenta line Subfigure (a).) Subfigure (b) shows crevasse growth rates for the nonlocal integral using separate weighting functions (Gaussian and Green's function) and the implicit gradient damage scheme. Subfigure (c) shows the crevasse growth rate for different orders of interpolation for the velocity solution. Subfigure (d) presents a mesh size study wherein the element size h is progressively reduced in the nonlocal damage zone.

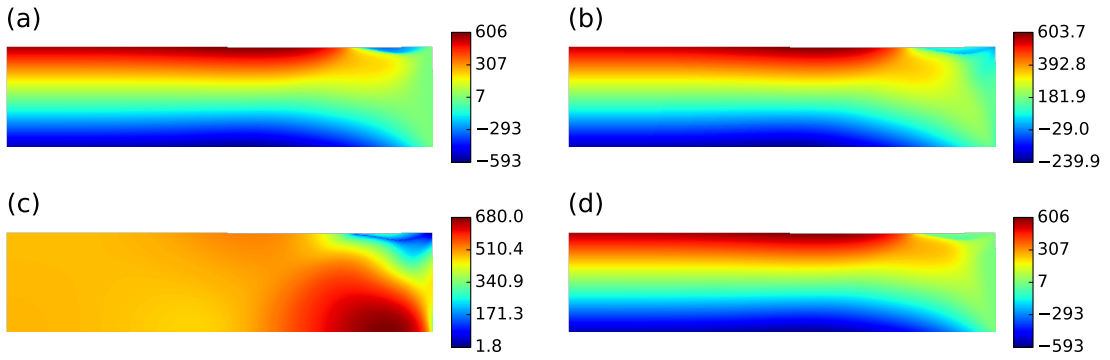

Figure 4.8: Stresses predicted by the Stokes flow rheological model for an ice slab under gravitational loading after 5 days. The stress components are: (a) horizontal Cauchy stress σ_{11}; (b) Hayhurst stress χ; (c) the von Mises stress σ^{v}; and (d) the max principal stress $\sigma^{(\mathrm{I})}$. All units are in kPa.

4.4.3.1 Glaciological stress predictions without damage

We first consider the case when damage is prescribed to be zero throughout the domain at all times. Both rheological models are simulated on unstructured meshes that are generated by specifying element sizes $h = 10$ m and $h = 2$ m on the left and right domain edges, respectively. We use a finer mesh resolution near the right edge (representing the glacier terminus) in order to accurately capture the stresses induced by warping (distortion). The contour plots of the horizontal Cauchy stress σ_{11} and stress invariants predicted by Stokes model are shown in Figure 4.8. Near the left edge of the domain the horizontal Cauchy stress σ_{11} is uniform in the horizontal direction with tension on the top and compression at the bottom and is qualitatively similar to the Hayhurst stress χ and the max principal stress $\sigma^{(\mathrm{I})}$, as evident from Figure 4.8; however, near the right edge the normal stress σ_{11} is much smaller and the shear stress σ_{12} much larger than elsewhere in the domain, as reflected in the von Mises stress plots in Figure 4.8(c). These large shear stresses near the right edge cause warping and even small compressive stresses at the upper-right corner. All the contour plots of stress and its invariants predicted from the Maxwell viscoelastic model look very similar those predicted by the Stokes model, so they are not shown here.

To measure the quantitative differences between the Stokes flow and Maxwell viscoelastic models, we consider two metrics: (1) errors (differences to be precise) in stress fields and their time evolution; and (2) time evolution of the displacement at the right edge of the domain (signifying the glacier terminus). We plot the relative error norms ε_{L^2} and ε_{L^∞} defined in Equations 4.37 and 4.38, respectively, for the Hayhurst stress χ versus time in Figures 4.9(a) and 4.9(c) over the short and long timescales, respectively. The two error measures show a time dependency due to the differences in the Maxwell viscoelastic and the viscous Stokes models, as explained in Section 4.4.2.1. Over the short timescale (i.e., up till five days), the ε_{L^2} error is consistently low ($< 3\%$), indicating good agreement between the two rheological models in the bulk domain; however, ε_{L^∞} is substantially high ($\approx 23\%$) and mainly arises from the discrepancies in stress distribution at locations near the upper-right corner of the domain. Over the long timescale (i.e., after 6 months), ε_{L^2} and ε_{L^∞} gradually increase to 27% and 70%, respectively; this happens because the stress predicted (under gravity loading) by the updated-Lagrangian Stokes flow formulation will slowly decay over time as the geometry of the slab changes (i.e., the slabs becomes thinner in the vertical direction, which reduces the over-burden pressure at the glacier bottom). The maximum creep displacement of the ice slab predicted by the viscoelastic and Stokes models, plotted in Figures 4.9(b) and 4.9(d), show excellent agreement during the first five days; however, after several months the Stokes model predicts a slower rate of creep flow. This study illustrates that in idealized rectangular glaciers without defects or notches both rheological models describe the same constitutive behavior (similar stress fields and maximum creep displacement) only over the short timescale, even though ε_{L^∞} in stress fields is considerably large near the right edge (terminus). In conclusion, the long time behavior predicted by the updated-Lagrangian Stokes formulation is more physical than that predicted by the total Lagrangian viscoelastic model.

We now consider a 10 m $\times$ 10 m notch at mid-length of the top surface of the rectangular domain subjected to gravity-driven creep flow, as shown in Figure 4.3(b), so as to

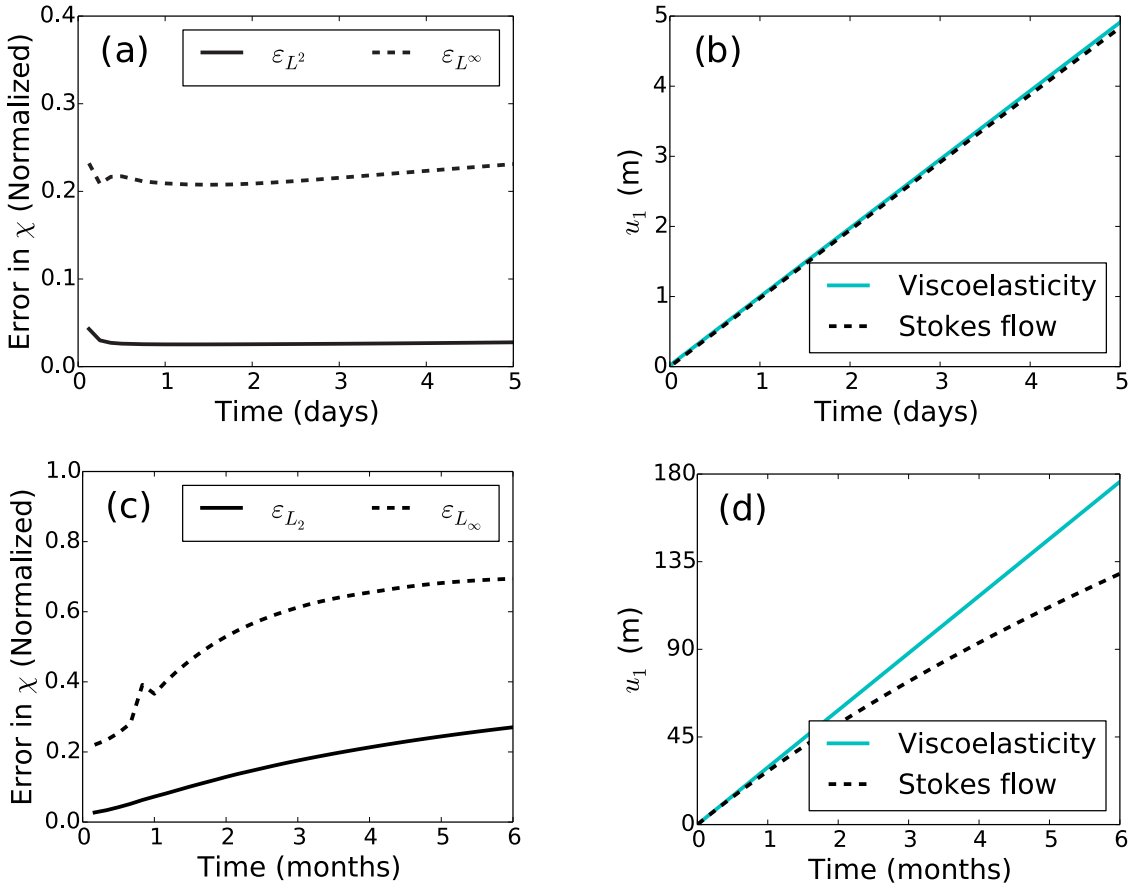

Figure 4.9: Viscoelastic and Stokes flow model predictions for gravity-driven creep flow. Subfigures (a) and (c) show the normalized errors ε_{L^2} and ε_{L^∞} (given by Eqs. 4.37 and 4.38, respectively) between viscoelastic and Stokes flow results for the Hayhurst stress χ. Subfigures (b) and (d) show the maximum horizontal displacement u_1 of the ice slab from both models.

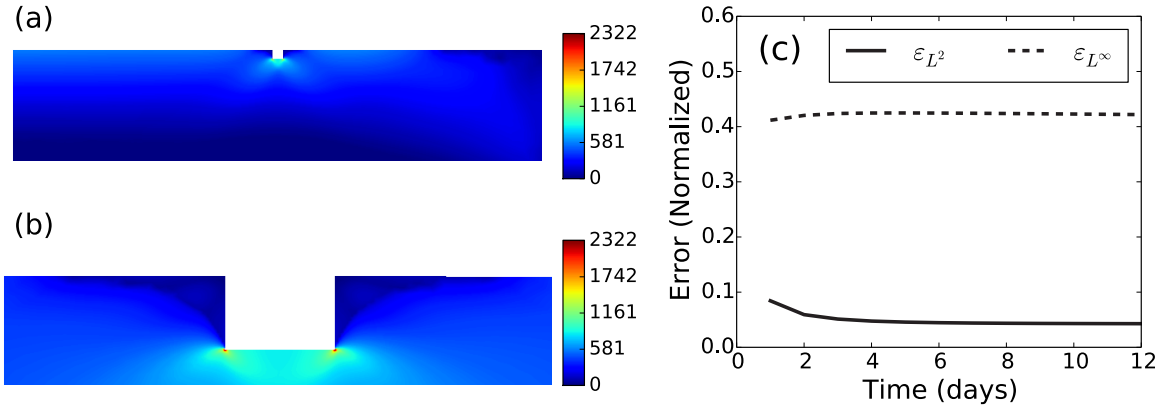

Figure 4.10: Hayhurst stress χ (in kPa) predicted by the Stokes flow rheological model for an ice slab under gravitational loading after 12 hours. Subfigure (a) shows χ over the whole domain; subfigure (b) a zoomed-in display of χ near the notch; and subfigure (c) displays the normalized errors ε_{L^2} and ε_{L^∞} between viscoelastic and Stokes flow solutions for χ.

study the effects of stress concentrations. Both rheological models are simulated on unstructured meshes that are highly refined around the notch with an element size $h = 0.25$ m. The field contour plot of the Hayhurst stress χ in the notched domain at time $t = 12$ hours predicted by the Stokes model is shown in Figures 4.10(a)–(b), which is in good qualitative agreement with that obtained from the viscoelastic model. The notch corners introduce stress concentrations (singularities, to be precise), as evident form Figure 4.10(b). The relative errors ε_{L^2} and ε_{L^∞} for the Hayhurst stress χ as defined in Equations (4.37) and (4.38), respectively, are shown in Figure 4.10(c). While the ε_{L^2} error is consistently low ($< 5\%$ for $t > 4$ hours), ε_{L^∞} is substantially large ($\approx 42\%$); this discrepancy arises not only from differences in the magnitude, but also in the spatial distribution of stress around the notch corners. An important detail to note is that we use an extremely fine mesh resolution ($h = 0.25$ m) to compare the stresses near the notch tip, whereas during damage growth simulations we take the mesh resolution to be reasonably coarse ($h = 2$ m). However, we observed the same trends in ε_{L^2} and ε_{L^∞} even in the coarser meshes.

4.4.3.2 Crevasse propagation under gravity-driven creep flow

We now simulate crevasse propagation in an idealized rectangular glacier under gravitational loading by employing the nonlocal continuum damage law presented in Section 4.2.4 in conjunction with the viscoelastic and Stokes flow rheological models. In all the following simulations, we disregarded the body force due to self-weight of ice in fully damaged zones by incorporating Equation (4.24) into the Stokes equations, which allows us to perform the simulations for the entire duration of crevasse propagation without excessive mesh distortion. Through numerical studies, we demonstrate that incorporating $\psi(D)$ is equivalent to implementing the element removal procedure discussed in Section 4.3.2. As before, we consider three metrics for comparing fracture behavior across the different simulation studies: (1) the time required for crack tip damage initiation (i.e., when the first material point reaches $D = D^{\max}$); (2) the time for full crack penetration of the slab; and (3) the geometrical differences in damage (fracture) morphologies. We use the notched domain shown in Figure 4.3(b) with the same boundary conditions as specified previously for gravity-driven creep flow. To eliminate any discrepancies arising from the time-dependent strain evolution in the Maxwell viscoelastic model, we first allow the stresses to reach steady-state by holding damage at zero for 12 hours and then letting damage evolve. Crack growth in both rheological models is simulated on coarser meshes that are structured around the notch and within the entire nonlocal damage zone with an element size $h = 2$ m; whereas, far from the notch and the damage zone the mesh is unstructured with a maximum element size $h = 12.5$ m. A mesh size study is also performed by varying the element size h within the nonlocal damage zone to demonstrate that the formulation predicts the same crevasse growth, so long as h is smaller than the nonlocal characteristic length scale l_c.

The crevasse growth results obtained from the simulation studies are shown in Figures 4.11 and 4.12. Both Stokes flow (with and without element removal) and viscoelastic rheological models predict identical damage morphology, wherein the crack initiates be-

neath the notch and then propagates vertically towards the bottom of the ice slab; so we only show the Stokes flow result (without element removal) as shown in Figure 4.11. The crevasse depth d is normalized by the domain height $H = 125$ m and plotted as a function of time for each simulation in Figure 4.12. These results indicate that the crack tip damage initiation begins at 107.5 hours and 112.528 hours in the Maxwell viscoelastic model and Stokes flow model, respectively. The Stokes flow model using the updated-Lagrangian Stokes formulation predicts that the crevasse penetrates 69% of the ice slab depth without element removal; whereas, the total Lagrangian Maxwell viscoelastic formulation predicts that the crevasse penetrates 72% of the slab depth. From Figure 4.12(a), it is apparent that the damage control strategy with $D^{\max} = 0.999$ gives consistent results compared to the element removal scheme, wherein the crevasse penetrates to 79% of the slab depth. Figure 4.12(b) indicates that the implicit gradient damage approach predicts faster crack tip damage initiation and crevasse growth rate; although, it predicts the same final crevasse depth as the nonlocal integral approach. However, if we consider a Green's function based weighting function, the explicit integral approach shows excellent agreement with the implicit gradient approach, because the Green's function is a weak solution to Equation (4.16) [Peerlings et al., 2001]. In Figure 4.12(c), we plot the crevasse depth versus time predicted by different order finite element approximations, including the commonly used P2-P1 (Taylor-Hood) element and a stabilized P1-P1 element. The P3-P1 and P2-P1 elements yield consistent results; whereas, the stabilized P1-P1 element predicts a different crack growth rate and final crevasse depth. This occurs because the stabilized P1-P1 does not well enforce the incompressibility constraint, which affects the Hayhurst stress around the crack tip. Finally, in Figure 4.12(d) we perform a mesh size study by progressively reducing the mesh size in the damage zone. Results indicate that the formulation predicts consistent damage evolution when taking an element size $h = 5, 2.5, 1.25$ m smaller than the characteristic length scale $l_c = 10$ m. Based on this study we arrive at the conclusion that the Stokes flow formulation is more appropriate than the viscoelastic

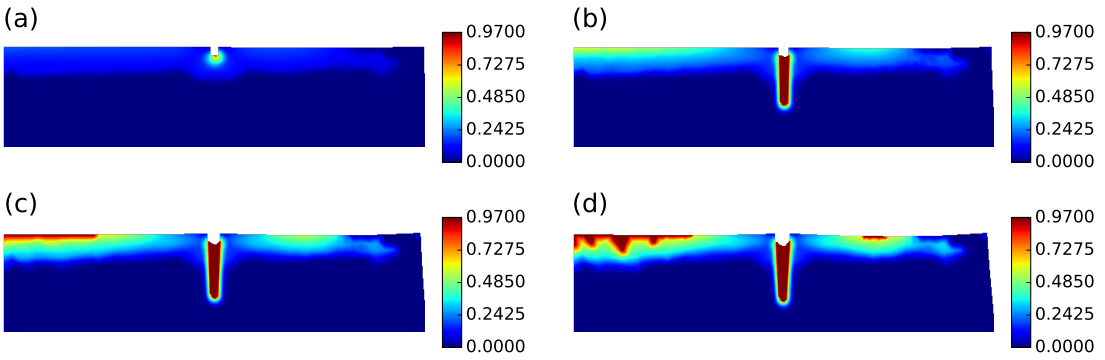

Figure 4.11: Crevasse propagation predicted by the Stokes flow rheological model for an ice slab under gravitational loading. The damage variable is shown at (a) crack tip damage initiation at 112.528 hours, (b) 10 days, (c) 15 days, and (d) 20 days.

formulation, because while both predict the same equilibrium crevasse depth over short time scales (3.4% difference is insignificant from glaciological standpoint), the former approach is more accurate over long timescales as it accounts for large deformation induced geometry changes.

4.4.4 Crevasse propagation in 3D

In this section, we extend the updated-Lagrangian formulation to simulate crevasse propagation in ice sheets in three dimensions (3D). The 3D implementation is verified using simple benchmark tests, wherein we compare the crevasse propagation induced by constant creep velocity and gravity driven flow predicted in 2D and 3D. Due to the enormity of 3D problems and the computational expense, we run the 3D simulations using parallel processing. We utilize the implicit gradient to incorporate nonlocality in damage, since the nonlocal integral technique would present problems when trying to access the nonlocal weights of material points between neighboring mesh partitions.

For each 2D simulation, we consider a rectangular domain of ice with length $L = 500$ m in the x_1 dimension and height $H = 125$ m in the x_2 dimension, and the mesh is refined around the anticipated damage zone with an element size of 5 m. A 10×10 m notch is cen-

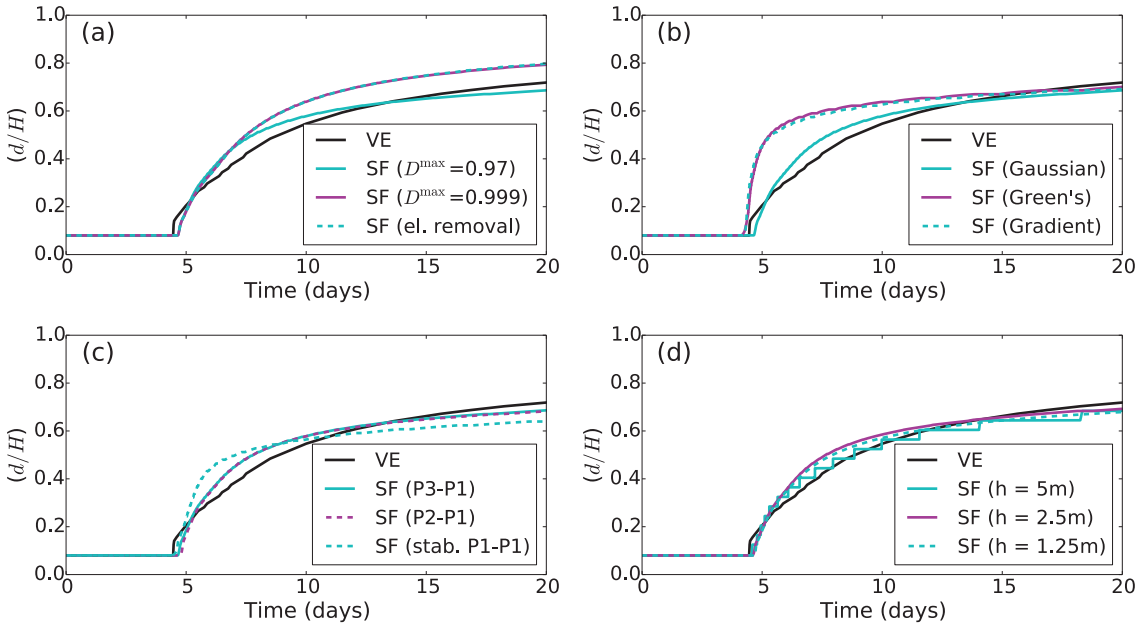

Figure 4.12: Crevasse depth (d) normalized with the domain height ($H = 125$ m) plotted as a function of time over 20 days. The abbreviations VE and SF refer to the viscoelastic and Stokes flow rheological models, respectively. Subfigure (a) shows a parametric study of $D^{\max}$ in order to compare between continuum damage and the element removal scheme. (Note that in all simulations we set $D^{\max} = 0.97$, except for the dashed magenta line Subfigure (a).) Subfigure (b) shows crevasse growth rates for the nonlocal integral using separate weighting functions (Gaussian and Green's function) and the implicit gradient damage scheme. Subfigure (c) shows the crevasse growth rate for different orders of interpolation for the velocity solution. Subfigure (d) presents a mesh size study wherein the element size h is progressively reduced in the nonlocal damage zone.

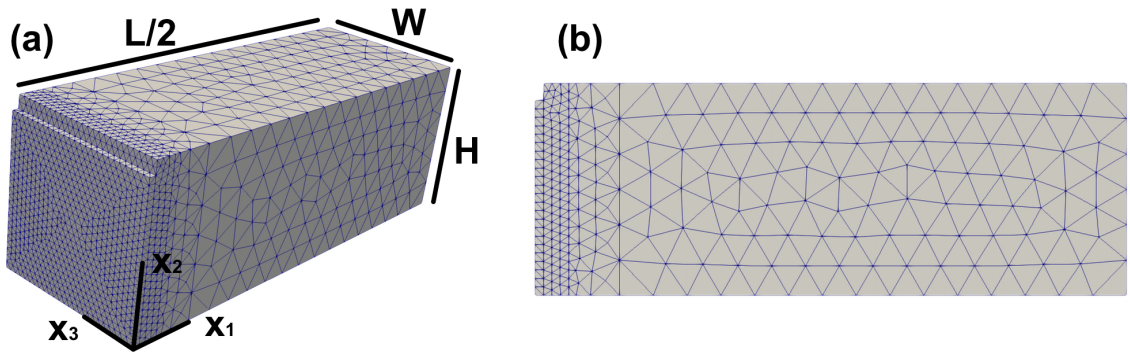

Figure 4.13: Illustration of the undeformed (a) 3D mesh and (b) 2D mesh.

tered along the top edge of the domain. For each 3D simulation, we assume a rectangular prism with length $L = 500$ m in the x_1 dimension, height $H = 125$ m in the x_2 dimension, and depth $W = 125$ m in the x_3 dimension. A $10 \times 10 \times 125$ m notch is centered along the top surface and cuts through the entire domain in the x_3 dimension. Due to the symmetry in both 2D and 3D domains, we only mesh half of the domain and apply symmetry boundary conditions to the plane intersecting the midpoint (i.e., $x_1 = L/2$) and whose normal vector is $\hat{e}_1$. An illustration of the undeformed 3D mesh is depicted in Figure 4.13.

4.4.4.1 Mode I creep crack growth in 3D

We first verify the 3D implementation by performing a constant creep velocity benchmark experiment. For this problem, we simulate a stand creep test by disregarding gravity and prescribing a constant, uniform velocity $v = 0.5$ m/day in the x_1 direction. In the 2D problem, we apply the velocity to the right edge of the rectangular domain; whereas in the 3D problem, we apply the velocity to the right surface (i.e., the plane intersecting the point $x_1 = L$ whose normal vector is $\hat{e}_1$). Free slip boundary conditions are applied to the bottom edge and bottom surface in the 2D and 3D domains, respectively, to restrain vertical movement. We also apply a symmetry boundary condition along the plane of symmetry (i.e., the plane intersecting the midpoint $x_1 = L/2$ and whose normal vector is $\hat{e}_1$) by restricting movement in the x_1 dimension. Finally, to be consistent with the plane strain assumption

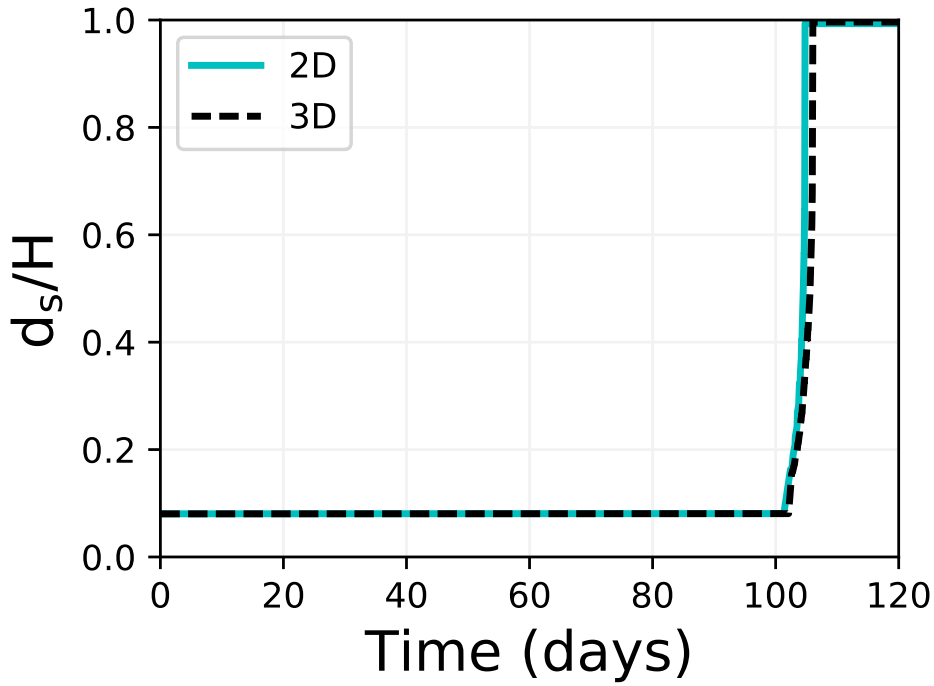

Figure 4.14: Surface crevasse depth (d_s) normalized with the domain height ($H = 125$ m) plotted as a function of time over 120 hours using the by the 2D and 3D updated-Lagrangian implementations.

made in 2D, we apply boundary conditions to prevent movement in the x_3 dimension along the "front" and "back" surfaces (i.e., the planes intersecting the points $x_3 = 0$ and $x_3 = W$ whose normal vectors are $\hat{e}_3$). The results of this study are shown in Figure 4.14, wherein we plot the normalized surface crevasse depth d_s/H versus time for five days. Both the 2D and 3D implementations predict crack tip damage initiation at time $t \approx 103$ hours, after which the crevasse rapidly penetrates through the full depth of the slab. This consistency verifies that the 3D model formulation is properly implemented and is applicable to more general problems.

4.4.4.2 Crevasse propagation under gravity-driven creep flow in 3d

We next verify the 3D implementation by performing a gravity-driven flow benchmark experiment. For this problem, we apply gravity as a body force $\rho_i \boldsymbol{g}$ where ρ_i is the density of ice and $\boldsymbol{g}$ is the acceleration due to gravity, whose only nonzero component acts in the

x_2 dimension. Free slip boundary conditions are applied to the bottom edge and bottom surface in the 2D and 3D domains, respectively, to restrain vertical movement. We also apply a symmetry boundary condition along the plane of symmetry (i.e., the plane intersecting the midpoint $x_1 = L/2$ and whose normal vector is $\hat{e}_1$) by restricting movement in the x_1 dimension. Finally, to be consistent with the plane strain assumption made in 2D, we apply boundary conditions to prevent movement in the x_3 dimension along the "front" and "back" surfaces (i.e., the planes intersecting the points $x_3 = 0$ and $x_3 = W$ whose normal vectors are $\hat{e}_3$). The results of this study are shown in Figure 4.15, wherein we plot the normalized surface crevasse depth d_s/H versus time for one month. Both the 2D and 3D implementations predict crack tip damage initiation at approximately one week. Afterward, the crevasses in the 2D and 3D domains penetrate to 72% and 70% of the slab depth, respectively, with the 2D crevasse propagating slightly faster. An image of the final 3D damage contour is provided in Figure 4.16. Overall, the 2D and 3D model formulations predict consistent crevasse evolution, thus verifying the 3D implementation and demonstrating its applicability to more general problems.

4.4.5 Discussion

The important observations and findings of this study are summarized below:

i. The gravity-driven flow is a varying body-force-controlled experiment, whereas the constant velocity creep flow is a displacement-controlled experiment; consequently we observe different crack growth behavior in both experiments, as evident from Figures 4.7 and 4.12. The constant velocity creep flow is a good benchmark test to study the differences between Stokes and viscoelastic models, although it has little physical relevance to glacier and ice sheet flow.

ii. Under gravity-driven flow, as damage begins to accumulate under the notch, the stress is redistributed within the damage zone; consequently, the crevasse growth rate

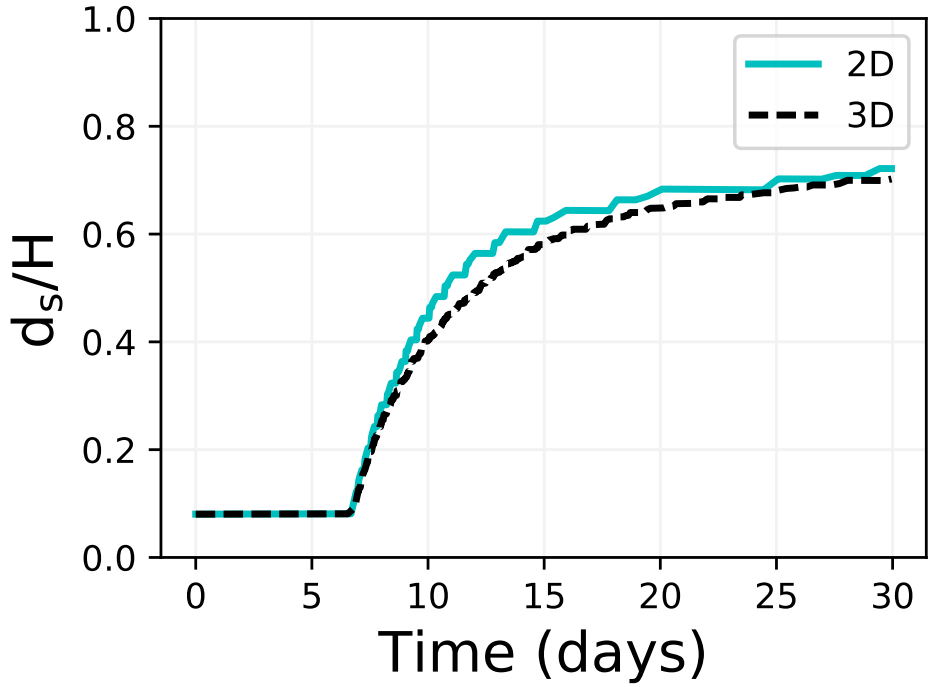

Figure 4.15: Surface crevasse depth (d_s) normalized with the domain height ($H = 125$ m) plotted as a function of time over 30 days using the by the 2D and 3D updated-Lagrangian implementations.

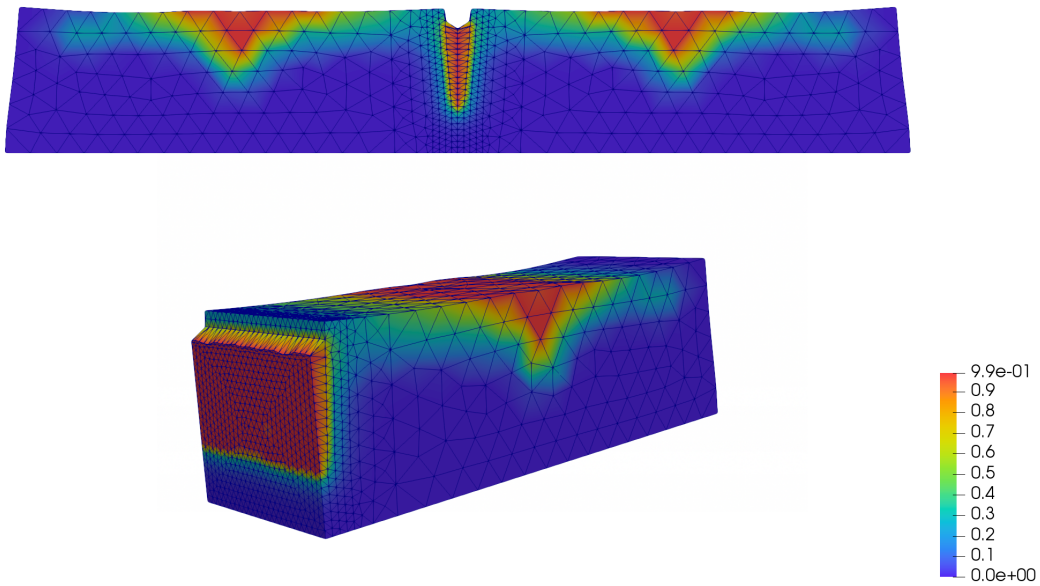

Figure 4.16: Damage contour after 30 days of gravity-driven flow in a 3D body. The red regions indicate fully damaged material (i.e., $D = D^{\max}$), whereas the blue regions indicate intact ice (i.e., $D \approx 0$).

curves from both Stokes and viscoelastic model predictions are in reasonably close agreement, with less than 3.4% error in final crevasse depths over shorter timescales. Noting that the final crevasse depth is a critical factor indicative of the stability of ice sheets, we can conclude that one may neglect the contribution of elastic (stress concentration) effects and only account for nonlinear viscous flow to simulate crevasse propagation.

iii. Under gravity-driven flow, surface crevasses do not propagate the full depth of the slab (i.e., normalized crevasse depth $d/H < 1$ after 20 days), unlike under constant velocity creep flow ($d/H = 1$ after 5 days); this is because the Hayhurst stress near the crack tip decreases as the crack grows longer. From our simulations, we observe that as the crevasse penetrates deeper the velocity gradients across the depth becomes smaller, leading to the progressive reduction in glaciological stress and crack growth rate with time. Thus, surface crevasse propagation under dry conditions (i.e., no hydraulic fracture) remains a quasi-static process, especially during the final stages, wherein the crevasse depth reaches its final (steady-state) depth, as evident from Figure 4.12. Therefore, inertial terms need not be included in the current quasi-static fracture simulation study.

iv. The value of the damage parameter $\hat{B}$ in Table 5.2 was calibrated from experiments on laboratory grown virgin ice using the Maxwell viscoelastic model in [Duddu and Waisman, 2012], which may be an order of magnitude larger than that corresponding to glacier ice. In our recent work [Mobasher et al., 2016], we show that the value $\hat{B}$ only affects crevasse growth rate but not the final (steady-state) crevasse depth; therefore, the conclusions related to surface crevasse depths and the stability of ice sheets remain valid.

v. From Figure 4.9, it is evident that the Stokes and viscoelastic models predict different physical behavior as large deformations accrue over longer time scales, and the

updated-Lagrangian formulation accounting for domain geometry changes is more appropriate than the total Lagrangian formulation. However, in order to conduct a physically accurate ice sheet flow and fracture simulation over long decadal time scales, one needs to account for mass inflow and outflow along with crack propagation and healing, which will be considered in our future research.

The overall conclusion of this study is that the updated-Lagrangian Stokes formulation is appropriate for studying gravity-flow induced glacier deformation and fracture even over short time scales, despite ignoring the elastic stress concentration effects. Furthermore, over long decadal timescales the proposed formulation would be more appropriate as it accounts for the geometry changes of the domain, when large deformations accrue over time.

4.5 Conclusion

We developed an updated-Lagrangian mixed finite element formulation based on the nonlinear Stokes flow equations and a nonlocal creep damage law to simulate crevasse propagation in glaciers. The main features of this new formulation are: (1) the updated-Lagrangian approach that enables us to track the geometry changes in the domain dynamically using an explicit mesh-update procedure and the evolution of continuum damage at material points, without needing to include the damage advection; (2) the nonlocal gradient and integral implementations of damage that alleviate the mesh sensitivity issues inherent to local damage models; (3) the higher-order mixed finite element discretization of the Stokes equations that eliminate "checkerboard" instabilities in pressure and allow accurate and efficient computation of stress and damage fields; and (4) the automated damage controls and element removal scheme that allow us to represent fully damaged material without introducing rank deficiencies to the finite element stiffness matrix. The formulation was verified against manufactured Stokes solutions and compared with the experimentally validated small-deformation Maxwell viscoelastic model through benchmark studies. Numerical simulations performed on idealized rectangular domains demonstrate that the Stokes flow model is suitable for simulating flow and fracture in ice as it is consistent with the Maxwell-type viscoelastic model over the shorter time scales of crevasse propagation (i.e., $t = 5$ - 20 days) under gravity-induced flow. Over long decadal time scales, we expect that the proposed update-Lagrangian approach is superior to the small-deformation total Lagrangian approach due to its ability to account for large deformations. Other interesting findings from the simulation studies are: (1) the P2-P1 (Taylor-Hood) element is about as accurate as the P3-P1 element, and so it is preferable because it is computationally less expensive; whereas, the classical stabilized P1-P1 element is not as accurate; (2) the gradient damage approach predicts faster damage initiation times and crack growth rates and narrower damage zone widths compared to the Gaussian function based integral damage approach, but it is consistent with the Green's function based integral damage approach;

(3) the element removal scheme simulating crack opening is consistent with the damage control strategy for $D^{\max} = 0.999$ upon the introduction of the ψ function that relaxes the incompressibility constraint and voids the density in damage zones. Our future work will involve using the proposed formulation together with parallel computing to simulate large scale problems, such as crevasse propagation in land ice sheets with realistic geometries and boundary conditions and iceberg calving from Antarctic ice shelves.

Acknowledgements

We gratefully acknowledge the funding support provided by the National Science Foundation's Office of Polar Programs via grants #PLR-1341428 and #PLR-1341568. We would like to thank Prof. Georg Stadler at New York University for the helpful discussions on nonlinear Stokes solvers and Prof. Kalyanababu Nakshathrala at University of Houston for the insightful discussions on stabilized mixed finite element formulations.

CHAPTER 5

DAMAGE MECHANICS APPROACH TO WATER-FILLED SURFACE CREVASSE PROPAGATION IN GLACIERS

5.1 Introduction

Crevasses are opening fractures in glaciers formed under the action of tensile stress. The full depth propagation of crevasses close the terminus of a glacier leads to iceberg calving, which is a dominant mode of mass loss from both the Greenland and Antarctic ice sheets. A major hurdle to parametrizing iceberg calving in numerical ice sheet models is that the underlying fracture mechanisms are extremely complex, involving mechanical, thermal, and hydraulic processes across multiple length and time scales. To parametrize calving appropriately it is important to describe both the position of the calving front in relation to ice thickness and seawater depth at the terminus as well as the calving rate determined by the speed of the glacier and the presence of meltwater in the crevasses [van der Veen, 1996]. Empirical calving laws based on water depth or ice thickness at the glacier terminus [Brown et al., 1982, Meier et al., 1994] do not explain the changes in calving rate in summer and winter months; whereas, fracture mechanics based calving laws [Weertman, 1973, van der Veen, 1998a, Nick et al., 2010a, Krug et al., 2014] that account for physical factors, such as mechanical stress and hydrofracture, can explain such seasonal changes in calving rates. With the recent emergence of creep damage mechanics models for simulating crevasse propagation [Pralong and Funk, 2005, Duddu et al., 2013] and the possibility of incorporating them in shallow shelf ice sheet models [Keller and Hutter, 2014a], an outstanding question is: *How do the crevasse penetration depths predicted by creep damage models* (assuming the gradual growth of micro-cracks into diffused macro-cracks) *compare against existing fracture mechanics models* (considering the abrupt growth

of sharp macro-cracks)? To address this question, we perform a comprehensive investigation comparing four existing fracture mechanics models for the propagation of water-filled surface crevasses in glaciers against the creep damage mechanics model for hydraulic fracture [Mobasher et al., 2016] implemented within a nonlinear full Stokes finite element formulation [Jiménez et al., 2017].

Typically, tidewater glaciers (where the terminus remains grounded) calve smaller icebergs with a characteristic size comparable to or less than the ice thickness [Bassis, 2011]. This calving behavior of tidewater glaciers is much different from that observed in freely floating ice shelves or ice tongues. Empirical calving models based on water depth and height-above-buouyancy [Meier and Post, 1987, van der Veen, 1996, 2002, Nick et al., 2007, 2009] describe the calving behavior of tidewater glaciers to a reasonable extent, but lack a mechanistic basis despite significant efforts [Benn et al., 2007b]. The fracture mechanics models hypothesize that crevasse propagation is dominated by the opening of brittle cracks in ice due to tensile stress, which is well supported by experimental observations [Rist et al., 1996, 1999]. The fracture mechanics models account for the tensile stress generated by both the extensional flow of glaciers and the hydrostatic pressure in water-filled crevasses, and calving is assumed to occur when the combination of surface and basal crevasses becomes equal to the ice thickness. In this chapter, we will investigate four fracture mechanics models for crevasse propagation applied to grounded glaciers: (1) the Nye (zero-stress) model [Nye, 1955, 1957]; (2) the Weertman (dislocation-based fracture mechanics) model [Weertman, 1971, 1973]; (3) the van der Veen (linear elastic fracture mechanics) model [van der Veen, 1998a,b]; and (4) the Krug (linear elastic fracture mechanics) model [Krug et al., 2014]. The main assumption behind fracture mechanics models is that the crevasse is a sharp interface (i.e., mathematical displacement discontinuity) and stress near the crevasse tip is unbounded (i.e., mathematical stress singularity), except for the Nye model. Furthermore, fracture mechanics models require the assumption of a pre-crack to determine if a crack would propagate and inherently cannot describe crack

initiation (except for the Nye model). A detailed review of these four models, including the underlying assumptions, salient model equations, and crevasse depth predictions is given in Section 5.2.

In contrast to the hypothesis of fracture mechanics models for iceberg calving, we argue that calving is a complex multi-scale and multi-physics creep fracture process [Mobasher et al., 2016]. For quasi-brittle materials such as concrete or ice that exhibit strain-softening, these assumptions of fracture mechanics models may not be appropriate as there is substantial micro-cracking within the fracture process zone, which is described by nonlocal damage theory [Pijaudier-Cabot and Bazant, 1987a, Bazant, 1994]. In fact, the multi-scale nature of the ice fracture is attributed to a bewildering variety of deformation and damage mechanisms at various length scales ranging from localized micro-scale (or milli-scale) cracks [Weertman, 1983, Hammonds and Baker, 2017] to rifts that exceed hundreds of kilometers [Larour et al., 2004, Bassis et al., 2008, Walker et al., 2013, Albrecht and Levermann, 2014]. The multi-physics nature of the process is due to both mechanical and thermal phenomena governed by gravity-induced viscous flow, hydraulic fracture, ocean forcing, and phase transformation due to melting and refreezing of ice. Furthermore, the complexity and diversity of calving patterns in glaciers is strongly linked to geometry [Bassis and Jacobs, 2013]. A "universal" calving model must account for this complexity in a feasible yet physically-consistent manner; however, the theoretical fracture mechanics models assuming linear elasticity, small strains and/or idealized geometries and far-field boundary conditions may be oversimplified. While calving is linked to brittle fracture of linear elastic ice over shorter time scales [Rist et al., 1999, van der Veen, 1998a,b], over longer times scales glacier and ice sheet flow is well described by a viscous creep constitutive law known as Glen's law [Glen, 1955, Cuffey and Paterson, 2010]. Therefore, to model calving in real-world glaciers and ice shelves, researchers have recently attempted to incorporate fracture mechanics into numerical ice sheet models based on the assumption that ice flow is governed by its incompressible, nonlinear viscous rheology [Sun et al., 2017,

Yu et al., 2017]. Although these numerical models overcome the limitations of purely theoretical models, they present other computational challenges; for example, the algorithms for evolving fractures can be cumbersome or *ad hoc* [Sun et al., 2017] and cannot account for subcritical damage growth [Yu et al., 2017].

An alternative approach to modeling calving within numerical ice flow models involves the use of continuum damage mechanics (CDM) [Pralong and Funk, 2005, Pralong et al., 2006, Duddu and Waisman, 2012, 2013c, Duddu et al., 2013, Mobasher et al., 2016, Jiménez et al., 2017], which offers certain advantages. First, CDM is easily incorporated into numerical models without requiring complicated algorithms for tracking the propagation of fractures. Second, CDM can model fracture initiation and propagation without requiring the presence of a pre-crack (i.e., subcritical damage), unlike theoretical fracture mechanics models (except for the Nye model). Pralong and Funk [2005] were the first to simulate creep damage in ice using an incompressible, nonlinearly viscous Stokes rheology. Duddu and Waisman [2013c] developed a nonlocal creep damage model for modeling crevasse propagation with thermodynamic consistency. Keller and Hutter [2014a] have further explored the plausibility of incorporating creep damage models into shallow shelf approximations. There are some concerns expressed about the formulation of damage mechanics models [Gagliardini et al., 2013], which we have addressed in a response article [Duddu and Waisman, 2013b]. Recently, Krug et al. [2014] combined damage mechanics with fracture mechanics, but damage mechanics is a stand-alone numerical technique for both dynamic and quasi-static fracture propagation in both quasi-brittle elasto-plastic [de Borst et al., 1995, Miehe et al., 2015] and viscoelastic materials [Murakami, 1983, Schapery, 1999, Lyakhovsky et al., 2011]. The purpose of this chapter is to demonstrate the viability of the damage mechanics approach to describe the propagation of water-filled crevasses in glaciers by comparing its results with those from theoretical fracture mechanics models.

The rest of the chapter is organized as follows: in Section 5.2, we review four the-

oretical mechanics models and conduct a comparative numerical study, which has never been done before in the literature; in Section 5.3, we present the governing equations of the nonlocal poro-damage mechanics model that combines the updated Lagrangian Stokes flow formulation detailed in Jiménez et al. [2017] and the poro-mechanics formulation detailed in Mobasher et al. [2016] for hydraulic fracture; in Section 5.4, we compare damage mechanics predictions for the penetration of dry and water-filled crevasses against the theoretical fracture mechanics models by considering an extensive set of parametric studies; in Section 5.5, we offer some concluding remarks. The reader is also referred to the appendix for supporting information and additional studies.

5.2 Review of Fracture Mechanics Models

Iceberg calving is a natural process that occurs when a combination of surface and basal crevasses propagates through the entire thickness of the ice shelf or glacier leading to the formation of icebergs. The widely accepted hypothesis is that calving is dominated by the opening of cracks due to tensile stress, so researchers have proposed fracture mechanics models to estimate crevasse penetration depth. In this section, we will briefly review four theoretical fracture mechanics models: (1) the Nye (zero-stress) model [Nye, 1955]; (2) the Weertman (dislocation-based fracture mechanics) model [Weertman, 1973]; (3) the van der Veen (linear elastic fracture mechanics) model [van der Veen, 1998a]; and (4) the Krug et al. (linear elastic fracture mechanics) model [Krug et al., 2014]. Additionally, we numerically solve the corresponding model equations and compare the predicted penetration depths of water-filled surface crevasses as a function of the resistive stress, water pressure in the crevasse and seawater pressure at the terminus. We restrict our study to idealized rectangular glaciers under plane strain with far-field boundary conditions, as illustrated in Figure 5.1.

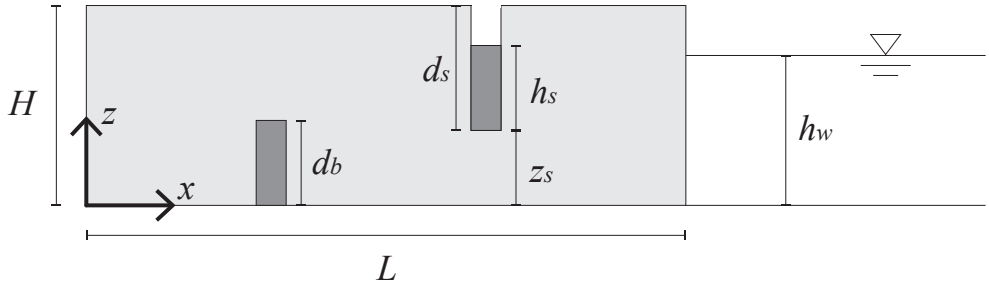

Figure 5.1: Schematic of ice slab with height H, length L, seawater level h_w, surface crevasse height d_s, water level h_s within the surface crevasse, and basal crevasse height d_b. The origin is set at the lower-left corner of the slab with x and z as the horizontal and vertical coordinates, respectively, and y is the out-of-plane coordinate forming a right-handed system orientation.

5.2.1 Constant Resistive Stress Approximation

Theoretical models generally predict crevasse penetration as a function of the horizontal Cauchy stress σ_{xx}, relying on the approximation that gravity-induced stress σ_{xx} varies linearly along the depth of the ice slab. Weertman [1957] has shown that under certain idealized conditions, σ_{xx} does vary linearly with depth and can be written in terms of a constant tensile stress R_{xx} resulting from longitudinal creep flow and a linearly varying lithostatic stress arising from the self-weight of ice

$$\sigma_{xx}(z) = R_{xx} - \rho_{\mathrm{i}} g \langle H - z \rangle, \tag{5.1}$$

where x, z are the in-plane horizontal and vertical coordinates, $\rho_{\mathrm{i}} = 917\ \mathrm{kg/m^3}$ is the density of ice, g is gravitational acceleration, H is the height of the slab, and the Macaulay brackets $\langle x \rangle = \frac{1}{2}(x + |x|)$. The tensile stress R_{xx} (also called the "resistive" stress) is given by

$$R_{xx} = \frac{1}{2}\rho_{\mathrm{i}} g H - \frac{1}{2}\rho_{\mathrm{w}} g \frac{h_w^2}{H}, \tag{5.2}$$

where $\rho_{\mathrm{w}} = 1020\ \mathrm{kg/m^3}$ is the density of seawater and h_w is the seawater depth at the slab terminus. The above equation for R_{xx} can be derived using three idealized conditions: (1) far from the terminus (i.e., in the so-called "far-field" region of the ice slab), the stresses in ice only vary with z coordinate; (2) viscous flow of ice is incompressible; and (3) the out-of-plane strain rate is negligible (i.e., $\dot{\varepsilon}_{yy} = 0$). Using the finite element method, we have checked that the constant R_{xx} approximation is valid when the above three conditions are satisfied (see Figure L13 in Appendix I). Interestingly, the far-field stress state in ice is independent of its rheology, so long as ice is assumed to be an incompressible material.

Remark 29 *In the literature, the resistive stress R_{xx} is often called the deviatoric stress, which is a misnomer. The conventional definition of the deviatoric stress is, $\boldsymbol{\tau} = \boldsymbol{\sigma} + p\boldsymbol{I}$,*

where $p = -\frac{1}{3}\text{trace}[\boldsymbol{\sigma}]$ *is the hydrostatic pressure and* $\boldsymbol{I}$ *is the second-order identity tensor. Thus, we obtain* $\tau_{xx} = \sigma_{xx} + p$ *and* $\tau_{xx} \neq R_{xx}$*, because the pressure* p *is generally different from the lithostatic stress* $\rho_i g\langle H - z\rangle$*. In fact,* $R_{xx} = 2\tau_{xx}$ *in the far-field region of the ice slab, and the derivation is provided in Appendix I.*

5.2.2 Nye Model

The Nye zero-stress model [Nye, 1957] is an early and simplistic theoretical model that states that crevasses will penetrate through an ice slab to the depth where tensile stresses vanish, that is, where the horizontal Cauchy stress σ_{xx} is zero. Two assumptions must be made for this model to apply: (1) that ice has zero tensile (fracture) strength; and (2) that the stress singularity at crevasse tips can be neglected, owing to stress smoothing in a uniform field of closely-spaced crevasses. Although the Nye model is rheology independent, it is standard to regard ice as an incompressible medium and solve Equation 48 for the position of the crevasse tip z_s measured from the bottom of the slab such that $\sigma_{xx}(z_s) = 0$. The maximum penetration depth of a surface crevasse $d_s = H - z_s$, is thus given by

$$d_s = \frac{R_{xx}}{\rho_i g}. \tag{5.3}$$

For an ice slab in a purely dry environment (i.e., the seawater level $h_w = 0$), the resistive stress $R_{xx} = \frac{1}{2}\rho_i g H$, and so the predicted surface crevasse depth $d_s = \frac{1}{2}H$.

The original Nye model did not account for the presence of hydraulic pressure in water-filled crevasses, however, later works [Jezek, 1984, Nick et al., 2010a, Bassis, 2011] have included an additional term into the horizontal stress balance that incorporates hydraulic pressure,

$$\sigma_{xx}(z) = R_{xx} - \rho_i g\langle H - z\rangle + \sigma_w(z), \tag{5.4}$$

where $\sigma_w(z)$ is the depth-varying hydraulic pressure acting on the crevasse walls. Because the hydraulic pressure acts to open the crevasse, it is assumed in the literature that this pressure induces a positive (tensile) stress within the ice, and crevasses are expected to penetrate to the depth where the net stress vanishes to zero [Weertman, 1980a, Jezek, 1984]. Thus, the pressure term σ_w can be expressed as,

$$\sigma_w(z) = \begin{cases} \rho_{\mathrm{w}} g \langle h_s - (z - z_s) \rangle & \text{if} \quad z \in [z_s,\ z_s + h_s], \\ 0 & \text{otherwise}, \end{cases} \tag{5.5}$$

where h_s is the hydraulic head within the surface crevasse. Let us consider a surface crevasse filled with water to some level $h_s = c_s d_s$ where the constant $c_s \in [0, 1]$. By solving Equation 5.4 for $\sigma_{xx}(z_s) = 0$, we obtain the depth of a surface crevasse as,

$$d_s = \begin{cases} \dfrac{R_{xx}}{\rho_{\mathrm{i}} g - c_s \rho_{\mathrm{w}} g} & \text{if} \quad c_s < \dfrac{\rho_{\mathrm{i}}}{\rho_{\mathrm{w}}}, \\ H & \text{if} \quad c_s \geq \dfrac{\rho_{\mathrm{i}}}{\rho_{\mathrm{w}}}. \end{cases} \tag{5.6}$$

For $c_s \geq \frac{\rho_{\mathrm{i}}}{\rho_{\mathrm{w}}}$, the horizontal stress $\sigma_{xx}(z_s) > 0$ for any z_s, thus indicating full depth penetration of the surface crevasse.

Remark 30 *Weertman [1977] derived an approximate analytical solution to show that crevasse penetration depth is equal to the Nye depth when fracture strength of ice is essentially zero and the crevasse spacing is much smaller than crevasse depths. Thus, the Nye zero stress model can be categorized as a fracture mechanics model but its applicability is limited to a perfectly uniform crevasse field, which is strictly an academic argument [De Robin, 1974, Weertman, 1974]. However, due to its simplicity researchers have employed the Nye model [Nick et al., 2010a, Bassis and Walker, 2012, DeConto and Pollard,*

2016, Sun et al., 2017], although it would underestimate the penetration depth of isolated or sufficiently far-apart surface crevasses.

5.2.3 Weertman Model

To address the limitation of the Nye model, Weertman [1973] applied dislocation-based fracture mechanics theory for elastic solids to the penetration of isolated crevasses in ice. The penetration depth d_s of a dry isolated surface crevasse is given by,

$$d_s = \frac{\pi}{2}\frac{R_{xx}}{\rho_{\mathrm{i}} g}, \tag{5.7}$$

for an empty (or dry) surface crevasse (i.e., $h_s = 0$). Weertman [1973] also derived analytical expressions for calculating the penetration depth of water-filled surface crevasses. The crevasse penetration depth is obtained by evaluating the crack opening displacement function (see Equation 11 in Weertman [1973]),

$$\mathscr{D}(z', d_s) = \frac{2(1-\nu)}{\mu}\left(\frac{\rho_{\mathrm{i}} g}{\pi}\left\{\sqrt{d_s^2-(z')^2}\left(d_s - \frac{\rho_{\mathrm{w}}}{\rho_{\mathrm{i}}}\sqrt{d_s^2-(h')^2}\right)\right.\right.$$

$$-(z')^2\log\left[\frac{d_s+\sqrt{d_s^2-(z')^2}}{(z')^2}\right] + \frac{\rho_{\mathrm{w}}}{2\rho_{\mathrm{i}}}((z')^2+(h')^2)\log\left|\frac{\sqrt{d_s^2-(h')^2}+\sqrt{d_s^2-(z')^2}}{\sqrt{d_s^2-(h')^2}-\sqrt{d_s^2-(z')^2}}\right|$$

$$\left.\left.-z'h'\frac{\rho_{\mathrm{w}}}{\rho_{\mathrm{i}}}\log\left|\frac{(z')\sqrt{d_s^2-(h')^2}+h'\sqrt{d_s^2-(z')^2}}{(z')\sqrt{d_s^2-(h')^2}-h'\sqrt{d_s^2-(z')^2}}\right|\right\} + (R_{xx}-R'_{xx})\sqrt{d_s^2-(z')^2}\right), \tag{5.8}$$

where $z' = H - z$ is the vertical coordinate measured from the top of the slab, the dry distance $h' = \langle d_s - h_s \rangle$, and the quantity R'_{xx} is given by,

$$R'_{xx} = 2\frac{\rho_{\mathrm{i}} g}{\pi}\left(d_s + h'\frac{\rho_{\mathrm{w}}}{\rho_{\mathrm{i}}}\left[\frac{\pi}{2} - \sin^{-1}\frac{h'}{d_s}\right] - \frac{\rho_{\mathrm{w}}}{\rho_{\mathrm{i}}}\sqrt{d_s^2-(h')^2}\right). \tag{5.9}$$

In the above equations, μ is the shear modulus and ν is Poisson's ratio for linearly elastic ice; however, in this model neither μ nor ν affects the surface crevasse penetration depth. The crevasse depth d_s is calculated by evaluating Equation 54 for the greatest value of d_s such that $\mathscr{D}(z', d_s) > 0$ for all $z' \in [0, d_s]$. In other words, the crevasse depth d_s is taken as the greatest depth for which the crack opening displacement (i.e., the separation distance between crevasse walls) is positive for all points along the crevasse. We have numerically solved the above analytical expressions using the bisection algorithm, and the details are given in Appendix J. To verify our implementation, we reproduce the Figure 7 results from Weertman [1973] in Figure 5.2(a) below by plotting the quantity $(2d_s\rho_{\mathrm{i}}g)/(\pi R_{xx})$ versus $(d_s - h_s)/d_s$ on a log-log scale.

Remark 31 *The asymptotic behavior near the point* $(d_s - h_s)/d_s = 0.0265$ *in Figure 5.2(a) indicates that a surface crevasse filled with water up to at least 97.35% of its depth will penetrate through the entirety of the ice slab, regardless of the value of tensile stress* R_{xx}. *On the other hand, as* $(d_s - h_s)/d_s \to 1$ *(i.e.,* $h_s \to 0$*, indicating a dry crevasse), the value of* $(2d_s\rho_{\mathrm{i}}g)/(\pi R_{xx}) \to 1$*, thus providing us with the relation in Equation 5.7.*

5.2.4 van der Veen Model

The Weertman model assumes that ice thickness is much larger than the crevasse penetration depth, thus neglecting the finite geometry effects on crevasse growth. To address this limitation, van der Veen [1998a] proposed a linear elastic fracture mechanics (LEFM) model for estimating crevasse evolution in glaciers by treating ice as an elastic body subject to the far-field stress state, as described by Equations 48 and 5.4. The penetration depth of surface crevasses is determined by equating the net stress intensity factor (SIF) K_I^{net} to the

experimentally measured critical SIF K_{Ic} as

$$K_I^{\text{net}} = K_I^{(1)}(R_{xx}, d_s) + K_I^{(2)}(d_s) + K_I^{(3)}(h_s, d_s) = K_{Ic} \tag{5.10}$$

where $K_I^{(1)}$, $K_I^{(2)}$, and $K_I^{(3)}$ are the SIFs resulting from the resistive stress, ice overburden pressure, and hydraulic pressure exerted on crevasse walls for water-filled crevasses, respectively. The terms for $K_I^{(1)}$, $K_I^{(2)}$, and $K_I^{(3)}$ are given as,

$$K_I^{(1)} = F(\lambda) R_{xx} \sqrt{\pi d_s}, \tag{5.11a}$$

$$K_I^{(2)} = \int_0^{d_s} \left[\frac{-2\rho_{\text{i}} g z'}{\sqrt{\pi d_s}} G(\lambda, \gamma) \right] \mathrm{d}z', \tag{5.11b}$$

$$K_I^{(3)} = \int_0^{d_s} \left[\frac{2\rho_{\text{w}} g \langle z' - h' \rangle}{\sqrt{\pi d_s}} G(\lambda, \gamma) \right] \mathrm{d}z', \tag{5.11c}$$

where $z' = H - z$ is the vertical coordinate measured from the top of the ice slab, the dry depth $h' = d_s - h_s$, the terms $\lambda = d_s/H$ and $\gamma = z'/d_s$, and the weighting functions $F(\lambda)$ and $G(\lambda, \gamma)$ are given by,

$$F(\lambda) = 1.12 - 0.23\lambda + 10.55\lambda^2 - 21.72\lambda^3 + 30.39\lambda^4, \tag{5.12}$$

and

$$\begin{aligned} G(\lambda, \gamma) = &\left[\frac{3.52(1-\gamma)}{(1-\lambda)^{3/2}} \right] - \left[\frac{4.35 - 5.28\gamma}{(1-\lambda)^{1/2}} \right] \\ &+ \left[\frac{1.3 - 0.3\gamma^{3/2}}{(1-\gamma^2)^{1/2}} + 0.83 - 1.76\gamma \right] [1 - (1-\gamma)\lambda]. \end{aligned} \tag{5.13}$$

The SIF terms given in Equation 57 are nonlinear functions of d_s, and so an iterative process is required to solve for d_s, as described in Appendix K. Each term takes into account the height of the ice slab through the parameter λ; however, the ice slab may be treated as a semi-infinite plane by setting $\lambda = 0$. To verify our numerical implementation of the SIF model using the bisection algorithm, we replicated the result in Figure 10 from van der

Veen [1998a] in Figure 5.2(b), where we plot the net stress intensity factor $K_I^{\text{net}} = K_I^{(1)} + K_I^{(2)} + K_I^{(3)}$ versus crevasse height d_s for three separate water levels h_s filling the surface crevasse that penetrates an ice slab of height $H = 500$ m. To generate the result in Figure 5.2(b), the resistive stress R_{xx} is held constant at 100 kPa.

Remark 32 *van der Veen [1998a] used different geometric factors $F(\lambda)$ and $G(\lambda,\gamma)$ for evaluating the SIFs corresponding to the constant resistive stress and linearly varying pressure terms, respectively; whereas van der Veen [1998b] used only one geometric parameter $G(\lambda,\gamma)$ for evaluating the SIFs corresponding to the net longitudinal stress. While the two approaches seem to be mathematically consistent, the numerical integration scheme for computing the SIFs leads to different crevasse depth predictions. Interestingly, the approach of van der Veen [1998b] for evaluating the net SIF is consistent with the Krug et al. [2014] model despite the difference in geometric factors.*

5.2.5 Krug et al. Model

The van der Veen model assumes that the resistive stress R_{xx} is constant over the ice depth while evaluating $K_I^{(1)}$, which may not be true for real cases. To address this issue, Krug et al. [2014] proposed a modified LEFM model wherein the net horizontal Cauchy stress σ_{xx} is multiplied by a different weighting function and then integrated over the depth of the crevasse. The Krug et al. [2014] model has been well established in fracture mechanics literature [Glinka and Shen, 1991, Moftakhar and Glinka, 1992, Tada et al., 2000] and is appropriate for an arbitrary stress profile applied to the crack. For the sake of completeness, the model is summarized below:

$$K_I = \int_0^{d_s} M(z',H)\left[R_{xx} - \rho_{\text{i}} g z' + \rho_{\text{w}} g \langle z' - h' \rangle\right] \mathrm{d}z' \tag{5.14}$$

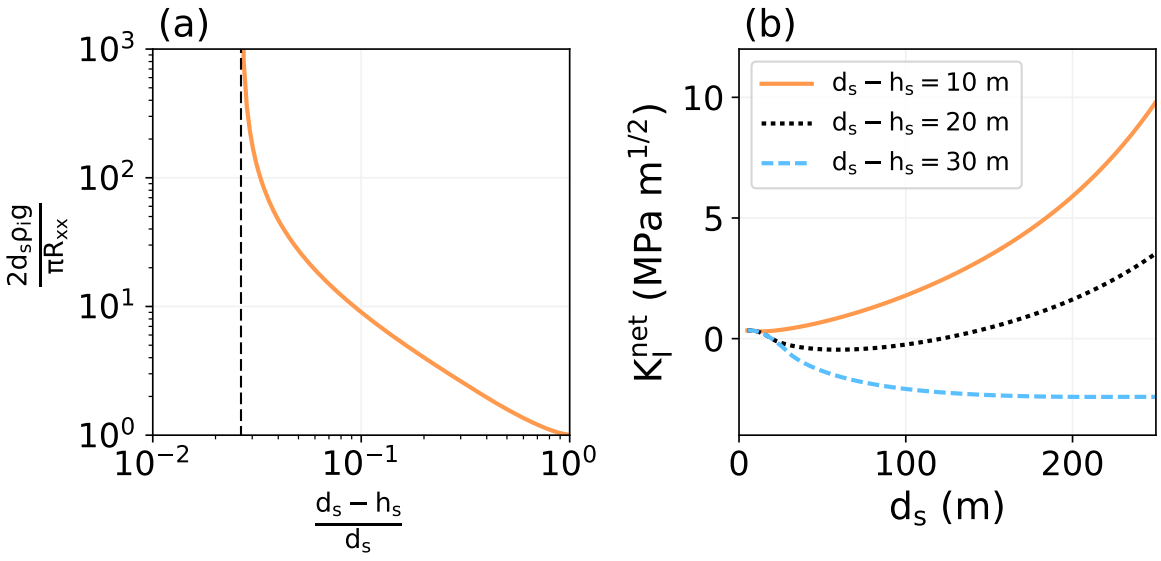

Figure 5.2: Verification study of LEFM models. (a) Plot of $\frac{d_s - h_s}{d_s}$ versus $\frac{2d_s\rho_i g}{\pi R_{xx}}$ computed using the Weertman model to predict surface crevasse penetration depth. This subfigure is a reproduction of Figure 7 from Weertman [1973]. (b) Net mode I stress intensity factor $K_I^{\text{net}} = K_I^{(1)} + K_I^{(2)} + K_I^{(3)}$ versus surface crevasse height d_s for three separate water levels h_s filling the crevasse, computed using the van der Veen model. The slab height $H = 500$ m, and the resistive stress R_{xx} is held constant at 100 kPa. This subfigure is a reproduction of the top-left portion of Figure 10 from van der Veen [1998a].

where $z' = H - z$ is the vertical coordinate measured from the top of the ice slab, the dry depth $h' = d_s - h_s$, and the weighting function $M(z', H)$ is given as [Glinka, 1996],

$$M(z', H) = \frac{2}{\sqrt{2\pi(d_s - z')}} \left[1 + M_1 \left(1 - \frac{z'}{d_s}\right)^{1/2} + M_2 \left(1 - \frac{z'}{d_s}\right) + M_3 \left(1 - \frac{z'}{d_s}\right)^{3/2} \right]. \tag{5.15}$$

The constants M_1, M_2, and M_3 are given by polynomial functions that account for the geometry of the ice slab,

$$\begin{aligned} M_1 &= 0.0719768 - 1.513476\lambda - 61.1001\lambda^2 + 1554.95\lambda^3 \\ &\quad - 14583.8\lambda^4 + 71590.7\lambda^5 - 205384\lambda^6 + 356469\lambda^7 \\ &\quad - 368270\lambda^8 + 208233\lambda^9 - 49544\lambda^{10}, \end{aligned} \tag{5.16a}$$

$$\begin{aligned} M_2 &= 0.246984 + 6.47583\lambda + 176.456\lambda^2 - 4058.76\lambda^3 \\ &\quad + 37303.8\lambda^4 - 181755\lambda^5 + 520551\lambda^6 - 904370\lambda^7 \\ &\quad + 936863\lambda^8 - 531940\lambda^9 + 127291\lambda^{10}, \end{aligned} \tag{5.16b}$$

$$\begin{aligned} M_3 &= 0.529659 - 22.3235\lambda + 532.074\lambda^2 - 5479.53\lambda^3 \\ &\quad + 28592.2\lambda^4 - 81388.6\lambda^5 + 128746\lambda^6 - 106246\lambda^7 \\ &\quad + 35780.7\lambda^8, \end{aligned} \tag{5.16c}$$

with $\lambda = d_s/H$. We note that near the crack tip (i.e., $z' \to d_s$), the function $M(z',H)$ approaches infinity due to the $z' - d_s$ term in the denominator. To avoid numerical integration errors near this singularity, it is suitable to integrate Equation 5.14 from $z' = 0$ to $z' = d_s - \varepsilon$ for some small value ε. In this work, we take $\varepsilon = 10^{-8}$.

Remark 33 *The integrands in Equations 57b, 57c, and 5.14 tend to infinity when the vertical coordinate $z' \to d_s$. This can result in an overestimation of the integral when using standard numerical integration techniques (e.g., the trapezoidal rule or Simpson's rule) in regions where the integrand rapidly approaches infinity. Specifically, the value computed for the integral becomes $+\infty$ when $\sigma_{xx} > 0$ and $-\infty$ when $\sigma_{xx} < 0$ at the crack tip. To avoid the overestimation of the integral using the Simpson's rule, we limit the upper bound on the integral to $z' = d_s - \varepsilon$ for some small value $\varepsilon \approx 0$. In our studies, we find that the integral*

converges to a finite value when taking $\varepsilon = 10^{-6}, 10^{-8}$, *and* 10^{-10}*; however, for* $\varepsilon = 10^{-12}$ *the integral becomes large and approaches infinity as* ε *is decreased further.*

5.2.6 Comparison of Crevasse Depth Predictions

We now compare the four fracture mechanics models discussed above with one another by predicting the surface crevasse penetration depth d_s as a function of the resistive stress R_{xx} and the hydraulic head h_s within the crevasse. In order to account for the tensile strength of ice in the van der Veen [1998a] model, we take the critical stress intensity factor $K_{Ic} = 0.1$ MPa $\sqrt{\text{m}}$. Let us first consider the penetration depth d_s predicted by the various calving models under dry conditions (i.e., $h_w = 0$ and $h_s = 0$) while varying R_{xx} in an ice slab with height $H = 500$ m. The Weertman [1973] and van der Veen [1998a] models predict similar penetration depths if we do not account for the finite geometry correction functions in the van der Veen [1998a] model, as depicted by the orange and magenta lines in Figure 5.3(a). However, when the correction functions are included to account for the finite thickness of the ice slab, the van der Veen [1998a] model predicts greater surface crevasse penetration depths under dry conditions. In general, the Nye zero-stress model predicts smaller penetration depths because it does not account for the stress concentration (or singularity) at the crevasse tip. Next, let us consider the case where we vary the hydraulic head h_s within the surface crevasse at three different sea levels: $h_w/H = 0\%$, 50%, and 90% (i.e., floating condition). For each value of h_w, the resistive stress R_{xx} is determined by Equation 49. The Weertman [1973] and van der Veen [1998a] models predict similar crevasse penetration depths regardless of the value of h_w or h_s if the finite geometry correction factors are ignored in the van der Veen [1998a] model, as indicated by the magenta lines in Figure 5.3. However, with the correction factors included, the van der Veen [1998a] model predicts substantially different penetration depths. The Nye zero-stress model only agrees with the fracture mechanics models for the $h_w/H = 90\%$ case; whereas, for $h_w/H = 0\%$ and 50%,

the Nye model under-predicts the crevasse penetration depth.

From the above comparative study, we find that:

i. The Weertman, van der Veen and Krug et al. models predict much deeper crack growth than the Nye model because they account for the stress singularity at the crevasse tip;

ii. Despite major differences between the Weertman and van der Veen models, both seem to be equivalent when the finite geometry correction functions are excluded from the latter model. The close agreement exists because the two models make the same assumptions about ice: namely, that ice is a linear elastic incompressible solid and that the ice slab is a semi-infinite plane with loading defined by far-field stress and idealized boundary conditions; and

iii. Despite the similarity in van der Veen and Krug et al. models, both seem to predict different crevasse depths when seawater height at the terminus is low, owing to the differences in the evaluation of net SIF. However, this discrepancy can be removed by using the same geometric correction factor $G(\lambda, \gamma)$ to all the SIFs in the van der Veen model in the manner proposed by van der Veen [1998b], which is demonstrated in Appendix L.

However, there are still several key questions to address in this study.

i. Is the Nye zero-stress model sufficient for predicting the penetration depth of crevasse fields in a realistic scenario? In a real ice sheet or glacier one, would seldom find perfectly uniform closely-spaced crevasses, which is a necessary condition for the Nye model to be applicable.

ii. Are fracture mechanics models consistent with damage mechanics models for estimating crevasse penetration depths? The LEFM theory states that stress is infinite (stress singularity) at the crevasse tip; however, micro-crack damage and nonlocal interactions will make the stress bounded.

iii. Are crevasses affected by the large deformations accruing over time due to creeping ice flow? The theoretical fracture mechanics models assume that fractures no matter how large do not influence the flow or stress state in the glacier, despite the fact that large viscous deformations can substantially change its geometry.

iv. Can a water-filled crevasse fully penetrate a grounded glacier when accounting for viscous creep and nonlocal damage interactions? The glaciological stress distribution at the crevasse tip is dependent on ice rheology (i.e., elastic vs. viscous) and stress relaxation in viscous materials can prevent the full penetration of crevasses, which is not accounted for in the theoretical models.

To resolve these questions, we employ the damage mechanics approach described in the next section to study crevasse evolution.

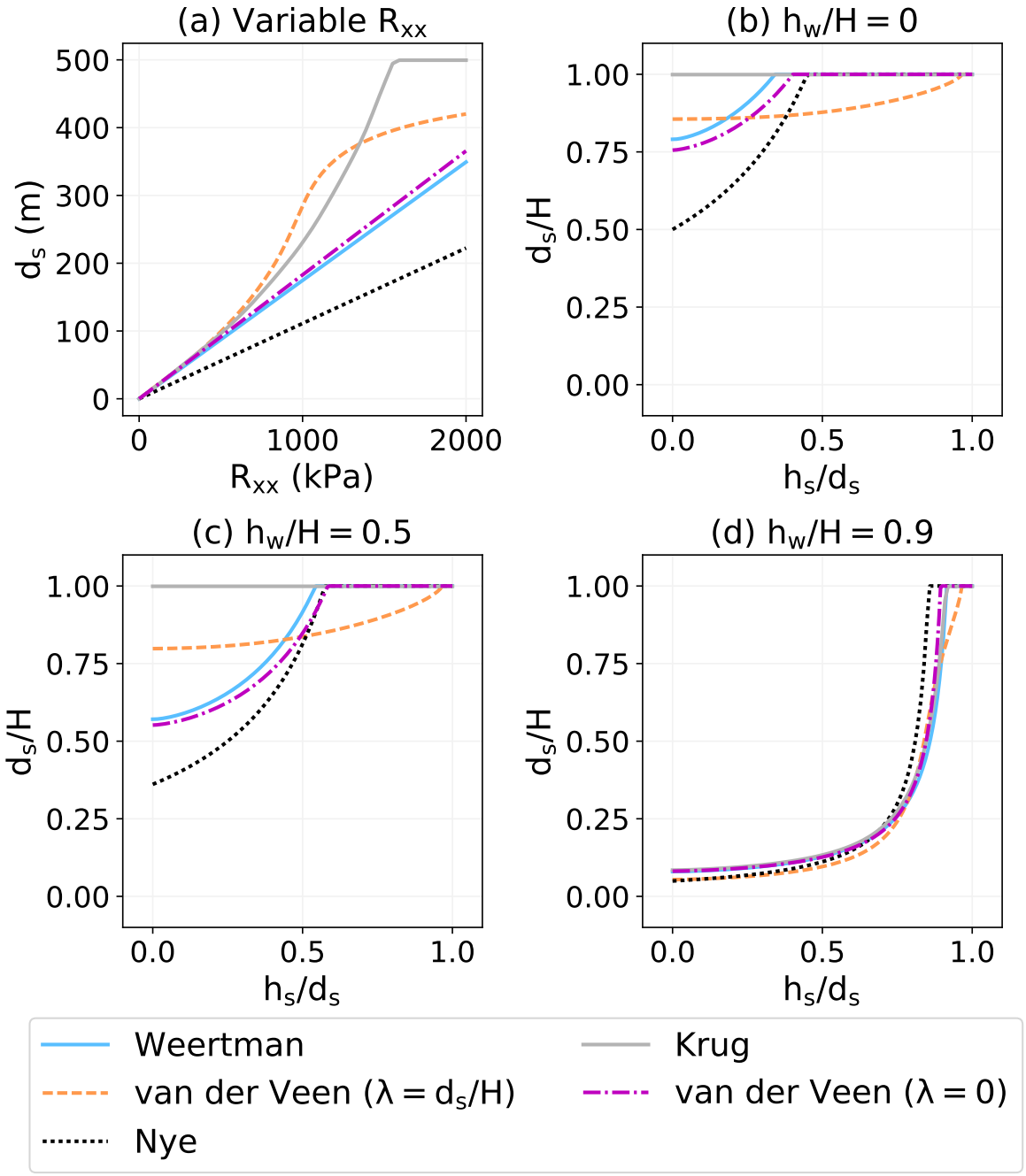

Figure 5.3: Surface crevasse penetration depth d_s predicted by the Nye zero-stress, Weertman [1973], van der Veen [1998a], and Krug et al. [2014] models as a function of (a) the resistive stress R_{xx} and (b-d) the hydraulic head h_s within the surface crevasse. In both plots, the magenta dash-dot lines correspond to the van der Veen [1998a] model including geometric correction factors that account for the height of the ice slab; whereas the dashed line correspond to the van der Veen [1998a] without the geometric factors included. We take the critical stress intensity factor $K_{Ic} = 0.1$ MPa $\sqrt{\text{m}}$, and the height of the ice slab considered is $H = 500$ m.

5.3 Nonlocal Poro-damage Mechanics Model

In this section, we briefly describe the extended damage mechanics approach for simulating the propagation of water-filled surface crevasses. This approach uniquely combines the creep damage model for ice presented in [Duddu and Waisman, 2012, 2013c] with the nonlinear Stokes formulation employed in [Jiménez et al., 2017] and the poromechanics based hydrofracture model proposed in [Mobasher et al., 2016] for simulating the propagation of water-filled crevasses in quasi-static regime. The advantage of the damage mechanics approach is that it can simulate the time-dependent propagation of fracture in a thermodynamically consistent and computationally efficient manner.

5.3.1 Viscous damage model

We represent damage using an isotropic scalar variable $D \in [0,1]$, where $D = 0$ and $D = 1$ represent the undamaged (virgin) and fully damaged state, respectively, at a material point in the continuum. Following the principle of effective stress [Kachanov, 1958, Rabotnov, 1963] and the hypothesis of strain equivalence [Lemaitre, 1971], the effective Cauchy stress tensor $\bar{\boldsymbol{\sigma}}$ in ice may be defined in terms of the "true" Cauchy stress tensor $\boldsymbol{\sigma}$ as,

$$\bar{\boldsymbol{\sigma}} = \frac{\boldsymbol{\sigma}}{(1-D)} = \frac{1}{(1-D)} \begin{bmatrix} \sigma_{xx} & \sigma_{xy} & \sigma_{xz} \\ \sigma_{xy} & \sigma_{yy} & \sigma_{yz} \\ \sigma_{xz} & \sigma_{yz} & \sigma_{zz} \end{bmatrix}. \tag{5.17}$$

The constitutive relations for damaged ice can thus be written in terms of the effective stress,

$$\bar{\boldsymbol{\sigma}} = \bar{\boldsymbol{\tau}} - \bar{p}\boldsymbol{I}, \tag{5.18}$$

$$\bar{\boldsymbol{\tau}} = 2\eta(\boldsymbol{v})\dot{\boldsymbol{\epsilon}}, \tag{5.19}$$

where $\bar{\boldsymbol{\tau}}$ is the effective deviatoric stress tensor; $\bar{p} = -\frac{1}{3}\text{trace}[\bar{\boldsymbol{\sigma}}]$ is the effective pressure; $\boldsymbol{I}$ is the identity tensor; $\eta(\boldsymbol{v})$ is the nonlinear viscosity and a function of the flow velocity $\boldsymbol{v}$; and $\dot{\boldsymbol{\epsilon}}$ is the viscous strain rate, defined as the symmetric gradient of velocity,

$$\dot{\boldsymbol{\epsilon}} = \frac{1}{2}\left(\nabla \boldsymbol{v} + \nabla^{\top} \boldsymbol{v}\right). \tag{5.20}$$

Assuming polycrystalline ice to be an isotropic and incompressible viscous fluid, the rheological model for ice flow is defined by the Glen-Nye law,

$$\dot{\boldsymbol{\epsilon}} = A\,(\bar{\tau}^{\text{eq}})^{N-1}\,\bar{\boldsymbol{\tau}}, \tag{5.21}$$

where A is a temperature-dependent viscosity coefficient, N is a viscosity exponent controlling the nonlinearity of the flow model, and $\bar{\tau}^{\text{eq}}$ is the equivalent deviatoric stress. The above expression can be inverted and rewritten in the same form as Equation 5.19,

$$\bar{\boldsymbol{\tau}} = A^{-1/N}\,(\dot{\varepsilon}^{\text{eq}})^{\frac{1}{N}-1}\,\dot{\boldsymbol{\epsilon}}, \tag{5.22}$$

where the equivalent strain rate is given by,

$$\dot{\varepsilon}^{\text{eq}} = \sqrt{\frac{1}{2}\dot{\boldsymbol{\epsilon}} : \dot{\boldsymbol{\epsilon}}}, \tag{5.23}$$

with the colon (:) indicating the inner product between two tensors. Comparing with Equation 5.19, the viscosity in Equation 5.22 is thus $\eta(\boldsymbol{v}) = \frac{1}{2}A^{-1/N}\,(\dot{\varepsilon}^{\text{eq}})^{\frac{1}{N}-1}$. For polycrystalline ice, the parameter N is generally calibrated as 3 which describes nonlinear viscous behavior for a non-Newtonian fluid; however, by setting $N = 1$, a linearly viscous rheological model is recovered. The values for all material parameters are given in Table 5.1.

Table 5.1: Material properties of ice at -10°C obtained from Jiménez et al. [2017].

Property	Value	Units
ρ_{i}	917	kg/m^3
A	7.156×10^{-7}	MPa^{-3} s^{-1}
N	3	–

5.3.2 Creep Damage Evolution Law

We consider that the failure of ice is caused by the progressive accumulation of microcracks and microvoids due to creep damage evolution. Because we assume damage evolution progresses only under a tensile stress state, we define the local damage rate at a material point as,

$$\dot{D}^{\mathrm{loc}} = \frac{\partial D^{\mathrm{loc}}}{\partial t} = \begin{cases} B\dfrac{\langle \bar{\chi} \rangle^r}{(1-D)^{k_\sigma}} & \text{if} \quad \bar{p} \leq 0, \\ 0 & \text{if} \quad \bar{p} > 0, \end{cases} \tag{5.24}$$

where B is a damage rate coefficient; r is a damage rate exponent; and $\bar{\chi}$ is the effective Hayhurst measure of stress, given by,

$$\bar{\chi} = \alpha \bar{\sigma}^{(\mathrm{I})} + \beta \bar{\sigma}^{\mathrm{v}} + (1-\alpha-\beta)\mathrm{trace}[\bar{\boldsymbol{\sigma}}], \tag{5.25}$$

where α and β are brittle and ductile weighting parameters, respectively; $\bar{\sigma}^{(\mathrm{I})}$ is the effective maximum principal stress; and $\bar{\sigma}^{\mathrm{v}} = \left(\frac{3}{2}\bar{\boldsymbol{\tau}} : \bar{\boldsymbol{\tau}}\right)^{1/2}$ is the effective von Mises stress. The parameter k_σ is experimentally calibrated and defined as,

$$k_\sigma = k_1 + k_2 \mathrm{trace}[\boldsymbol{\sigma}]. \tag{5.26}$$

Table 5.2: Damage law parameters obtained from Jiménez et al. [2017].

Parameter	Value	Units
B	5.23×10^{-7}	$\text{MPa}^{-r}\ \text{s}^{-1}$
r	0.43	–
α	0.21	–
β	0.63	–
k_1	-2.63	–
k_2	7.24	MPa^{-1}
l_c	10	m

To maintain thermodynamic consistency and alleviate mesh sensitivity, we implement a nonlocal implicit gradient formulation for the creep damage rate [Jiménez et al., 2017] ,

$$\dot{D} - \frac{1}{2} l_c^2 \nabla^2 \dot{D} = \dot{D}^{\text{loc}}. \tag{5.27}$$

where the nonlocal length scale $l_c = 10$ m. In order to prevent rank deficiency in the tangent stiffness matrix, we set a maximum limit on damage $D^{\max} = 0.99$. The values of all other damage parameters are given in Table 5.2.

Remark 34 *In the proposed implementation, creep damage growth is restricted to locations where the hydrostatic pressure is tensile (i.e., $p = \leq 0$ by definition). We found this criterion to be more appropriate when modeling crevasse propagation using a scalar isotropic damage variable, which cannot distinguish between damage in the form of micro-voids as opposed to micro-cracks. Alternatively, it is possible to restrict damage growth to locations where the maximum principal stress is tensile and account for damage-induced anisotropy due to micro-cracks using a tensorial damage variable [Pralong and Funk, 2005, Duddu and Waisman, 2012], but it increases the computational complexity and cost.*

5.3.3 Poro-Mechanics Formulation

In this section, we extend the continuum damage mechanics formulation to incorporate hydraulic fracture in the quasi-static setting, wherein water can permeate the damage zone and exert hydrostatic pressure. Our approach is based on Biot's theory of poroelasticity [Biot, 1955] that formalizes Terzaghi's effective stress principle [Terzaghi, 2007]. Accordingly, the Cauchy stress in a saturated porous media may be defined as

$$\boldsymbol{\sigma} = (1-\phi)\widetilde{\boldsymbol{\sigma}} - \phi\, p_w \boldsymbol{I}, \tag{5.28}$$

where ϕ is the porosity of ice, $\widetilde{\boldsymbol{\sigma}}$ is the solid effective stress, and p_w is the hydraulic pressure. Similar to the formulation in [Mobasher et al., 2016, 2017], we assume that isotropic damage represents void space within the continuum and has the same effect as porosity. Thus, we can rewrite the above equation by replacing porosity with the isotropic damage variable as

$$\boldsymbol{\sigma} = (1-D)\bar{\boldsymbol{\sigma}} - D p_w \boldsymbol{I}, \tag{5.29}$$

where p_w is the hydraulic pressure within the damage zone defined as,

$$p_w = \rho_{\mathrm{w}} g \langle h - z \rangle, \tag{5.30}$$

with h as the hydraulic head and z as the vertical coordinate. Combining the constitutive relations for damaged ice from Equations 5.18 and 5.19 and substituting them into Equation 5.29, we obtain the poro-damage mechanics constitutive equation for viscous ice rheology that incorporates hydraulic pressure within the damage zone,

$$\boldsymbol{\sigma} = (1-D)\left[2\eta(\boldsymbol{v})\dot{\boldsymbol{\epsilon}} - \bar{p}\boldsymbol{I}\right] - D p_w \boldsymbol{I}. \tag{5.31}$$

Note that we ignore the effects of phase change (i.e., the melting or freezing of ice) during the hydraulic fracture process, although this is commonly observed in the field.

5.4 Comparison of Damage Mechanics and Fracture Mechanics Models

In this section we compare the fracture mechanics models reviewed in Section 2 against the damage mechanics model discussed in Section 3. The damage mechanics model is implemented using the finite element method (FEM) in FEniCS software [Jiménez et al., 2017]; the reader is referred to the URL https://my.vanderbilt.edu/cpml/research/nsf-plr-1341428/ where codes are available for download. For each simulation we consider an idealized, rectangular ice slab of length L and height H. The ice slab is grounded on a rigid, frictionless (free-slip) surface and terminates at the ocean with a seawater depth h_w, as depicted in Figure 5.1. Gravity loading is applied as a body force $\rho_{\mathrm{i}}\boldsymbol{g}$ where ρ_{i} is the density of ice and $\boldsymbol{g}$ is the acceleration due to gravity. To disregard the free translation motion of the ice slab, we apply a boundary condition to enforce zero horizontal flow velocity at the left edge of the domain. On the right edge of the domain (i.e., the ice terminus), we apply a Neumann boundary condition corresponding to the hydrostatic pressure induced by seawater.

5.4.1 Model Sensitivity Studies

In a previous work (see Section 4.1 in Jiménez et al. [2017]), we have verified the nonlinear Stokes formulation describing ice sheet flow by showing that numerical results converge to a known analytical solution with progressive mesh refinement. In this section, we demonstrate the viability of the nonlocal creep damage mechanics formulation by conducting parametric and mesh sensitivity studies. For each study, we consider a grounded ice slab with height $H = 125$ m and length $L = 500$ m under dry conditions, that is, no water in surface crevasses ($h_s = 0$) and no seawater pressure at the ice terminus ($h_w = 0$).

Mesh sensitivity: We first demonstrate that the nonlocal damage mechanics formulation is not sensitive to the finite element mesh size by conducting a series of crack growth simulations using a progressively refined mesh. For each simulation, we use a structured mesh in the anticipated damage zone with element sizes $l_{\mathrm{elem}} = 5$, 2.5, and 1.25 m. An initial

10×10 m damage zone is centered along the top of the ice slab, and we only permit damage to nucleate beneath the initial damage zone. This is done by setting the local damage rate $\dot{D}^{\text{loc}} = 0$ at integration points beyond the distance l_c from the vertical line centered at the initial notch (i.e., at $x = L/2$). The results of this study are shown in Figure 5.4(a), wherein we plot the surface crevasse penetration depth ratio d_s/H. The crevasse depth d_s is obtained by measuring the lowest vertical coordinate of all fully-damaged material points and then subtracting from the slab height, as follows:

$$d_s = H - \min\{z \mid D(x,z) = D^{\max}\}. \tag{5.32}$$

The damage mechanics model predicts the same crevasse depth d_s versus time for up to six months, provided that the finite element size l_{elem} is smaller than the nonlocal damage characteristic length scale l_c.

Parametric sensitivity: We next demonstrate that the damage mechanics formulation predicts the same final crevasse penetration depth for different values of the length scale parameter l_c. For each simulation, we use a structured mesh in the anticipated damage zone with element sizes $l_c = 20$, 10, 5, and 2.5 m. An initial $l_c \times l_c$ m damage zone is centered along the top of the ice slab, and we only permit damage to nucleate beneath the initial damage zone. The results of this study are shown in Figure 5.4(b), wherein we plot the surface crevasse depth d_s normalized with slab height H. While the size of l_c affects the rate of crevasse propagation, it does not affect the final crevasse penetration depth. As the length scales is reduced the damage process zone near the crack tip becomes smaller, thus damage propagation occurs rapidly post-initiation similar to the unstable crack propagation described by linear elastic fracture mechanics.

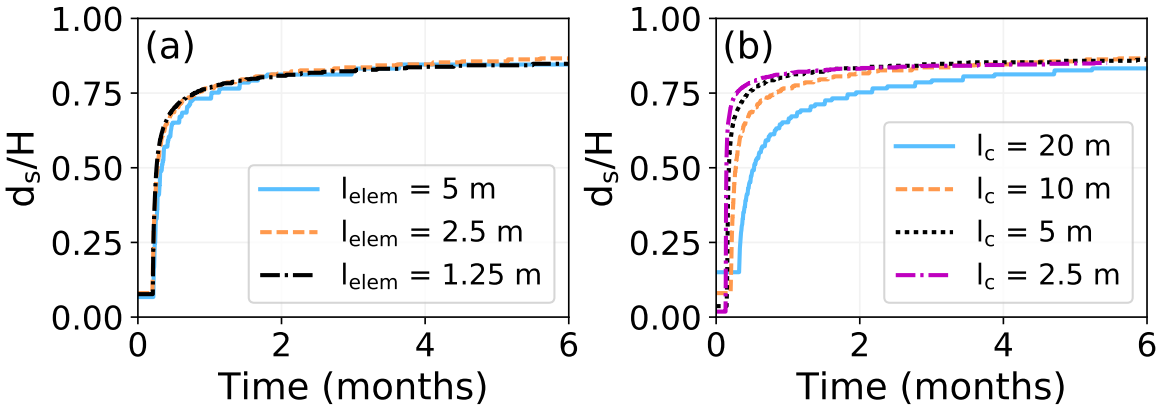

Figure 5.4: Surface crevasse depth d_s normalized with the domain height H versus time for (a) varying nonlocal length scale size and (b) varying mesh size.

5.4.2 Growth of an Isolated Surface Crevasse in Dry Environment

We first simulate the propagation of isolated surface crevasses through ice slabs of varying thickness $H = 125$, 250, and 500 m in a dry environment (i.e., $h_w = 0$, $h_s = 0$) under gravity loading. Our aim is to compare the final crevasse penetration depth ratio obtained using the nonlinear Stokes model with nonlocal damage against those from theoretical fracture mechanics models. For each experiment the slab length $L = 4H$, and the domain is discretized using triangular finite elements. To be consistent with the fracture mechanics approach, an initial defect (10×10 m notch) is prescribed along the top surface of the slab, and the domain is discretized using a structured mesh with element size $l_{\text{elem}} = 2.5$ m, underneath the initial notch. We set the initial defect at the center of the slab so that it is sufficiently far from the terminus, so that the σ_{xx} profile throughout the depth of the slab matches the "far-field" stress profile of Equation 48. To simulate the propagation of an isolated crevasse, we only allow damage to nucleate or accumulate beneath the initial defect, but we also repeat the experiment while allowing damage to accumulate everywhere in order to investigate the influence of damage in the "far-field" region on the isolated crevasse.

Figure 5.5 shows the surface crevasse penetration depth ratio d_s/H versus time for the

isolated surface crevass in relation to ice thickness, as predicted by our damage mechanics model. We also show the final crevasse depth ratios predicted by fracture mechanics models [Nye, 1957, Weertman, 1973, van der Veen, 1998a]. For the van der Veen solution we assume $K_{Ic} = 0$, and we take into account the depth of the ice slab by setting the geometric parameter $\lambda = d_s/H$ in Equations 58-59. The ratio d_s/H for the isolated crevasses predicted by our simulations ˜88% regardless of the slab height if damage is only permitted to nucleate under the initial defect, as shown in Figure 5.5(a). The thickness of the ice slab H seems to only influence the time required for the crevasse to reach its final penetration depth, which is deeper than both Weertman's and Nye's model predictions. For larger values of H, the tensile stresses in the ice slab are greater and hence damage accumulates more rapidly resulting in faster crevasse propagation. The final crevasse depth in this case seems to agree almost exactly with the van der Veen's model prediction. In Figure 5.5(b) we plot d_s/H versus time while permitting damage to accumulate everywhere in the domain. In this case, the crevasse penetrates to ˜88% of the slab depth when $H = 250$ and 500 m; however, when 125 m, the crevasse only penetrates to 83.6% of the slab's depth. This occurs because new crevasses forming elsewhere in the domain inhibit the growth of the primary crevasse (i.e., the crevasse propagating under the initial defect).

We now repeat the study while employing the updated-Lagrangian description in conjunction with the mesh update scheme, developed in Jiménez et al. [2017], wherein the positions of finite element nodes are updated to account for the changes in ice slab geometry due to large creep deformations accruing over time. We plot d_s/H versus time results obtained from this study in Figure 5.6. Regardless of the value of H, the crevasse penetrates deeper into the ice slab when the mesh is updated than when the mesh is not updated (compare Figure 5.5a and Figure 5.6a). This indicates that large-deformation-induced domain geometry changes can alter the stress state in the glacier and lead to deeper crevasse propagation. The influence of large deformation is especially evident in the case where $H = 500$ m and damage is allowed to accumulate everywhere in the domain (the blue line

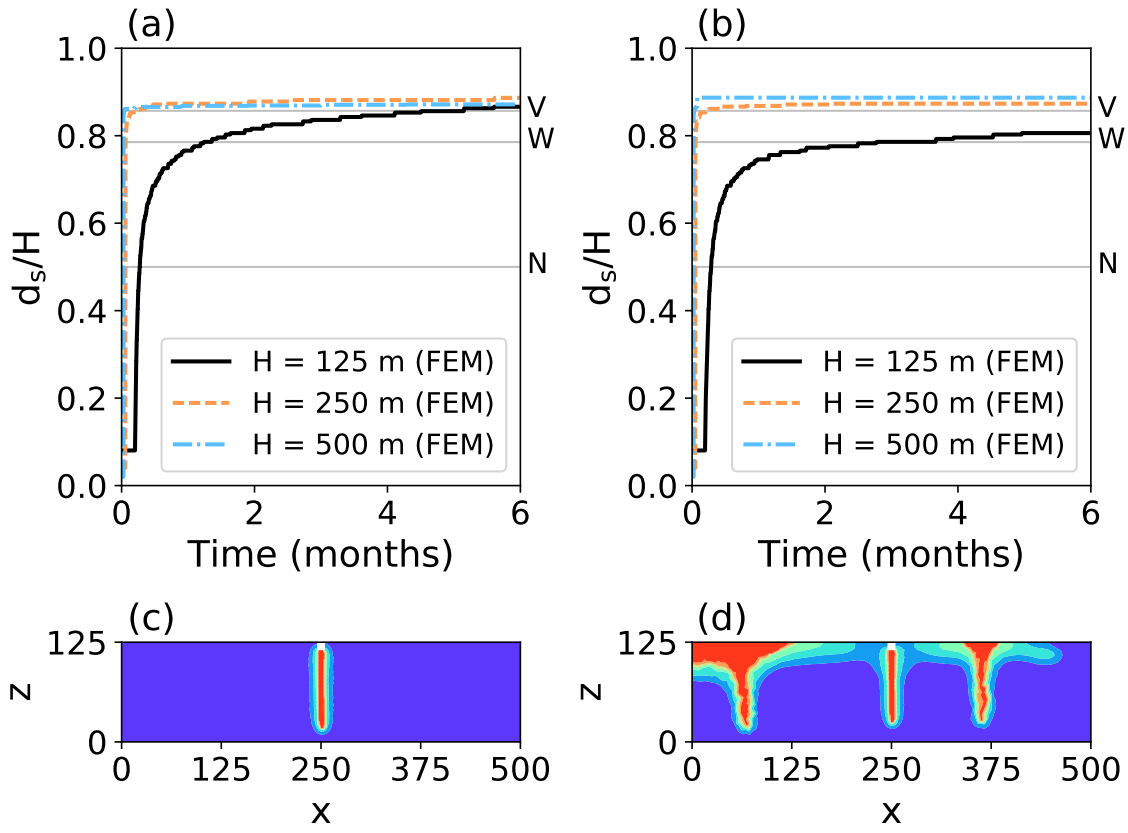

Figure 5.5: Surface crevasse depth d_s normalized with the domain height H versus time for varying slab heights. In subfigure (a), damage is only allowed to accumulate underneath the initial defect; in subfigure (b), damage is allowed to accumulate everywhere in the domain. The final damage profiles corresponding to subplots (a) and (b) are shown in subfigures (c) and (d), respectively, for the $H = 125$ m case. The red regions display where the damage variable $D = D^{\max}$, indicating the presence of a crevasse; whereas the blue regions display where D is close to zero (i.e., intact ice).

in Figure 5.6b), wherein the crevasse fully penetrates the ice slab. The crevasse first penetrates to 94.4% of the slab depth until tensile stress at the crack tip diminishes; however, as ice creeps and domain geometry changes, bending stresses along the crevasse walls contribute to damage nucleation beneath the crevasse tip, leading to the full penetration of the crevasse. While it is a rational argument that large deformation of ice sheets can influence crevasse propagation, in this study we do not consider snow accumulation in crevasse that leads to healing, so crevasses eventually propagation the entire depth of the ice slab.

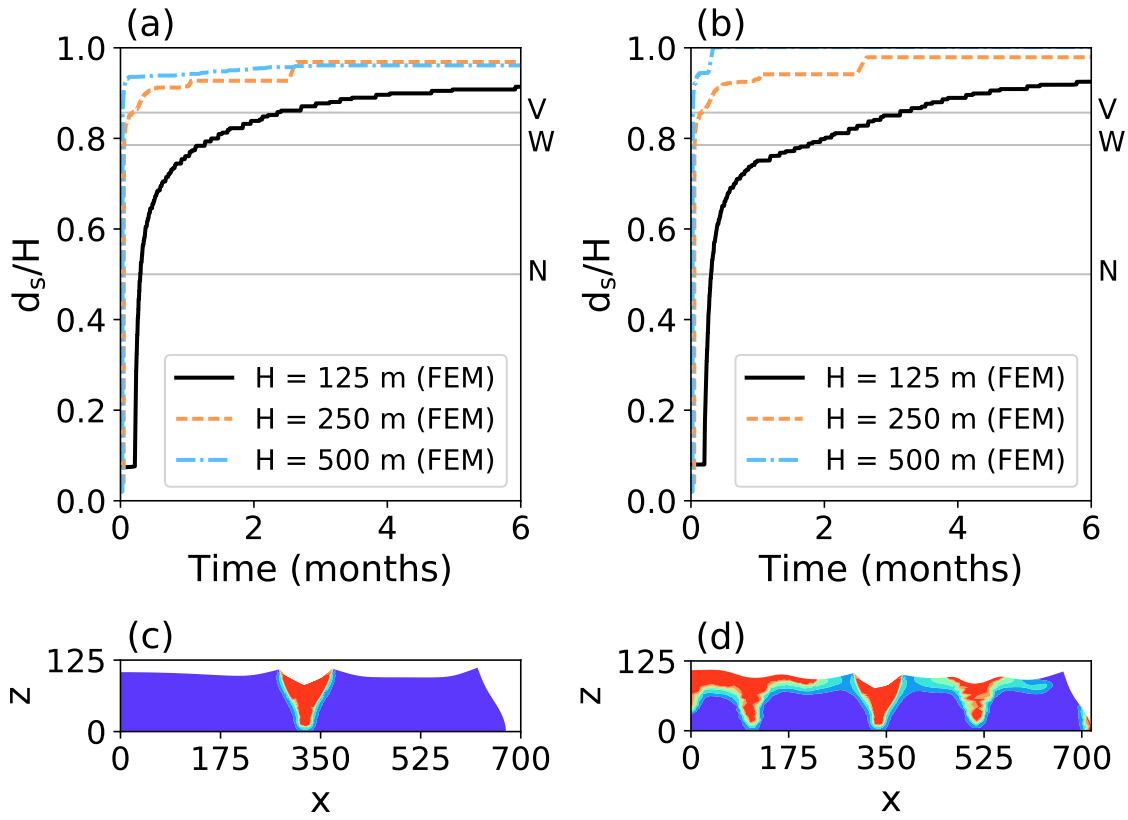

Figure 5.6: Surface crevasse depth d_s normalized with the domain height H versus time for varying slab heights using the mesh update scheme. In subfigure (a), damage is only allowed to accumulate underneath the initial defect; in subfigure (b), damage is allowed to accumulate everywhere in the domain.

5.4.3 Growth of Closely-spaced Surface Crevasses in Dry Environment

We next simulate the evolution of a field of closely-spaced crevasses in an ice slab with thickness H = 250 m and length L = 1,000 m in a dry environment (i.e., $h_w = 0$, $h_s = 0$) under gravity loading. Our aim is to compare the final crevasse penetration depth ratio obtained using the nonlinear Stokes model with nonlocal damage against that from the Nye zero-stress model, which is 50% of the ice slab's height in this case. In our computational model, we specify the uniform multiple crevasse field by evenly distributing small pre-damaged zones (i.e., fully damaged finite elements) along the top of the surface of the slab of size 10×40 m that are spaced 50 m apart from one another. The entire finite element

mesh is structured with an element size $l_{\text{elem}} = 2.5$ m, and damage is permitted to accumulate everywhere throughout the domain. The results of this experiment are displayed in Figure 5.7, wherein we show contour plots of the damage variable D at different simulation times.

From Figure 5.7(b) it is evident that damage accumulates near most of the initial crevasse tips; however, the damage evolves most rapidly near the crevasse at the left edge of the domain because the Hayhurst stress is the largest near that feature. As this first crevasse propagates downwards the other crevasses do not evolve much at all. Once the first crevasse penetrates about 61% of the slab's depth, the location of the maximum Hayhurst stress shifts to the initial defect at $x = 650$ m (which we refer to as the "secondary crevasse"). At that point, the second crevasse begins to rapidly propagate while the other crevasses throughout the slab do not evolve. Once the second crevasse propagates about 80% of the slab depth, the third crevasse begins to propagate at $x = 350$ m. The simulation depicts a different damage evolution process than the theoretical model, which assumes the existence of a uniform multiple crevasse field where each crevasse will propagate to the Nye depth where the tensile stress vanishes (i.e., 50% of the slab). As De Robin [1974] argues "in practice one will not have a perfectly uniform field of crevasses" and our simulation describes the more realistic situation. To summarize, the Nye model predicts that all the crevasses will propagate to the same depth, whereas the numerical study indicates that only a few crevasses propagate that are approximately 300 m apart (i.e., close to one ice thickness apart). Further, the simulation results show that only one crevasse propagates at a time as if it were an isolated crevasse, although the maximum crevasse penetration depth of any crevasse is less than the isolated crevasse penetration depth.

5.4.4 Surface Crevasse Growth in Wet Environment

In this section, we simulate the propagation of isolated, water-filled surface crevasses in the ice slab under gravity loading as a function of the water level h_s within the crevasses

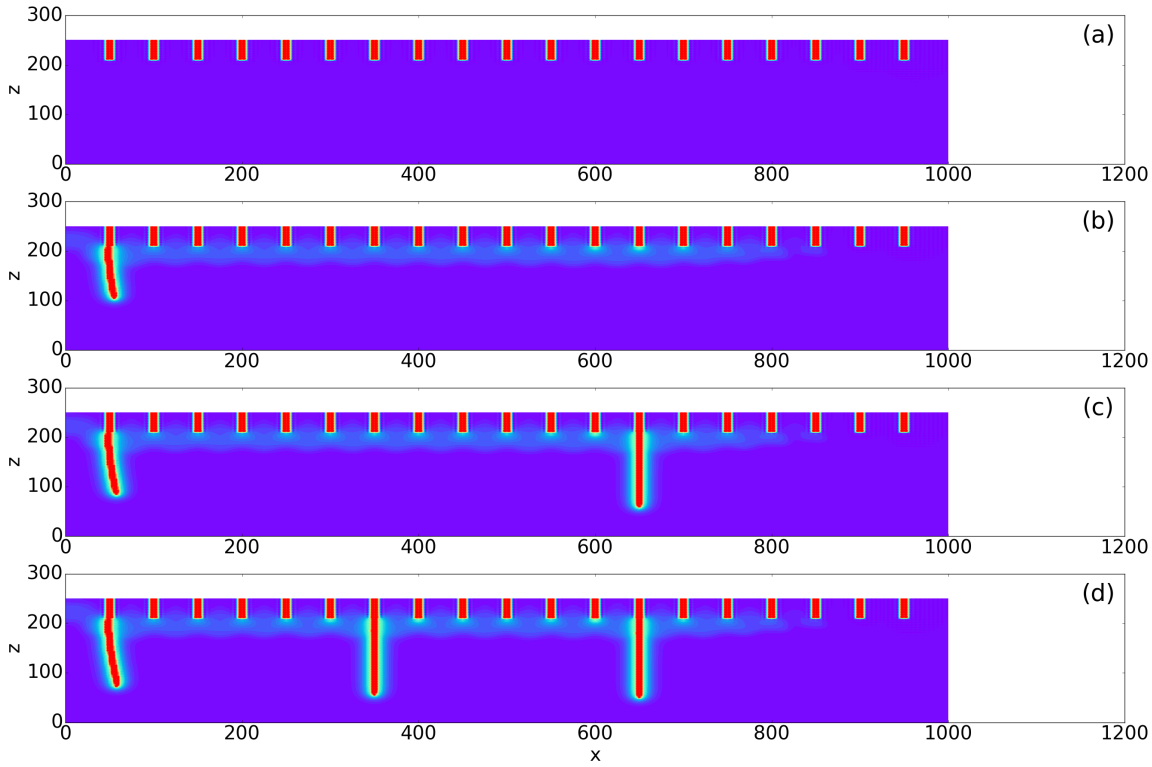

Figure 5.7: Crack propagation predicted by the nonlinearly viscous constitutive model in an ice slab at (a) initial time, (b) 66.36 hours, (c) 71.56 hours, and (d) 81.42 hours of gravity-driven creep flow. The red regions display where the damage variable $D = D^{\max}$, indicating the presence of a crevasse; whereas the blue regions display where D is close to zero (i.e., intact ice).

and the seawater depth h_w at the ice slab's terminus. Our aim is to compare final crevasse penetration depths predicted by the damage mechanics model for different ice rheologies (i.e., elastic, viscous, nonlinear viscous) against the three theoretical fracture mechanics models. For each loading case, we consider an ice slab of depth $H = 125$ m and length $L = 500$ m, and we prescribe a 10×10 m initial defect as a pre-damaged zone centered along the top surface of the slab. To be consistent with the fracture mechanics models, damage is only permitted to nucleate beneath the initial damage zone where the mesh is structured with an element size $l_{\text{elem}} = 2.5$ m. The hydrostatic pressure from seawater is applied as a traction (Neumann) boundary condition normal to the right edge of the ice slab with magnitude $-\rho_{\text{w}} g \langle h_w - z \rangle$, and the hydraulic pressure p_w within the crevasse (damage

zone) is applied using the poro-mechanics formulation with magnitude $p_w = \rho_w g \langle h_s - z \rangle$. In order to keep the ratio of h_s/d_s constant, we dynamically compute the crevasse depth d_s at each time step in the simulation and then readjust the water level h_s accordingly.

Figure 5.8 shows the normalized crevasse depth d_s/H for isolated crevasses filled with water to varying levels, $h_s/d_s = 0\%$, 25%, 50%, 75%, and 100%, within ice slabs terminating at the ocean with varying sea levels, $h_w/H = 0\%$, 50%, and 90% (floating level), as predicted by the four theoretical models [Nye, 1957, Weertman, 1973, van der Veen, 1998a, Krug et al., 2014] and our computational model. For the Krug et al. [2014] and van der Veen [1998a] models, we set $K_{Ic} = 0$ MPa $\sqrt{\text{m}}$ and include the geometry factors, thus accounting for the finite thickness of the ice slab; whereas, the Weertman [1973] model assumes the ice slab to be a semi-infinite plane. It is interesting that our numerical results for crevasse penetration in a finite ice slab agree well with the van der Veen [1998a] and Krug et al. [2014] model results for a semi-infinite ice slab, that is, when geometry factors are *excluded* in the stress intensity factor (SIF) calculation (Figures 11d–11f in Appendix L). However, the numerical results do not match well with the Krug et al. [2014] and van der Veen [1998a] model results (see Figs. 5.8b and 5.8c) when the geometric factors are *included* in the SIF calculation. The reason for this discrepancy is that the geometric factors in the LEFM models were not derived assuming the same loading conditions considered in the gravity-driven flow problem, that is, gravity-induced stresses in an ice slab grounded on a free-slip surface, as shown in Figure 5.1. Rather, the geometric factors were derived assuming a cantilever beam (i.e., with no grounding) with an applied moment at the end. Even through the "far-field" horizontal Cauchy stress σ_{xx} is the same for these two loading scenarios, the absence of the grounding line completely changes the value of the SIF. Thus, the crevasse penetration depths predicted by the LEFM models with geometric factors included are not physically relevant for glaciological problems. A more detailed explanation is provided in Appendix M. In all cases, the Krug et al. [2014] model predicts deeper crevasse penetration than the damage mechanics model, unless the crevasse penetrates the full-depth (see Fig.

5.8b).

Figures 5.9a, 5.9c, and 5.9d show the simulation results for nonlinearly viscous, linear elastic, and linearly viscous rheological models, respectively when using the Hayhurst stress (HHS) damage criterion (i.e., $\alpha = 0.21$ and $\beta = 0.63$ in Equation 5.25). Each rheology model shows qualitative agreement with the theoretical solutions, wherein higher water levels h_s/d_s within the crevasse result in deeper surface penetration, except when the ice slab is at near floating condition (i.e., $h_w/H \neq 90\%$). For the near floating condition, the simulation results predict little damage growth beyond the depth of the initial defect, irrespective of the rheology model. This occurs because the numerically computed stress is compressive beneath the crack tip, so damage does not develop. In Figure 5.9b, we plot the simulation results when using a maximum principal stress (MPS) criterion for purely brittle failure of ice (i.e., $\alpha = 1$ and $\beta = 0$ in Equation 5.25) and relaxing the pressure criterion for damage initiation in Equation 5.24. In the case of $h_w/H = 50\%$, the simulation results using the MPS criterion match exactly with the Weertman [1973] model; however, we do not necessarily conclude that the MPS criterion is better than the HHS criterion for damage evolution. We also investigated the h_w/H versus h_s/d_s in an ice slab with height $H = 250$ m while using the HHS damage criterion, and the simulations results exactly match with the Weertman [1973] model for the $h_w/H = 50\%$ case (see Fig. 12 in Appendix L).

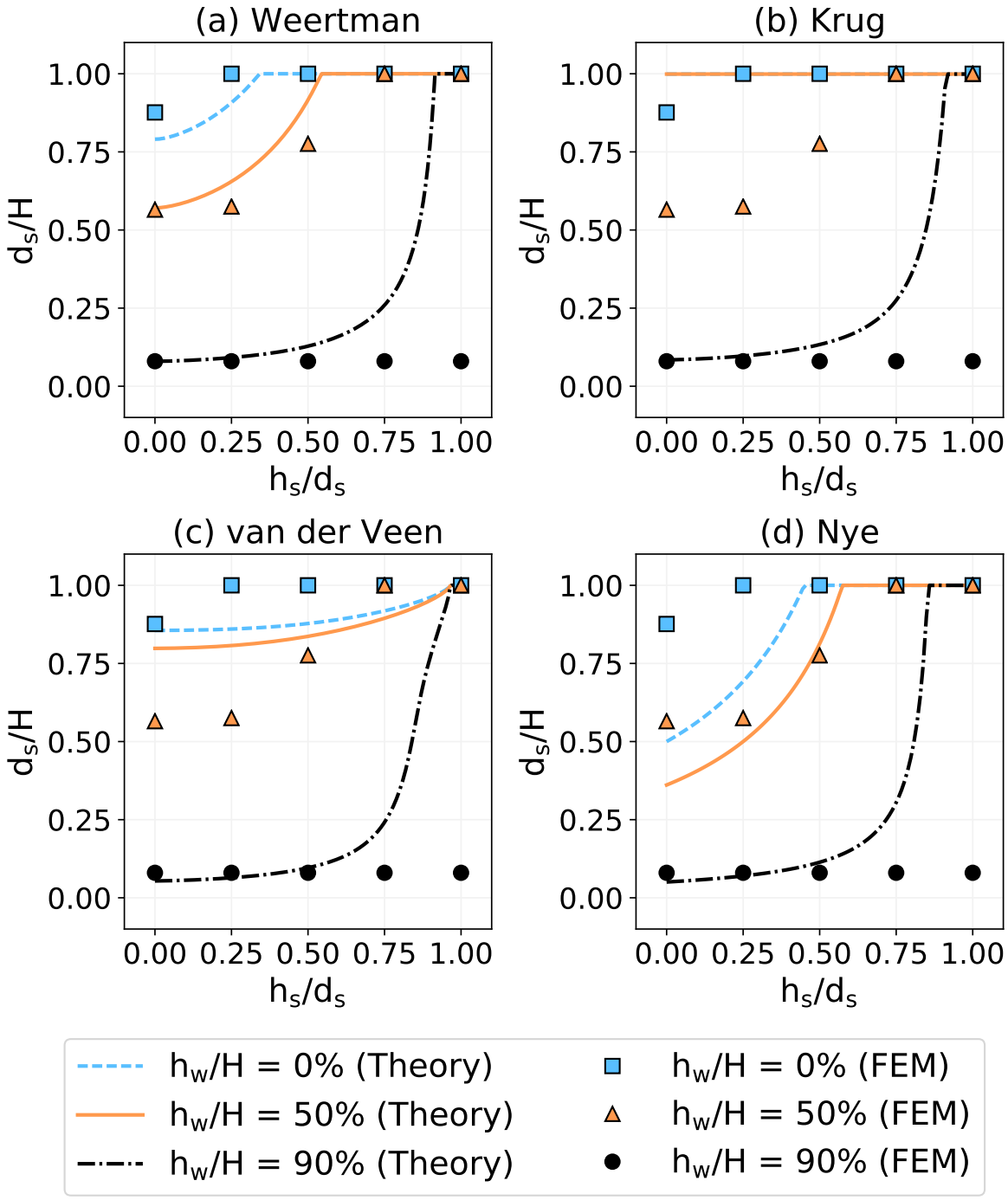

Figure 5.8: Surface crevasse depth d_s normalized with the domain height $H = 125$ m for varying water levels h_s filling the surface crevasse. The solid, dashed, and dotted lines depict the stress-based solutions for different seawater depths h_w at the terminus. The markers represent simulation (FEM) results using the nonlinearly viscous (Stokes flow) rheological model for different depths.

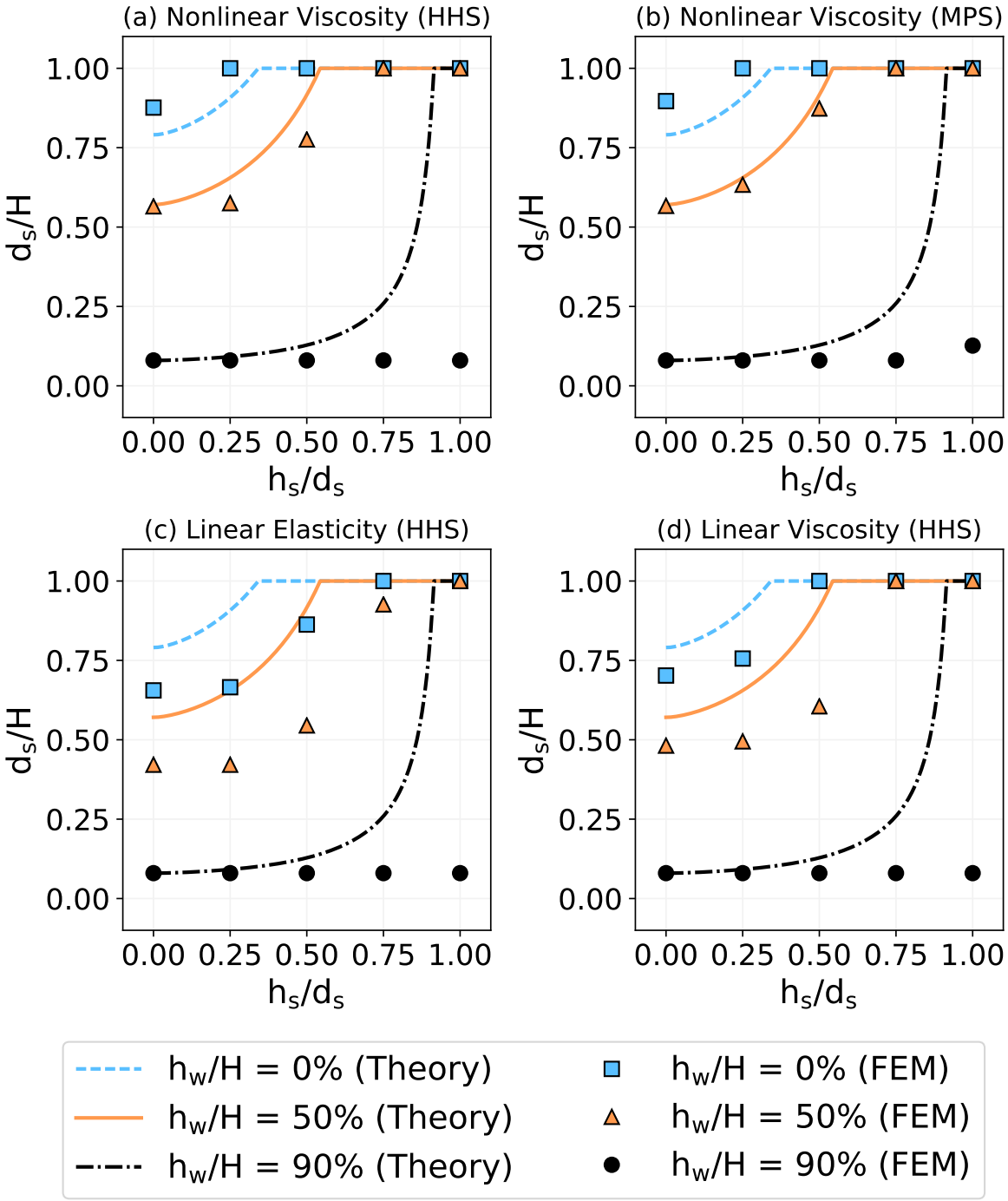

Figure 5.9: Surface crevasse depth d_s normalized with the domain height $H = 125$ m for varying water levels h_s filling the surface crevasse. The solid, dashed, and dotted lines depict the stress-based solutions for different seawater depths h_w at the terminus. The markers represent simulation (FEM) results using different rheological models: (a-b) nonlinear viscosity; (c) incompressible linear elasticity; and (d) linear viscosity. The terms (HHS) and (MPS) denote a Hayhurst stress and maximum principal stress-based damage criterion, respectively.

5.5 Conclusion

In this chapter, we reviewed and compared four theoretical fracture mechanics models for estimating crevasse penetration depths against one another: (1) the Nye [1955] zero-stress model; (2) the Weertman [1973] dislocation-based fracture mechanics model; (3) the van der Veen [1998a] linear elastic fracture mechanics (LEFM) model; and (4) the Krug et al. [2014] LEFM model. We also compared the nonlocal continuum damage mechanics (CDM) approach [Jiménez et al., 2017] against these theoretical models by estimating the penetration depths of dry and water-filled surface crevasses in grounded glaciers. The damage mechanics approach illustrates that the presence of water pressure within crevasses results in deeper penetration into the glacier, thus it is consistent with the fracture mechanics approaches. Numerical results show good agreement with Weertman [1973] model, except when the glacier is near floatation (i.e., $h_w/H = 0.9$). Our results also indicate that the mechanisms responsible for crevasse propagation are sensitive to ice rheology and large deformation effects. Through extensive simulation studies, we have addressed the four key questions raised in Section 5.2.6:

i. Numerical results suggest that the Nye zero-stress model would underestimate the penetration depth of crevasses because the underlying assumption of a perfectly uniform field of closely-spaced crevasses is unrealistic. Rather than evolving uniformly, the crevasses propagate independently one at a time and penetrate almost as deeply as an isolated crevasse (see Fig. 5.7). Additionally, our results indicate that the deeper crevasses are spaced at distance approximately equal to ice thickness (see Fig. 5.7d), which is much larger than the minimum spacing predicted by the LEFM models [Nemat-Nasser et al., 1979]. Therefore, we conclude that theoretical Nye model is not appropriate for estimating penetration depths of surface crevasses; however, in a numerical model it may still be appropriate if used recursively until the tensile stress at the crevasse tip vanishes [Ultee and Bassis, 2016].

ii. The theoretical fracture mechanics models are not consistent with one another, except when the glacier is at near floatation (see Fig 5.3). If the geometric parameter λ is disregarded in the van der Veen and Krug models by setting $\lambda = 0$, then the two models are consistent with the Weertman model (see Figure 11 in Appendix L). The creep damage mechanics approach also seems to be most consistent with the Weertman model, except when $h_w/H = 90\%$, in which case the damage model deviates from all the fracture mechanics models (see Fig. 5.8). This occurs because the nonlocal damage evolution law reduces the stress concentration at the crevasse tip, and damage growth is consequently limited to a small region around the initial crack. In the fracture mechanics models, the stress at the crevasse tip remains tensile enough for the crevasse to penetrate because the crevasse is assumed to be a sharp discontinuity rather than a diffused damage zone. The failure behavior of quasi-brittle materials (e.g., ice and concrete) is better described by nonlocal damage theory [Bazant, 1994] than LEFM theory. Therefore, we hypothesize that damage mechanics models are more appropriate for estimating crevasse penetration depths, although this needs to validated with observational or remote sensing data.

iii. We found that large creep deformations accruing over longer time scales influence the penetration depth of surface crevasses. Typically, considering the effects large deformations within an updated-Lagrangian formulation leads to deeper crevasse penetration (see Fig. 5.6), as opposed to ignoring them within a Lagrangian formulation (see Fig. 5.5). This occurs because glacier geometry changes induced by large deformations can cause additional bending stresses along the crevasse walls, thus prying open the crevasses deeper into the glacier.

iv. Fully water-filled crevasses can penetrate the entire thickness of a grounded glacier when accounting for viscous creep and nonlocal damage, except under near-floatation conditions. We find that the predicted crevasse depths are larger when considering

the nonlinearly viscous behavior of ice as opposed to linear elastic or linear viscous behavior (see Fig. 5.9). We also find that the predicted crevasse depths are relatively insensitive to the brittle-ductile damage model parameters α and β (compare Figs. 5.9a and 5.9b). Furthermore, the predicted crevasse depth is insensitive to the nonlocal damage length scale l_c and finite element mesh size l_{elem} (see Fig. 5.4), which reduces the parametric uncertainty when calibrating damage mechanics-based calving laws to observational or remote sensing data on crevasse locations, depths, and spacing.

In conclusion, we believe that the damage mechanics approach is appropriate for simulating the propagation of water-filled surface crevasses and estimating their maximum penetration depths. In our future work, we aim to establish this approach for simulating the propagation of water-filled basal crevasse propagation in glaciers and ice shelves.

Acknowledgements

We gratefully acknowledge the funding support provided by the National Science Foundation's Office of Polar Programs via grants #PLR-1341428 and #PLR-1341568.

CHAPTER 6

CAN A WATER-FILLED CREVASSE PENETRATE THE ENTIRE THICKNESS OF GLACIER? A SIMULATION STUDY.

6.1 Introduction

It is the general consensus that crevasses (fractures) in glaciers and ice sheets are formed under the action of tensile stress induced by longitudinal creeping flow. Additionally, the hydraulic pressure imposed by water (e.g., seawater or meltwater) filling the crevasse is theorized to increase the crevasse penetration depth through the ice sheet thickness. The full penetration of crevasses near the ice sheet terminus ultimately leads to iceberg calving, a mechanism responsible for significant mass loss from Greenland and Antarctic ice sheets into the ocean. Consequently, a variety of stress-based calving models have been presented in the literature to characterize calving mathematically by predicting the penetration depth of surface and basal crevasses. The most basic of these is the Nye zero-stress model Nye [1955] which assumes that ice has no tensile strength; thus, the crevasse will penetrate to any depth where tensile stress exists. More rigorous calving models rooted in dislocation mechanics [Weertman, 1973] and linear elastic fracture mechanics (LEFM) [van der Veen, 1998a,b, Krug et al., 2014] have been developed to account for stress concentrations at the crevasse tip, thus predicting deeper penetration than the Nye model. These latter fracture mechanics models were derived assuming ideal conditions in ice, such as a rectangular (or semi-infinite) domain with far-field boundary conditions, however, and their applicability to the general loading scenario is questionable. Furthermore, the theoretical fracture mechanics models treat ice an incompressible, linear elastic material and fracture as an instantaneous event. In reality, ice has the properties of a nonlinearly viscous, incompressible fluid over long time scales, but it behaves as a compressible solid over the short

(instantaneous) time scale.

The alternate approach to studying crevasse evolution in ice sheets is numerical analysis. Damage mechanics offers an attractive framework for modeling crevasse initiation and propagation through ice slabs for multiple reasons: firstly, damage mechanics is easily implemented within the finite element analysis, making it feasible to incorporate into large-scale ice sheet models (e.g., CISM); secondly, the damage mechanics framework is flexible in that it allows customizable damage criteria while being independent ice rheology; and thirdly, damage mechanics is applicable for studying crevasse evolution in arbitrary loading scenarios (not only ideal conditions). Previous works [Pralong and Funk, 2005, Duddu and Waisman, 2013c, Jiménez et al., 2017] have employed creep damage mechanics approaches to model the time-dependent crevasse evolution in nonlinearly viscous or viscoelastic ice. Recently, Mobasher et al. [2016, 2017] presented a poro-mechanics formulation for incorporating hydraulic fracture into a local creep damage mechanics model to simulate the evolution of water-filled surface and basal crevasses in viscoelastic ice. The same approach was adopted in Chapter 5 using a *nonlocal* creep damage mechanics model paired with nonlinearly viscous rheology, wherein we compared numerically predicted surface crevasse penetration depths against a variety of theoretical fracture mechanics models [Nye, 1955, Weertman, 1973, van der Veen, 1998a, Krug et al., 2014]. In the previous study we found that the creep damage model is at least qualitatively consistent with fracture mechanics when predicting water-filled surface crevasse evolution in grounded ice sheets with seawater pressure at the terminus, except when the seawater level is near the floating depth. The discrepancy in the floating depth case was attributed to softening-induced stress relaxation at the crack tip resulting from the nonlocal smearing of damage. In light of our findings in the previous study we note two key differences between the nonlocal creep damage mechanics implementation and the theoretical fracture mechanics models: (1) the theoretical models consider brittle fracture to be an instantaneous event, whereas the creep model introduces time and rate dependencies on the damage nucleation; and (2) the theo-

retical models consider the fracture as a sharp (zero or near zero-thickness) discontinuity in the material domain, whereas the nonlocal damage model resolves the fracture using a smeared approach.

In this present study, we will investigate two additional damage mechanics approaches for simulating brittle, time-independent (instantaneous) fracture in elastic ice, namely, the cohesive zone model (CZM) and the phase field model (PFM), which are inherently more consistent with the theoretical fracture mechanics models. The cohesive zone model resolves the potential crack path as a degradable, zero-thickness interface whose constitutive behavior is governed by a traction-separation law. The fundamental cohesive parameter is the Griffith critical fracture energy, G_c, which is a material property characterizing the rate of energy released through the separation of material to create a fracture surface. Traditionally, the CZM has been used to model debonding and delamination behavior in composite materials [Jimenez and Duddu, 2016]; however, recent works have employed the CZM for more general applications, including grain boundary separation in polycrystalline materials and hydraulic fracture [Chen et al., 2009, Carrier and Granet, 2012]. In this work, we will implement the CZM to model the initiation and propagation of surface and basal crevasses through ice. Alongside the CZM we consider the phase field model, which has recently been used to model brittle fracture by resolving the discontinuity as a smeared damage interface with a characteristic length scale l_c. Early phase field models were derived by relating the softening of material to the energy release rate G_c, and thus have some thermodynamic consistency [Miehe et al., 2010]; however, the PFM has also been recast into a more generalized, modular format allowing for arbitrary failure criteria [Miehe et al., 2015]. In spite of its recent popularity, the PFM is not fully mature as a damage mechanics technique. Most works in the literature only apply the PFM to evaluate benchmark problems, whereas the direct application of the PFM to practical problems (i.e., thermoelastic fracture in brittle solids [Miehe et al., 2015] and hydraulic fracture [Wilson and Landis, 2016]) is sparse.

The primary goal of this current study is to simulate the evolution of water-filled surface and basal crevasses through ice sheets using time-independent approaches for brittle fracture and to compare the numerically predicted crevasse penetration depths against the theoretical fracture mechanics model predictions. The secondary goal is to identify the conditions necessary for crevasse initiation and discuss these in light of the constitutive assumptions often made for ice (i.e., incompressibility). To this end, we deploy the CZM and PFM as sharp and diffuse damage mechanics approaches using the finite element method. The rest of this chapter is organized as follows: in Section 6.2, we will present the CZM and PFM formulations for modeling the evolution of water-filled crevasses through ice; in Section 6.3, we will conduct a series of numerical studies to investigate the applicability of the two damage mechanics approaches to fracture, along with a brief study on the influence of the compressibility ratio on ice; and in Section 6.4, we will offer concluding remarks.

6.2 Model formulation

In this section, we review two damage mechanics based approaches for modeling the evolution of water-filled crevasses in linear elastic ice. First, we present an augmented cohesive zone model (CZM) that incorporates hydraulic pressure into the traction-separation relation. Next, we review the phase field model (PFM) for brittle fracture governed by strain energy density based and maximum principal stress based failure criteria. As we discuss the preliminary concepts of the phase field formulation, we also describe the model in the context of the continuum damage mechanics (CDM) framework. Afterward, we describe the constitutive model for damaged, incompressible, linear elastic ice and incorporate a poro-mechanics formulation [Mobasher et al., 2016, 2017] for hydraulic fracture.

6.2.1 Cohesive zone model

The cohesive zone model (CZM) is a numerical approach to progressive fracture evolution which considers the crack as a sharp (zero-thickness) interface. Cohesive (interface) elements are distributed along the potential crack surface between bulk (continuum) elements, and the cohesive constitutive behavior is governed by a traction-separation law. Typically, the traction-separation law comprises an initial linear-elastic response to loading followed with irreversible damage-softening behavior. The most common (and basic) traction-separation laws include two fundamental parameters, namely, the cohesive strength $\sigma_{\max}$, which is the maximum traction that the interface can support; and the critical strain energy release rate G_c. In practice, G_c is determined experimentally with relative ease, whereas $\sigma_{\max}$ is chosen for numerical purposes. Park and Paulino [2012] have shown that as $\sigma_{\max}$ approaches infinity, the cohesive zone model tends towards the linear elastic fracture mechanics (LEFM) solution. This behavior is observed because as the value of $\sigma_{\max}$ increases, the size of the cohesive length scale decreases, which is consistent with the LEFM assumption of an infinitesimally small fracture process zone. Decreasing the

length scale requires an increasingly refined finite element mesh for a numerical accuracy [Harper and Hallett, 2010], however, and so a low value for $\sigma_{\max}$ is often chosen for convenience. Some traction-separation laws include additional parameters that control the shape of the damage-softening zone, however, global results are generally insensitive to the shape of the traction-separation law [Jimenez and Duddu, 2016]. Irrespective of the shape, any traction-separation law may be written in the general form [Alfano and Crisfield, 2001],

$$\begin{Bmatrix} T_{\mathrm{n}} \\ T_{\mathrm{t}} \end{Bmatrix} = (1 - D(\delta_{\mathrm{n}}, \delta_{\mathrm{t}})) \begin{bmatrix} K_{\mathrm{n}}^0 & 0 \\ 0 & K_{\mathrm{t}}^0 \end{bmatrix} \begin{Bmatrix} \delta_{\mathrm{n}} \\ \delta_{\mathrm{t}} \end{Bmatrix}, \tag{6.1}$$

where $T_{\mathrm{n}},\ T_{\mathrm{t}}$ denote tractions; $\delta_{\mathrm{n}},\ \delta_{\mathrm{t}}$ denote the interface separations; $K_{\mathrm{n}}^0,\ K_{\mathrm{t}}^0$ denote the undamaged interface stiffnesses; and the subscripts "n" and "t" denote the normal and tangent directional components, respectively. The isotropic damage variable $D \in [0,1]$ is a function of the cohesive separations, and the function chosen for D ultimately controls the traction-separation shape. A review of bilinear, polynomial, and exponential traction-separation laws is provided in Section 3.2; for this study, we utilize the bilinear traction-separation law described in Section 3.2.1.

Remark 35 *In continuum damage mechanics, the damage is interpreted as the ratio of the area of voids to total area along the principal planes of a representative domain of material. Thus, the damage variable $D \in [0,1]$, with $D = 0$ and $D = 1$ representing undamaged (virgin) material and fully-damaged material states, respectively. In the CZM framework, the damage may be interpreted as the ratio of micro-crack area to total surface area along the zero-thickness cohesive interface.*

Herein, we present an augmented traction-separation law that incorporates hydraulic fracture. As we interpret damage to represent the ratio of isotropic void area to total area along the cohesive interface, we assume that water can permeate the damaged material and

exert hydrostatic pressure along the interface. Our implementation is based on the poro-mechanics approach in Mobasher et al. [2016, 2017] for hydraulic fracture in ice sheets using continuum damage mechanics, which extends Biot's theory of poroelasticity [Biot, 1955] by considering damage to have the same effect on the material behavior as porosity. Poroelasticity theory states that the Cauchy stress $\boldsymbol{\sigma}$ in a porous media is given by,

$$\boldsymbol{\sigma} = (1-\phi)\widetilde{\boldsymbol{\sigma}} - \phi p_w \boldsymbol{I}, \tag{6.2}$$

where $\widetilde{\boldsymbol{\sigma}}$ is the effective Cauchy stress tensor, ϕ is the material porosity, p_w is the hydraulic pressure, and $\boldsymbol{I}$ is the identity tensor. The above equation can be recast as a damage mechanics formulation simply by replacing the porosity ϕ with the damage variable D:

$$\boldsymbol{\sigma} = (1-D)\widetilde{\boldsymbol{\sigma}} - D p_w \boldsymbol{I}. \tag{6.3}$$

The poro-mechanics approach to hydraulic fracture may be similarly applied to the CZM by introducing a new term to the traction-separation law in Equation 6.1 that accounts for hydraulic pressure in the damaged zone. The *augmented* traction-separation law is thus written as,

$$\begin{Bmatrix} T_\mathrm{n} \\ T_\mathrm{t} \end{Bmatrix} = (1-D(\delta_\mathrm{n},\delta_\mathrm{t})) \begin{bmatrix} K_\mathrm{n}^0 & 0 \\ 0 & K_\mathrm{t}^0 \end{bmatrix} \begin{Bmatrix} \delta_\mathrm{n} \\ \delta_\mathrm{t} \end{Bmatrix} - D(\delta_\mathrm{n},\delta_\mathrm{t}) p_w \begin{Bmatrix} 1 \\ 0 \end{Bmatrix}, \tag{6.4}$$

with the hydraulic pressure defined by,

$$p_w = \rho_w g \langle h - z \rangle, \tag{6.5}$$

where ρ_w, g, h, and z denote the density of water, gravity acceleration, water level, and the vertical coordinate respectively. Because hydrostatic pressure only acts in the direction

normal to the surface (i.e., the cohesive interface), we apply p_w in Equation 6.4 to the normal traction T_{n}.

6.2.2 Phase field model

Unlike the cohesive zone model, the main concept behind phase field modeling of fracture is to represent a sharp material discontinuity (i.e., a fracture) Γ using a smeared interface $\Gamma_l(D)$ [Miehe et al., 2010, 2015, de Borst and Verhoosel, 2016],

$$\Gamma_l(D) = \int_\Omega \gamma_l(D, \nabla D)\, \mathrm{d}V, \tag{6.6}$$

for some crack surface density function $\gamma_l(D, \nabla D)$ defined on a material domain Ω. The scalar phase field variable $D \in [0,1]$ represents an isotropic damage field that describes the ratio of void space (i.e., cracks) to solid (intact) material within a representative area of the material's microstructure; hence, $D = 0$ corresponds to an undamaged material state, whereas $D = 1$ indicates complete failure. In the one-dimensional setting, the sharp interface Γ is represented using a piecewise function for damage,

$$D(x) = \begin{cases} 1 & x = 0, \\ 0 & \text{otherwise}, \end{cases} \tag{6.7}$$

with the discontinuity (crack) centered at $x = 0$. We consider a continuous, but non-smooth approximation to Eq. (6.7),

$$D(x) = \exp\left\{ \frac{-|x|}{l_c} \right\}, \tag{6.8}$$

satisfying the conditions $D(0) = 1$ and $D(\pm\infty) = 0$, and with a characteristic length scale l_c controlling the extent of the damage spread. A visual comparison between the above two equations and the effect of the length scale parameter is provided in Figure 6.1. Obviously,

as $l_c \to 0$ the damage spread decreases, and the shape of Eq. (6.8) tends towards the piecewise function in Eq. (6.7). In the multi-dimensional case, we define the smeared interface $\Gamma_l(D)$ as the functional [Miehe et al., 2010],

$$\Gamma_l(D) := \int_\Omega \underbrace{\frac{1}{2l_c}\left(D^2 + l_c^2 |\nabla D|^2\right)}_{\gamma_l(D,\nabla D)} \, \mathrm{d}V, \tag{6.9}$$

which gives a measure for the surface area of the crack. The integrand in the above equation is none other than the crack surface density function $\gamma_l(D,\nabla D)$, as presented in Eq. (6.6). The Euler-Lagrange equation associated with Eq. (6.9) is,

$$D - l_c^2 \Delta D = 0, \tag{6.10}$$

with Δ indicating the Laplace operator. We note that, in the one-dimensional setting, the function in Eq. (6.8) describing the spread of damage throughout the smeared interface is a solution to the above differential equation.

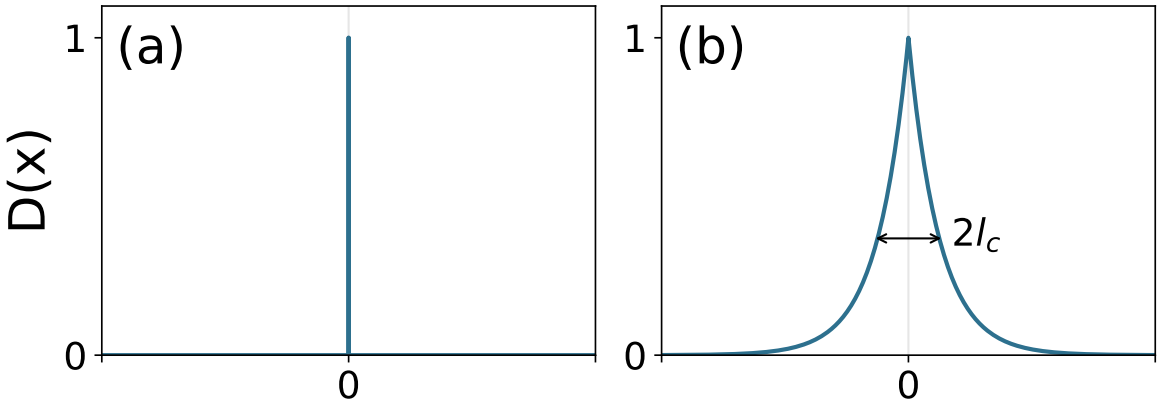

Figure 6.1: One-dimensional damage profile for (a) a sharp interface described by Eq. (6.7) and (b) a smeared interface described by Eq. (6.8).

6.2.2.1 Strain energy density-based phase field model

Let us consider the energy release associated with the growth of a sharp discontinuity $\Gamma \subset \Omega$ through a brittle fracture mechanism. The work required to create a surface Γ may be approximated as the work required for material softening (resulting from damage nucleation) over the smeared interface,

$$W_c(D) := \int_\Omega G_c \gamma_l(D, \nabla D) \, \mathrm{d}V \approx \int_\Gamma G_c \, \mathrm{d}A, \tag{6.11}$$

where G_c is the Griffith's critical energy release rate. The potential energy of the volume Ω including a smeared interface $\Gamma_l(D)$ is given by,

$$U_{\text{pot}} = \int_\Omega \Psi_e + G_c \gamma_l(D, \nabla D) \, \mathrm{d}V, \tag{6.12}$$

where $\Psi_e := \Psi_e(\boldsymbol{\epsilon}, D)$ is the elastic strain energy density given as a function of the damage field D and applied strain tensor $\boldsymbol{\epsilon}$. The effect of damage on the strain energy density is prescribed using a material degradation function $\theta(D)$:

$$\Psi_e(\boldsymbol{\epsilon}, D) = \theta(D)\Psi_e^d(\boldsymbol{\epsilon}) + \Psi_e^i(\boldsymbol{\epsilon}), \tag{6.13}$$

with Ψ_e^d indicating the component of Ψ_e affected by damage and Ψ_e^i indicating the "intact" component of Ψ_e not affected by damage. It is commonly assumed that damage only influences the behavior of materials under tensile loading [Miehe et al., 2010, 2015, de Borst and Verhoosel, 2016], whereas under compressive loading the material experiences crack surface contact (or crack closure). Thus, Ψ_e^d and Ψ_e^i are typically determined by performing a spectral decomposition of the strain tensor into positive (tensile) and negative (compres-

sive) components,

$$\boldsymbol{\epsilon}^{+} = \sum_{a=1}^{3} \left\langle \boldsymbol{\varepsilon}^{(a)} \right\rangle_{+} \hat{\boldsymbol{n}}_a \otimes \hat{\boldsymbol{n}}_a, \tag{6.14a}$$

$$\boldsymbol{\epsilon}^{-} = \sum_{a=1}^{3} \left\langle \boldsymbol{\varepsilon}^{(a)} \right\rangle_{-} \hat{\boldsymbol{n}}_a \otimes \hat{\boldsymbol{n}}_a, \tag{6.14b}$$

where $\boldsymbol{\varepsilon}^{(a)}$ are the principal strains, $\hat{\boldsymbol{n}}_a$ are the principal strain directions, $\otimes$ indicates the dyadic product, and $\langle\cdot\rangle_{+}$ and $\langle\cdot\rangle_{-}$ are the positive and negative Macaulay brackets, respectively, given by,

$$\langle x \rangle_{+} = \frac{1}{2}\left(x + |x|\right), \tag{6.15a}$$

$$\langle x \rangle_{-} = \frac{1}{2}\left(x - |x|\right). \tag{6.15b}$$

The positive and negative components of the strain tensor satisfy the condition, $\boldsymbol{\epsilon} = \boldsymbol{\epsilon}^{+} + \boldsymbol{\epsilon}^{-}$. Although it is common to apply fourth-order projection tensors to obtain the positive and negative strain projections, as pointed out by Wu and Xu [2013], $\boldsymbol{\epsilon}^{+}$ and $\boldsymbol{\epsilon}^{-}$ may be more easily obtained by multiplying by positive and negative projection second-order tensors,

$$\boldsymbol{\epsilon}^{+} = \mathbf{M}^{+} \cdot \boldsymbol{\epsilon}, \tag{6.16a}$$

$$\boldsymbol{\epsilon}^{-} = \mathbf{M}^{-} \cdot \boldsymbol{\epsilon}. \tag{6.16b}$$

The second-order tensors $\mathbf{M}^{+}$ and $\mathbf{M}^{-}$ are given by,

$$\mathbf{M}^{+} = \sum_{a=1}^{3} H\left\{\boldsymbol{\varepsilon}^{(a)}\right\} \hat{\boldsymbol{n}}_a \otimes \hat{\boldsymbol{n}}_a, \tag{6.17a}$$

$$\mathbf{M}^{-} = \sum_{a=1}^{3} H\left\{-\boldsymbol{\varepsilon}^{(a)}\right\} \hat{\boldsymbol{n}}_a \otimes \hat{\boldsymbol{n}}_a, \tag{6.17b}$$

with $H\{\cdot\}$ denoting the heaviside function. The strain energy density functions Ψ_e^d and Ψ_e^i obtained through spectral decomposition are thereby written as,

$$\Psi_e^d = \mu\boldsymbol{\epsilon}^+ : \boldsymbol{\epsilon}^+ + \frac{\lambda}{2}\langle \mathrm{tr}(\boldsymbol{\epsilon})\rangle_+^2, \tag{6.18a}$$

$$\Psi_e^i = \mu\boldsymbol{\epsilon}^- : \boldsymbol{\epsilon}^- + \frac{\lambda}{2}\langle \mathrm{tr}(\boldsymbol{\epsilon})\rangle_-^2, \tag{6.18b}$$

where $\mathrm{tr}(\cdot)$ is the trace operator, μ is the material bulk modulus, λ is Lamé's first parameter, and ":" indicates the inner product between two tensors. The phase field equation for fracture is obtained by the minimization of U_{pot} in Eq. (6.12) with respect to the damage field D, which yields [Miehe et al., 2010, de Borst and Verhoosel, 2016],

$$\theta'(D)\Psi_e^d + \frac{G_c}{l_c}\left(D - l_c^2\Delta D\right) = 0. \tag{6.19}$$

For numerical stabilization purposes [Miehe et al., 2010], a viscous regularization term $\eta\dot{D}$ may be introduced to the above equation,

$$\eta\dot{D} + \left(D - l_c^2\Delta D\right) + \frac{l_c}{G_c}\theta'(D)\Psi_e^d = 0, \tag{6.20}$$

where $\dot{D}$ is the damage rate and η is a damping parameter. To enforce the irreversibility of damage (i.e., $\dot{D} > 0$), we also substitute Ψ_e^d with the history function,

$$\hat{\Psi}_e^d(\boldsymbol{x},t) = \max_{\substack{\boldsymbol{x}\in\Omega \\ s\in[0,t]}} \left\{\Psi_e^d(\boldsymbol{x},s)\right\}, \tag{6.21}$$

which corresponds to the maximum strain energy density at a material point $\boldsymbol{x}$ throughout the entire loading history. Finally, we choose the degradation function $\theta(D) = (1-D)^2$ to

satisfy the conditions,

$$\begin{cases} \theta(D) \in [0,1] \; \forall \; D \in [0,1], \\ \theta(0) = 1, \quad \theta(1) = 0, \\ \theta'(D) \leq 0, \quad \theta'(1) = 0, \end{cases} \tag{6.22}$$

which permits damage evolution and enforces the upper bound on the phase field (damage) variable as one [de Borst and Verhoosel, 2016]. The strain energy density-based phase field equation is thus fully represented as,

$$\eta \dot{D} + \left(D - l_c^2 \Delta D\right) = 2\frac{l_c}{G_c}(1-D)\hat{\Psi}_e^d. \tag{6.23}$$

Remark 36 *The Cauchy stress tensor may be obtained by taking $\sigma_{ij} = \partial \Psi_e / \partial \varepsilon_{ij}$, with the strain energy density Ψ_e decomposed into* damaged *and* intact *components for tensile and compressive loading, respectively (as in Eq. 6.13). Thus, the Cauchy stress may have an asymmetric tension-compression response wherein the degradation due to damage is only considered for tensile loads. Incorporating this damage-induced asymmetry into the constitutive model results in a nonlinear system of equations which must be solved iteratively. Nguyen et al. [2015] presented an alternate, linearized approach wherein the projection tensors are computed using the strains from the previous time step.*

6.2.2.2 Modular phase-field model

In the previous section, we described a phase field formulation using thermodynamic arguments based on the strain energy density. Here, we present a more general and modular framework for phase field modeling [Miehe et al., 2015]. The general form of the phase

field equation is written as,

$$\underbrace{\eta \dot{D}}_{\text{evolution}} + \underbrace{\left(D - l_c^2 \Delta D\right)}_{\text{geometric resistance}} + \underbrace{\frac{1}{2}\theta'(D)\mathscr{H}}_{\text{driving force}} = 0, \tag{6.24}$$

which contains three fundamental terms that govern (1) the phase field rate of evolution, (2) the geometric resistance imposed by surrounding material, and (3) the driving force for damage growth. The evolution term comprises the damage rate $\dot{D}$, which we approximate using a forward Euler scheme,

$$\dot{D} = \frac{D(t) - D(t - \Delta t)}{\Delta t}, \tag{6.25}$$

and a damping parameter η. The geometric resistance term is essentially a damage gradient whose spread is dictated by the characteristic length scale l_c. de Borst and Verhoosel [2016] pointed out that phase field models are essentially gradient damage models, with the fundamental difference being the driving force term: gradient damage models do not generally require a degradation function $\theta(D)$ in the driving force, and so the driving force in gradient damage models does not approach zero as $D \to 1$. The driving force term is defined using the function $\mathscr{H}$ which represents the history of the crack driving function $\mathscr{D}$,

$$\mathscr{H}(\boldsymbol{x}, t) = \max_{\substack{\boldsymbol{x} \in \Omega \\ s \in [0,t]}} \left\{ \mathscr{D}(\boldsymbol{x}, s) \right\}, \tag{6.26}$$

thus guaranteeing irreversibility of damage. The crack driving function $\mathscr{D}$ can take several forms. In the previous section, we discussed a crack driving function based on the strain energy density Ψ_e for linear elastic solids; however, as suggested by Miehe et al. [2015], simpler damage criteria are applicable for advanced problems (e.g., nonlinear elasticity,

anisotropy). In this work, we consider a Rankine-type crack driving function,

$$\mathscr{D} = \zeta \left\langle \bar{\sigma}^{\mathrm{I}} - \sigma_{\mathrm{th}} \right\rangle^2 \tag{6.27}$$

where $\langle \cdot \rangle$ are the Macaulay brackets, $\bar{\sigma}^{\mathrm{I}}$ is the effective maximum principal stress, and σ_{th} is a stress threshold. The parameter ζ is introduced for normalization so that the driving force $\mathscr{D}$ is dimensionless, and its calibration is discussed in the results section.

6.2.3 Constitutive model for damaged ice

The constitutive stress-strain relation for the phase field model is obtained by taking the derivative of the strain energy density with respect to strain,

$$\sigma_{ij} = \frac{\partial \Psi_e}{\partial \varepsilon_{ij}} = \theta(D) \frac{\partial \Psi_e^d}{\partial \varepsilon_{ij}} + \frac{\partial \Psi_e^i}{\partial \varepsilon_{ij}}, \tag{6.28}$$

where ε_{ij} are components of the strain tensor, given by the symmetric gradient of the displacement field $\boldsymbol{u}$,

$$\varepsilon_{ij} = \frac{1}{2} \left(\frac{\partial u_i}{\partial x_j} + \frac{\partial u_j}{\partial x_i} \right). \tag{6.29}$$

In this work we take the degradation function as $\theta(D) = (1-D)^2$ in order to satisfy the conditions listed in Eq (6.22). We also note that the "damaged" and "intact" components of the strain energy density, Ψ_e^d and Ψ_e^i, respectively, be may obtained through spectral decomposition of the strain tensor. For isotropic elasticity, the Cauchy stress may be represented in terms of the shear modulus $\mu = \frac{E}{2(1+\nu)}$ and Lamé's first parameter $\lambda = \frac{E\nu}{(1+\nu)(1-2\nu)}$ as,

$$\sigma_{ij} = \left[(1-D)^2 + \alpha \right] \left(2\mu \varepsilon_{ij}^+ + \lambda \langle \varepsilon_{kk} \rangle_+ \delta_{ij} \right) + \left(2\mu \varepsilon_{ij}^- + \lambda \langle \varepsilon_{kk} \rangle_- \delta_{ij} \right), \tag{6.30}$$

where the numerical parameter α is chosen as,

$$\alpha = \begin{cases} 10^{-6} & D = 1, \\ 0 & D < 1, \end{cases} \tag{6.31}$$

in order to prevent rank deficiency in the finite element stiffness matrix. Neglecting the spectral decomposition of strain, the Cauchy stress may also be written more simply as,

$$\sigma_{ij} = \left[(1-D)^2 + \alpha\right]\left(2\mu\varepsilon_{ij} + \lambda\varepsilon_{kk}\delta_{ij}\right). \tag{6.32}$$

To incorporate hydraulic fracture, we apply the poro-mechanics formulation for previously discussed in Sections 5.3.3 and 6.2.1, in which we considered isotropic damage to have the same effect on material behavior as porosity. For the sake of completion, we hereby write the full constitutive relation for linear elastic ice that incorporates hydraulic pressure in the damaged zone:

$$\sigma_{ij} = \left[(1-D)^2 + \alpha\right]\left(2\mu\varepsilon_{ij} + \lambda\varepsilon_{kk}\delta_{ij}\right) - Dp_w\delta_{ij}. \tag{6.33}$$

We note that the above formulation is not consistent with the mixture theory (see equation 6.2) if damage is assumed to be the same as porosity.

6.3 Numerical results

In this section, we perform a series of numerical studies using the augmented cohesive zone model (CZM) and the phase field model (PFM) with strain energy density (Ψ_e) based and maximum principal stress (σ^{I}) based crack driving forces to predict the evolution of water-filled surface and basal crevasses through glaciers. For brevity, we will refer to the phase field models with strain energy density and maximum principal stress based crack driving forces as the Ψ_e-PFM and σ^{I}-PFM, respectively. For all simulations using the Ψ_e-PFM, we consider the spectral decomposition of strain and implement the constitutive model in Equation 6.30; whereas, for the σ^{I}-PFM we neglect spectral decomposition and implement the constitutive model in Equation 6.32. Both the CZM and PFM models are implemented numerically using the finite element method. We employ the commercial software Abaqus for the CZM and utilize the User Element (UEL) subroutine for the cohesive elements; whereas, the bulk (i.e., non-interface) material is modeled using continuum plane strain elements with linear elastic behavior. For the PFM, we employ the open-source finite element software FEniCS (http://www.fenicsproject.org), wherein we manually supply the variational form of the linear elasticity and phase field equations. We first verify the CZM and PFM implementations using a single edge notch benchmark test for mode I fracture. Next, we apply the CZM and PFM to predict the penetration depths of dry and water-filled surface crevasses in marine-terminating grounded ice sheets and compare model results against the crevasse penetrations depths predicted by the dislocation mechanics based model proposed by Weertman [1973]. Lastly, we study the conditions necessary for the growth of basal crevasses in ice sheets.

6.3.1 Single edge notched tension test

The single edge notched tension test is a commonly used experiment for the purpose of verifying numerical implementations of phase field models [Miehe et al., 2010, 2015,

Nguyen et al., 2015]. The domain considered for this experiment is a unit square plate with a horizontal notch spanning from the midpoint of the left edge to the center of the plate, as shown in Figure 6.2. Dirichlet boundary conditions are applied to the bottom domain edges to prevent horizontal and vertical displacement. Horizontal displacement is also constrained along the top edge of the domain, and vertical displacement u_D is applied as a boundary condition to induce tension in the domain resulting in mode I fracture. Although we will later utilize the phase field model to simulate crevasse evolution in ice, for this experiment we use the material properties of steel (i.e., $E = 210$ kN/mm^2 and $\nu = 0.3$) so that we can compare our model results with the results from the literature [Miehe et al., 2010]. We employ both the Ψ_e-PFM and σ^{I}-PFM, described in Equations 6.23, 6.24 and 6.27, to illustrate the viability of both approaches. Following Miehe et al. [2010], we choose $l_c = 0.015$ mm as the phase field length scale parameter and $G_c = 2.7 \times 10^{-3}$ kN/mm as the critical strain energy release rate for steel. The normalization parameter $\zeta = 2 \times 10^{-2}$ (kN/mm^2)$^{-2}$ is calibrated for the σ^{I}-PFM to match the benchmark examples for this test, and the stress threshold $\sigma_{\mathrm{th}} = 0$. We obtain the cohesive strength $\sigma_{\max} = 6.15$ kN/mm^2 for the CZM using the widely known Hillerborg et al. [1976] equation,

$$\sigma_{\max} = \sqrt{\frac{EG_c}{l_{c,\mathrm{coh}}}}, \tag{6.34}$$

where the size of the cohesive length scale $l_{c,\mathrm{coh}}$ is assumed to be the same as the phase field length scale l_c. The domain is discretized using unstructured triangular finite elements for the PFM simulations, and within the expected damage zone (i.e., around the initial notch) we set the element size $l_{\mathrm{elem}} = 0.005$ mm, which is sufficiently smaller than the length scale parameter. For the CZM simulation, we discretize the domain using unstructured quadrilateral finite elements. The cohesive zone is inserted as a zero-thickness interface continuing from the initial notch, as depicted in Figure 6.2 using an orange dashed line, with an element size $l_{\mathrm{elem}} = 0.00025$ mm.

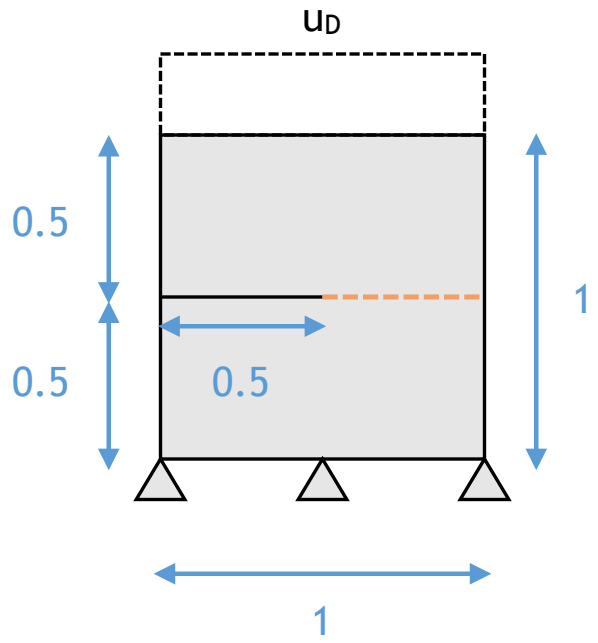

Figure 6.2: Schematic of the single edge notched tension test with an applied vertical displacement u_D. The domain dimensions have units mm.

The results of this study are shown in Figure 6.4 wherein we plot the total load in the vertical direction versus the displacement of the top edge of the domain for the Ψ_e-PFM, σ^{I}-PFM, and CZM. We also show the result obtained using the virtual crack closure technique (VCCT), which is generally consistent with the LEFM solution Banks-Sills [1991], Krueger [2002]. An illustration of the final crack path is provided in Figure 6.3 for the Ψ_e-PFM (we note that the Ψ_e-PFM and σ^{I}-PFM have identical crack paths). Following damage initiation at the crack tip (i.e., when the first element fails), the crack propagates horizontally at a fast (near-instantaneous) rate. The load-displacement curves obtained using both the Ψ_e-PFM and σ^{I}-PFM agree exactly with the result from literature [Miehe et al., 2010, Nguyen et al., 2015], thus verifying the two approaches. The CZM test with $\sigma_{\max} = 6.15$ kN/mm^2 matches exactly with the VCCT solution. The CZM and VCCT both predict linear elastic behavior prior to failure, and after peak load the domain fails almost instantaneously. On the other hand, we observe that the PFM models exhibit softening behavior prior to peak load, owing to the damage accumulating throughout the domain and

softening the material. We also note that the Ψ_e-PFM slightly overshoots the CZM and VCCT on the load-displacement curve; this indicates that although the Ψ_e-PFM is based on the critical fracture energy G_c, it is not necessarily consistent with the LEFM solution. On the other hand, the σ^{I}-PFM may be calibrated to match the load-displacement curve in Miehe et al. [2010] by adjusting the normalization parameter ζ.

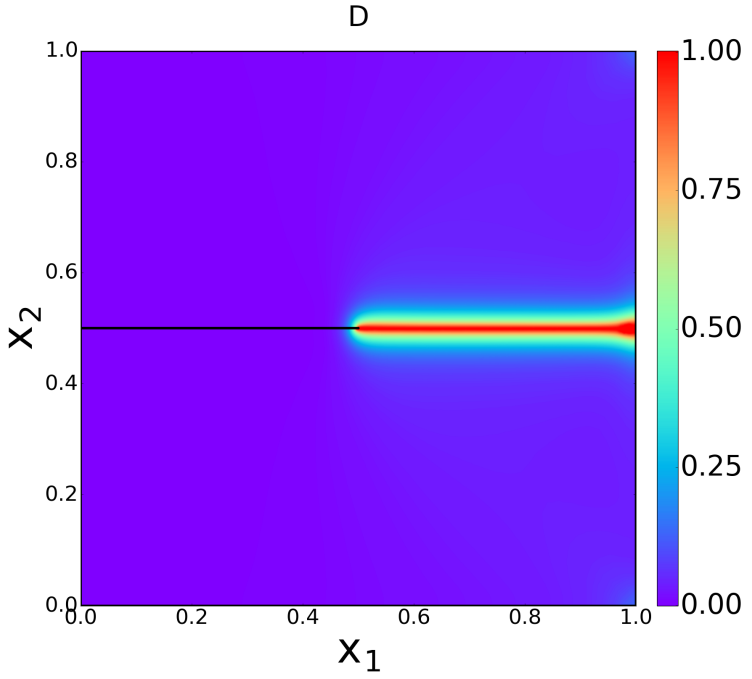

Figure 6.3: Final damage contour predicted by the Ψ_e-PFM for the single edge notched tension test. The red regions (i.e., $D = 1$) indicate fully damaged material, whereas the blue regions (i.e., $D = 0$) indicate intact material.

6.3.2 Mode I benchmark test

We next perform a pure mode I benchmark test to compare the Ψ_e-PFM, σ^{I}-PFM, CZM, and VCCT using the material parameters for incompressible ice, which are provided in Table 6.1. The critical strain energy release rate G_c for ice is computed using the relation,

$$G_c = K_{IC}^2 \frac{1-\nu^2}{E}, \tag{6.35}$$

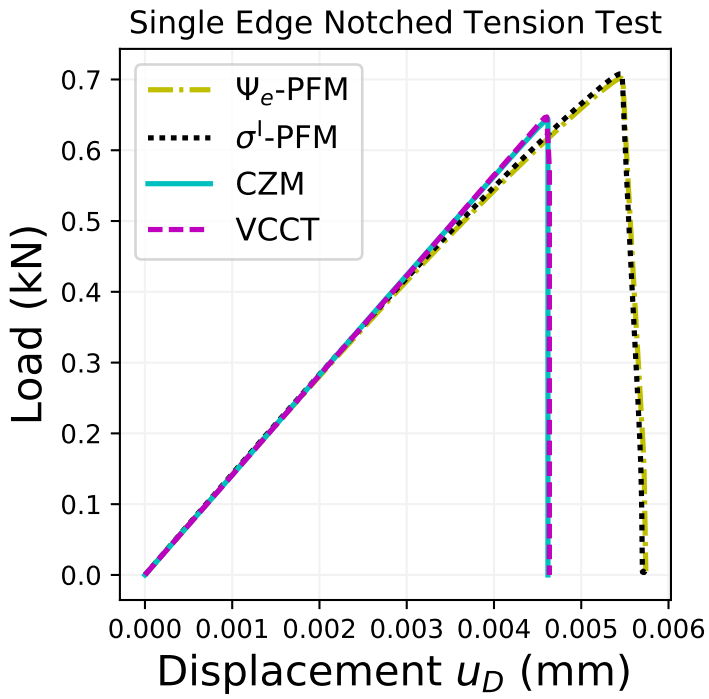

Figure 6.4: Load versus displacement measured during the single edge notched tension test using the Ψ_e-PFM, σ^{I}-PFM, CZM, and VCCT methods.

where $K_{IC} = 0.4$ MPa $\sqrt{\mathrm{m}}$, which is the upper bound obtained from a range of experimentally calibrated critical stress intensity factors for ice [Rist et al., 1996, van der Veen, 1998a]. The experimental setup of the mode I test is identical to the single edge notched tension test performed in the previous section; however, the domain is scaled to have the dimensions 100 m $\times$ 100 m, and we modify the boundary conditions so as to induce a uniaxial tension in the direction of loading. Rollers are applied to the bottom domain boundary to prevent vertical displacement, and a controlled vertical displacement u_D is applied to the top edge of the domain. Horizontal displacement is not constrained anywhere in the domain except for the lower-left corner, which we pin to prevent free translation in the horizontal direction. The results of this study are shown in Figure 6.5, wherein we plot the load versus displacement curve obtained using the different damage mechanics approaches. As before, the CZM and VCCT curves match exactly; however, the Ψ_e-PFM result largely overshoots the CZM and VCCT curves. This indicates that the Ψ_e-PFM is not necessarily consistent

Table 6.1: Material parameters of linear elastic ice.

Parameter	Value	Units
E	9500	MPa
ν	0.4995	–
K_{Ic}	0.4	MPa $\sqrt{\text{m}}$
G_c	1.264×10^{-5}	MPa $\cdot$ m
ρ_i	917	kg/m^3

with the other damage frameworks that are based on G_c. The strain energy density may also be an inappropriate crack driving force for incompressible materials. When we repeat this experiment while setting Poisson's ratio $\nu = 0.3$ (thus, assuming compressible material) the Ψ_e-PFM shows much better agreement with the CZM and VCCT, as demonstrated in Figure 6.6. The load-displacement curve predicted by the σ^{I}-PFM is plotted in Figure 6.5 with the normalization parameter ζ calibrated to 2×10^{-10} MPa^{-2} and damping parameter $\eta = 5 \times 10^3$ s^{-1}. Following the assumption that ice has no tensile strength, we take $\sigma_{\text{th}} = 0$. Rather than immediate failure following the post-peak behavior, we observe a softening process owing to the large value taken for the damping parameter η. Calibrating a smaller η would result in sharper post-peak behavior more consistent with the CZM and PFM; however, we take $\eta = 5 \times 10^3$ s^{-1} since a large value is required to prevent excessive damage growth in the load-controlled experiments, which will be discussed in the next section.

6.3.3 Evolution of water-filled surface crevasses

In this section, we simulate the evolution of water-filled surface crevasses through a marine-terminating, grounded ice slab under gravity loading. Our aim is to compare the final crevasse penetration depths predicted by the PFM and CZM against the depths predicted by the Weertman [1973] fracture mechanics model. For each simulation, we consider an idealized, rectangular ice slab as depicted in Figure 5.1 with domain height $H = 125$ m and length $L = 500$ m. Rollers are applied to the bottom and left boundaries of the domain to

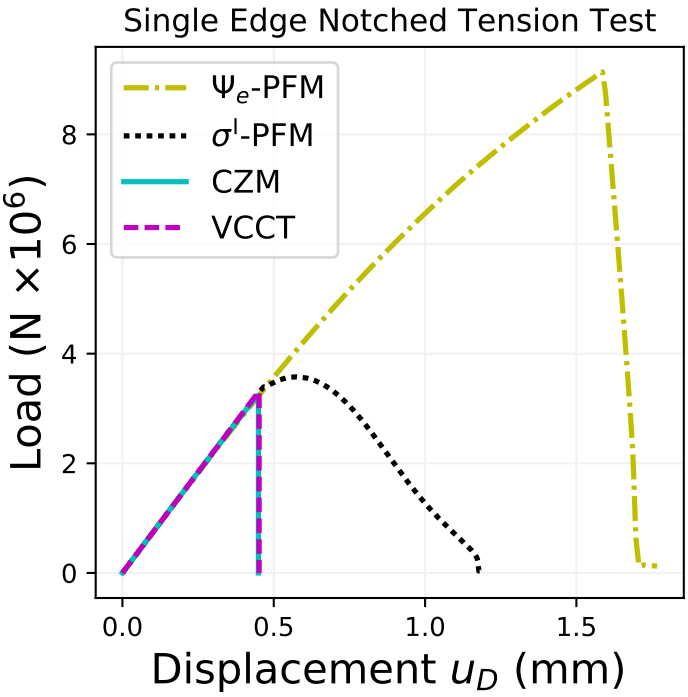

Figure 6.5: Load versus displacement measured during the single edge notched tension test using the Ψ_e-PFM, σ^{I}-PFM, CZM, and VCCT methods for incompressible ice (Poisson's ratio $\nu = 0.4995$).

prevent vertical and horizontal displacements, respectively. Gravity loading is applied as a body force $\rho_i \boldsymbol{g}$ where ρ_i is the density of ice, and $\boldsymbol{g}$ is the gravity acceleration. Seawater-induced hydrostatic pressure with a water depth h_w and water density $\rho_w = 1020$ kg/m^3 is applied as a Neumann boundary condition to the right edge of the domain, whereas the poro-mechanics formulations for the CZM and PFM are implemented for modeling hydrostatic pressure within the crevasse with water depth h_s. The ice is modeled as a near-incompressible linear elastic solid with Young's modulus $E = 9500$ MPa and Poisson's ratio $\nu = 0.4995$.

6.3.3.1 Phase field model approach

Herein we apply the Ψ_e-PFM and σ^{I}-PFM to model the propagation of water-filled surface crevasses through glaciers. All simulations in this section are performed using FEniCS

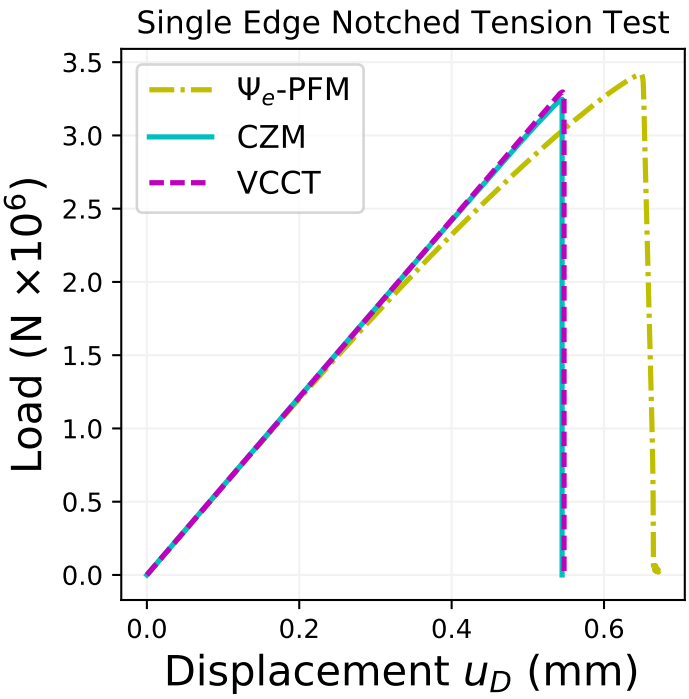

Figure 6.6: Load versus displacement measured during the single edge notched tension test using the Ψ_e-PFM, σ^{I}-PFM, CZM, and VCCT methods for compressible ice (Poisson's ratio $\nu = 0.3$).

software on a triangular mesh with 2nd-order (quadratic) finite elements. In order to control where fracture initiates, we prescribe an initial defect with size $l_c \times l_c$ centered along the top surface of the domain with $l_c = 2.5$ m. The defect is modeled as a pre-damaged zone by setting the damage variable $D = 1$ at integration points within the corresponding mesh region. The anticipated damage zone (i.e., underneath the initial defect) is meshed using a structured triangular grid with element size $l_{\mathrm{elem}} = 0.625$ m, whereas far from the damage zone we use a relatively coarse and unstructured mesh. All the numerical parameters associated with Ψ_e-PFM based and σ^{I}-PFM are provided in Table 6.2.

The results of this study are presented in Figures 6.7-6.9. Let us first discuss the crevasse penetration predicted for the dry loading case (i.e., $h_w = 0$ and $h_s = 0$) by the Ψ_e-PFM, as shown in Figures 6.7(a) and 6.7(b) wherein we plot the damage contours at intermediate and final damage states. From these figures we observe that the surface crevasse

splits into two branches. Additionally, a significant amount of damage accumulates at the lower-right portion of the domain due to horizontal large tensile strains near the terminus. Eventually, damage develops to a large extent throughout the entire domain ($D > 0.8$ at most of the material points), and failure occurs along the left domain boundary due to the boundary constraints. From this result we conclude that the Ψ_e-PFM is not suitable for modeling surface crevasse penetration without additional damage controls (e.g., a strain energy density threshold); however, developing a robust Ψ_e based formulation is the topic for another study. For the rest of this section, we proceed to model surface crevasse evolution using the σ^{I}-PFM.

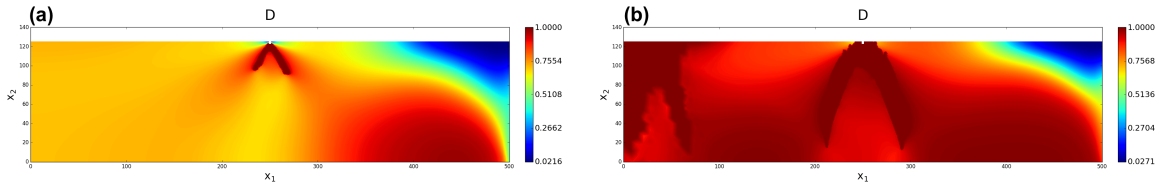

Figure 6.7: (a) Intermediate and (b) final damage contours predicted using the Ψ_e-PFM for an ice slab undergoing gravity loading. The dark red regions depict fully-damaged material (i.e., $D = 1$), whereas the dark blue regions depict intact material (i.e., $D \approx 0$).

The damage field predicted using the σ^{I}-PFM is shown in Figures 6.8(a) and 6.8(b) for the dry loading scenario (i.e., $h_w = 0$ and $h_s = 0$). In order to prevent damage from developing in regions where the stress is in a compressive state, we only permit damage nucleation in regions where $\sigma_{kk} > 0$. Using the σ^{I}-PFM, the crevasse initiates as a single crack that penetrates vertically through the ice slab before other crevasses propagate through the ice slab with spacing on the order of one ice thickness apart. Figure 6.9 shows the normalized crevasse depth d_s/H plotted versus varying water levels $h_s/d_s = 0\%, 25\%, 50\%, 75\%$, and 100% for different seawater depths at the terminus $h_w/H = 0\%, 25\%, 50\%, 75\%$, and 90% (i.e., the floating depth of ice), as predicted by the Weertman [1973] fracture mechanics model and by the σ^{I}-PFM with the parameter ζ calibrated to the value 1×10^{-9} Pa^{-2}. The σ^{I}-PFM shows good agreement with the Weertman [1973] model except when the ratio $h_w/H < 0.5$; however, the parameter ζ can be re-calibrated to better fit these loading sce-

narios at the expense of poorer agreement with the lower h_w/H ratios. We also note the importance of choosing a sufficiently large damping parameter η. Because the experiment is load-controlled, the domain immediately reaches the peak loading state, and damage grows very rapidly; without sufficient damping, most material points in the domain fail very suddenly. On the other hand, when choosing a large damping parameter, damage only develops in significant portions near stress concentration points, resulting in the initiation and propagation of individual crevasses.

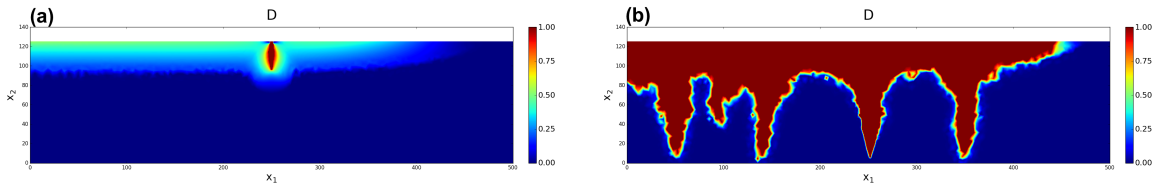

Figure 6.8: (a) Intermediate and (b) final damage contours predicted using the σ^{I}-PFM for an ice slab undergoing gravity loading. The dark red regions depict fully-damaged material (i.e., $D = 1$), whereas the dark blue regions depict intact material (i.e., $D \approx 0$).

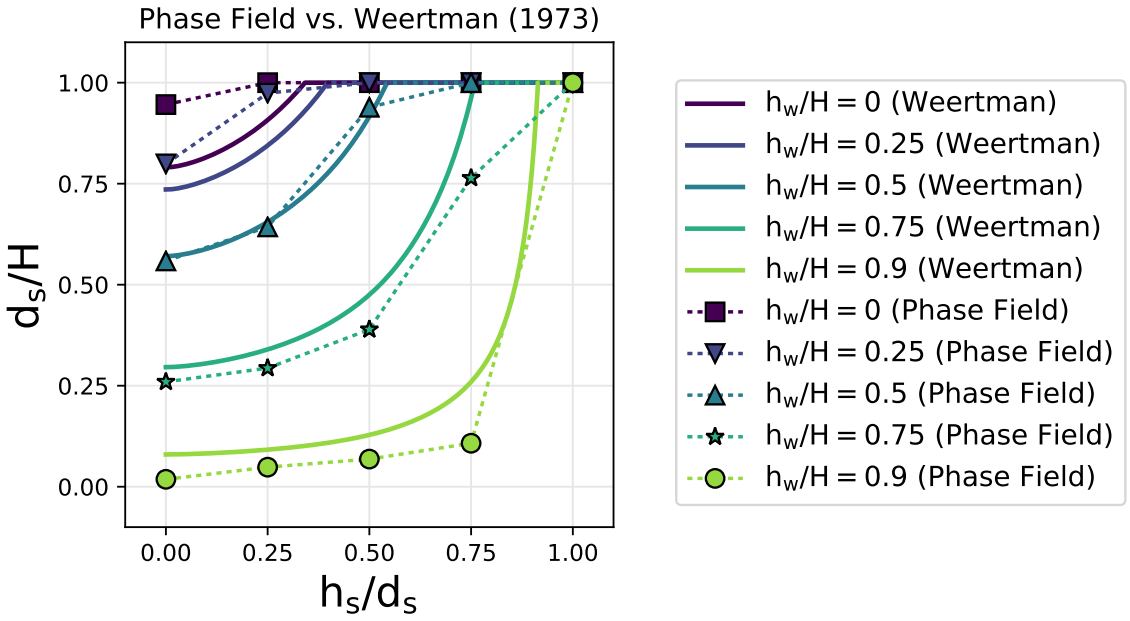

Figure 6.9: Surface crevasse depth d_s normalized with the domain height $H = 125$ m for varying water levels h_s filling the surface crevasse. The solid lines and dotted lines with markers depict the Weertman [1973] solution and σ^{I}-PFM predictions, respectively, for varying water levels h_w at the terminus.

Table 6.2: Phase field model parameters for ice.

Parameter	Value	Units
l_c	2.5	m
ζ	1×10^{-9}	Pa^{-2}
η	5×10^{3}	s^{-1}
σ_{th}	0	Pa

6.3.3.2 Cohesive zone model approach

In this section, we apply the CZM to model the propagation of water-filled surface crevasses through an ice sheet. All simulations in this section are performed using Abaqus software on an unstructured quadrilateral mesh with 1st-order (linear) finite elements. The cohesive zone is modeled as a zero-thickness interface that cuts vertically through the entire depth of the slab at the center of the domain (i.e., $x = L/2$). The cohesive interface elements have zero-thickness and length $l_{\text{elem}} = 0.1$ m, and their constitutive behavior is governed by the augmented traction-separation law discussed in Section 6.2.1; whereas, the bulk (continuum) elements have linear elastic behavior. Because damage can only occur along the cohesive interface, there is no need to prescribe an initial defect. The cohesive normal and tangent stiffness parameters, K_{n}^0 and K_{t}^0, respectively, are both chosen as 1×10^6 kPa/m, which is sufficiently large to avoid inducing an artificial compliance to the domain. The cohesive strength parameters $\sigma_{\max}$ and $\tau_{\max}$ are both chosen at the (considerably low) value of 1 kPa in order to remain consistent with the fracture mechanics models which assume that ice has no tensile strength Nye [1955], Weertman [1973]. Finally, we assume that the critical strain energy release rate (SERR) is the same value G_c for all failure modes; that is, $G_{\text{IC}} = G_{\text{IIC}} = G_c$ where G_{IC} and G_{IIC} are the mode I and mode II critical SERRs, respectively. All the cohesive parameters used for this study are given in Table 6.3.

The results of this study are shown in Figure 6.10, wherein we plot the normalized crevasse depth d_s/H versus varying water levels $h_s/d_s = 0\%, 25\%, 50\%, 75\%$, and 100% for different seawater depths at the terminus $h_w/H = 0\%, 25\%, 50\%, 75\%$, and 90% (i.e.,

the floating depth of ice), as predicted by the theoretical fracture mechanics model of Weertman [1973] and by the CZM. The CZM shows excellent agreement with the Weertman [1973] model when the ratio $h_w/H > 0.5$; however, for lower h_w/H ratios the CZM generally overestimates the crevasse penetration depth. For comparative purposes we also plot the CZM-predicted crevasse penetration depths along the PFM-predicted depths in Figure 6.11. The CZM and σ^{I}-PFM results show good agreement for all h_w/H ratios, which suggest the validity of both approaches for modeling crevasse penetration; however, the PFM is easier to incorporate into large scale ice sheet models and is also capable of predicting arbitrary crack paths, whereas for the CZM the potential crack path must be assumed *a priori*.

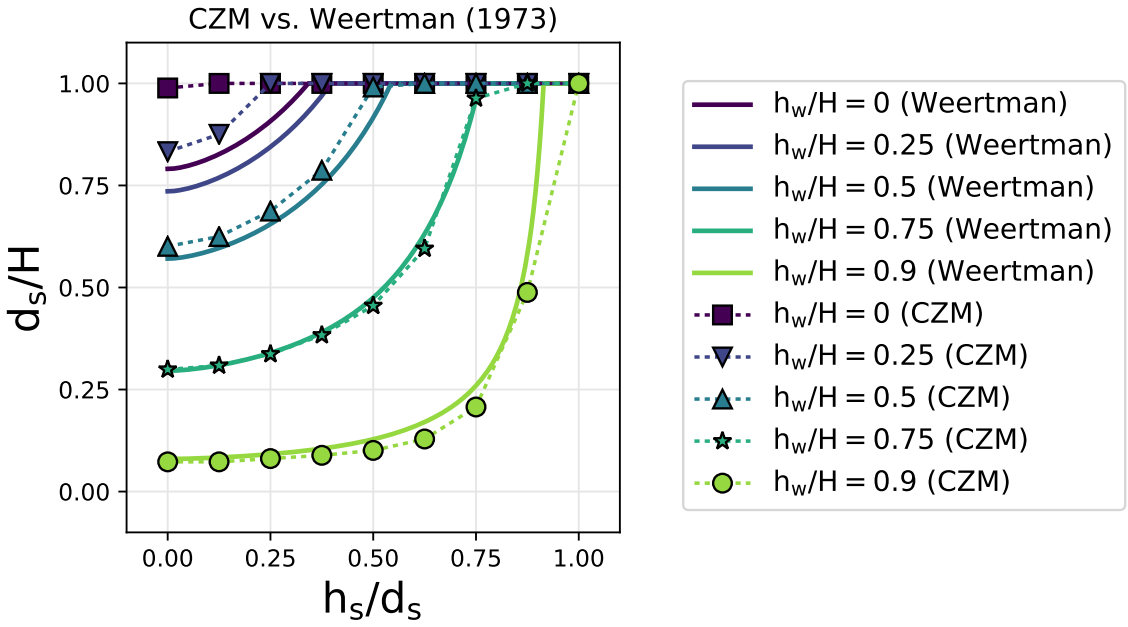

Figure 6.10: Surface crevasse depth d_s normalized with the domain height $H = 125$ m for varying water levels h_s filling the surface crevasse. The solid lines and dotted lines with markers depict the Weertman [1973] solution and CZM predictions, respectively, for varying water levels h_w at the terminus.

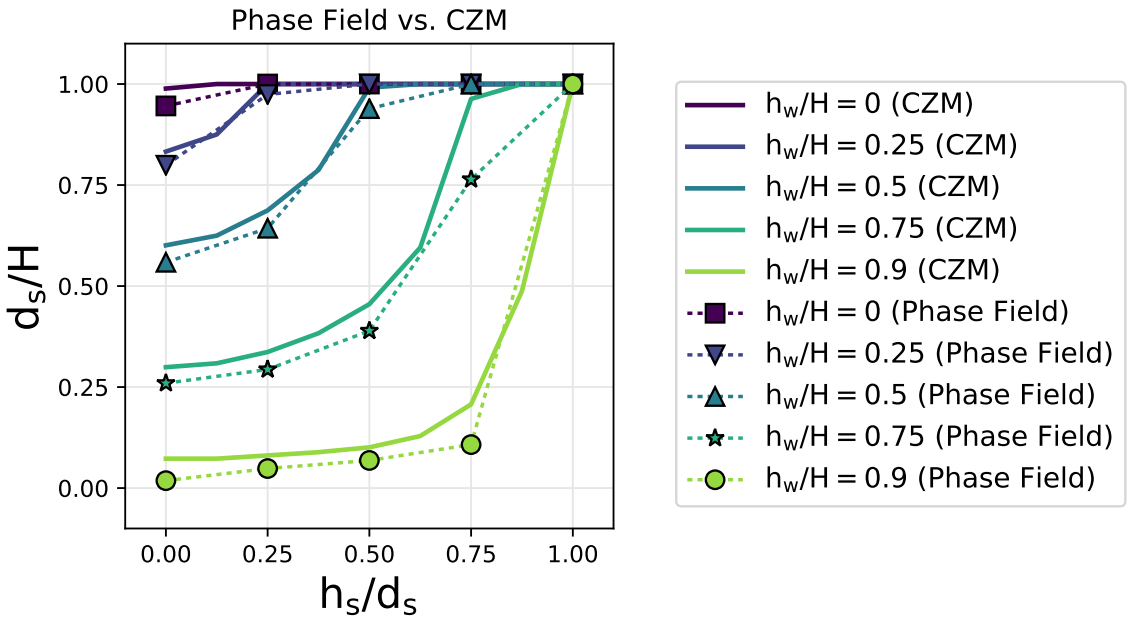

Figure 6.11: Surface crevasse depth d_s normalized with the domain height $H = 125$ m for varying water levels h_s filling the surface crevasse. The solid lines and dotted lines with markers depict the CZM and σ^{I}-PFM predictions, respectively, for varying water levels h_w at the terminus.

Table 6.3: Cohesive zone model parameters for ice.

Parameter(s)	**Value**	**Units**
G_{IC}, G_{IIC}	0.01264	kPa · m
$\sigma_{\max}$, $\tau_{\max}$	1	kPa
K_{n}^0, K_{t}^0	1×10^6	kPa/m

6.3.4 Evolution of water-filled basal crevasses

In this section, we investigate the evolution of water-filled basal crevasses through grounded, marine-terminating glaciers under gravity loading. We first discuss the constitutive assumptions made for ice (i.e., the Poisson's ratio) and comment on the conditions necessary for a basal crevasse to initiate or propagate. Next, we apply several numerical models to simulate the propagation of water-filled basal crevasses. For all simulations performed for this study, we consider an idealized rectangular domain as depicted in Figure 5.1 with height $H = 125$ m and length $L = 500$ m. We assume the seawater depth

$h_w = \frac{\rho_i}{\rho_w} H \approx 90\%$, which is the floating depth of ice, and the hydrostatic pressure is applied as a Neumann boundary condition on the right-hand domain edge. We also assume that the hydraulic head within the basal crevasse is the same as the seawater level h_w. The hydraulic pressure within the damage zone is implemented using the poro-mechanics formulation presented in Sections 6.2.1 and 6.2.3. Gravity is applied as a body force $\rho_i \boldsymbol{g}$, where $\boldsymbol{g}$ is the acceleration due to gravity, and rollers are applied as Dirichlet boundary conditions to prevent vertical and horizontal movement on the bottom and left-hand boundaries, respectively.

Let us first investigate the stresses induced by the presence of a water-filled basal crevasse within a glacier for different compressibility ratios. In Figure 6.12, we plot the horizontal Cauchy stress σ_{xx} versus depth above a 10 m basal crevasse obtained by finite element analysis using a linear elastic constitutive relation for ice with varying Poisson's ratios. The ice slab has the properties and loading conditions described in the previous paragraph (i.e., gravity loading and hydrostatic pressure at the terminus and within the basal crevasse). In this case, the basal crevasse is modeled as a zero-thickness seam with hydraulic pressure applied as a Neumann boundary condition along the crevasse walls. For the near-incompressible case, we observe that σ_{xx} is compressive at the crevasse tip, although the crevasse still acts as a stress concentrator; whereas, when Poisson's ratio $\nu = 0.35$, the Cauchy stress is both highly magnified and tensile near the crevasse tip. In general, decreasing Poisson's ratio will result in less compression at the bottom of the glacier, which is evident by considering the expression for horizontal Cauchy stress in the "far-field" of a compressible ice slab,

$$\sigma_{xx} = \frac{\nu}{1-\nu}\left[\frac{1}{2}\rho_i g H - \rho_i g \langle H - z \rangle\right] - \frac{1}{2}\rho_w g \frac{h_w^2}{H}. \tag{6.36}$$

Note that in the above equation, when considering the incompressible case (i.e., $\nu = 0.5$) we obtain the common expression $\sigma_{xx} = R_{xx} - \rho_i g \langle H - z \rangle$, where the "resistive" stress

$R_{xx} = \frac{1}{2}\rho_i g H - \frac{1}{2}\rho_w g \frac{h_w^2}{H}$ (see Equation 48).

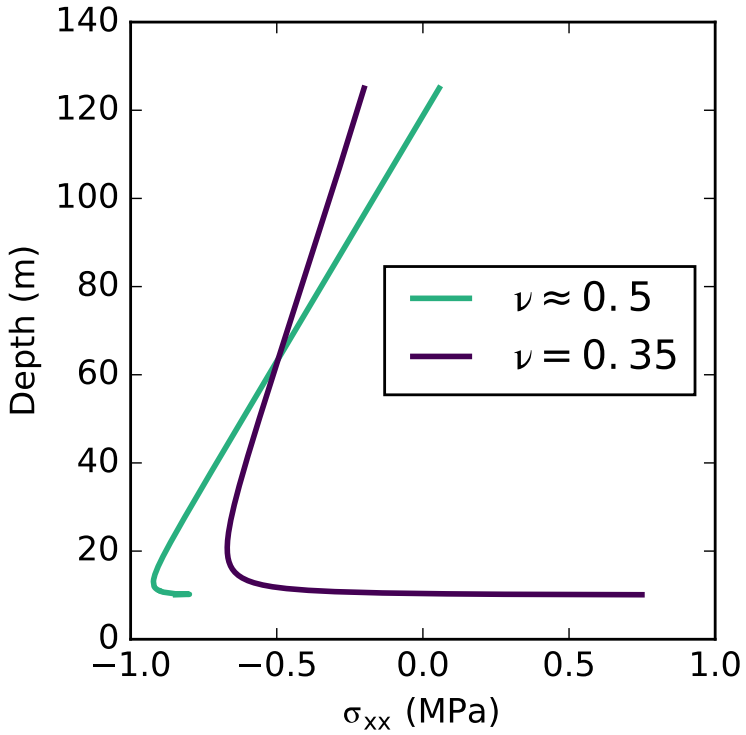

Figure 6.12: Horizontal Cauchy stress σ_{xx} versus depth above a 10 m basal crevasse in the "far-field" region of a glacier. The light green and dark purple lines correspond to the stress when using near-incompressible and compressible rheology for ice, respectively.

We now simulate the propagation of basal crevasses in both compressible and incompressible ice using the σ^{I}-PFM, the Ψ_e-PFM, the CZM, and the nonlocal creep damage mechanics model proposed in Jiménez et al. [2017]. For this set of experiments, we choose a smaller length scale $l_c = 1.25$ m and prescribe an initial basal crevasse with height 10 m. For the PFM and creep damage models, the initial notch is modeled as a continuum damage zone with width 1.25 m; whereas, in CZM, we simply set $D = 1$ within all the interface elements below the height 10 m. The results of this study are presented in Table 6.4, wherein we list the normalized basal crevasse penetration depths d_b/H for all the various damage mechanics models with different compressibility ratios. In the case where we model ice as a near-incompressible material (i.e., when $\nu = 0.4995$), we observe that

Table 6.4: Penetration depths of basal crevasses using different damage mechanics approaches.

Approach	Poisson's ratio	Normalized Basal Crevasse Penetration Depth
Nonlocal creep	0.4995	8 %
CZM	0.4995	8 %
Ψ_e-PFM	0.4995	8 %
σ^{I}-PFM	0.4995	8 %
Nonlocal creep	0.35	96.84 %
CZM	0.35	100 %
Ψ_e-PFM	0.35	94.07 %
σ^{I}-PFM	0.35	98.71 %

the basal crevasse does not extend past the initial depth of 8%. This occurs because the damage mechanics models require a tensile stress state for damage to nucleate, and tensile stresses do not occur at the crevasse tip when considering ice as an incompressible material. Interestingly, the stress intensity factors computed at the crack tip using the displacement correlation method are positive, which would imply crack growth. When modeling ice as a compressible material, we observe basal crevasse growth using multiple damage mechanics based models. An illustration of the final damage contour predicted by the Ψ_e-PFM is shown in Figure 6.13. Interestingly, each damage mechanics model predicts either full or nearly full penetration of the crevasse through the domain thickness. These results imply that incompressible constitutive behavior for ice may not be sufficient for predicting basal crevasse growth in grounded glaciers on free-slip surfaces. It has been suggested that the evolution of basal crevasses is a complex multi-physics problem which is influenced by melting along with tensile opening [Bassis and Ma, 2014]. A more comprehensive analysis on the physical conditions required for basal crevasses to initiate and propagate is a topic for future study.

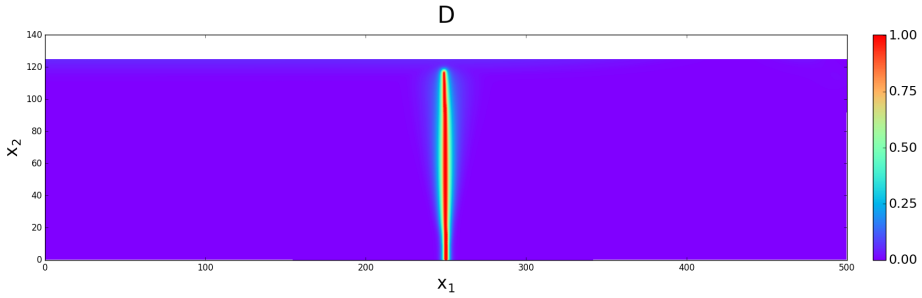

Figure 6.13: Final damage contour predicted by the Ψ_e-PFM when modeling the evolution of a basal crevasse in compressible ice with Poisson's ratio $\nu = 0.35$. The red regions (i.e., where $D = 1$) indicate fully damaged ice; whereas the blue regions (i.e., where $D \approx 0$) indicate intact ice.

6.4 Conclusions

In this chapter, we presented two damage mechanics approaches for time-independent, brittle fracture, namely the cohesive zone model (CZM) and the phase field model (PFM), to simulate the propagation of water-filled surface and basal crevasses through grounded, marine-terminating glaciers. First, we established the validity of the CZM and PFM models using both strain energy density based and maximum principal stress based crack driving forces (denoted as the Ψ_e-PFM and σ^{I}-PFM, respectively) by performing a single edge notch tension test and mode I tension test. Next, we employed the CZM, Ψ_e-PFM, and σ^{I}-PFM to simulate the propagation of water-filled surface crevasses through a glacier and compared numerical results against the Weertman [1973] dislocation mechanics based model. We discovered that the Ψ_e-PFM is not an appropriate technique for simulating surface crevasse growth due to the unrealistic damage morphology likely due to the incompressibility of ice; however, the σ^{I}-PFM predicted more realistic crevasse growth. The CZM and σ^{I}-PFM both showed excellent agreement with the Weertman [1973] model when the seawater depth at the terminus is large (i.e., $h_w/H \geq 50\%$); however, for lesser seawater depths the numerical models tended to overestimate the crevasse penetration depth. This differs considerably from the behavior observed in creep damage models (Chapter 5), which failed to predict any crevasse growth in the near floating condition (i.e., $h_w/H = 90\%$).

We also studied the conditions necessary for basal crevasse evolution in glaciers. Although theoretical fracture mechanics models generally assume ice to be incompressible, we observed through finite element analysis that the Cauchy stress at the tip of a water-filled basal crevasse is in a compressive state if considering incompressible ice. However, when considering compressible ice with Poisson's ratio $\nu = 0.35$, the stresses at the crevasse tip are both tensile and sufficiently large to enhance damage growth. We employed the CZM, Ψ_e-PFM, σ^{I}-PFM, and the nonlocal creep damage mechanics model to simulate basal crevasse growth. All four approaches predicted zero basal crevasse propagation in

the incompressible ice; and all four approaches predicted full or nearly-full crevasse penetration when taking $\nu = 0.35$.

From this study, we conclude that the time-independent, brittle damage mechanics formulations are more consistent with the theoretical fracture mechanics models than the creep damage mechanics. While the CZM shows excellent agreement with the Weertman [1973] model, it is more difficult to implement than continuum damage models, and the crack path must be assumed a priori. The PFM, on the other hand, is consistent with the CZM when predicting crevasse penetration depths and may be more easily included in large-scale models for ice sheet dynamics. Finally, we conclude incompressible rheology is insufficient for modeling basal crevasse growth in grounded glaciers, unless other (e.g., thermal) physical mechanisms or different boundary conditions (i.e., grounded to floating) are accounted for in the process of crevasse evolution.

CHAPTER 7

CONCLUSIONS

This dissertation presented various applications of damage mechanics for modeling sharp and diffuse fracture evolution using the cohesive zone model (CZM), nonlocal continuum damage mechanics (CDM), and phase field model (PFM) for brittle fracture. The CZM was implemented to model fatigue delamination of composites, whereas the CDM approach was chosen for modeling diffuse fracture in ice.

In Chapter 2, a discrete damage zone model (DDZM) for temperature dependent mixed mode delamination in composites under high cycle fatigue loading was developed from the original model for quasi-static loading [Liu et al., 2012], by adding fatigue and static damage components. The proposed model employs the interface element as a discrete spring placed at the finite element nodes and its constitutive law is derived entirely from damage laws, specifically, by combining Mazars law for static damage growth [Mazars, 1986] and Peerlings law for fatigue damage growth [Peerlings et al., 2000]. The model parameters were calibrated under pure mode I, pure mode II, and 50% mode II loadings. A quadratic relation was proposed to evaluate the parameters for other mode mix ratios (25% and 75% mode II) and then model results were verified with the numerical results of [Blanco et al., 2004], which demonstrates the validity of the model. The advantage of the DDZM approach is that it offers a lot of flexibility for incorporating different damage models to describe interface failure behavior under different loading and environmental conditions.

In Chapter 3, the issue of parametric sensitivity of CZMs was investigated for high-cycle fatigue delamination with respect to static cohesive parameter and fatigue damage functions based on strain energy release rate (SERR), separation and strain. The separation

and strain based fatigue damage functions are highly sensitive to cohesive stiffness and strength parameters but are relatively less sensitive to cohesive shape. The SERR based fatigue damage function is almost insensitive to cohesive stiffness and shape but is slightly sensitive to cohesive strength. Considering that the initial stiffness is usually treated as an adjustable penalty parameter, it seems more appropriate to formulate fatigue damage rate as a function of the SERR. Unlike bilinear and exponential static cohesive laws, the polynomial cohesive law has a higher-order smoothness (C^1 continuity) and yields linear Paris plots in combination with all three fatigue damage functions; this is attributed to the lack of sudden transition between a linear-elastic and damage-softening regime in the polynomial law. Considering the high sensitivity of fatigue crack growth rate predictions to the cohesive strength and that it is factor in determining the cohesive zone size, more robust methodologies are necessary to establish the interface cohesive strength for a given composite material.

In Chapter 4, an updated-Lagrangian mixed finite element formulation was developed based on the nonlinear Stokes flow equations and a nonlocal creep damage law to simulate crevasse propagation in glaciers. The main features of this new formulation are: (1) an updated-Lagrangian approach enables tracking of geometry changes in the domain dynamically using an explicit mesh-update procedure and the evolution of continuum damage at material points, without the need to include the damage advection; (2) the nonlocal implementation of damage and damage controls alleviates the mesh dependency issues inherent to local damage models; (3) the P3-P1 mixed finite element implementation alleviates "checkerboard" instabilities in pressure and allows the efficient simulation of incompressible viscous deformation of ice; and (4) the automated element removal scheme allows for the representation of fully damaged material without introducing rank deficiencies to the finite element stiffness matrix. The formulation was tested and validated using the previously established small-deformation Maxwell viscoelastic model as the benchmark. Numerical simulations performed on idealized rectangular domains demonstrate that the Stokes flow

model is suitable for simulating flow and fracture in ice because it is consistent with the Maxwell-type viscoelastic model over the shorter time scales of crevasse propagation (i.e., $t = 5$ - 20 days) under gravity-induced flow. Over long decadal time scales, it is expected that the proposed update-Lagrangian approach is superior to the small-deformation total Lagrangian approach due to its ability to account for large deformations.

In Chapter 5, we reviewed and compared four theoretical fracture mechanics models for estimating crevasse penetration depths against one another: (1) the Nye [1955] zero-stress model; (2) the Weertman [1973] dislocation-based fracture mechanics model; (3) the van der Veen [1998a] linear elastic fracture mechanics (LEFM) model; and (4) the Krug et al. [2014] LEFM model. We also compared the nonlocal continuum damage mechanics (CDM) approach [Jiménez et al., 2017] against these theoretical models by estimating the penetration depths of dry and water-filled surface crevasses in grounded glaciers. The damage mechanics approach illustrates that the presence of water pressure within crevasses results in deeper penetration into the glacier, and thus it is qualitatively consistent with the fracture mechanics approaches. Numerical results show good agreement with Weertman [1973] model, except when the glacier is near floatation (i.e., $h_w/H = 0.9$). Our results also indicate that the mechanisms responsible for crevasse propagation are sensitive to ice rheology and large deformation effects. Overall, we believe that the damage mechanics approach is appropriate for simulating the propagation of water-filled surface crevasses and estimating their maximum penetration depths.

In Chapter 6, we presented two damage mechanics approaches for time-independent, brittle fracture, namely the cohesive zone model (CZM) and the phase field model (PFM), to simulate the propagation of water-filled surface and basal crevasses through grounded, marine-terminating glaciers. We employed the CZM and PFM to simulate the propagation of water-filled surface crevasses through a glacier and compared numerical results against the Weertman [1973] dislocation mechanics based model. We discovered that the PFM with a strain energy density based crack driving force is not an appropriate technique for sim-

ulating surface crevasse growth due to the unrealistic damage morphology; however, implementing a maximum principal stress based crack driving force predicted more realistic crevasse growth. The CZM and PFM both showed excellent agreement with the Weertman [1973] model when the seawater depth at the terminus is large (i.e., when the seawater depth is greater than or equal to 50% of the slab thickness); however, for lesser seawater depths the numerical models tended to overestimate the crevasse penetration depth. We also studied the conditions necessary for basal crevasse evolution in glaciers and observed through finite element analysis that the Cauchy stress at the tip of a water-filled basal crevasse is in a compressive state if considering incompressible ice. However, when considering compressible ice, the stresses at the crevasse tip are both tensile and sufficiently large to stimulate damage growth. We employed the CZM, PFM, and the nonlocal creep damage mechanics model to simulate basal crevasse growth. Each approach predicted zero basal crevasse propagation in the incompressible ice; and each approach predicted full or nearly-full crevasse penetration when considering compressible ice. From this, we conclude that it is necessary to consider the compressibility of ice when modeling basal crevasse growth in grounded glaciers, unless other physical mechanisms (e.g., melting, grounded-to-floating transition) are accounted for in the process of crevasse evolution.

CHAPTER 8

Appendix

Appendix A Relation between ρ and Ψ

The mixed mode bending test was proposed by Reeder and Crews [Reeder and Crews, 1990], shown in Figure A1. A concentrated load P is applied through the rigid lever, and

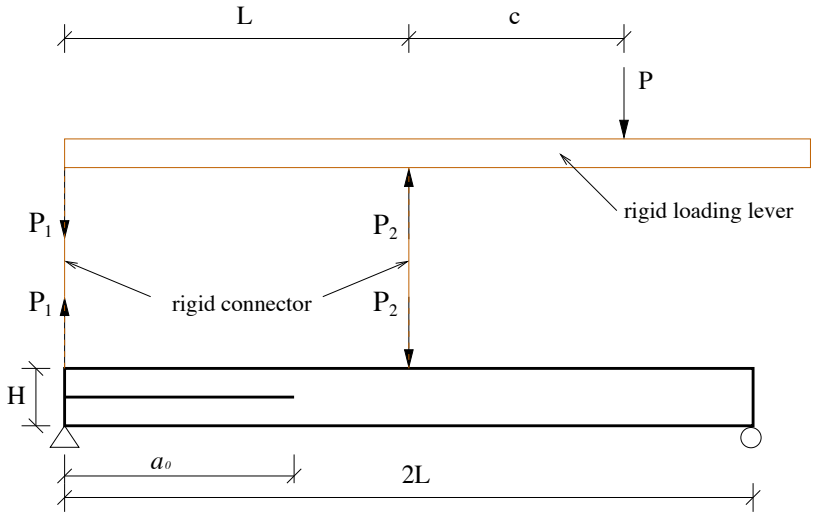

Figure A1: The geometry and boundary conditions for mixed mode bending (MMB) test.

the forces transferred to the beam obtained from equilibrium are,

$$P_1 = P\frac{c}{L}, \quad P_2 = P\frac{c+L}{L} \tag{1}$$

This mixed mode bending (MMB) system can be considered as the superposition of Mode I and Mode II [Reeder and Crews, 1990], as shown in Figure A2. Due to the y-axis symmetry of the mode II four point end notch fracture (ENF) test, it is sufficient to consider one-half of the beam as a cantilever [Robinson et al., 2005, Williams, 1988]. Now, following equations

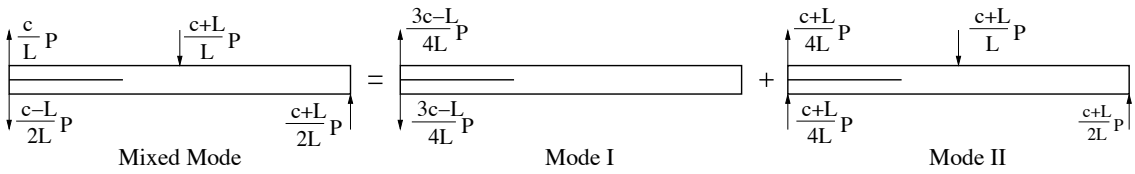

Figure A2: Superposition analysis of the mixed mode bending (MMB) system (Redrawn from Reeder and Crews [Reeder and Crews, 1990])

(2.38) and (2.41), we can write the strain energy release rate under Mode I and Mode II as,

$$G_{\mathrm{I}} = \left(\frac{3c-L}{4L}\right)^2 \frac{P^2 a_0^2}{WEI} \tag{2}$$

$$G_{\mathrm{II}} = \left(\frac{c+L}{4L}\right)^2 \frac{3P^2 a_0^2}{4WEI} \tag{3}$$

Substituting the above two expressions for G_I and G_{II} into Equation 2.26 we get the following relation for the mode ratio Ψ:

$$\Psi = \frac{G_{\mathrm{II}}}{G_{\mathrm{I}} + G_{\mathrm{II}}} = \frac{3\left(\frac{c}{L}+1\right)^2}{3\left(\frac{c}{L}+1\right)^2 + 4\left(3\frac{c}{L}-1\right)^2}. \tag{4}$$

An alternative mixed mode test is configured as shown in Figure A3, which is equivalent to the MMB test shown in Figure A1. The forces applied on the upper and lower arm are

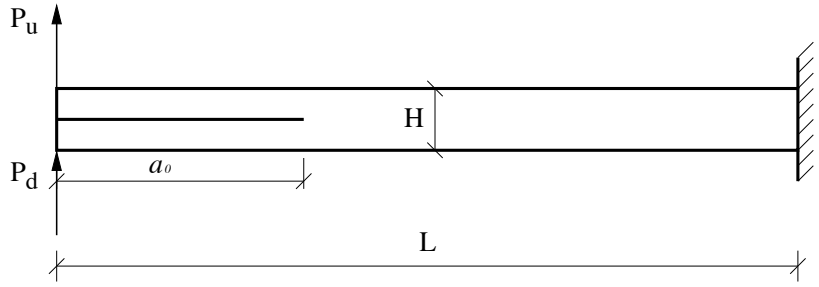

Figure A3: Geometry and boundary conditions for an alternative mixed mode bending (MMB) test

obtained from the superposition of Mode I and Mode II, given as,

$$P_{\mathrm{u}} = P\frac{c+L}{4L} + P\frac{3c-L}{4L} \tag{5}$$

$$P_{\mathrm{d}} = P\frac{c+L}{4L} - P\frac{3c-L}{4L} \tag{6}$$

The ratio between these two applied forces is defined as ρ, written as,

$$\rho = \frac{P_{\mathrm{d}}}{P_{\mathrm{u}}} = \frac{\left(\frac{c}{L}+1\right) - \left(3\frac{c}{L}-1\right)}{\left(\frac{c}{L}+1\right) + \left(3\frac{c}{L}-1\right)} = \frac{1 - \frac{\left(3\frac{c}{L}-1\right)}{\left(\frac{c}{L}+1\right)}}{1 + \frac{\left(3\frac{c}{L}-1\right)}{\left(\frac{c}{L}+1\right)}}. \tag{7}$$

From equation 4 we get,

$$\left(\Psi^{-1}-1\right) = \frac{4\left(3\frac{c}{L}-1\right)^2}{3\left(\frac{c}{L}+1\right)^2}. \tag{8}$$

Substituting the above equation in equation 7 we obtain the following relationship for the force ratio ρ in terms of the mode ratio Ψ:

$$\rho = \frac{1 - \frac{\sqrt{3}}{2}(\Psi^{-1}-1)^{1/2}}{1 + \frac{\sqrt{3}}{2}(\Psi^{-1}-1)^{1/2}} \tag{9}$$

Appendix B Relation between K_e^0 and Ψ

Herein, we derive the relation used in Section 2.3.2 for calculating the undamaged effective stiffness K_e^0 of a spring element under mixed mode conditions. Let us consider a mixed-mode condition when the normal and tangential separations are δ_n^* and δ_t^*, respectively. Under this deformation state, let the equivalent separation reach the critical value, that is,

$$(\delta_e^{cr})^2 = (\delta_t^*)^2 + (\delta_n^*)^2 \tag{10}$$

Let us consider the case when $\delta_n^* < \delta_n^{cr}$ and $\delta_t^* < \delta_t^{cr}$, that is, the loading condition falls within the elastic zones of the normal and tangential damage laws, respectively. Now, the strain energy release rates under Mode I and Mode II are given by,

$$G_I = \frac{1}{2} K_n^0 (\delta_n^*)^2 \text{ and } G_{II} = \frac{1}{2} K_t^0 (\delta_t^*)^2. \tag{11}$$

where K_n^0 and K_t^0 are the undamaged normal and tangential stiffnesses of the spring element. In terms of the equivalent stiffness and separations, the total strain energy release under this mixed mode condition is given by,

$$G = \frac{1}{2} K_e^0 (\delta_e^{cr})^2 \tag{12}$$

Now, the mixed mode ratio is defined as,

$$\Psi = \frac{G_{II}}{G} = \frac{K_t^0 (\delta_t^*)^2}{K_e^0 (\delta_e^{cr})^2}, \tag{13}$$

and

$$1 - \Psi = \frac{G_I}{G} = \frac{K_n^0 (\delta_n^*)^2}{K_e^0 (\delta_e^{cr})^2}; \tag{14}$$

Rearranging the above two expressions we get,

$$(\delta_{\mathrm{t}}^{*})^2 = \left(\frac{\Psi}{K_{\mathrm{t}}^0}\right) K_{\mathrm{e}}^0 (\delta_{\mathrm{e}}^{\mathrm{cr}})^2; \text{ and } (\delta_{\mathrm{n}}^{*})^2 = \left(\frac{1-\Psi}{K_{\mathrm{n}}^0}\right) K_{\mathrm{e}}^0 (\delta_{\mathrm{e}}^{\mathrm{cr}})^2; \tag{15}$$

Substituting the above relations into equation (10) and simplifying, we get the relation,

$$\frac{1}{K_{\mathrm{e}}^0} = \frac{\Psi}{K_{\mathrm{t}}^0} + \frac{1-\Psi}{K_{\mathrm{n}}^0} \tag{16}$$

The above relation can be rearranged to obtain equation (2.25). Clearly, under pure Mode I conditions ($\Psi = 0$), we have $K_{\mathrm{e}}^0 = K_{\mathrm{n}}^0$ and under pure Mode II conditions ($\Psi = 1$), we have $K_{\mathrm{e}}^0 = K_{\mathrm{t}}^0$.

Appendix C Influence of static CZM parameters for monotonic crack growth

Here, we use the common load-deflection ($P-\Delta$) curve to investigate the sensitivity of monotonic delamination crack growth results to the CZM parameters G_{IC}, $\sigma_{\max}$, and K_{n}^{0} and to the shape of the $T-\delta$ law. The $P-\Delta$ curve is obtained by conducting a DCB test with controlled displacement of the cantilever arms. The reaction force P at the ends of the cantilever arms is then measured and plotted as a function of deflection Δ of the arms. For this analysis, we use the experimental setup shown in Figure D5, except that we apply controlled displacement instead of moments. First, we obtain a $P-\Delta$ curve using the bilinear $T-\delta$ law with values for G_{IC}, $\sigma_{\max}$, and K_{n}^{0} given in Table E2. We then vary the value of each parameter one by one while holding the others constant. The $P-\Delta$ curves obtained from this are shown in Figures C4a-c. Next, we obtain $P-\Delta$ curves using the polynomial and exponential $T-\delta$ laws with the same values of G_{IC} and $\sigma_{\max}$ given in Table E2 to compare to the bilinear case; the result is shown in Figure C4d. From Figure C4 it is clear that results for static loading are largely insensitive to the parameters $\sigma_{\max}$, K_{n}^{0} and to the $T-\delta$ shape, and only the critical fracture energy G_{IC} has a substantial influence. This is verified to be true even for mode II and mixed-mode loading cases (results are not shown here). The conclusions of this study may not be valid for any arbitrary choice of cohesive parameters and the geometric length scales of the problem domain. As Needleman [2014] points out, when the cohesive length scale is large compared to the geometric length scale, the predicted load-displacement behavior of the beam can be much more sensitive to the shape of the $T-\delta$ law and cohesive strength.

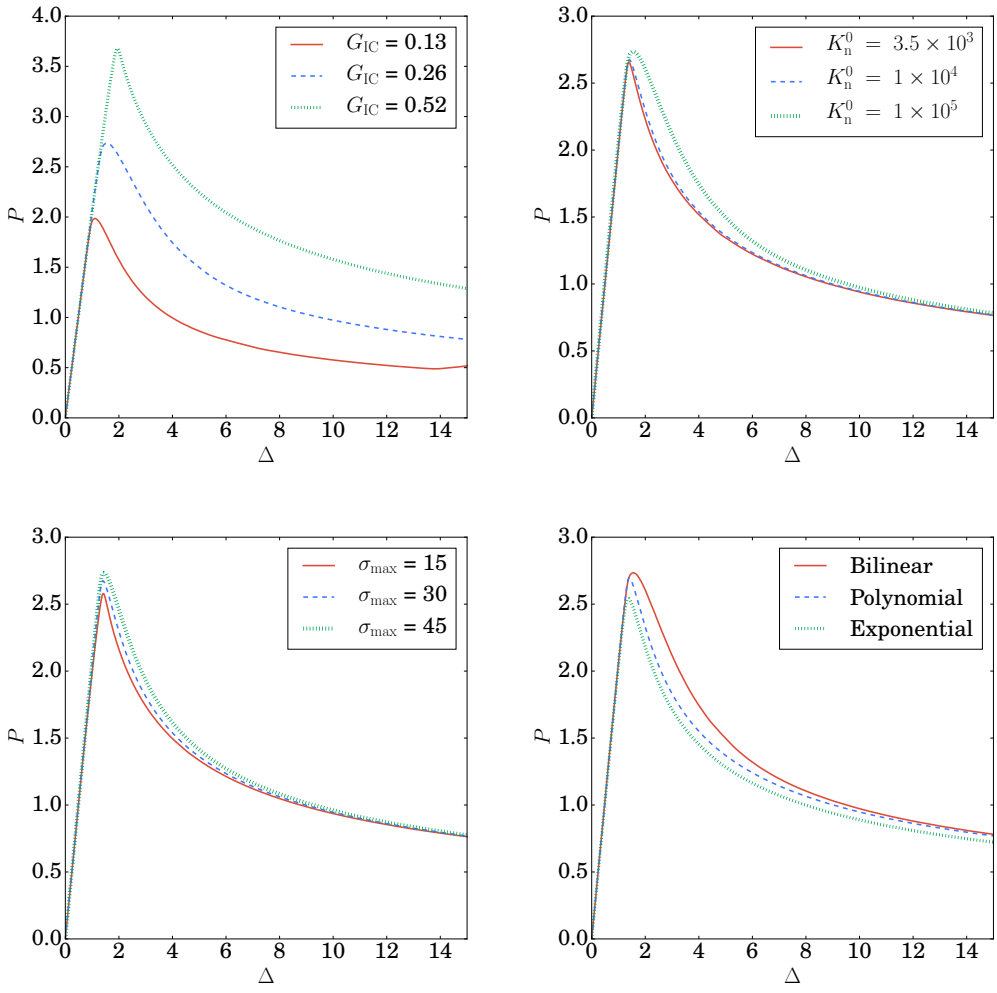

Figure C4: Load-deflection curves of a double cantilever beam test. Sensitivity of results to static parameters is shown by: (a) variation of G_{IC}; (b) variation K_n^0; (c) variation of σ_{max}; (d) variation of $T - \delta$ shape.

Appendix D Calibration of mode I fatigue parameters

The setup of the mode I double cantilever beam (DCB) test with applied moment M is shown in Figure D5, wherein one end of the beam is given a fixed boundary condition and the other end has a pre-crack splitting the beam depth in half. A cohesive interface is assigned behind the precrack so that once the DCB is loaded appropriately the crack will grow. The geometry of the DCB model is depicted in Figure D5 where L is the length of the beam, a_0 is the initial crack length, H is the thickness of the beam, and M is an applied moment. The moment M is linearly increased from zero to the maximum amplitude and then held constant, at which point fatigue cycling is initiated. Numerical results are displayed on Paris plots wherein the rate of crack growth with respect to loading cycles $\mathrm{d}a/\mathrm{d}N$ and the normalized mode I strain energy release rate $\Delta G_{\mathrm{I}}/G_{\mathrm{IC}}$ are plotted on a log-log scale. The mode I strain energy G_{I} is related to the applied moment M as [Reeder and Crews, 1990, Williams, 1988],

$$G_{\mathrm{I}} = \frac{M^2}{W E_{\mathrm{xx}} I} \tag{17}$$

where W is the in-plane depth of the beam and I is the moment of inertia of the cantilever arms. For an applied moment M and corresponding G_{I}, the fatigue crack growth rate $\mathrm{d}a/\mathrm{d}N$ is calculated as the ratio of the incremental crack length Δa along the interface and the number of loading cycles ΔN required to advance the crack length by Δa. Herein, we measure ΔN by recording the number cycles between the failure (i.e., $D_{\mathrm{t}} = 1$) of the first and fourth integration points along the interface, $N^{\mathrm{fail}}_{\mathrm{IP}\,1}$ and $N^{\mathrm{fail}}_{\mathrm{IP}\,4}$ respectively. Thus, $\Delta N = N^{\mathrm{fail}}_{\mathrm{IP}\,4} - N^{\mathrm{fail}}_{\mathrm{IP}\,1}$, and $\Delta a = 3h/2$, where h is the structured finite element mesh size.

Fatigue parameters C_i and m_i for $i = \{1, 2, 3\}$ for the three different damage functions are calibrated assuming a bilinear traction-separation law with static cohesive parameters given in Table E2. The calibration is performed by comparing model results to the least squares best fit line [Blanco et al., 2004] of the experimental data of Asp et al. [2001] on a Paris plot, as shown in Figure D6. The SERR based fatigue damage function yields

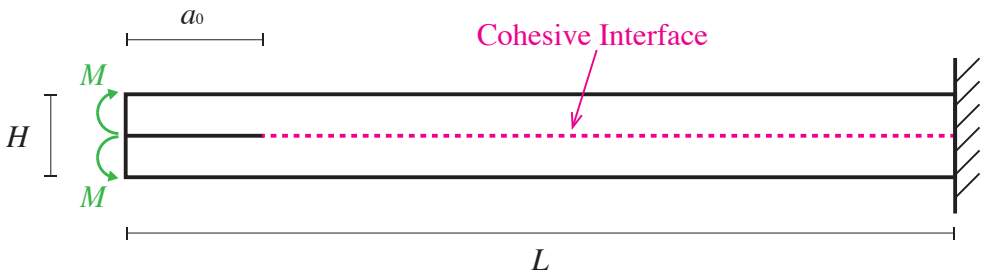

Figure D5: Setup of the double cantilever beam (DCB) test. Dimensions: $L = 150$mm, $a_0 = 35$mm, $H = 3.1$mm.

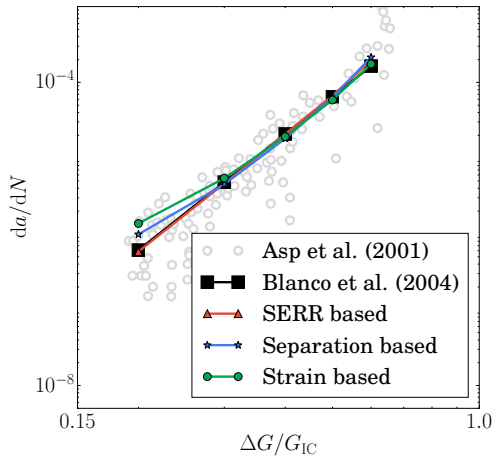

Figure D6: Calibration of SERR, separation, and strain based fatigue damage functions under pure mode I loading.

a straight line that closely matches the linear Paris law; the strain and separation based fatigue damage functions yield slightly curved lines, although they do not deviate beyond the range of experimental data. The calibrated fatigue parameters are shown in Table E3.

Appendix E Calibration of mixed-mode fatigue parameters

The mixed mode bending (MMB) test is employed for this analysis, wherein two moments M and ρM are applied to the ends of the cantilever arms to induce mixed mode delamination. Beam dimensions are specified in Figure E7. The moments M and ρM are linearly increased from zero to the maximum amplitude and then held constant, at which point fatigue cycling initiates. The corresponding mixed mode SERR G is related to the applied moment M as [Reeder and Crews, 1990],

$$G = G_{\mathrm{I}} + G_{\mathrm{II}} \tag{18}$$

where,

$$G_{\mathrm{I}} = \left(\frac{2\sqrt{3}}{\left(\psi^{-1}-1\right)^{-1/2} + \frac{\sqrt{3}}{2}} \right)^2 \frac{3M^2}{48WE_{\mathrm{xx}}I}, \tag{19}$$

$$G_{\mathrm{II}} = \left(\frac{4}{1 + \frac{\sqrt{3}}{2}\left(\psi^{-1}-1\right)^{1/2}} \right)^2 \frac{3M^2}{64WE_{\mathrm{xx}}I}. \tag{20}$$

The mode-mix ratio ψ is defined as $G_{\mathrm{II}}/(G_{\mathrm{I}} + G_{\mathrm{II}})$ and ρ is given by,

$$\rho = \begin{cases} -1 & \psi = 0 \\ \dfrac{1 - \frac{\sqrt{3}}{2}\left(\psi^{-1}-1\right)^{1/2}}{1 + \frac{\sqrt{3}}{2}\left(\psi^{-1}-1\right)^{1/2}} & 0 < \psi \leq 1 \end{cases} \tag{21}$$

Parameters C_i and m_i are calibrated for the three damage functions in the same way as described in the previous section, assuming the bilinear $T - \delta$ law with static CZM parameters given in Table E2. The calibrated parameters for 50% mixed mode loading are

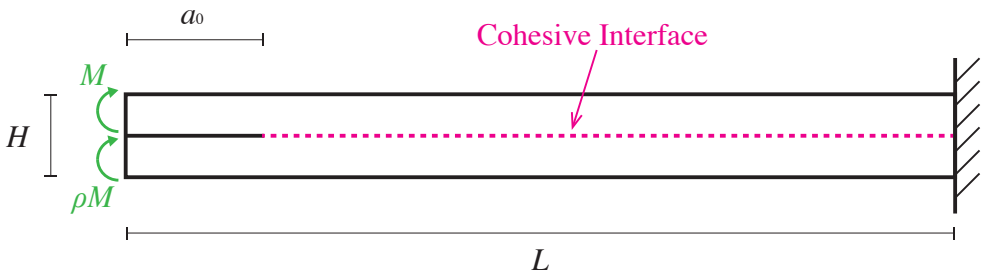

Figure E7: Setup of the mixed mode bending (MMB) test. Dimensions: $L = 150$mm, $a_0 = 35$mm, $H = 3.1$mm.

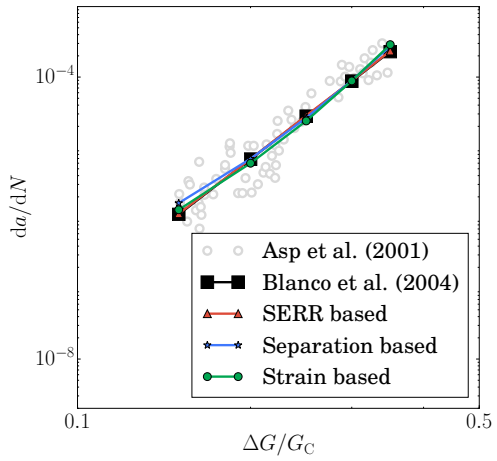

Figure E8: Calibration of SERR based, Separation based, and Strain based damage functions under 50% mixed mode loading.

presented in Table E3 and a plot of the calibration is shown in Figure E8.

Table E1: Material properties of carbon fiber/epoxy laminated composite HTA/6367C obtained from Asp et al. [2001]

Property (Units)	E_{11} (MPa)	$E_{22} = E_{33}$ (MPa)	$G_{12} = G_{13}$ (MPa)	$\nu_{12} = \nu_{13}$
Value	1.2×10^5	1.05×10^4	5.52×10^3	0.3

Table E2: Static cohesive parameters for the bilinear law (all values except K_n^0 and K_t^0 are assumed from Harper and Hallett [2010])

Parameter (Units)	K_n^0 $\left(\frac{N}{mm^3}\right)$	K_t^0 $\left(\frac{N}{mm^3}\right)$	G_{IC} $\left(\frac{N}{mm}\right)$	G_{IIC} $\left(\frac{N}{mm}\right)$	G_C $\left(\frac{N}{mm}\right)$	σ_{max} $\left(\frac{N}{mm^2}\right)$	τ_{max} $\left(\frac{N}{mm^2}\right)$
	1×10^4	2×10^4	0.26	1.002	0.447	30	60

Table E3: Fatigue damage parameters

Parameter (Units)	Mode I	Mixed Mode
C_1 $(\mathrm{mm/cycle})$	1.62×10^{-3}	1.125×10^{-1}
m_1 $(--)$	4.2	5.5
C_2 $(1/\mathrm{cycle})$	6.0	7×10^{4}
m_2 $(--)$	3.6	6.5
C_3 $(1/\mathrm{cycle})$	6×10^{-1}	8.75×10^{4}
m_3 $(--)$	4.2	8.0

Algorithm 7 : An iterative algorithm for computing damage for the separation-based fatigue damage function

Assume the system state (i.e., damage and separation) is known after N cycles, and the separations δ_{n}, δ_{t} are known at $N+\Delta N$ cycles. Then, the goal is to compute the damage state at $N+\Delta N$ cycles. Let r represent residual error in the iterative scheme, and r_{tol} is the error tolerance.

(1) Compute $D_{\mathrm{s}}(N+\Delta N)$ from the cohesive traction-separation law. Then, $\Delta D_{\mathrm{s}} = D_{\mathrm{s}}(N+\Delta N) - D_{\mathrm{s}}(N)$.

(2) Compute $\delta_\mu = (1-\mu)\dot{\varepsilon}(N) + \mu\dot{\varepsilon}(N+\Delta N)$ where $\dot{\varepsilon} = \sqrt{(\delta_{\mathrm{n}})^2 + (\delta_{\mathrm{t}})^2}$. In this study we take $\mu = 0.5$.

(3) Initialize, $j = 0$:

(i) ${}^0D = D(N)$

(ii) Select ${}^0r >> r_{tol}$

(4) While $|{}^j r| > r_{tol}$:

(i) Compute fatigue damage increment for $j = \{0,1,2,...\}$:

$$\begin{aligned} {}^jD_\mu &= (1-\mu)D(N) + \mu\ {}^jD \\ \Delta D_{\mathrm{f}} &= \Delta N \left(\frac{C_2}{1+m_2}\right) \exp\left(\lambda\ {}^jD_\mu\right) \left(\frac{\delta_\mu}{\delta_{\mathrm{f}}}\right)^{m_2+1} \end{aligned}$$

(ii) Compute ${}^j r$:

$${}^j r = {}^jD - (D(N) + \Delta D_{\mathrm{s}} + \Delta D_{\mathrm{f}})$$

(iii) Compute the Jacobian:

$$\frac{\partial\ {}^j r}{\partial\ {}^jD} = 1 - \lambda\mu\Delta N \left(\frac{C_2}{1+m_2}\right) \exp\left(\lambda\ {}^jD_\mu\right) \left(\frac{\delta_\mu}{\delta_{\mathrm{f}}}\right)^{m_2+1}$$

(iv) Update damage:

$${}^{j+1}D = {}^jD - \left(\frac{\partial\ {}^j r}{\partial\ {}^jD}\right)^{-1} {}^j r \tag{22}$$

(v) Update iteration count: $j = j+1$

(5) Finally, $D(N+\Delta N) = {}^jD = D_{\mathrm{t}}$. For post-processing, $D_{\mathrm{f}} = D_{\mathrm{t}} - D_{\mathrm{s}}$.

Appendix F Small-deformation Maxwell viscoelasticity

Appendix F.1 Constitutive law

Here we review the salients features of the small-deformation Maxwell viscoelastic model based on a total Lagrangian approach for simulating creep damage evolution in ice [Duddu and Waisman, 2013c]. Considering that polycrystalline ice behaves isotropically and assuming small deformations, the total strain ε^{t} and total strain rate $\dot{\varepsilon}^{\mathrm{t}}_{ij}$ can be additively decomposed into its elastic and viscous components as

$$\varepsilon^{\mathrm{t}}_{ij} = \varepsilon^{\mathrm{e}}_{ij} + \varepsilon^{\mathrm{v}}_{ij}; \quad \dot{\varepsilon}^{\mathrm{t}}_{ij} = \dot{\varepsilon}^{\mathrm{e}}_{ij} + \dot{\varepsilon}^{\mathrm{v}}_{ij}, \tag{23}$$

where the subscript indices denote tensor components. The elastic stress-strain relationship in the effective space and physical space are given by

$$\widetilde{\sigma}_{ij} = C_{ijkl}\varepsilon^{\mathrm{e}}_{kl}; \quad \sigma_{ij} = C^{\mathrm{dam}}_{ijkl}\varepsilon^{\mathrm{e}}_{kl}, \tag{24}$$

where σ_{ij} is the Cauchy stress tensor, C_{ijkl} is the fourth-order stiffness tensor, and $C^{\mathrm{dam}}_{ijkl} = (1-D)C_{ijkl}$. For linear elasticity, the components of C_{ijkl} are

$$C_{ijkl} = \frac{E_Y}{3(1-2\nu)}\delta_{ij}\delta_{kl} + \frac{E_Y}{2(1+\nu)}\left(\delta_{ik}\delta_{jl} + \delta_{il}\delta_{jk} - \frac{2}{3}\delta_{ij}\delta_{lk}\right), \tag{25}$$

where $E_Y = 9500$ MPa and $\nu = 0.35$ are the Young's modulus and Poisson's ratio of ice, respectively, and δ_{ij} is Kronecker's delta.

The viscous strain rate $\dot{\varepsilon}^{\mathrm{v}}$ is given by the power law [Betten, 1986, Karr and Choi, 1989]

$$\dot{\varepsilon}^{\mathrm{v}}_{ij} = \frac{3}{2}K_N\left(\frac{3}{2}\widetilde{\tau}_{kl}\widetilde{\tau}_{kl}\right)^{(N-1)/2}\widetilde{\tau}_{ij}, \tag{26}$$

where the coefficient $K_N = 1.588 \times 10^{-7}$ MPa^{-3} s^{-1} at $T = -10°C$ and exponent $N = 3$ are viscous parameters, and $\widetilde{\tau}_{ij}$ is the effective deviatoric stress. Note the similarity to Equation 4.17, which is based on the Glen's flow law [Glen, 1955] and repeated below:

$$\dot{\varepsilon}_{ij} = A\,(\widetilde{\tau}^{\mathrm{eq}})^{N-1}\,\widetilde{\tau}_{ij} \tag{27}$$

For the exponent $N = 3$, a relationship between K_N and A can be established by equating $\dot{\varepsilon}^{\mathrm{v}}_{ij}$ and $\dot{\varepsilon}_{ij}$

$$\frac{3}{2}K_N\left(\frac{3}{2}\widetilde{\tau}_{kl}\widetilde{\tau}_{kl}\right)\widetilde{\tau}_{ij} = A(\widetilde{\tau}^{\mathrm{eq}})^2\widetilde{\tau}_{ij}. \tag{28}$$

By removing the $\widetilde{\tau}_{ij}$ term from each side of the equation and then substituting the relation $(\widetilde{\tau}^{\mathrm{eq}})^2 = \frac{1}{2}\widetilde{\tau}_{kl}\widetilde{\tau}_{kl}$, it follows that $\frac{9}{2}K_N = A$. In this study, we select an experimentally calibrated value for A used in the Stokes model and then calculate K_N for the Maxwell viscoelastic model.

Appendix F.2 Maxwell viscoelastic model in deviatoric space

In this section, we show that the small-deformation viscoelastic model behaves like a Maxwell model in deviatoric space. Let us additively decompose the strain into volumetric (denoted with superscript vol) and deviatoric (superscript dev) components

$$\varepsilon^{\mathrm{t}\ \mathrm{vol}}_{ij} = \frac{1}{3}\varepsilon^{\mathrm{t}}_{kk}\delta_{ij}, \quad \varepsilon^{\mathrm{t}\ \mathrm{dev}}_{ij} = \varepsilon^{\mathrm{t}}_{ij} - \varepsilon^{\mathrm{t}\ \mathrm{vol}}_{ij}, \tag{29}$$

with $\varepsilon^{\mathrm{e}}_{ij}$ and $\varepsilon^{\mathrm{v}}_{ij}$ similarly split into volumetric and deviatoric parts. The additive decomposition of strain in Equation (23) still holds in the volumetric and deviatoric spaces such that $\varepsilon^{\mathrm{t}\ \mathrm{vol}}_{ij} = \varepsilon^{\mathrm{e}\ \mathrm{vol}}_{ij} + \varepsilon^{\mathrm{v}\ \mathrm{vol}}_{ij}$ and $\varepsilon^{\mathrm{t}\ \mathrm{dev}}_{ij} = \varepsilon^{\mathrm{e}\ \mathrm{dev}}_{ij} + \varepsilon^{\mathrm{v}\ \mathrm{dev}}_{ij}$. Then, the effective Cauchy stress and

deviatoric stress can be represented in terms of $\varepsilon_{ij}^{\mathrm{e\ vol}}$ and $\varepsilon_{ij}^{\mathrm{e\ dev}}$ as

$$\widetilde{\sigma}_{ij} = \frac{E_Y}{(1-2\nu)}\left(\varepsilon_{ij}^{\mathrm{e\ vol}}\right) + \frac{E_Y}{(1+\nu)}\left(\varepsilon_{ij}^{\mathrm{e\ dev}}\right), \quad \widetilde{\tau}_{ij} = \frac{E_Y}{(1+\nu)}\left(\varepsilon_{ij}^{\mathrm{e\ dev}}\right). \tag{30}$$

Since the viscous strain rate $\dot{\varepsilon}_{ij}^{\mathrm{v}}$ of ice is driven purely by deviatoric stresses (Eq. 26), the volumetric component $\dot{\varepsilon}_{ij}^{\mathrm{v\ vol}} = 0$, thus leaving $\dot{\varepsilon}_{ij}^{\mathrm{v}} = \dot{\varepsilon}_{ij}^{\mathrm{v\ dev}}$. For the deviatoric component of total strain rate $\dot{\varepsilon}_{ij}^{\mathrm{t\ dev}}$ we now have

$$\begin{aligned} \dot{\varepsilon}_{ij}^{\mathrm{t\ dev}} &= \dot{\varepsilon}_{ij}^{\mathrm{e\ dev}} + \dot{\varepsilon}_{ij}^{\mathrm{v\ dev}} \\ &= \left[\frac{(1+\nu)}{E_Y}\right]\dot{\widetilde{\tau}}_{ij} + \left[\frac{3}{2}K_N\left(\frac{3}{2}\widetilde{\tau}_{kl}\widetilde{\tau}_{kl}\right)^{(N-1)/2}\right]\widetilde{\tau}_{ij}, \end{aligned} \tag{31}$$

which matches the form of the 1D Maxwell viscoelastic model

$$\dot{\varepsilon} = \frac{\dot{\sigma}}{\hat{E}_Y} + \frac{\sigma}{\hat{\eta}}, \tag{32}$$

where $\hat{\eta}$ is a viscosity parameter and $\hat{E}_Y$ is an elastic modulus parameter. The $1/2\mu$ term is analagous to the elastic coefficient $1/\hat{E}$, and $\left[\frac{3}{2}K_N\left(\frac{3}{2}\widetilde{\tau}_{kl}\widetilde{\tau}_{kl}\right)^{(N-1)/2}\right]$ is analagous to the viscosity coefficient $1/\hat{\eta}$.

Appendix F.3 Total Lagrangian implementation

We select a total Lagrangian frame of reference to describe motion in the viscoelastic model. Motion is characterized by a displacement field $\boldsymbol{u}\left({}^0\boldsymbol{x},t\right) = u_i\hat{\boldsymbol{e}}_i$ representing the positions of points relative to the initial reference configuration ${}^0\Omega$ with coordinates ${}^0\boldsymbol{x} = {}^0x_i\hat{\boldsymbol{e}}_i$. The kinematic strain-displacement relation is taken by assuming small deformations

$$\varepsilon_{ij}^{\mathrm{t}} = \frac{1}{2}\left(\frac{\partial\, u_i}{\partial\, {}^0x_j} + \frac{\partial\, u_j}{\partial\, {}^0x_i}\right). \tag{33}$$

The strong form of the viscoelastic equation is written with respect to reference coordinates The equilibrium equation of the viscoelasticity model is taken as a force balance describing the time-dependent deformation of solids in response to applied loads. The solution of the equilibrium equation is a displacement field $\boldsymbol{u}(\boldsymbol{X},t)$ representing the positions of points relative to some reference configuration with coordinates $\boldsymbol{X}$, and thus describes motion through a Lagrangian frame of reference. In indicial form, the equilibrium equation is written as,

$$\frac{\partial\ \sigma_{ij}}{\partial\ {}^0x_j} + b_i = 0 \qquad \text{on } {}^0\Omega, \tag{34}$$

with Dirichlet and Neumann boundary conditions

$$\begin{aligned} u_i &= \bar{u}_i \quad \text{on } {}^0\Gamma^{\mathrm{D}}, \\ \sigma_{ij}\hat{n}_j &= \bar{\mathscr{T}}_i \quad \text{on } {}^0\Gamma^{\mathrm{N}}, \end{aligned} \tag{35}$$

where σ_{ij} and b_i are components of the Cauchy stress tensor and external body force vector, respectively; $\bar{\boldsymbol{u}}$ is a Dirichlet boundary condition (i.e., applied displacement); $\hat{\boldsymbol{n}}$ is an outward normal unit vector along the boundary; and $\bar{\mathscr{T}}$ is a vector of applied tractions. The full details of the finite element implementation of this total Lagrangian formulation can be found in [Duddu and Waisman, 2013c].

Appendix G Lower-order alternatives to mixed finite elements

It is well known that solving the Stokes equations with equal-order interpolation of velocity and pressure does not satisfy the Ladyzhenskaya–Babuška–Brezzi (LBB) stability condition, thus leading to "checkerboard" oscillations in the pressure solution. To avoid this, a mixed-order finite element is typically employed which uses quadratic (P2) or cubic (P3) interpolation for the velocity field, while using a linear (P1) interpolation for pressure. Increasing the order of interpolation can significantly increase the computational expense, however, especially for large-scale simulations and 3D problems. Thus, several stabilized lower-order methods have been proposed, namely, the stabilized P1-P1 [Hughes and Franca, 1987, Franca and Stenberg, 1991, Gunzburger and Nicolaides, 1993] and the MINI-element [Arnold et al., 1984].

Appendix G.1 Stabilized P1-P1 element

The stabilized P1-P1 element assumes equal-order (linear) interpolation for velocity and pressure and satisfies the LBB condition by introducing a stabilization term (highlighted with blue text) to the variational form. Following [Hughes and Franca, 1987, Franca and Stenberg, 1991], we write the weak form as,

Find ${}^{n+1}\boldsymbol{v} \in \mathscr{V}$ and ${}^{n+1}\widetilde{p} \in \mathscr{S}$ such that $\forall\, \boldsymbol{w} \in \mathscr{V}$ and $q \in \mathscr{S}$:

$$\left.\begin{aligned}
&\int_{{}^{n}\Omega} \frac{\partial\, w_i}{\partial\, {}^{n}x_j} \left\{ [1 - {}^{n}D]\, \eta\, ({}^{n+1}\boldsymbol{v}) \left[\frac{\partial\, {}^{n+1}v_i}{\partial\, {}^{n}x_j} + \frac{\partial\, {}^{n+1}v_j}{\partial\, {}^{n}x_i} \right] \right\} \mathrm{d}\Omega \\
&- \int_{{}^{n}\Omega} [1 - {}^{n}D] \frac{\partial\, w_i}{\partial\, {}^{n}x_i} {}^{n+1}\widetilde{p}\, \mathrm{d}\Omega + \zeta h^2 \int_{{}^{n}\Omega} \left(\frac{\partial\, q}{\partial\, {}^{n}x_j} \frac{\partial\, p}{\partial\, {}^{n}x_j} \right) \mathrm{d}\Omega \\
&- \int_{{}^{n}\Omega} \psi({}^{n}D) w_i\, {}^{n}b_i\, \mathrm{d}\Omega - \zeta h^2 \int_{{}^{n}\Omega} \left(\frac{\partial\, q}{\partial\, {}^{n}x_j} \psi({}^{n}D)\, {}^{n}b_j \right) \mathrm{d}\Omega \\
&\int_{{}^{n}\Gamma^{\mathrm{N}}} w_i\, {}^{n}\bar{\mathscr{T}}_i\, \mathrm{d}\Gamma = 0 \\
&\int_{{}^{n}\Omega} \psi({}^{n}D) q \frac{\partial\, {}^{n+1}v_i}{\partial\, {}^{n}x_i}\, \mathrm{d}\Omega = 0
\end{aligned}\right\} \quad \text{on } {}^{n}\Omega, \qquad (36)$$

where h is the element size and $\zeta = 2 \times 10^{-10}$ is a chosen stabilization parameter. The first stabilization term in Equation (36) essentially is the $\varepsilon(\nabla q, \nabla p)$ term in [Brezzi and Pitkaranta, 1984] circumvents the LBB condition, and the second stabilization term makes the formulation mathematically consistent [Hughes and Stewart, 1996]. However, the drawback of this particular stabilized formulation is that the choice of ζ is typically made in an *ad hoc* manner [Turner et al., 2009]. While the stabilized P1-P1 element alleviates the checkerboard oscillations in pressure, we found that the incompressibility condition is still not well enforced. This can lead to deviatoric stresses inconsistent with those predicted by P3-P1 or P2-P1 elements, thus changing the Hayhurst stress around the notch tip and causing different rates of crevasse growth.

Appendix G.2 MINI-element

Another stable alternative to mixed-order elements is the enriched MINI-element [Arnold et al., 1984]. The MINI-element assumes linear velocity interpolants enriched using a bubble function, and thus has fewer degrees of freedom than a mixed-order finite element. A caveat is that triangular (T3) and tetrahedral (T4) MINI-elements alleviate oscillations

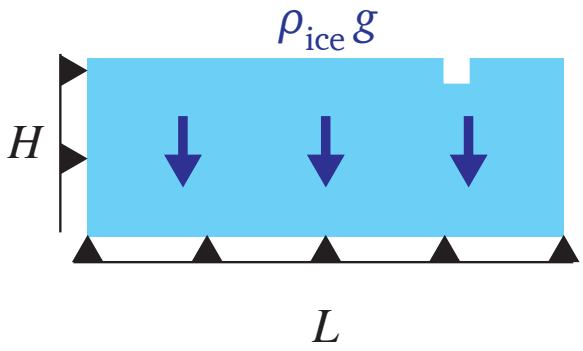

Figure G9: Domain setup with gravitational body force $\rho_{\text{ice}} g$ and a 10 m $\times$ 10 m notch placed along the top surface of the slab, where $H = 125$ m and $L = 500$ m. The notch is centered at the "three-quarter" mark, that is, 375 m from the left edge of the slab.

in pressure, but quadrilateral (Q4) and hexahedral (Q8) MINI-elements can suffer from instability, according to Turner et al. [Turner et al., 2009]. Herein, we compare the performance of MINI-elements to P3-P1, P2-P1, and stabilized P1-P1 elements by simulating crack growth under gravity-driven creep flow for 3 months. The performance of the MINI-element is evaluated by plotting the predicted crevasse depth versus time, which is the most important result from a ice sheet stability perspective. The direct enforcement of the free-slip Dirichlet boundary condition is difficult in FEniCS software, and so we implement no-slip boundary conditions along the the left and bottom boundaries instead; however, we note that weak formulations using penalty or Nitsche's method can be used to implement free slip conditions, which will be considered in future studies. The purpose of this study is to simply check the viability of the MINI-element for simulating crevasse propagation. All simulations are performed on a rectangular slab of ice that is 500 m $\times$ 125 m (length L $\times$ height H), as shown in Figure G9. A 10 m $\times$ 10 m notch is centered at the three-quarter mark along the slab, that is, 375 m from the left edge.

The results of this study are shown in Figure G10 wherein we plot the normalized crevasse depth d versus time t. In Table G4, we also list the crack tip damage initiation times and final normalized crevasse depth for each element type considered. The different elements predict very similar crack tip damage initiation times (i.e., around 9 days)

Table G4: Crack tip damage initiation time (in days) and final normalized crevasse depth d after 90 days for the gravity-driven flow problem with no-slip boundary conditions.

Element	**Damage Initiation**	**Final Depth**
MINI	8.26 days	46.6%
Stab. P1-P1	9.25 days	48.2%
P2-P1	9.21 days	51.3%
P3-P1	8.88 days	52.8%

and similar crack growth rates following damage initiation; however the P3-P1 and P2-P1 elements ultimately predict deeper crack penetration than the MINI- and stabilized P1-P1 elements. Although the MINI- and stabilized P1-P1 elements slightly under-predict the final crevasse depth, the simulations ran more than four times faster than the simulation using P3-P1 elements on the same mesh (i.e., the same number of triangular cells). We conclude from this study that the MINI-element is a stable alternative to the P3-P1 element; however, the stabilized P1-P1 element is easier to implement in FEniCS software and runs slightly faster than the MINI-element due to fewer degrees of freedom. The stabilized P1-P1 element also agrees slightly better with the P3-P1 and P2-P1 elements in terms of crack tip damage initiation time and final crevasse depth. Further, developments in stabilized methods is required to address the discrepancies in damage evolution in nonlinear viscous media.

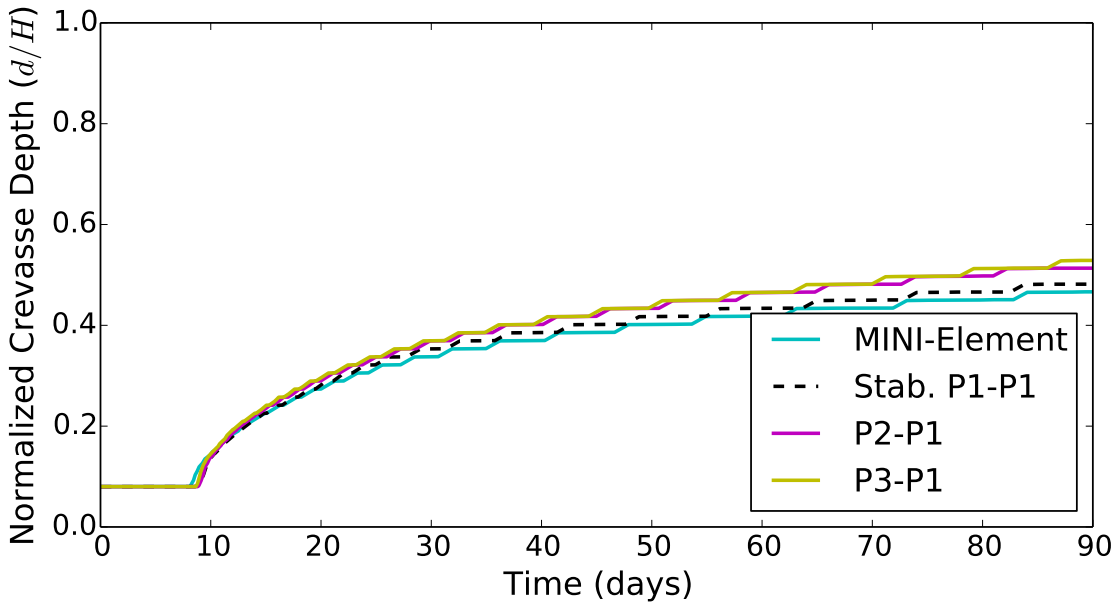

Figure G10: Crevasse depth (d) normalized with the domain height ($H = 125$ m) plotted as a function of time over 90 days for different finite element types.

Appendix H Newton's method

The Newton's method is an alternative scheme to the Picard (fixed point) iterations presented Algorithm 5 in Chapter 4 for solving the nonlinear Stokes equations [Isaac et al., 2015]. Whereas the Picard iteration scheme linearizes the PDE by making the nonlinear viscosity a function of velocity ${}^{n+1}_{(m)}\boldsymbol{v}$ from the previous iteration, the Newton's method linearizes the PDE by introducing velocity and pressure increments and linearizing the viscosity using a Taylor expansion,

$$\eta\left({}^{n+1}_{(m+1)}\boldsymbol{v}\right) = \eta\left({}^{n+1}_{(m)}\boldsymbol{v}\right) + \frac{\partial\eta}{\partial\,{}^{n+1}_{(m)}\boldsymbol{v}} \cdot {}^{n+1}\delta\boldsymbol{v}, \tag{37}$$

where ${}^{n+1}\delta\boldsymbol{v}$ is the velocity increment and ${}^{n+1}\delta\widetilde{p}$ is the pressure increment defined as

$$\begin{aligned} {}^{n+1}\delta\boldsymbol{v} &= {}^{n+1}_{(m+1)}\boldsymbol{v} - {}^{n+1}_{(m)}\boldsymbol{v}, \\ {}^{n+1}\delta\widetilde{p} &= {}^{n+1}_{(m+1)}\widetilde{p} - {}^{n+1}_{(m)}\widetilde{p}, \end{aligned} \tag{38}$$

between Newton iterations m and $m+1$. The derivative term in Equation (37) can be evaluated by applying the chain rule,

$$\begin{aligned} \frac{\partial\eta}{\partial\,{}^{n+1}_{(m)}\boldsymbol{v}} \cdot {}^{n+1}\delta\boldsymbol{v} &= \frac{\partial\eta}{\partial\mathscr{D}_{\mathrm{II}}\left({}^{n+1}_{(m)}\boldsymbol{v}\right)} \frac{\partial\mathscr{D}_{\mathrm{II}}\left({}^{n+1}_{(m)}\boldsymbol{v}\right)}{\partial\mathscr{D}\left({}^{n+1}_{(m)}\boldsymbol{v}\right)} : \frac{\partial\mathscr{D}\left({}^{n+1}_{(m)}\boldsymbol{v}\right)}{\partial\,{}^{n+1}_{(m)}\boldsymbol{v}} \cdot {}^{n+1}\delta\boldsymbol{v} \\ &= \frac{\partial\eta}{\partial\mathscr{D}_{\mathrm{II}}\left({}^{n+1}_{(m)}\boldsymbol{v}\right)} \mathscr{D}\left({}^{n+1}_{(m)}\boldsymbol{v}\right) : \mathscr{D}\left({}^{n+1}\delta\boldsymbol{v}\right), \end{aligned} \tag{39}$$

where the term $\mathscr{D}(\cdot)$ is the symmetric gradient operator,

$$\mathscr{D}(\boldsymbol{v}) = \frac{1}{2}\left(\nabla\boldsymbol{v} + \nabla\boldsymbol{v}^{\top}\right), \tag{40}$$

which yields the strain rate tensor when operating on velocity. Because $\mathscr{D}(\cdot)$ is a linear operator, it follows that

$$\mathscr{D}\left({}^{n+1}\boldsymbol{\delta v}\right) = \mathscr{D}\left({}^{n+1}_{(m+1)}\boldsymbol{v}\right) - \mathscr{D}\left({}^{n+1}_{(m)}\boldsymbol{v}\right). \tag{41}$$

The term $\mathscr{D}_{\mathrm{II}}(\cdot)$ is the second strain rate invariant given by

$$\mathscr{D}_{\mathrm{II}}(\boldsymbol{v}) = \frac{1}{2}\mathscr{D}(\boldsymbol{v}) : \mathscr{D}(\boldsymbol{v}), \tag{42}$$

such that $\dot{\varepsilon}^{\mathrm{eq}} = \sqrt{\mathscr{D}_{\mathrm{II}}(\boldsymbol{v})}$. The nonlinear viscosity $\eta(\boldsymbol{v}) = \frac{1}{2}B\left[\mathscr{D}_{\mathrm{II}}(\boldsymbol{v}) + \gamma\right]^{-1/3}$ with regularization parameter $\gamma = 10^{-14}$. Thus, the derivative of η with respect to $\mathscr{D}_{\mathrm{II}}$ is taken as

$$\frac{\partial \eta}{\partial \mathscr{D}_{\mathrm{II}}\left({}^{n+1}_{(m)}\boldsymbol{v}\right)} = -\frac{1}{3}\left[\frac{\eta\left({}^{n+1}_{(m)}\boldsymbol{v}\right)}{\mathscr{D}_{\mathrm{II}}\left({}^{n+1}_{(m)}\boldsymbol{v}\right) + \gamma}\right]. \tag{43}$$

Let us now write the weak form of the nonlinear Stokes equations on the current reference configuration ${}^{n}\Omega$ in tensorial notation at particular iteration $m+1$:

Find ${}^{n+1}\boldsymbol{\delta v} \in \mathscr{V}$ and ${}^{n+1}\delta\widetilde{p} \in \mathscr{S}$ such that $\forall\ \boldsymbol{w} \in \mathscr{V}$ and $q \in \mathscr{S}$:

$$\left.\begin{aligned} \int_{{}^{n}\Omega} \Big\{ & \mathscr{D}(\boldsymbol{w}) : 2\left[1 - {}^{n}D\right]\eta\left({}^{n+1}_{(m+1)}\boldsymbol{v}\right)\mathscr{D}\left({}^{n+1}_{(m+1)}\boldsymbol{v}\right) \\ & - \left[1 - {}^{n}D\right]\left[\nabla\cdot\boldsymbol{w}\right]\left[{}^{n+1}_{(m+1)}\widetilde{p}\right] - \psi\left({}^{n}D\right)\boldsymbol{w}\cdot{}^{n}\boldsymbol{b}\Big\}\mathrm{d}\Omega = 0, \\ & \int_{{}^{n}\Omega} \psi\left({}^{n}D\right) q\left[\nabla\cdot{}^{n+1}_{(m+1)}\boldsymbol{v}\right]\ \mathrm{d}\Omega = 0, \end{aligned}\right\} \tag{44}$$

where $\boldsymbol{w}$ is a test function for an appropriate vector space $\mathscr{V}$, and q is a test function for an appropriate scalar space $\mathscr{S}$. Using Equations (15-21), The Newton linearization of the above equation can thus be defined as:

Find ${}^{n+1}\boldsymbol{\delta v} \in \mathscr{V}$ and ${}^{n+1}\delta\widetilde{p} \in \mathscr{S}$ such that $\forall\, \boldsymbol{w} \in \mathscr{V}$ and $q \in \mathscr{S}$:

$$\left.\begin{aligned}
&\int_{{}^{n}\Omega} \mathscr{D}(\boldsymbol{w}) : \left\{ 2\left[1 - {}^{n}D\right] \eta \left({}^{n+1}_{(m)}\boldsymbol{v} \right) \mathscr{D}\left({}^{n+1}\boldsymbol{\delta v} \right) \right\} \, \mathrm{d}\Omega \\
&+ \int_{{}^{n}\Omega} \mathscr{D}(\boldsymbol{w}) : \left\{ 2\left[1 - {}^{n}D\right] \eta \left({}^{n+1}_{(m)}\boldsymbol{v} \right) \mathscr{D}\left({}^{n+1}_{(m)}\boldsymbol{v} \right) \right\} \, \mathrm{d}\Omega \\
&+ \int_{{}^{n}\Omega} \mathscr{D}(\boldsymbol{w}) : \{ 2\left[1 - {}^{n}D\right] \frac{\partial \eta}{\partial \mathscr{D}_{\mathrm{II}}\left({}^{n+1}_{(m)}\boldsymbol{v} \right)} [\mathscr{D}\left({}^{n+1}_{(m)}\boldsymbol{v} \right) : \\
&\qquad \mathscr{D}\left({}^{n+1}\boldsymbol{\delta v} \right)] \mathscr{D}\left({}^{n+1}_{(m)}\boldsymbol{v} \right) \} \, \mathrm{d}\Omega \\
&- \int_{{}^{n}\Omega} \left[1 - {}^{n}D\right] \nabla \cdot \boldsymbol{w} \, \left[{}^{n+1}\boldsymbol{\delta}\widetilde{p} - {}^{n+1}_{(m)}\widetilde{p} \right] \, \mathrm{d}\Omega \\
&- \int_{{}^{n}\Omega} \boldsymbol{\psi}\left({}^{n}D \right) \boldsymbol{w} \cdot {}^{n}\boldsymbol{b} \, \mathrm{d}\Omega - \int_{{}^{n}\Gamma^{\mathrm{N}}} \boldsymbol{w} \cdot {}^{n}\bar{\mathscr{T}} \, \mathrm{d}\Gamma = 0, \\
&\\
&\int_{{}^{n}\Omega} \boldsymbol{\psi}\left({}^{n}D \right) q \nabla \cdot \left[{}^{n+1}\boldsymbol{\delta v} + {}^{n+1}_{(m)}\boldsymbol{v} \right] \, \mathrm{d}\Omega = 0,
\end{aligned}\right\} \quad \text{on } {}^{n}\Omega, \tag{45}$$

The algorithmic implementation is provided below in Algorithm 8. To verify the Newton's method, we repeat the study from Section 4.4.1 wherein show that the nonlinear Stokes formulation converges to the manufactured solution presented in [Dohrmann and Bochev, 2004, Worthen et al., 2014] for incompressible flow. This solution is given by

$$\begin{aligned}
v_1^* &= x_1 + x_1^2 - 2x_1x_2 + x_1^3 - 3x_1x_2^2 + x_1^2x_2, \\
v_2^* &= -x_2 - 2x_1x_2 + x_2^2 - 3x_1^2x_2 + x_2^3 - x_1x_2^2, \\
p^* &= x_1x_2 + x_1 + x_2 + x_1^3x_2^2 - 4/3.
\end{aligned} \tag{46}$$

For this study we employ P2-P1 (Taylor-Hood) elements and take the viscosity parameter $N = 3.5$, as was done in Section 4.1. Starting with a 4×4 structured mesh over the unit domain Ω, we progressively refine the mesh by reducing the element size by half. For each

mesh size we compute the L^2 error norms,

$$\varepsilon_{\boldsymbol{v}} = \sqrt{\frac{\sum_{k=1}^{\mathrm{N^{P2}}} \left(||\boldsymbol{v}||_k - ||\boldsymbol{v}^*||_k\right)^2}{\sum_{k=1}^{\mathrm{N^{P2}}} \left(||\boldsymbol{v}^*||_k\right)^2}}, \quad \varepsilon_p = \sqrt{\frac{\sum_{k=1}^{\mathrm{N^{P1}}} \left(p_k - p_k^*\right)^2}{\sum_{k=1}^{\mathrm{N^{P1}}} \left(p_k^*\right)^2}}, \tag{47}$$

for velocity magnitude and pressure, respectively, which are reported in Table H5. In the above equations, $\mathrm{N^{P1}}$ and $\mathrm{N^{P2}}$ are the number of nodes in the P2 and P1 spaces, respectively; and $||\boldsymbol{v}||_k$ and p_k are the velocity magnitude and pressure, respectively, at the k-th node. The $\varepsilon_{\boldsymbol{v}}$ and ε_p error norms and rates of convergence with respect to mesh size are nearly identical to those reported in Section 4.4.1 (i.e., when using the Picard iteration scheme), thus verifying the approach. The Newton's method also required far fewer iterations than the Picard iteration scheme to converge to the solution within the same error tolerance, as detailed in Table H6. From this verification study we conclude that the Newton's method is computationally more efficient than the Picard iteration scheme under ideal conditions (e.g., a convex domain). However, upon the introduction of a notch or a damage zone in the domain, we found that the Newton's method when implemented in FEniCS is not guaranteed to converge, whereas the Picard iteration scheme never fails to converge. We suspect the issue with the Newton's method arises due to either interpolation errors during the automated assembly of the system tangent in FEniCS, or, due to the choice of the regularization parameter γ incorporated to avoid zero-viscosity when assuming zero or constant velocity initial guess for the Stokes equations. We expect to investigate this further as we begin to simulate crevasse propagation in 3D using parallel computing and scalable algorithms.

Algorithm 8 : Newton iteration scheme for Stokes flow in 2D

Let ${}^{n+1}_{(m)}\boldsymbol{v}$ denote the velocity vector with horizontal components ${}^{n+1}_{(m)}v_1$ and ${}^{n+1}_{(m)}v_2$, respectively, and ${}^{n+1}_{(m)}\widetilde{p}$ denote the effective pressure determined on the updated reference configuration ${}^{n+1}\Omega$ at Newton iteration m. Likewise let ${}^{n+1}\delta\boldsymbol{v}$ and ${}^{n+1}\delta\widetilde{p}$ denote the velocity and effective pressure increments, respectively, between Newton iterations m and $m+1$ as presented in Equation (38).

i. Initialize at $m = 0$ by setting ${}^{n+1}_{(0)}\boldsymbol{v} = {}^{n}\boldsymbol{v}$ and ${}^{n+1}_{(0)}\widetilde{p} = {}^{n}\widetilde{p}$ everywhere in the domain.

ii. Initialize the maximum relative error ε to be greater than the chosen tolerance ε_{tol}.

iii. While $\varepsilon > \varepsilon_{\text{tol}}$:

   (a) Solve the Stokes equations (Eq. 45) to obtain the viscosity and pressure increments, ${}^{n+1}\delta\boldsymbol{v}$ and ${}^{n+1}\delta\widetilde{p}$, respectively. This is done in FEniCS software using the `solve()` function.

   (b) Obtain the updated solutions for velocity and pressure: ${}^{n+1}_{(m+1)}\boldsymbol{v} = {}^{n+1}\delta\boldsymbol{v} + {}^{n+1}_{(m)}\boldsymbol{v}$ and ${}^{n+1}_{(m+1)}\widetilde{p} = {}^{n+1}\delta\widetilde{p} + {}^{n+1}_{(m)}\widetilde{p}$.

   (c) Calculate relative L^2 error norms: $\varepsilon_1 = \frac{||{}^{n+1}\delta v_1||}{||{}^{n+1}_{(m+1)}v_1||}$, $\varepsilon_2 = \frac{||{}^{n+1}\delta v_2||}{||{}^{n+1}_{(m+1)}v_2||}$, $\varepsilon_p = \frac{||{}^{n+1}\delta\widetilde{p}||}{||{}^{n+1}_{(m+1)}\widetilde{p}||}$.

   (d) Determine the maximum relative error: $\varepsilon = \max\{\varepsilon_1, \varepsilon_2, \varepsilon_p\}$.

   (e) Update the iteration count: $m = m + 1$.

iv. Upon convergence: ${}^{n+1}v_1 = {}^{n+1}_{(m+1)}v_1$, ${}^{n+1}v_2 = {}^{n+1}_{(m+1)}v_2$, and ${}^{n+1}\widetilde{p} = {}^{n+1}_{(m+1)}\widetilde{p}$.

Table H5: Numerical verification study of the nonlinear Stokes model using Newton iteration scheme. The L^2 error norms ε_v and ε_p for velocity magnitude and pressure, respectively, given in Equations (47) are presented for different mesh sizes.

Mesh	**#DoF**	ε_v	**Rate**	ε_p	**Rate**
4×4	187	$5.36\text{e}-4$	$--$	$9.74\text{e}-2$	$--$
8×8	659	$5.00\text{e}-5$	3.42	$1.54\text{e}-2$	2.66
16×16	2467	$3.64\text{e}-6$	3.78	$1.95\text{e}-3$	2.98
32×32	9539	$2.36\text{e}-7$	3.95	$2.67\text{e}-4$	2.87

Table H6: Number of iterations required to converge within the error tolerance $\varepsilon_{\text{tol}} = 10^{-8}$ for the Picard iteration scheme and the Newton's method. The asymptotic convergence of the Newton's method is evident from the relatively few iterations required for convergence as compared to the Picard iteration scheme.

Mesh	**Picard Iterations**	**Newton Iterations**
4×4	45	6
8×8	24	5
16×16	26	5
32×32	26	5

Appendix I Proof of the Relation between Restrictive and Horizontal Deviatoric Stress

To show that $R_{xx} = 2\tau_{xx}$, where R_{xx} is the restrictive stress and τ_{xx} is the horizontal deviatoric stress in the "far-field" region of an ice slab, we begin with the common expression of the horizontal Cauchy stress σ_{xx} in terms of R_{xx} and the lithostatic pressure $\rho_i g\langle H - z\rangle$ as,

$$\sigma_{xx} = R_{xx} - \rho_i g\langle H - z\rangle, \tag{48}$$

where R_{xx} is given as,

$$R_{xx} = \frac{1}{2}\rho_{\mathrm{i}} g H - \frac{1}{2}\rho_{\mathrm{w}} g \frac{h_w^2}{H}. \tag{49}$$

Let us also recall the definition of the deviatoric stress as a function of the strain rate (following the constitutive relations),

$$\boldsymbol{\tau} = 2\eta\dot{\boldsymbol{\epsilon}}, \tag{50}$$

where $\dot{\boldsymbol{\epsilon}}$ is the strain rate tensor. Because of the plane strain assumption, the out-of-plane component $\dot{\varepsilon}_{yy} = 0$. We also assume that ice is incompressible, and so $\dot{\varepsilon}_{xx} + \dot{\varepsilon}_{yy} + \dot{\varepsilon}_{zz} = 0$. From these conditions it follows that $\dot{\varepsilon}_{xx} + \dot{\varepsilon}_{zz} = 0$, and hence $\tau_{xx} = -\tau_{zz}$. Let us now consider the definition of the Cauchy stress,

$$\boldsymbol{\sigma} = \boldsymbol{\tau} - p\boldsymbol{I}, \tag{51}$$

where p is the hydrostatic pressure and $\boldsymbol{I}$ is the identity tensor. Considering $\sigma_{xx} = \tau_{xx} - p$ from the above expression and equating it with Equation 48, we obtain,

$$R_{xx} - \rho_{\mathrm{i}} g\langle H - z\rangle = \tau_{xx} - p. \tag{52}$$

Now, assuming that atmospheric pressure is negligible, we obtain $\sigma_{zz} = 0$ as a natural boundary condition along the top surface of the ice slab where $z = H$; and from Equation 51, it follows that $\tau_{zz} - p = 0$. Because of the incompressibility and plain strain assumptions previously discussed, it also follows that $-\tau_{xx} - p = 0$. Substituting this latter expression, which is only valid at $z = H$, into the expression , we obtain,

$$R_{xx} - \rho_i h \langle H - H \rangle = \tau_{xx} - (-\tau_{xx}), \tag{53}$$

and so it follows that $R_{xx} = 2\tau_{xx}$. Because R_{xx} and τ_{xx} are both constant through the depth of the ice slab, this relation holds throughout the slab depth. Finite element method (FEM) results show good agreement with this conclusion, as shown by the blue dashed lines in Figure L13 in this document.

Appendix J Procedure for solving the Weertman [1973] model

In this section, we describe the algorithmic procedure for evaluating the Weertman [1973] dislocation mechanics-based model. The surface crevasse depth d_s is calculated by evaluating the crack opening displacement function $\mathscr{D}(z',d_s)$ for the greatest value of d_s such that $\mathscr{D}(z',d_s) > 0$ for all $z' \in [0,d_s]$, where $z' = H - z$ is the vertical coordinate measured from the top of the ice slab. In other words, the crevasse depth d_s is taken as the greatest depth for which the crack opening displacement (i.e., the separation distance between crevasse walls) is positive for all points along the crevasse. The the crack opening displacement function $\mathscr{D}(z',d_s)$ is written as,

$$\mathscr{D}(z',d_s) = \frac{2(1-\nu)}{\mu}\left(\frac{\rho_i g}{\pi}\left\{\sqrt{d_s^2-(z')^2}\left(d_s - \frac{\rho_w}{\rho_i}\sqrt{d_s^2-(h')^2}\right)\right.\right.$$

$$-(z')^2\log\left[\frac{d_s+\sqrt{d_s^2-(z')^2}}{(z')}\right] + \frac{\rho_w}{2\rho_i}((z')^2+(h')^2)\log\left|\frac{\sqrt{d_s^2-(h')^2}+\sqrt{d_s^2-(z')^2}}{\sqrt{d_s^2-(h')^2}-\sqrt{d_s^2-(z')^2}}\right|$$

$$\left.\left.-z'h'\frac{\rho_w}{\rho_i}\log\left|\frac{(z')\sqrt{d_s^2-(h')^2}+h'\sqrt{d_s^2-(z')^2}}{(z')\sqrt{d_s^2-(h')^2}-h'\sqrt{d_s^2-(z')^2}}\right|\right\} + (R_{xx}-R'_{xx})\sqrt{d_s^2-(z')^2}\right), \quad (54)$$

where the dry distance $h' = \langle d_s - h_s \rangle$, and the quantity R'_{xx} is given by,

$$R'_{xx} = 2\frac{\rho_i g}{\pi}\left(d_s + h'\frac{\rho_w}{\rho_i}\left[\frac{\pi}{2} - \sin^{-1}\frac{h'}{d_s}\right] - \frac{\rho_w}{\rho_i}\sqrt{d_s^2-(h')^2}\right). \quad (55)$$

The parameters μ and ν represent the shear modulus and Poisson's ratio, respectively; however, the crevasse penetration depth is independent of these values. Because Equation 54 is a highly nonlinear function of the surface crevasse depth d_s, we must use an iterative procedure for computing d_s such that $\mathscr{D}(z',d_s) > 0$ for all $z' \in [0,d_s]$. To this end, we implement the bisection method as described in Algorithm 9.

Algorithm 9 : Bisection method for solving the Weertman [1973] model

i. Known values: height of the slab H, water level at terminus h_w, water level in crevasse h_s.

ii. Compute restrictive stress $R_{xx} = \frac{1}{2}\rho_i g H - \frac{1}{2}\rho_w g \frac{h_w^2}{H}$.

iii. Initial bisection points: ${}^a d_s = H \times 10^{-3}$; ${}^b d_s = H/2$; and ${}^c d_s = H \times (1 - 10^{-3})$.

iv. Initialize error as $\varepsilon = 1$.

v. while $|\varepsilon| > 10^{-6}$:

(a) ${}^a\mathscr{D}_{\min} = \min\{\mathscr{D}(z',\ {}^a d_s)\} > 0 \ \ \forall \ \ z' \in (0,\ {}^a d_s)$
${}^b\mathscr{D}_{\min} = \min\{\mathscr{D}(z',\ {}^b d_s)\} > 0 \ \ \forall \ \ z' \in (0,\ {}^b d_s)$
${}^c\mathscr{D}_{\min} = \min\{\mathscr{D}(z',\ {}^c d_s)\} > 0 \ \ \forall \ \ z' \in (0,\ {}^c d_s)$

(b) if ${}^a\mathscr{D}_{\min} > 0$ and ${}^b\mathscr{D}_{\min} > 0$ and ${}^c\mathscr{D}_{\min} > 0$:
The crevasse fully penetrates. $d_s = H$, end loop.

(c) else if ${}^a\mathscr{D}_{\min} > 0$ and ${}^b\mathscr{D}_{\min} > 0$ and ${}^c\mathscr{D}_{\min} < 0$:
The crevasse depth d_s is between the bounds ${}^b d_s$ and ${}^c d_s$. Update the bounds for bisection:
${}^a d_s = {}^b d_s$
${}^c d_s = {}^c d_s$
${}^b d_s = \frac{1}{2}({}^a d_s + {}^c d_s)$
Error: $\varepsilon = ({}^a d_s - {}^c d_s)$
Continue loop if $|\varepsilon| > 10^{-6}$.

(d) else if ${}^a\mathscr{D}_{\min} > 0$ and ${}^b\mathscr{D}_{\min} < 0$ and ${}^c\mathscr{D}_{\min} < 0$:
The crevasse depth d_s is between the bounds ${}^a d_s$ and ${}^b d_s$. Update the bounds for bisection:
${}^a d_s = {}^a d_s$
${}^c d_s = {}^b d_s$
${}^b d_s = \frac{1}{2}({}^a d_s + {}^c d_s)$
Error: $\varepsilon = ({}^a d_s - {}^c d_s)$
Continue loop if $|\varepsilon| > 10^{-6}$.

(e) else if ${}^a\mathscr{D}_{\min} < 0$ and ${}^b\mathscr{D}_{\min} < 0$ and ${}^c\mathscr{D}_{\min} < 0$:
There is zero crevasse penetration. $d_s = 0$, end loop.

vi. If the loop terminates with $|\varepsilon| \leq 10^{-6}$, then take $d_s = {}^b d_s$ for the last computed value of ${}^b d_s$.

Appendix K Procedure for solving the van der Veen [1998a] model

In this section, we describe the algorithmic procedure for evaluating the van der Veen [1998a] linear elastic fracture mechanics (LEFM) model. The penetration depth of surface crevasses is determined by equating the net stress intensity factor (SIF) K_I^{net} to the experimentally measured critical SIF K_{Ic} as,

$$K_I^{\text{net}} = K_I^{(1)}(R_{xx}, d_s) + K_I^{(2)}(d_s) + K_I^{(3)}(h_s, d_s) = K_{Ic} \tag{56}$$

where $K_I^{(1)}$, $K_I^{(2)}$, and $K_I^{(3)}$ are the SIFs resulting from the restrictive stress, ice overburden pressure, and hydraulic pressure exerted on crevasse walls for water-filled crevasses, respectively. The terms for $K_I^{(1)}$, $K_I^{(2)}$, and $K_I^{(3)}$ are given as,

$$K_I^{(1)} = F(\lambda) R_{xx} \sqrt{\pi d_s}, \tag{57a}$$

$$K_I^{(2)} = \int_0^{d_s} \left[\frac{-2\rho_{\text{i}} g z'}{\sqrt{\pi d_s}} G(\lambda, \gamma) \right] \mathrm{d}z', \tag{57b}$$

$$K_I^{(3)} = \int_0^{d_s} \left[\frac{2\rho_{\text{w}} g \langle z' - h' \rangle}{\sqrt{\pi d_s}} G(\lambda, \gamma) \right] \mathrm{d}z', \tag{57c}$$

where $z' = H - z$ is the vertical coordinate measured from the top of the ice slab, the dry depth $h' = d_s - h_s$, the terms $\lambda = d_s/H$ and $\gamma = z'/d_s$, and the weighting functions $F(\lambda)$ and $G(\lambda, \gamma)$ are given by,

$$F(\lambda) = 1.12 - 0.23\lambda + 10.55\lambda^2 - 21.72\lambda^3 + 30.39\lambda^4, \tag{58}$$

and

$$\begin{aligned} G(\lambda, \gamma) = &\left[\frac{3.52(1-\gamma)}{(1-\lambda)^{3/2}} \right] - \left[\frac{4.35 - 5.28\gamma}{(1-\lambda)^{1/2}} \right] \\ &+ \left[\frac{1.3 - 0.3\gamma^{3/2}}{(1-\gamma^2)^{1/2}} + 0.83 - 1.76\gamma \right] [1 - (1-\gamma)\lambda]. \end{aligned} \tag{59}$$

The SIF terms given in Equation 57 are nonlinear functions of d_s, and so an iterative process is required to solve for d_s. To this end, we implement the bisection method as described in Algorithm 10.

Algorithm 10 : Bisection method for solving the van der Veen [1998a] model

i. Known values: height of the slab H, water level at terminus h_w, water level in crevasse h_s.

ii. Compute restrictive stress $R_{xx} = \frac{1}{2}\rho_i g H - \frac{1}{2}\rho_w g \frac{h_w^2}{H}$.

iii. Initial bisection points: ${}^a d_s = H \times 10^{-3}$; ${}^b d_s = H/2$; and ${}^c d_s = H \times (1 - 10^{-3})$.

iv. Initialize error as $\varepsilon = 1$.

v. while $|\varepsilon| > 10^{-6}$:

(a) $${}^a K_I^{\text{net}} = K_I^{(1)}(R_{xx}, {}^a d_s) + K_I^{(2)}({}^a d_s) + K_I^{(3)}(h_s, {}^a d_s)$$
$${}^b K_I^{\text{net}} = K_I^{(1)}(R_{xx}, {}^b d_s) + K_I^{(2)}({}^b d_s) + K_I^{(3)}(h_s, {}^b d_s)$$
$${}^c K_I^{\text{net}} = K_I^{(1)}(R_{xx}, {}^c d_s) + K_I^{(2)}({}^c d_s) + K_I^{(3)}(h_s, {}^c d_s)$$

(b) if ${}^a K_I^{\text{net}} > K_{Ic}$ and ${}^b K_I^{\text{net}} > K_{Ic}$ and ${}^c K_I^{\text{net}} > K_{Ic}$:
The crevasse fully penetrates. $d_s = H$, end loop.

(c) else if ${}^a K_I^{\text{net}} > K_{Ic}$ and ${}^b K_I^{\text{net}} > K_{Ic}$ and ${}^c K_I^{\text{net}} < K_{Ic}$:
The crevasse depth d_s is between the bounds ${}^b d_s$ and ${}^c d_s$. Update the bounds for bisection:
${}^a d_s = {}^b d_s$
${}^c d_s = {}^c d_s$
${}^b d_s = \frac{1}{2}({}^a d_s + {}^c d_s)$
Error: $\varepsilon = ({}^a d_s - {}^c d_s)$
Continue loop if $|\varepsilon| > 10^{-6}$.

(d) else if ${}^a K_I^{\text{net}} > K_{Ic}$ and ${}^b K_I^{\text{net}} < K_{Ic}$ and ${}^c K_I^{\text{net}} < K_{Ic}$:
The crevasse depth d_s is between the bounds ${}^a d_s$ and ${}^b d_s$. Update the bounds for bisection:
${}^a d_s = {}^a d_s$
${}^c d_s = {}^b d_s$
${}^b d_s = \frac{1}{2}({}^a d_s + {}^c d_s)$
Error: $\varepsilon = ({}^a d_s - {}^c d_s)$
Continue loop if $|\varepsilon| > 10^{-6}$.

(e) else if ${}^a K_I^{\text{net}} < K_{Ic}$ and ${}^b K_I^{\text{net}} < K_{Ic}$ and ${}^c K_I^{\text{net}} < K_{Ic}$:
There is zero crevasse penetration. $d_s = 0$, end loop.

vi. If the loop terminates with $|\varepsilon| \leq 10^{-6}$, then take $d_s = {}^b d_s$ for the last computed value of ${}^b d_s$.

Appendix L Influence of geometric correction factors in LEFM models

In this section, we compare the predictions made by different LEFM-based calving models for the penetration depth of surface crevasses when geometric correction factors are included or neglected. We discussed two LEFM-based models, namely, the van der Veen [1998a] and Krug et al. [2014] models, in Sections 5.2.4 and 5.2.5. Herein we also consider the van der Veen [1998b] model, which (in a similar fashion to the Krug et al. [2014] model) calculates the net stress intensity factor (SIF) at the crevasse tip by integrating the net horizontal stress σ_{xx} multiplied by a single weighting function $G(\lambda,\gamma)$. The net SIF is written as,

$$K_I = \int_0^{d_s} G(\lambda,\gamma)\left[R_{xx} - \rho_{\mathrm{i}} g z' + \rho_{\mathrm{w}} g \langle z' - h' \rangle\right] \mathrm{d}z', \tag{60}$$

where $z' = H - z$ and $G(\lambda,\gamma)$ is given in Equation 59. To compare the van der Veen [1998a], van der Veen [1998b], and Krug et al. [2014] LEFM models, we plot the normalized crevasse depth d_s/H versus the water level h_s/d_s within the surface crevasse for various seawater depths h_w, while accounting for the geometry of the domain. Domain geometry is factored into each respective model by setting $\lambda = d_s/H$ in the weighting functions $G(\lambda,\gamma)$ and $M(z',H)$. The results of this study are shown in Figures L12(a-c). From these figures it is evident that the van der Veen [1998b] and Krug et al. [2014] models predict the same crevasse penetration depths: unless the seawater level h_w is close to the floating depth (i.e., 90%), both models predict full penetration for surface crevasses irrespective of the water level h_s within the crevasse. On the other hand, the van der Veen [1998a] does not predict full penetration for any surface crevasse unless $h_s/d_s \approx 0.9$.

Next, we eliminate the influence of domain geometry by setting $\lambda = 0$ in each LEFM model. The results of this study are shown in Figures L12(d-f) wherein we plot d_s/H versus h_s/d_s for varying seawater depths. Interestingly, all three LEFM models predict the same crevasse penetration depths and also show close agreement with the Weertman [1973] model when the geometric factors are not included.

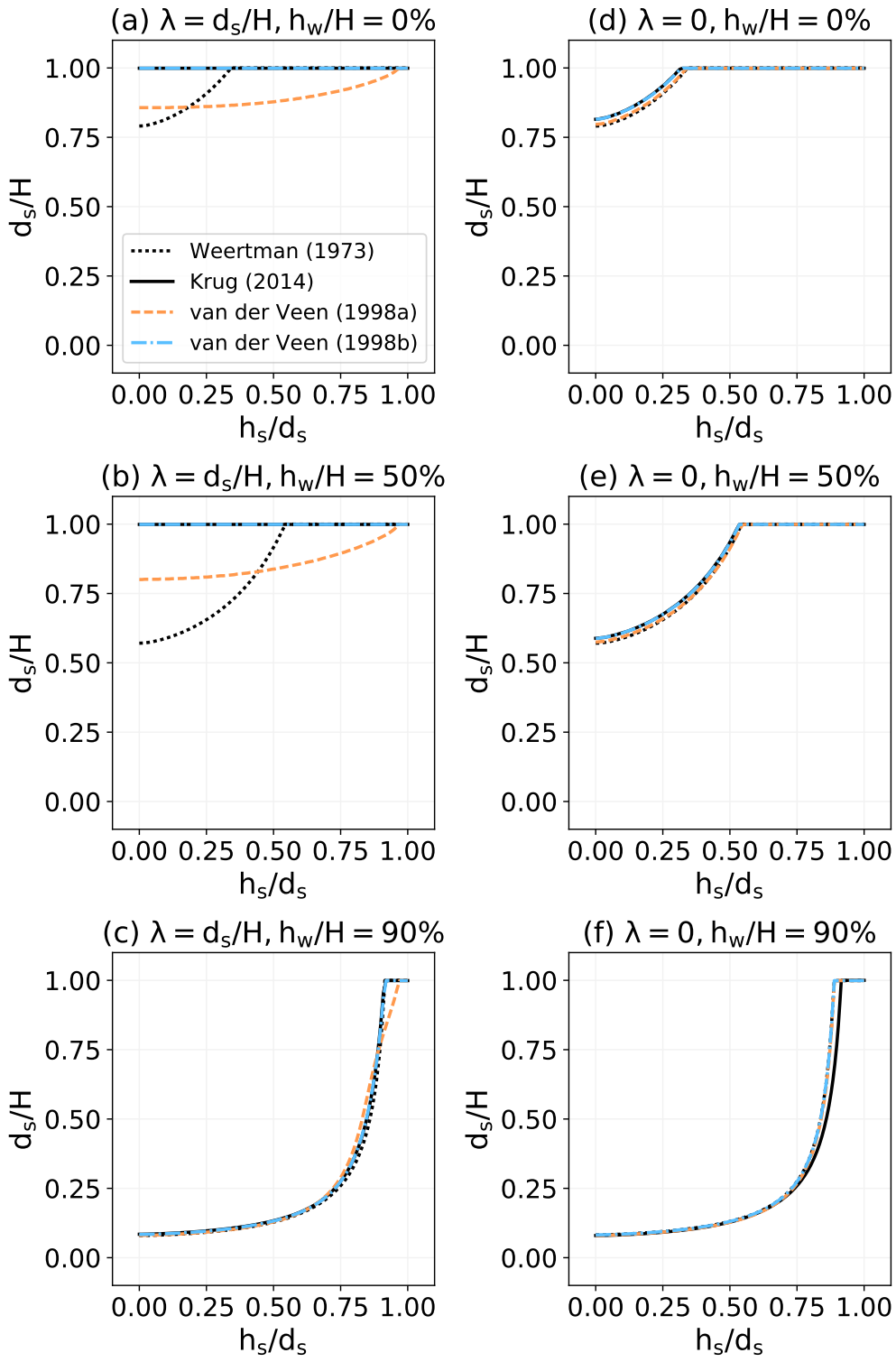

Figure L11: Surface crevasse depth d_s normalized with the domain height $H = 125$ m for varying water levels h_s filling the surface crevasse. The black dotted lines, black solid lines, orange dashed lines, and blue dot-dash lines correspond to the Weertman [1973], Krug et al. [2014], van der Veen [1998a], and van der Veen [1998b] models, respectively. In subfigures (a-c), domain geometry is taken into account by setting $\lambda = d_s/H$; whereas, in subfigures (d-f) we disregard domain geometry by setting $\lambda = 0$.

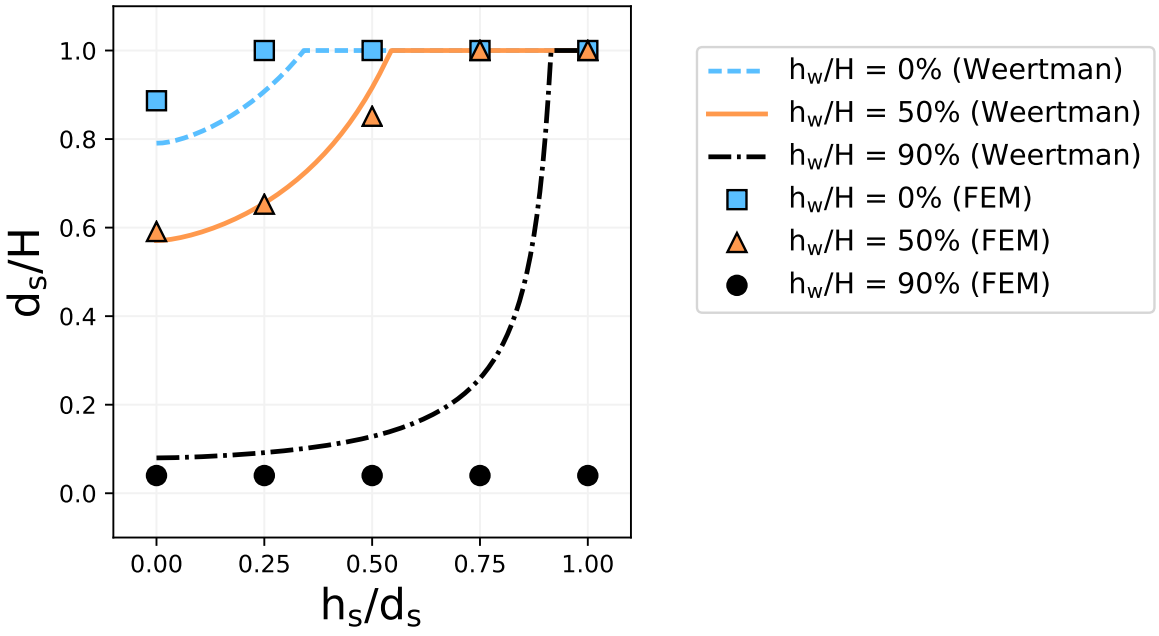

Figure L12: Surface crevasse depth d_s normalized with the domain height $H = 250$ m for varying water levels h_s filling the surface crevasse. The blue dashed, orange solid, and black dash-dotted lines depict the Weertman [1973] solutions for $h_w/H = 0\%, 50\%$ and 90%, respectively. The markers represent simulation (FEM) results using the nonlinearly viscous rheological model.

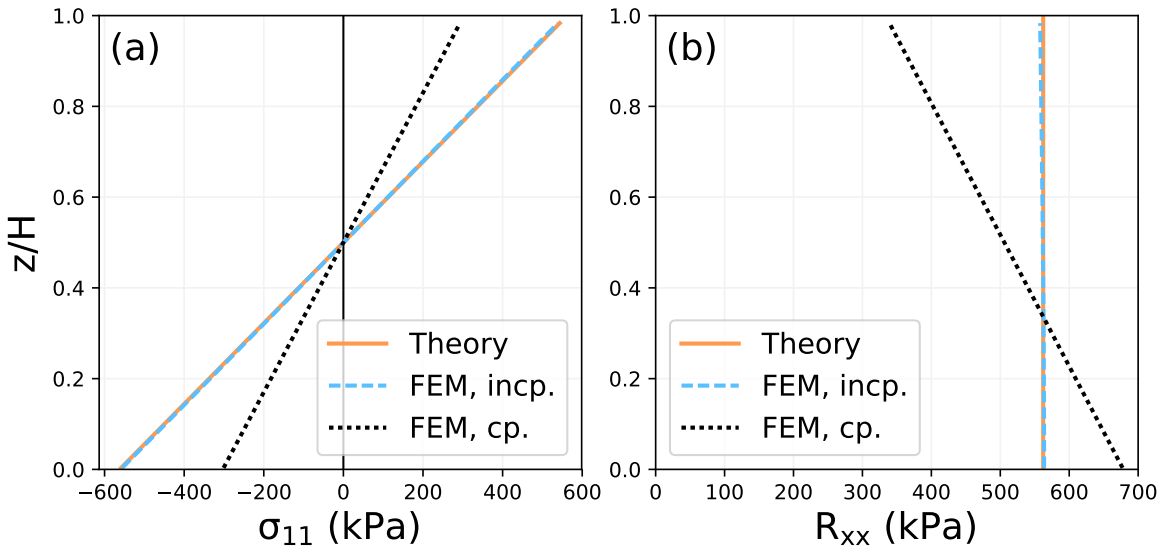

Figure L13: (a) Horizontal Cauchy stress σ_{xx} and (b) restrictive stress R_{xx} plotted against the normalized depth z/H through a glacier in the "far-field" region (i.e., far from the terminus). The orange solid lines in subfigures (a) and (b) are given by the theory from Equations 48 and 49, respectively. The blue dashed lines and black dotted indicate the represent the finite element method predicted stresses respectively using incompressible and compressible linear elastic rheological models. Interestingly, when assuming incompressibility, the far-field stress state is independent of the rheology.

Appendix M On the appropriateness of geometric factors in LEFM models

In this section, we investigate the appropriateness of the geometric factors included in the theoretical linear elastic fracture mechanics (LEFM) models [van der Veen, 1998a,b, Krug et al., 2014] described in section 5.2, which account for the finite geometry of the ice slab when computing crevasse penetration depths. We perform the investigation by comparing the mode I stress intensity factor K_{I} predicted by the theoretical models against the values predicted using numerical techniques, namely, the displacement correlation method (DCM), which is implemented within the finite element analysis. Throughout this study we consider two loading configurations on a rectangular ice slab with length L = 1000 m and height $H = 125$ m. The first loading configuration is the "cantilever" case, wherein we restrain one end of the domain and apply a horizontal stress that varies linearly with depth on the other end, as depicted in Figure M14(a). The second loading configuration is the "gravity" case, wherein we apply a free-slip (i.e., rollers) boundary condition to the bottom of the domain and apply gravity loading as a body force, as depicted in Figure M14(b). Far from the free edge, we note that the cantilever and gravity loading conditions induce the same horizontal Cauchy stress profile in the far-field, as shown in Figures M14(c-d).

To compute the mode I stress intensity factor K_{I}, we consider a zero-thickness crack with depth d_s penetrating into the ice slab in the "far-field" region of the ice slab (i.e., where σ_{xx} varies linearly with depth). The crack is modeled as a seam in the finite element mesh with initially overlapping nodes along the crack path. As loading is applied to the domain, the crack interface opens, and we employ the displacement correlation method (DCM) described in Gupta et al. [2017] to compute the stress intensity factor K_{I} at the crack tip. The results of this study are shown in Figures M15 through M17, wherein we plot the numerically computed K_{I} versus crack depth d_s and compare against the K_{I} values predicted by the theoretical LEFM models of van der Veen [1998a], van der Veen [1998b], and Krug et al. [2014] with and without considering the finite thickness of the ice slab (we neglect the finite thickness by setting $H = +\infty$, which gives $\lambda = 0$, in the respective

equations). In all figures, the thick black lines with circular markers represent finite element (FEM) results; the dotted or dashed lines correspond to the LEFM models *with* finite thickness considered; and the solid red lines correspond to the LEFM models *without* finite thickness considered. Let us first consider the case of dry crevasses. In Figure M15, we plot the K_{I} vs. d_s curve for the different loading configurations and different seawater depths at the terminus. The FEM results from the "cantilever" loading configuration show excellent agreement with the theoretical LEFM models we account for the finite thickness of the domain. However, the FEM results from the "gravity" loading configuration do not agree with the theoretical LEFM models with finite thickness accounted for. In fact, in the gravity case the FEM results agree better with the LEFM models *without* finite thickness considered. We observe the same trend when we consider wet surface crevasses (i.e., with hydraulic pressure applied along the crevasse walls) and wet basal crevasses, as shown in Figures M16 and M17.

In conclusion, the results indicate that the geometric factors in the LEFM-based calving models were calibrated and are valid for the cantilever loading configuration. However, these geometric factors are not applicable to the gravity loading configuration, which is the loading configuration typically assumed in the glaciology literature [van der Veen, 1998a,b] when studying the penetration of surface and basal crevasses through grounded ice sheets.

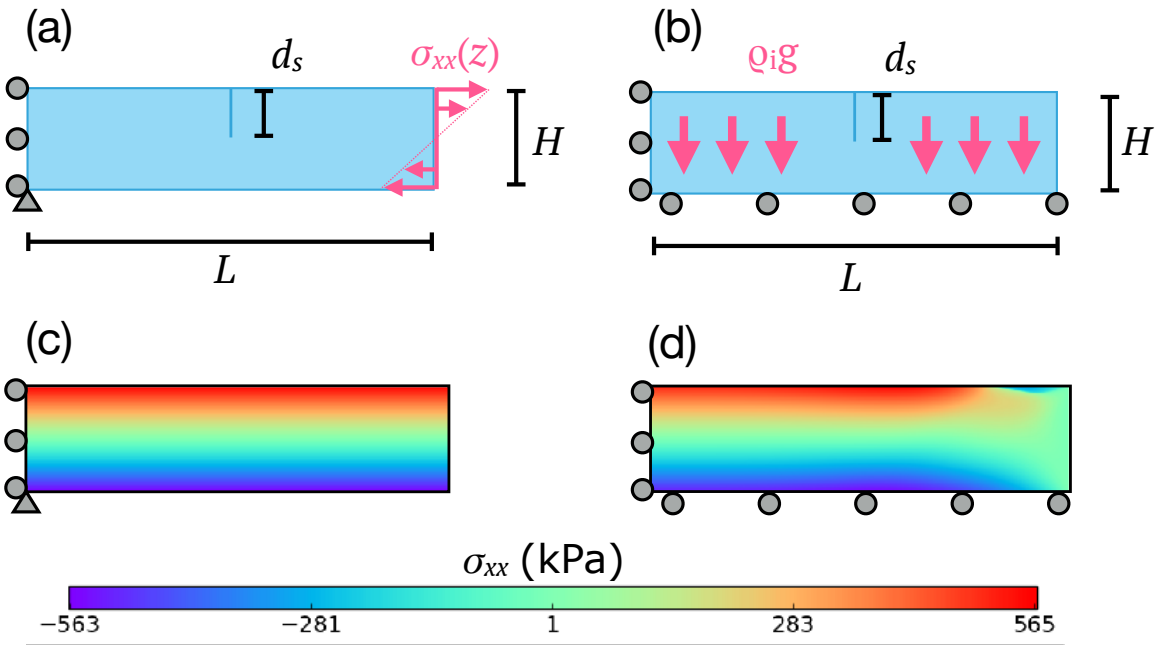

Figure M14: (a) Cantilever beam with applied loading on the right-hand edge, with a vertical crack with depth d_s extending from the top surface in the center of the domain. (b) Ice slab resting on a free-slip surface under gravity loading, with a vertical crack with depth d_s extending from the top surface in the center of the domain. (c) Horizontal Cauchy stress σ_{xx} in the domain predicted by loading case in subfigure (a) when $d_s = 0$ (i.e., when there is no crevasse) and $h_w/H = 0\%$. (d) Horizontal Cauchy stress σ_{xx} in the domain predicted by loading case in subfigure (b) when $d_s = 0$.

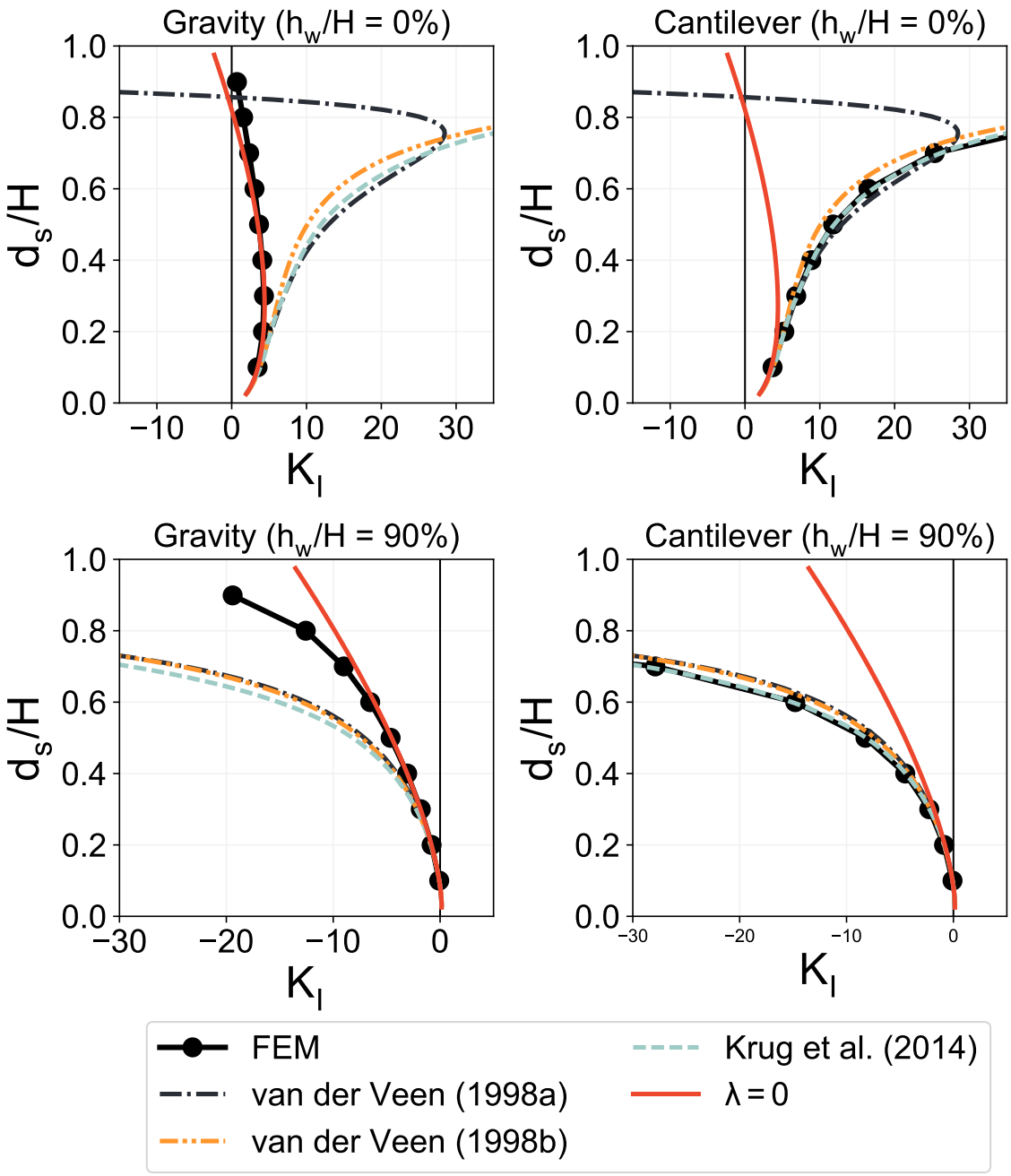

Figure M15: Comparison of stress intensity factors computed using the finite element method (FEM) and theoretical techniques [van der Veen, 1998a,b, Krug et al., 2014] for dry surface crevasses under different conditions. The subfigures on the left-hand side correspond to gravity-driven flow on a free slip surface (see Figure M14b), and the subfigures on the right-hand side correspond to the loaded cantilever beam (see Figure M14a).

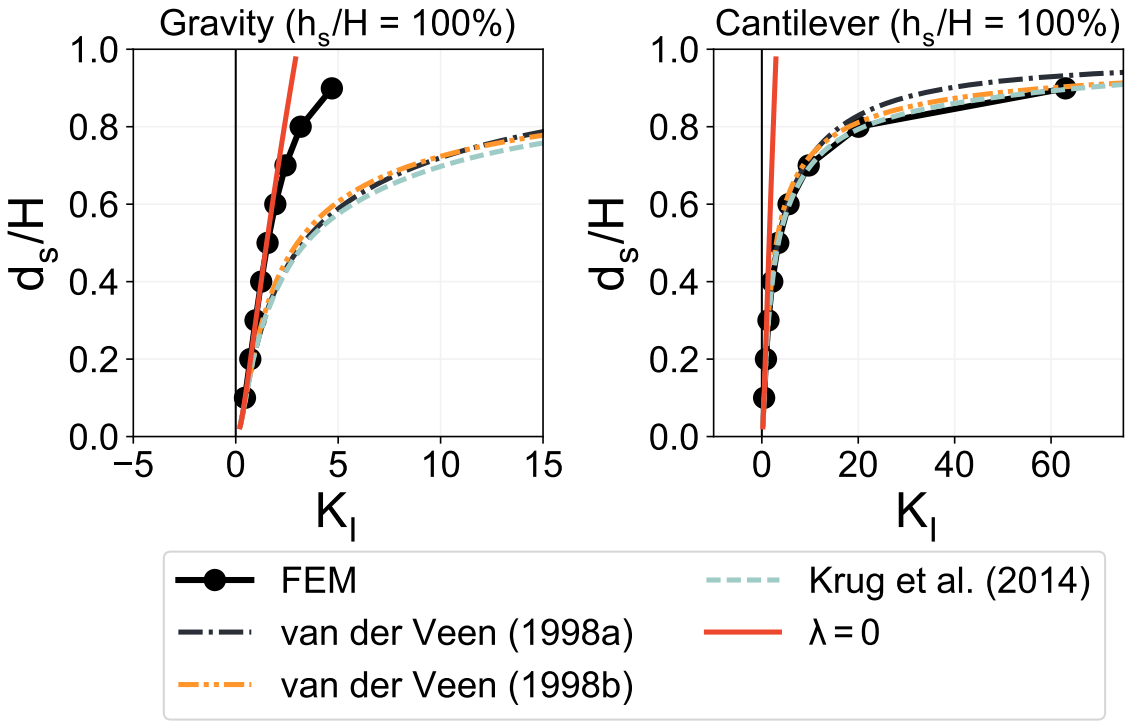

Figure M16: Comparison of stress intensity factors computed using the finite element method (FEM) and theoretical techniques [van der Veen, 1998a,b, Krug et al., 2014] for water-filled surface crevasses under different conditions. The subfigure on the left-hand side corresponds to gravity-driven flow on a free slip surface (see Figure M14b), and the subfigure on the right-hand side corresponds to the loaded cantilever beam (see Figure M14a).

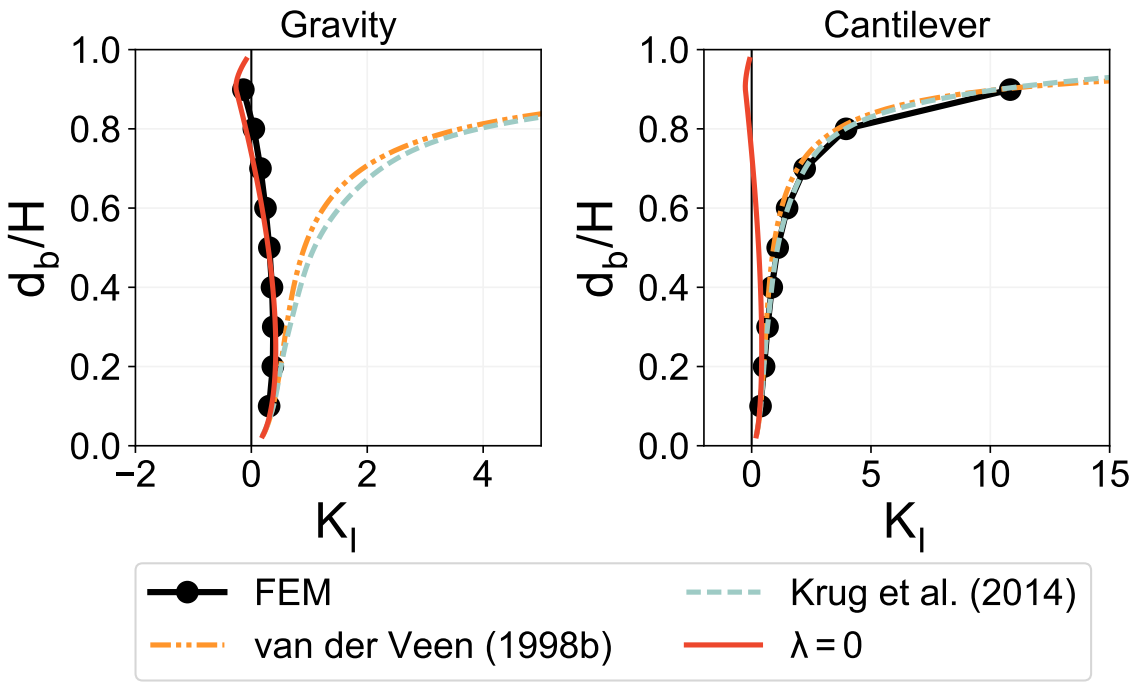

Figure M17: Comparison of stress intensity factors computed using the finite element method (FEM) and theoretical techniques [van der Veen, 1998a,b, Krug et al., 2014] for water-filled basal crevasses under different conditions. The subfigure on the left-hand side corresponds to gravity-driven flow on a free slip surface, and the subfigure on the right-hand side corresponds to the loaded cantilever beam.

BIBLIOGRAPHY

T. Albrecht and A. Levermann. Fracture-induced softening for large-scale ice dynamics. *The Cryosphere*, 8(2):587–605, 2014. doi: 10.5194/tc-8-587-2014.

G. Alfano and M.A. Crisfield. Finite element interface models for the delamination analysis of laminated composites: Mechanical and computational issues. *International Journal for Numerical Methods in Engineering*, 50:1701–1736, 2001.

M. Alfano, F. Furgiuele, A. Leonardi, C. Maletta, and G.H. Paulino. Mode I fracture of adhesive joints using tailored cohesive zone models. *International Journal of Fracture*, 157:193–204, 2009.

J. M. Amundson, M. Fahnestock, M. Truffer, J. Brown, M. P. Luthi, and R. J. Motyka. Ice môølange dynamics and implications for terminus stability, jakobshavn isbrôø, greenland. *Journal of Geophysical Research: Earth Surface*, 115(F1), 2010. ISSN 2156-2202. doi: 10.1029/2009JF001405. F01005.

D. N. Arnold, F. Brezzi, and M. Fortin. A stable finite element for the stokes equations. *CALCOLO*, 21(4):337–344, 1984. ISSN 1126-5434.

L.E. Asp. The effects of moisture and temperature on the interlaminar delamination toughness of a carbon/epoxy composite. *Journal of Composites Technology & Research*, 58 (6):967–977, 1998.

L.E. Asp, A. Sjögren, and E.S. Greenhalgh. Delamination growth and thresholds in a carbon/epoxy composites under fatigue loading. *Journal of Composites Technology & Research*, 23(2):55–68, 2001.

Claudio Baiocchi, Franco Brezzi, and Leopoldo P. Franca. Virtual bubbles and galerkin-

least-squares type methods (ga.l.s.). *Computer Methods in Applied Mechanics and Engineering*, 105(1):125 – 141, 1993. ISSN 0045-7825.

L. Banks-Sills. Application of the Finite Element Method to Linear Elastic Fracture Mechanics. *Applied Mechanics Reviews*, 44:447, 1991. doi: 10.1115/1.3119488.

G.I. Barenblatt. The mathematical theory of equilibrium cracks in brittle fracture. *Advances in Applied Mechanics*, 7:55–129, 1962.

J. N. Bassis and C. C. Walker. Upper and lower limits on the stability of calving glaciers from the yield strength envelope of ice. *Proceedings of the Royal Society of London A: Mathematical, Physical and Engineering Sciences*, 468(2140):913–931, 2012. ISSN 1364-5021. doi: 10.1098/rspa.2011.0422. URL http://rspa.royalsocietypublishing.org/content/468/2140/913.

J. N. Bassis, H. A. Fricker, R. Coleman, and J. B. Minster. An investigation into the forces that drive ice-shelf rift propagation on the amery ice shelf, east antarctica. *Journal of Glaciology*, 54(184):17–27, 2008. doi: 10.3189/002214308784409116. URL ⟨GotoISI⟩://WOS:000254545800002. n/a.

Jeremy N Bassis. The statistical physics of iceberg calving and the emergence of universal calving laws. *Journal of Glaciology*, 57(201):3–16, 2011.

JN Bassis and S Jacobs. Diverse calving patterns linked to glacier geometry. *Nature Geoscience*, 6(10):833–836, 2013.

J.N. Bassis and Yue Ma. Evolution of basal crevasses links ice shelf stability to ocean forcing. 409, 11 2014.

Klaus-Jurgen Bathe, Ekkehard Ramm, and Edward L. Wilson. Finite element formulations for large deformation dynamic analysis. *International Journal for Numerical Methods in Engineering*, 9:353–386, 1975.

Z. P. Bazant. Size effect on structural strength: A review. *Archives of Applied Mechanics*, 69(9-10):703–725, 1999.

Zdenek P Bazant and Gilles Pijaudier-Cabot. Nonlocal continuum damage, localization instability and convergence. *Journal of applied mechanics*, 55(2):287–293, 1988.

Zdeneõk P. Bazant. Nonlocal damage theory based on micromechanics of crack interactions. *Journal of Engineering Mechanics*, 120(3):593–617, 1994. doi: 10.1061/(ASCE)0733-9399(1994)120:3(593).

Y. Bazilevs. *Isogeometric Analysis of turbulence and fluid-structure interaction*. PhD thesis, University of Texas at Austin, 2007.

Ted Belytschko, Jame Shau-Jen Ong, Wing Kam Liu, and James M. Kennedy. Hourglass control in linear and nonlinear problems. *Computer Methods in Applied Mechanics and Engineering*, 43(3):251 – 276, 1984. ISSN 0045-7825.

Douglas I Benn, Nicholas RJ Hulton, and Ruth H Mottram. 'calving laws','sliding laws' and the stability of tidewater glaciers. *Annals of glaciology*, 46(1):123–130, 2007a.

Douglas I. Benn, Charles R. Warren, and Ruth H. Mottram. Calving processes and the dynamics of calving glaciers. *Earth-Science Reviews*, 82(3):143 – 179, 2007b. ISSN 0012-8252. doi: https://doi.org/10.1016/j.earscirev.2007.02.002. URL http://www.sciencedirect.com/science/article/pii/S0012825207000396.

J. Betten, S. Sklepus, and A. Zolochevsky. A creep damage model for initially isotropic materials with different properties in tension and compression. *Engineering Fracture Mechanics*, 59(5):623 – 641, 1998. ISSN 0013-7944.

J. Betten, S. Sklepus, and A. Zolochevsky. A microcrack description of creep damage in crystalline solids with different behaviour in tension and compression. *International Journal of Damage Mechanics*, 8:197–232, 1999.

Josef Betten. Applications of tensor functions to the formulation of constitutive equations involving damage and initial anisotropy. *Engineering Fracture Mechanics*, 25(5):573 – 584, 1986. ISSN 0013-7944.

M. A. Biot. Theory of elasticity and consolidation for a porous anisotropic solid. *Journal of Applied Physics*, 26(2):182–185, 1955. doi: 10.1063/1.1721956.

B. Blackman, J.P. Dear, A.J. Kinloch, and S. Osiyemi. The calculation of adhesive fracture energies from double-cantilever beam test specimens. *Journal of Materials Science Letters*, 10:253–256, 1991.

B.R.K. Blackman, H. Hadavinia, A.J. Kinloch, M. Paraschi, and J.G. Williams. The calculation of adhesive fracture energies in mode I: Revisiting the tapered double cantilever beam (TDCB) test. *Engineering Fracture Mechanics*, 70:233–248, 2003a.

B.R.K. Blackman, H. Hadavinia, A.J. Kinloch, and J.G. Williams. The use of a cohesive zone model to study the fracture of fibre composites and adhesively-bonded joints. *International Journal of Fracture*, 119:25–46, 2003b.

B.R.K. Blackman, A.J. Kinloch, M. Paraschi, and W.S. Teo. Measuring the mode I adhesive fracture energy, G_{IC}, of structural adhesive joints: the results of an international round-robin. *International Journal of Adhesion & Adhesives*, 23:293–305, 2003c.

N. Blal, L. Daridon, Y. Monerie, and S. Pagano. Criteria on the artificial compliance inherent to the intrinsic cohesive zone. *Comptes Rendus Mcanique*, 339(12):789 – 795, 2011. ISSN 1631-0721.

N. Blanco, E.K. Gamstedt, L.E. Asp, and J. Costa. Mixed-mode delamination growth in carbon-fibre composite laminates under cyclic loading. *International Journal of Solids and Structures*, 41(15):4219–4235, 2004.

C. P. Borstand, A. Khazendar, E. Larour, M. Morlighem, E. Rignot, and M. P. Schodlok. A damage mechanics assessment of the Larsen B ice shelf prior to collapse: Toward a physically-based calving law. *Geophysical Research Letters*, 39, 2012.

J.L. Bouvard, J.L. Chaboche, F. Feyel, and F. Gallerneau. A cohesive zone model for fatigue and creep–fatigue crack growth in single crystal superalloys. *International Journal of Fatigue*, 31(5):868 – 879, 2009. ISSN 0142-1123.

F. Brezzi and J. Pitkaranta. *On the stabilization of finite element approximations of the Stokes equations, Notes on Numerical Fluid Mechanics*, volume 10. 1984.

Franco Brezzi and Michel Fortin. *Mixed and Hybrid Finite Element Methods*. Springer, 1991.

U. Brink and E. Stein. On some mixed finite element methods for incompressible and nearly incompressible finite elasticity. *Computational Mechanics*, 19(1):105–119, 1996. ISSN 1432-0924.

Alexander N. Brooks and Thomas J.R. Hughes. Streamline upwind/petrov-galerkin formulations for convection dominated flows with particular emphasis on the incompressible navier-stokes equations. *Computer Methods in Applied Mechanics and Engineering*, 32 (1):199 – 259, 1982. ISSN 0045-7825.

C.S. Brown, M.F. Meier, and A. Post. Calving speed of alaska tidewater glaciers, with application to columbia glacier. *Geological Survey Professional Paper 1258-C*, 1982.

P.P. Camanho, C.G. Dávila, and M.F. De Moura. Numerical simulation of mixed-mode progressive delamination in composite materials. *Journal of Composite Materials*, 37 (16):1415–1424, 2003.

Benoit Carrier and Sylvie Granet. Numerical modeling of hydraulic fracture problem in permeable medium using cohesive zone model. *Engineering Fracture Mechan-*

ics, 79(Supplement C):312 – 328, 2012. ISSN 0013-7944. doi: https://doi.org/10.1016/j.engfracmech.2011.11.012. URL http://www.sciencedirect.com/science/article/pii/S0013794411004206.

N. Chandra, H. Li, C. Shet, and H. Ghonem. Some issues in the application of cohesive zone models for metal-ceramic interfaces. *International Journal of Solids and Structures*, 39:2827–2855, 2002.

Zuorong Chen, A.P. Bunger, Xi Zhang, and Robert G. Jeffrey. Cohesive zone finite element-based modeling of hydraulic fractures. *Acta Mechanica Solida Sinica*, 22 (5):443 – 452, 2009. ISSN 0894-9166. doi: https://doi.org/10.1016/S0894-9166(09)60295-0. URL http://www.sciencedirect.com/science/article/pii/S0894916609602950.

K.M. Cuffey and W.S.B. Paterson. *The Physics of Glaciers*. Elsevier Science, 2010. ISBN 9780080919126.

W. C. Cui and M. R. Wisnom. A combined stress-based and fracture-mechanics-based model for predicting delamination in composites. *Composites*, 24(6):467–474, 1993.

A. de Andres, J.L. Perez, and M. Ortiz. Elastoplastic finite element analysis of three-dimensional fatigue crack growth in aluminium shafts subjected to axial loading. *International Journal of Solids and Structures*, 36(15):2231–2258, 1999.

R. de Borst. Some recent issues in computational failure mechanics. *International Journal for Numerical Methods in Engineering*, 52:63–95, 2001.

R. de Borst. Numerical aspects of cohesive-zone models. *Engineering Fracture Mechanics*, 70:1743–1757, 2003.

R. de Borst, J. Pamin, R. H. J. Peerlings, and L. J. Sluys. On gradient-enhanced damage and plasticity models for failure in quasi-brittle and frictional materials. *Computational*

Mechanics, 17(1):130–141, Dec 1995. ISSN 1432-0924. doi: 10.1007/BF00356485. URL https://doi.org/10.1007/BF00356485.

Rene de Borst and Clemens V. Verhoosel. Gradient damage vs phase-field approaches for fracture: Similarities and differences. *Computer Methods in Applied Mechanics and Engineering*, pages –, 2016. ISSN 0045-7825. doi: http://dx.doi.org/10.1016/j.cma.2016.05.015.

M.F.S.F. de Moura and J.P.M. Gonçalves. Cohesive zone model for high-cycle fatigue of adhesively bonded joints under mode i loading. *International Journal of Solids and Structures*, 51(5):1123 – 1131, 2014. ISSN 0020-7683.

G. Q. De Robin. Depth of water-fitted crevasses that are closely spaced. *Journal of Glaciology*, 13(69):543?543, 1974. doi: 10.3189/S0022143000023285.

R. M. DeConto and D. Pollard. Contribution of antarctica to past and future sea-level rise. *Nature*, 531:591–597, 2016. doi: 10.1038/nature17145.

T. Diehl. On using a penalty-based cohesive-zone finite element approach, part i: Elastic solution benchmarks. *International Journal of Adhesion and Adhesives*, 28(4–5):237 – 255, 2008. ISSN 0143-7496. Peel testing.

B.C. Do, W. Liu, Q.D. Yang, and X.Y. Su. Improved cohesive stress integration schemes for cohesive zone elements. *Engineering Fracture Mechanics*, 107(0):14 – 28, 2013. ISSN 0013-7944.

C. R. Dohrmann and P. B. Bochev. A stabilized finite element method for the stokes problem based on polynomial pressure projections. *International Journal for Numerical Methods in Fluids*, 46:183–201, September 2004. doi: 10.1002/fld.752.

R. Duddu and H. Waisman. On the continuum damage mechanics approach to modeling of polar ice fracture: A reply. *Journal of glaciology*, 59(216):799–801, 2013a.

Ravindra Duddu and Haim Waisman. A temperature dependent creep damage model for polycrystalline ice. *Mechanics of Materials*, 46:23 – 41, 2012. ISSN 0167-6636.

Ravindra Duddu and Haim Waisman. On the continuum damage mechanics approach to modeling of polar ice fracture: a reply. *Journal of Glaciology*, 59(216):799?801, 2013b. doi: 10.3189/2013JoG13J083.

Ravindra Duddu and Haim Waisman. A nonlocal continuum damage mechanics approach to simulation of creep fracture in ice sheets. *Computational Mechanics*, 51(6):961–974, 2013c. ISSN 1432-0924.

Ravindra Duddu, Luc L. Lavier, Thomas J.R. Hughes, and Victor M. Calo. A finite strain eulerian formulation for compressible and nearly incompressible hyperelasticity using high-order b-spline finite elements. *International Journal for Numerical Methods in Engineering*, 89(6):762–785, 2012. ISSN 1097-0207.

Ravindra Duddu, Jeremy Bassis, and Haim Waisman. A numerical investigation of surface crevasse propagation in glaciers using nonlocal continuum damage mechanics. *Geophysical research letters*, 40(12):3064–3068, 2013.

D.S. Dugdale. Yielding of steel sheets containing slits. *Journal of the Mechanics and Physics of Solids*, 8(2):100–104, 1960.

T. Elguedj, Y. Bazilevs, V. M. Calo, and T. J. R Hughes. B and F projection methods for nearly incompressible linear and non-linear elasticity and plasticity using higher-order NURBS elements. *Computer Methods in Applied Mechanics and Engineering*, 197: 2732–2762, 2008.

T. Ferracin, C.M. Landis, F. Delannay, and T. Pardoen. On the determination of the cohesive zone properties of an adhesive layer from the analysis of the wedge-peel test. *International Journal of Solids and Structures*, 40(11):2889 – 2904, 2003. ISSN 0020-7683.

D. P. Flanagan and T. Belytschko. A uniform strain hexahedron and quadrilateral with orthogonal hourglass control. *International Journal for Numerical Methods in Engineering*, 17(5):679–706, 1981. ISSN 1097-0207.

Louis Foucard, Anup Aryal, Ravindra Duddu, and Franck Vernerey. A coupled eulerian–lagrangian extended finite element formulation for simulating large deformations in hyperelastic media with moving free boundaries. *Computer Methods in Applied Mechanics and Engineering*, 283:280 – 302, 2015. ISSN 0045-7825.

J.W. Foulk, D.H. Allen, and K.L.E. Helms. Formulation of a three-dimensional cohesive zone model for application to a finite element algorithm. *Computer Methods in Applied Mechanics and Engineering*, 183(1–2):51 – 66, 2000. ISSN 0045-7825.

Leopoldo P. Franca and Rolf Stenberg. Error analysis of galerkin least squares methods for the elasticity equations. *SIAM Journal on Numerical Analysis*, 28(6):1680–1697, 1991.

Leopoldo P. Franca, Sergio L. Frey, and Thomas J.R. Hughes. Stabilized finite element methods: I. application to the advective-diffusive model. *Computer Methods in Applied Mechanics and Engineering*, 95(2):253 – 276, 1992. ISSN 0045-7825.

Olivier Gagliardini, JÈrÙme Weiss, Paul Duval, and Maurine Montagnat. On duddu and waisman (2012, 2013) concerning continuum damage mechanics applied to crevassing and iceberg calving. *Journal of Glaciology*, 59(216):797?798, 2013. doi: 10.3189/2013JoG13J049.

J. W. Glen. The creep of polycrystalline ice. *Proceedings of the Royal Society of London A: Mathematical, Physical and Engineering Sciences*, 228(1175):519–538, 1955. ISSN 0080-4630.

G. Glinka. Development of weight functions and computer integration procedures for calculating stress intensity factors around cracks subjected to complex stress fields. Technical Report Progress Report No. 1, Stress and Fatigue-Fracture Design, Inc., 1996.

G. Glinka and G. Shen. Universal features of weight functions for cracks in mode i. *Engineering Fracture Mechanics*, 40(6):1135 – 1146, 1991. ISSN 0013-7944. doi: https://doi.org/10.1016/0013-7944(91)90177-3. URL http://www.sciencedirect.com/science/article/pii/0013794491901773.

V.K. Goyal, E.R. Johnson, and C.G. Davila. Irreversible constitutive law for modeling the delamination process using interfacial surface discontinuities. *Composite Structures*, 65 (3-4):434–446, 2004.

V.K. Goyal, E.R. Johnson, and V.K. Goyal. Predictive strength-fracture model for composite bonded joints. *Composite Structures*, 82(3):434–446, 2008.

M. Gunzburger and R.A. Nicolaides. *Incompressible Computational Fluid Dynamics*. Cambridge University Press, 1993.

P. Gupta, C.A. Duarte, and A. Dhankhar. Accuracy and robustness of stress intensity factor extraction methods for the generalized/extended finite element method. *Engineering Fracture Mechanics*, 179(Supplement C):120 – 153, 2017. ISSN 0013-7944. doi: https://doi.org/10.1016/j.engfracmech.2017.03.035.

P.A. Gustafson and A.M. Waas. The influence of adhesive constitutive parameters in cohesive zone finite element models of adhesively bonded joints. *International Journal of Solids and Structures*, 46(10):2201 – 2215, 2009. ISSN 0020-7683. Special Issue in Honor of Professor Liviu Librescu.

Kevin Hammonds and Ian Baker. Quantifying damage in polycrystalline ice via x-ray computed micro-tomography. *Acta Materialia*, 127:463 – 470, 2017. ISSN 1359-6454. doi: https://doi.org/10.1016/j.actamat.2017.01.046. URL https://www.sciencedirect.com/science/article/pii/S1359645417300587.

P.W. Harper and S.R. Hallett. Cohesive zone length in numerical simulations of composite delamination. *Engineering Fracture Mechanics*, 75(16):4774–4792, 2008.

P.W. Harper and S.R. Hallett. A fatigue degradation law for cohesive interface elements development and application to composite materials. *International Journal of Fatigue*, 32(11):1774–1787, 2010.

D. R. Hayhurst. Creep-rupture under multi-axial states of stress. *Journal of Mechanics of Physics and Solids*, 20(6), 1972.

A. Hillerborg, M. Modéer, and P.E. Petersson. Analysis of crack formation and crack growth in concrete by means of fracture mechanics and finite elements. *Cement and Concrete Research*, 6:773–782, 1976.

T. J. R. Hughes and G. Sangalli. Variational multiscale analysis: the fineäêscale green's function, projection, optimization, localization, and stabilized methods. *SIAM Journal on Numerical Analysis*, 45(2):539–557, 2007.

Thomas J.R. Hughes. Multiscale phenomena: Green's functions, the dirichlet-to-neumann formulation, subgrid scale models, bubbles and the origins of stabilized methods. *Computer Methods in Applied Mechanics and Engineering*, 127(1–4):387 – 401, 1995. ISSN 0045-7825.

Thomas J.R. Hughes and Leopoldo P. Franca. A new finite element formulation for computational fluid dynamics: Vii. the stokes problem with various well-posed boundary conditions: Symmetric formulations that converge for all velocity/pressure spaces. *Computer Methods in Applied Mechanics and Engineering*, 65(1):85 – 96, 1987. ISSN 0045-7825.

Thomas J.R. Hughes and James R. Stewart. A space-time formulation for multiscale phenomena. *Journal of Computational and Applied Mathematics*, 74(1):217 – 229, 1996. ISSN 0377-0427. doi: http://dx.doi.org/10.1016/0377-0427(96)00025-8.

Thomas J.R. Hughes, Leopoldo P. Franca, and Marc Balestra. A new finite element formulation for computational fluid dynamics: V. circumventing the babuška-brezzi condition:

a stable petrov-galerkin formulation of the stokes problem accommodating equal-order interpolations. *Computer Methods in Applied Mechanics and Engineering*, 59(1):85 – 99, 1986. ISSN 0045-7825.

Thomas J.R. Hughes, Leopoldo P. Franca, and Gregory M. Hulbert. A new finite element formulation for computational fluid dynamics: Viii. the galerkin/least-squares method for advective-diffusive equations. *Computer Methods in Applied Mechanics and Engineering*, 73(2):173 – 189, 1989. ISSN 0045-7825.

Tobin Isaac, Georg Stadler, and Omar Ghattas. Solution of nonlinear stokes equations discretized by high-order finite elements on nonconforming and anisotropic meshes, with application to ice sheet dynamics. *SIAM Journal on Scientific Computing*, 37(6):B804–B833, 2015. doi: 10.1137/140974407. URL http://dx.doi.org/10.1137/140974407.

Kenneth C. Jezek. A modified theory of bottom crevasses used as a means for measuring the buttressing effect of ice shelves on inland ice sheets. *Journal of Geophysical Research: Solid Earth*, 89(B3):1925–1931, 1984. ISSN 2156-2202. doi: 10.1029/JB089iB03p01925. URL http://dx.doi.org/10.1029/JB089iB03p01925.

W-G. Jiang, S.R. Hallet, B.G. Green, and M.R. Wisnom. A concise interface constitutive law for analysis of delamination and splitting in composite materials and its application to scaled notched tensile specimens. *International Journal for Numerical Methods in Engineering*, 69(9):1982–1995, 2007.

S. Jimenez, X. Liu, R. Duddu, and H. Waisman. A discrete damage zone model for mixed-mode delamination of composites under high-cycle fatigue. *International Journal of Fracture*, 190(1-2):53–74, 2014. ISSN 0376-9429.

Stephen Jimenez and Ravindra Duddu. On the parametric sensitivity of cohesive zone models for high-cycle fatigue delamination of composites. *International Journal of Solids and Structures*, 82(Supplement C):111 – 124, 2016. ISSN 0020-7683. doi: https://doi.

org/10.1016/j.ijsolstr.2015.10.015. URL http://www.sciencedirect.com/science/article/pii/S002076831500431X.

Stephen Jiménez, Ravindra Duddu, and Jeremy Bassis. An updated-lagrangian damage mechanics formulation for modeling the creeping flow and fracture of ice sheets. *Computer Methods in Applied Mechanics and Engineering*, 313:406 – 432, 2017. ISSN 0045-7825. doi: http://dx.doi.org/10.1016/j.cma.2016.09.034.

Milan Jirásek and Peter Grassl. Evaluation of directional mesh bias in concrete fracture simulations using continuum damage models. *Engineering Fracture Mechanics*, 75(8): 1921 – 1943, 2008. ISSN 0013-7944.

M. Juntti, L.E. Asp, and R. Olsson. Assessment of evaluation methods for the mixed-mode bending test. *Journal of Composites Technology and Research*, 21(1):37–48, 1999.

L. M. Kachanov. Time of the rupture process under creep conditions. *Izvestia Akademii Nauk SSSR. Otdelenie Tekhnicheskich Nauk*, 8(8):26–31, 1958.

Dale G. Karr and Kyungsik Choi. A three-dimensional constitutive damage model for polycrystalline ice. *Mechanics of Materials*, 8(1):55 – 66, 1989. ISSN 0167-6636.

K.B. Katnam, A.D. Crocombe, H. Sugiman, and H. Khoramishad. Static and fatigue failures of adhesively bonded laminate joints in moist environments. *International Journal of Damage Mechanics*, 20(8), 2011. ISSN 1217-1242.

Luiz F. Kawashita and Stephen R. Hallett. A crack tip tracking algorithm for cohesive interface element analysis of fatigue delamination propagation in composite materials. *International Journal of Solids and Structures*, 49(21):2898 – 2913, 2012. ISSN 0020-7683.

Arne Keller and Kolumban Hutter. Conceptual thoughts on continuum damage mechanics

for shallow ice shelves. *Journal of Glaciology*, 60(222):685Äì693, 2014a. doi: 10.3189/2014JoG14J010.

Arne Keller and Kolumban Hutter. Conceptual thoughts on continuum damage mechanics for shallow ice shelves. *Journal of Glaciology*, 60(222):685–693, 2014b.

M. Kenane and M. L. Benzeggagh. Mixed-mode delamination fracture toughness of unidirectional glass/epoxy composites under fatigue loading. *Composites Science and Technology*, 57:597–605, 1997.

R. Khan, Z. Khan, F. Al-Sulaiman, and N. Merah. Fatigue life estimates in woven carbon fabric/epoxy composites at non-ambient temperatures. *Journal of Composite Materials*, 36(22):2517–2535, 2002.

H. Khoramishad, A.D. Crocombe, K.B. Katnam, and I.A. Ashcroft. Predicting fatigue damage in adhesively bonded joints using a cohesive zone model. *International Journal of Fatigue*, 32(7):1146 – 1158, 2010. ISSN 0142-1123.

H. Khoramishad, A.D. Crocombe, K.B. Katnam, and I.A. Ashcroft. Fatigue damage modelling of adhesively bonded joints under variable amplitude loading using a cohesive zone model. *Engineering Fracture Mechanics*, 78(18):3212 – 3225, 2011. ISSN 0013-7944.

Ronald Krueger. Virtual crack closure technique: History, approach, and applications. 57, 05 2002.

J. Krug, J. Weiss, O. Gagliardini, and G. Durand. Combining damage and fracture mechanics to model calving. *The Cryosphere*, 8(6):2101–2117, 2014. doi: 10.5194/tc-8-2101-2014. URL https://www.the-cryosphere.net/8/2101/2014/.

B. Landry and G. LaPlante. Modeling delamination growth in composites under fatigue loadings of varying amplitudes. *Composites: Part B Engineering*, 43(2):533–541, 2012.

Eric Larour, Eric Rignot, and Denis Aubry. Processes involved in the propagation of rifts near hemmen ice rise, ronne ice shelf, antarctica. *Journal of Glaciology*, 50(170): 329Äì341, 2004. doi: 10.3189/172756504781829837.

M.J. Lee, T.M. Cho, W.S. Kim, B.C. Lee, and J.J. Lee. Determination of cohesive parameters for a mixed-mode cohesive zone model. *International Journal of Adhesion and Adhesives*, 30(5):322 – 328, 2010. ISSN 0143-7496. Special Issue on Joint Design.

J. Lemaitre. Evaluation of dissipation and damage in metals. *In: proceedings of the International Congress on the Mechanical Behavior of Materials (I.C.M.), Kyoto, Japan, 1*, 1971.

J. Lemaitre. *A Course on Damage Mechanics*. Springer, New York., 1992.

W. Leng, L. Ju, M. Gunzburger, and S. Price. Manufactured solutions and the verification of three-dimensional stokes ice-sheet models. *The Cryosphere*, 7(1):19–29, 2013.

Wei Leng, Lili Ju, Max Gunzburger, Stephen Price, and Todd Ringler. A parallel high-order accurate finite element nonlinear stokes ice sheet model and benchmark experiments. *Journal of Geophysical Research: Earth Surface*, 117(F1):n/a–n/a, 2012. ISSN 2156-2202. F01001.

S. Li and S. Ghosh. Multiple cohesive crack growth in brittle materials by the extended Voronoi cell finite element model. *International Journal of Fracture*, 141:373–393, 2006.

S. Li, M.D. Thouless, A.M. Waas, J.A. Schroeder, and P.D. Zavattieri. Mixed-mode cohesive-zone models for fracture of an adhesively bonded polymer-matrix composite. *Engineering Fracture Mechanics*, 73(1):64–78, 2006.

C.D.M. Liljedahl, A.D. Crocombe, M.A. Wahab, and I.A. Ashcroft. Damage modelling of adhesively bonded joints. *International Journal of Fracture*, 141:147–161, 2006.

X. Liu, R. Duddu, and H. Waisman. Discrete damage zone model for fracture initiation and propagation. *Engineering Fracture Mechanics*, 92:1–18, 2012.

Vladimir Lyakhovsky, Yariv Hamiel, and Yehuda Ben-Zion. A non-local visco-elastic damage model and dynamic fracturing. *Journal of the Mechanics and Physics of Solids*, 59(9):1752 – 1776, 2011. ISSN 0022-5096. doi: https://doi.org/10.1016/j.jmps.2011.05.016. URL http://www.sciencedirect.com/science/article/pii/S0022509611001256.

Arif Masud and Thomas J.R. Hughes. A stabilized mixed finite element method for darcy flow. *Computer Methods in Applied Mechanics and Engineering*, 191(39-40):4341 – 4370, 2002.

J. Mazars. A description of micro- and macroscale damage of concrete structures. *Engineering Fracture Mechanics*, 25:729–737, 1986.

M. F. Meier and Austin Post. Fast tidewater glaciers. *Journal of Geophysical Research: Solid Earth*, 92(B9):9051–9058, 1987. ISSN 2156-2202. doi: 10.1029/JB092iB09p09051. URL http://dx.doi.org/10.1029/JB092iB09p09051.

Mark Meier, Scott Lundstrom, Dan Stone, Barclay Kamb, Hermann Engelhardt, Neil Humphrey, William W. Dunlap, Mark Fahnestock, Robert M. Krimmel, and Roy Walters. Mechanical and hydrologic basis for the rapid motion of a large tidewater glacier: 1. observations. *Journal of Geophysical Research: Solid Earth*, 99(B8):15219–15229, 1994. ISSN 2156-2202. doi: 10.1029/94JB00237. URL http://dx.doi.org/10.1029/94JB00237.

Y. Mi, M.A. Crisfield, G.A.O. Davies, and H.B. Hellweg. Progressive delamination using interface elements. *Journal of Composite Materials*, 32:1246–1272, 1998a.

Y. Mi, M.A. Crisfield, G.A.O. Davies, and H.B. Hellweg. Progressive delamination using interface elements. *Journal of Composite Materials*, 32:1246–1272, 1998b.

Christian Miehe, Martina Hofacker, and Fabian Welschinger. A phase field model for rate-independent crack propagation: Robust algorithmic implementation based on operator splits. *Computer Methods in Applied Mechanics and Engineering*, 199(45):2765 – 2778, 2010. ISSN 0045-7825. doi: https://doi.org/10.1016/j.cma.2010.04.011.

Christian Miehe, Lisa-Marie Schänzel, and Heike Ulmer. Phase field modeling of fracture in multi-physics problems. part i. balance of crack surface and failure criteria for brittle crack propagation in thermo-elastic solids. *Computer Methods in Applied Mechanics and Engineering*, 294(Supplement C):449 – 485, 2015. ISSN 0045-7825. doi: https://doi.org/10.1016/j.cma.2014.11.016.

William Mitchell. *Exact and numerical solutions for Stokes flow in glaciers*. PhD thesis, University of Alaska, Fairbanks, 2012.

M. E. Mobasher, R. Duddu, J. N. Bassis, and H. Waisman. Modeling hydraulic fracture of glaciers using continuum damage mechanics. *Journal of Glaciology*, page (Accepted), 2016.

Mostafa E. Mobasher, Luc Berger-Vergiat, and Haim Waisman. Non-local formulation for transport and damage in porous media. *Computer Methods in Applied Mechanics and Engineering*, 324(Supplement C):654 – 688, 2017. ISSN 0045-7825. doi: https://doi.org/10.1016/j.cma.2017.06.016. URL http://www.sciencedirect.com/science/article/pii/S0045782517301470.

A.A. Moftakhar and G. Glinka. Calculation of stress intensity factors by efficient integration of weight functions. *Engineering Fracture Mechanics*, 43(5):749 – 756, 1992. ISSN 0013-7944. doi: https://doi.org/10.1016/0013-7944(92)90005-Y. URL http://www.sciencedirect.com/science/article/pii/001379449290005Y.

Peter L. Moore. Deformation of debris-ice mixtures. *Reviews of Geophysics*, 52(3):435–467, 2014. ISSN 1944-9208. doi: 10.1002/2014RG000453. 2014RG000453.

J.J. Munoz, U. Galvanetto, and P. Robinson. On the numerical simulation of fatigue-driven delamination using interface elements. *International Journal of Fatigue*, 28(10):1136–1146, 2006.

S. Murakami. Notion of continuum damage mechanics and its application to anisotropic creep damage theory. *Journal of Engineering Materials and Technology - Transactions of the ASME*, 105(2):99–105, 1983.

S. Murakami, M. Kawai, and H. Rong. Finite element analysis of creep crack growth by a local approach. *International Journal of Mechanical Sciences*, 30(7):491 – 502, 1988. ISSN 0020-7403.

K.B. Nakshatrala, D.Z. Turner, K.D. Hjelmstad, and A. Masud. A stabilized mixed finite element method for darcy flow based on a multiscale decomposition of the solution. *Computer Methods in Applied Mechanics and Engineering*, 195(33-36):4036 – 4049, 2006.

A. Needleman. A continuum model for void nucleation by inclusion debonding. *Journal of Applied Mechanics*, 54:525–531, 1987.

A. Needleman. Some issues in cohesive surface modeling. *Procedia* {*IUTAM*}, 10(0): 221 – 246, 2014. ISSN 2210-9838. Mechanics for the World: Proceedings of the 23rd International Congress of Theoretical and Applied Mechanics, {ICTAM2012}.

S. Nemat-Nasser, A. Oranratnachai, and L. M. Keer. Spacing of water-free crevasses. *Journal of Geophysical Research: Solid Earth*, 84(B9):4611–4620, 1979. ISSN 2156-2202. doi: 10.1029/JB084iB09p04611. URL http://dx.doi.org/10.1029/JB084iB09p04611.

R. W. Neu and H. Sehitoglu. Thermomechanical fatigue, oxidation, and creep: II Life prediction. *Metallurgical Transactions A - Physical Metallurgy And Materials Science*, 20(9):1769–1783, 1989.

O. Nguyen, E. A. Repetto, M. Ortiz, and R. A. Radovitzky. A cohesive model of fatigue crack growth. *International Journal of Fracture*, 110(4):351–369, 2001.

T.T. Nguyen, J. Yvonnet, Q.-Z. Zhu, M. Bornert, and C. Chateau. A phase field method to simulate crack nucleation and propagation in strongly heterogeneous materials from direct imaging of their microstructure. *Engineering Fracture Mechanics*, 139(Supplement C):18 – 39, 2015. ISSN 0013-7944. doi: https://doi.org/10.1016/j.engfracmech.2015.03.045.

F. M. Nick, C. J. van der Veen, and J. Oerlemans. Controls on advance of tidewater glaciers: Results from numerical modeling applied to columbia glacier. *Journal of Geophysical Research: Earth Surface*, 112(F3):n/a–n/a, 2007. ISSN 2156-2202. doi: 10.1029/2006JF000551. URL http://dx.doi.org/10.1029/2006JF000551. F03S24.

F. M. Nick, A. Vieli, I. M. Howat, and I. Joughin. Large-scale changes in greenland outlet glacier dynamics triggered at the terminus. *Nature Geoscience*, 2:110–114, 2009.

FM Nick, CJ Van der Veen, A Vieli, and DI Benn. A physically based calving model applied to marine outlet glaciers and implications for the glacier dynamics. *Journal of Glaciology*, 56(199):781–794, 2010a.

FM Nick, CJ Van der Veen, A Vieli, and DI Benn. A physically based calving model applied to marine outlet glaciers and implications for the glacier dynamics. *Journal of Glaciology*, 56(199):781–794, 2010b.

K.-F. Nilsson, L.E. Asp, J.E. Alpman, and L. Nystedt. Delamination buckling and growth for delaminations at different depths in a slender composite panel. *International Journal of Solids and Structures*, 38(17):3039–3071, 2001.

J. F. Nye. The flow law of ice from measurements in glacier tunnels, laboratory experiments and the Jungfraufirn borehole experiment. *Proceedings of the Royal Society of London A: Mathematical, Physical and Engineering Sciences*, 219:477–489, 1953.

J. F. Nye. Comments on dr. loewe?s letter and notes on crevasses. *Journal of Glaciology*, 2(17):512?514, 1955. doi: 10.3189/S0022143000032652.

J. F. Nye. The distribution of stress and velocity in glaciers and ice-sheets. *Proc. R. Soc. London*, pages 113–133, 1957.

T.K. O'Brien. Composite interlaminar shear fracture toughness, giic: shear measurement or sheer myth? *Composite materials: fatigue and fracture*, 7:3 – 18, 1998.

E. Onate and J. M. Carbonell. Updated lagrangian mixed finite element formulation for quasi and fully incompressible fluids. *Computational Mechanics*, 54:1583–1596, 2014.

M.H.J.W. Paas, P.J.G. Schreurs, and W.A.M. Brekelmans. A continuum approach to brittle and fatigue damage: theory and numerical procedures. *International Journal of Solids and Structures*, 30(4):579–599, 1993.

P. Paris and F. Erdogan. Critical analysis of propagation laws. *Journal of Basic Engineering*, 85:528–534, 1963.

P. Paris, M. Gomez, and W. Anderson. A rational analytical theory of fatigue. *The Trend in Engineering*, 13:9–14, 1961.

K. Park and G.H. Paulino. Computational implementation of the PPR potential-based cohesive model in abaqus: Educational perspective. *Engineering Fracture Mechanics*, 93 (0):239 – 262, 2012. ISSN 0013-7944.

K. Park, G.H. Paulino, and J.R. Roesler. A unified potential-based cohesive model of mixed-mode fracture. *Journal of Mechanics and Physics of Solids*, 57:891–908, 2009.

J.A. Pascoe, R.C. Alderliesten, and R. Benedictus. Methods for the prediction of fatigue delamination growth in composites and adhesive bonds – a critical review. *Engineering Fracture Mechanics*, 112–113(0):72 – 96, 2013. ISSN 0013-7944.

J. Payan and C Hochard. Damage modelling of laminated carbon/epoxy composites under static and fatigue loadings. *International Journal of Fatigue*, 24(2-4):299–306, 2002.

R. H. J. Peerlings, M. G. D. Geers, R. de Borst, and W.A.M. Brekelmans. A critical comparison of nonlocal and gradient-enhanced softening continua. *International Journal of Solids and Structures*, 38(44-45):7723–7746, 2001.

R.H.J. Peerlings, W.A.M. Brekelmans, R. de Borst, and M.G.D. Geers. Gradient-enhanced damage modelling of high-cyclic fatigue. *International Journal for Numerical Methods in Engineering*, 49(12):1547–1569, 2000.

K.B. Pettersson, J.M. Neumeister, E.K. Gamstedt, and H. Öberg. Stiffness reduction, creep, and irreversible strains in fiber composites tested in repeated interlaminar shear. *Composite Structures*, 76(1–2):151 – 161, 2006. ISSN 0263-8223. Fifteenth International Conference on Composite Materials ICCM-15 Fifteenth International Conference on Composite Materials.

Gilles Pijaudier-Cabot and Zdenek P. Bazant. Nonlocal damage theory. *Journal of Engineering Mechanics*, 113(10):1512–1533, 1987a. doi: 10.1061/(ASCE)0733-9399(1987)113:10(1512).

Gilles Pijaudier-Cabot and Zdenek P Bazant. Nonlocal damage theory. *Journal of engineering mechanics*, 113(10):1512–1533, 1987b.

C. Plate, R. Müller, A. Humbert, and D. Gross. Evaluation of the criticality of cracks in ice shelves using finite element simulations. *The Cryosphere*, 6(5):973–984, 2012. doi: 10.5194/tc-6-973-2012.

A. Pralong and M. Funk. Dynamic damage model of crevasse opening and application to glacier calving. *Journal of Geophysical Research: Solid Earth*, 110(B1), 2005. ISSN 2156-2202.

A. Pralong, K. Hutter, and M. Funk. Anisotropic damage mechanics for viscoelastic ice. *Continuum Mechanics and Thermodynamics*, 17(5):387–408, Feb 2006. doi: 10.1007/s00161-005-0002-5. URL https://doi.org/10.1007/s00161-005-0002-5.

Y. Qiu, M.A. Crisfield, and G. Alfano. An interface element formulation for the simulation of delamination with buckling. *Engineering Fracture Mechanics*, 68:1755–1776, 2001.

Y. N. Rabotnov. On the equations of state for creep. *Progress in Applied Mechanics, the Prager Anniversary*, 8, 1963.

J.R. Reeder and J.R. Crews. Mixed-mode bending method for delamination testing. *AIAA Journal*, 28(7):1270–1276, 1990.

M. A. Rist, P. R. Sammonds, S. A. F. Murrell, P. G. Meredith, C. S. M. Doake, H. Oerter, and K. Matsuki. Experimental and theoretical fracture mechanics applied to antarctic ice fracture and surface crevassing. *Journal of Geophysical Research: Solid Earth*, 104 (B2):2973–2987, 1999. ISSN 2156-2202. doi: 10.1029/1998JB900026. URL http://dx.doi.org/10.1029/1998JB900026.

MA Rist, PR Sammonds, SAF Murrell, PG Meredith, Hans Oerter, and CSM Doake. Experimental fracture and mechanical properties of antarctic ice: preliminary results. *Annals of glaciology*, 23(1):284–292, 1996.

P. Robinson, T. Besant, and D. Hitchings. Delamination growth prediction using a finite element approach. *2nd ESIS TC4 Conference on Fracture of Polymers, Composites and Adhesives, Switzerland*, 27:135–147, 2000.

P. Robinson, U. Galvanetto, D. Tumino, G. Bellucci, and D. Violeau. Numerical simulation of fatigue-driven delamination using interface elements. *International Journal for Numerical Methods in Engineering*, 63(13):1824–1848, 2005.

K. L. Roe and T. Siegmund. An irreversible cohesive zone model for interface fatigue crack growth simulation. *Engineering Fracture Mechanics*, 70(2):209–232, 2003.

R.A. Schapery. Nonlinear viscoelastic and viscoplastic constitutive equations with growing damage. *International Journal of Fracture*, 97(1):33–66, Apr 1999. doi: 10.1023/A:1018695329398. URL https://doi.org/10.1023/A:1018695329398.

J.C.J. Schellenkens and R. de Borst. A non-linear finite element approach for the analysis of mode-i free edge delamination in composites. *International Journal of Solids and Structures*, 30(9):1239–1253, 1993.

E. M. Schulson and P. Duval. *Creep and fracture of ice*. Cambridge University Press, Cambridge, 2009.

K. Shivakumar, H. Chen, F. Abali, D. Le, and C. Davis. A total fatigue life model for mode i delaminated composite laminates. *International Journal of Fatigue*, 28(1):33 – 42, 2006. ISSN 0142-1123.

F. Sidoroff. *Description of Anisotropic Damage Application to Elasticity*, pages 237–244. Springer Berlin Heidelberg, Berlin, Heidelberg, 1981. ISBN 978-3-642-81582-9. doi: 10.1007/978-3-642-81582-9_35. URL http://dx.doi.org/10.1007/978-3-642-81582-9_35.

T. Siegmund. A numerical study of transient fatigue crack growth by use of an irreversible cohesive zone model. *International Journal of Fatigue*, 26(9):929–939, 2004.

A. Sjogren and L.E. Asp. Effects of temperature on delamination growth in a carbon/epoxy composite under fatigue loading. *International Journal of Fatigue*, 24(2-4):179–184, 2002.

B. Skallerud and Z.L. Zhang. A 3D numerical study of ductile tearing and fatigue crack

growth under nominal cyclic plasticity. *International Journal of Solids and Structures*, 34(24):3141–3161, 1997.

S. Sun, S. Cornford, R. Gladstone, L. Zhao, and J. Moore. Ice shelf fracture parameterization in an ice sheet model. *The Cryosphere Discussions*, 2017:1–23, 2017. doi: 10.5194/tc-2017-53. URL https://www.the-cryosphere-discuss.net/tc-2017-53/.

Barna Aladar Szabo and Ivo Babuška. *Finite element analysis*. John Wiley & Sons, 1991.

H. Tada, P. Paris, and G. H. Irwin. *The Stress Analysis of Cracks Handbook, Third Edition*. The American Society of Mechanical Engineers, New York, NY, 2000. ISBN 0791801535.

Karl Terzaghi. *Stress Conditions for Failure in Soils*, pages 7–25. John Wiley and Sons, Inc., 2007. ISBN 9780470172766. doi: 10.1002/9780470172766.ch2. URL http://dx.doi.org/10.1002/9780470172766.ch2.

I. K. Tezaur, M. Perego, A. G. Salinger, R. S. Tuminaro, and S. F. Price. Albany/felix: a parallel, scalable and robust, finite element, first-order stokes approximation ice sheet solver built for advanced analysis. *Geoscientific Model Development*, 8(4):1197–1220, 2015a.

I. K. Tezaur, M. Perego, A. G. Salinger, R. S. Tuminaro, and S. F. Price. Albany/felix: a parallel, scalable and robust, finite element, first-order stokes approximation ice sheet solver built for advanced analysis. *Geoscientific Model Development*, 8(4):1197–1220, 2015b. doi: 10.5194/gmd-8-1197-2015.

D. Z. Turner, K. B. Nakshatrala, and K. D. Hjelmstad. On the stability of bubble functions and a stabilized mixed finite element formulation for the stokes problem. *International Journal for Numerical Methods in Fluids*, 60(12):1291–1314, 2009. ISSN 1097-0363.

D. Z. Turner, K. B. Nakshatrala, and K. D. Hjelmstad. A variational multiscale newtonôøschur approach for the incompressible navierôøstokes equations. *International Journal for Numerical Methods in Fluids*, 62(2):119–137, 2010. ISSN 1097-0363.

A. Turon, J. Costa, P.P. Camanho, and C.G. Davila. Simulation of delamination in composites under high-cycle fatigue. *Composites: Part A*, 38(11):2270–2282, 2007a.

A. Turon, C.G. Dávila, P.P. Camanho, and J. Costa. An engineering solution for mesh size effects in the simulation of delamination using cohesive zone models. *Engineering Fracture Mechanics*, 74(10):1665 – 1682, 2007b. ISSN 0013-7944.

Lizz Ultee and Jeremy Bassis. The future is nye: an extension of the perfect plastic approximation to tidewater glaciers. *Journal of Glaciology*, 62(236):1143?1152, 2016. doi: 10.1017/jog.2016.108.

A. Ural, V.R. Krishnan, and K.D. Papoulia. A cohesive zone model for fatigue crack growth allowing for crack retardation. *International Journal of Solids and Structures*, 46 (11–12):2453 – 2462, 2009. ISSN 0020-7683.

N. Valoroso and L. Champaney. A damage-mechanics-based approach for modelling decohesion in adhesively bonded assemblies. *Engineering Fracture Mechanics*, 73(18):2774 – 2801, 2006. ISSN 0013-7944.

M.J. van den Bosch, P.J.G. Schreurs, and M.G.D. Geers. An improved description of the exponential xu and needleman cohesive zone law for mixed-mode decohesion. *International Journal of Fracture*, 73:1220–1234, 2006.

C. J. van der Veen. Tidewater calving. *Journal of Glaciology*, 42(141):375–385, 1996.

C. J. van der Veen. Calving glaciers. *Progress in Physical Geography*, 26(1):96–122, 2002. doi: 10.1191/0309133302pp327ra.

C. J. van der Veen. *Fundamentals of Glacier Dynamics*. CRC Press, 2013. ISBN 978-1-4398-3566-1.

CJ Van der Veen. Fracture mechanics approach to penetration of bottom crevasses on glaciers. *Cold Regions Science and Technology*, 27(3):213–223, 1998a.

CJ Van der Veen. Fracture mechanics approach to penetration of surface crevasses on glaciers. *Cold Regions Science and Technology*, 27(1):31–47, 1998b.

C.J. van der Veen. Fracture mechanics approach to penetration of surface crevasses on glaciers. *Cold Regions Science and Technology*, 27(1):31 – 47, 1998a. ISSN 0165-232X.

CJ van der Veen. Fracture mechanics approach to penetration of bottom crevasses on glaciers. *Cold Regions Science and Technology*, 27(3):213–223, 1998b.

Clemens V. Verhoosel, Michael A. Scott, Thomas J. R. Hughes, and René de Borst. An isogeometric analysis approach to gradient damage models. *International Journal for Numerical Methods in Engineering*, 86(1):115–134, 2011. ISSN 1097-0207.

A. Vieli and F. M. Nick. Understanding and modelling rapid dynamic changes of tidewater outlet glaciers: issues and implications. *Surveys in Geophysics*, 32(4-5):437–458, 2011.

C. C. Walker, J. N. Bassis, H. A. Fricker, and R. J. Czerwinski. Structural and environmental controls on antarctic ice shelf rift propagation inferred from satellite monitoring. *Journal of Geophysical Research: Earth Surface*, 118(4):2354–2364, 2013. ISSN 2169-9011. doi: 10.1002/2013JF002742. URL http://dx.doi.org/10.1002/2013JF002742.

E.K. Walker. Analysis of stresses and strains near the end of a crack traversing a plate the effect of stress ratio during crack propagation and fatigue for 2024-T3 and 7076-T6 aluminum. *In: Effect of environment and complex load history on fatigue life, ASTM STP 462. Philadelphia: American Society for Testing and Materials*, 24:1–14, 1970.

Y. Wang and H. Waisman. Progressive delamination analysis of composite materials using xfem and a discrete damage zone model. *Computational Mechanics*, 2014.

J. Weertman. Deformation of floating ice shelves. *Journal of Glaciology*, 3(21):38–42, 1957.

J. Weertman. Theory of water-filled crevasses in glaciers applied to vertical magma transport beneath oceanic ridges. *Journal of Geophysical Research*, 76(5):1171–1183, 1971. ISSN 2156-2202. doi: 10.1029/JB076i005p01171. URL http://dx.doi.org/10.1029/JB076i005p01171.

J. Weertman. Can a water-filled crevasse reach the bottom surface of a glacier? In *IASH Publications*, number 95, pages 139–145, 1973.

J. Weertman. Depth of water-filled crevasses that are closely spaced. *Journal of Glaciology*, 13(69):544?544, 1974. doi: 10.3189/S0022143000023297.

J. Weertman. Penetration depth of closely spaced water-free crevasses. *Journal of Glaciology*, 18(78):37–46, 1977. doi: DOI:10.1017/S0022143000021493. URL https://www.cambridge.org/core/article/penetration-depth-of-closely-spaced-waterfree-crevasses/3D626935E7FF16146E174D442FE62693.

J Weertman. Bottom crevasses. *Journal of Glaciology*, 25(91):185–188, 1980a.

J Weertman. Bottom crevasses. *Journal of Glaciology*, 25(91):185–188, 1980b.

J Weertman. Creep deformation of ice. *Annual Review of Earth and Planetary Sciences*, 11(1):215–240, 1983.

J.G. Williams. On the calculation of energy release rates for cracked laminates. *International Journal of Fracture*, 36(2):101–119, 1988.

Zachary A. Wilson and Chad M. Landis. Phase-field modeling of hydraulic fracture. *Journal of the Mechanics and Physics of Solids*, 96(Supplement C):264 – 290, 2016.

ISSN 0022-5096. doi: https://doi.org/10.1016/j.jmps.2016.07.019. URL http://www.sciencedirect.com/science/article/pii/S002250961630285X.

Jennifer Worthen, Georg Stadler, Noemi Petra, Michael Gurnis, and Omar Ghattas. Towards adjoint-based inversion for rheological parameters in nonlinear viscous mantle flow. *Physics of the Earth and Planetary Interiors*, 234:23 – 34, 2014. ISSN 0031-9201.

Jennifer A. Worthen. *Inverse problems in mantle convection: models, algorithms, and applications*. PhD thesis, The University of Texas at Austin, 2012.

Jian-Ying Wu and Shi-Lang Xu. Reconsideration on the elastic damage/degradation theory for the modeling of microcrack closure-reopening (mcr) effects. *International Journal of Solids and Structures*, 50(5):795 – 805, 2013. ISSN 0020-7683. doi: https://doi.org/10.1016/j.ijsolstr.2012.11.012. URL http://www.sciencedirect.com/science/article/pii/S0020768312004751.

D. Xie and A.M. Waas. Discrete cohesive zone model for mixed-mode fracture using finite element analysis. *Engineering Fracture Mechanics*, 73:1783–1796, 2006.

D. Xie, A.G. Salvi, C. Sun, and A.M. Waas. Discrete cohesive zone model to simulate static fracture in 2D triaxially braided carbon fiber composites. *Journal of Composite Materials*, 40(22):2025–2046, 2006.

X.-P. Xu and A. Needleman. Numerical simulations of fast crack growth in brittle solids. *Journal of the Mechanics and Physics of Solids*, 42(9):1397–1434, 1994.

B. Yang and K.A. Ravi-Chandar. Antiplane shear crack growth under quasistatic loading in a damaging material. *International Journal of Solids and Structures*, 35(28-29):3695–3715, 1998.

B. Yang, S. Mall, and K.A. Ravi-Chandar. A cohesive zone model for fatigue crack growth

in quasibrittle materials. *International Journal of Solids and Structures*, 38(22-23):3927–4394, 2001.

H. Yu, E. Rignot, M. Morlighem, and H. Seroussi. Iceberg calving of thwaites glacier, west antarctica: full-stokes modeling combined with linear elastic fracture mechanics. *The Cryosphere*, 11(3):1283–1296, 2017. doi: 10.5194/tc-11-1283-2017. URL https://www.the-cryosphere.net/11/1283/2017/.

Huai Zhang, Lili Ju, Max Gunzburger, Todd Ringler, and Stephen Price. Coupled models and parallel simulations for three-dimensional full-stokes ice sheet modeling. *Numerical Mathematics: Theory, Methods and Applications*, 4:396–418, 8 2011. ISSN 2079-7338.